An Experimental and Theoretical Study of Binary Droplet Collisions

Karrar Hayder Neamah Al-Dirawi

Submitted in accordance with the requirements for the degree of
Doctor of Philosophy

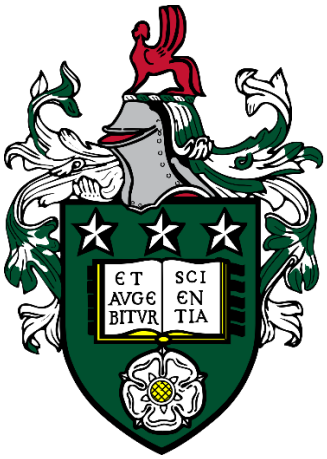

The University of Leeds
School of Chemical Engineering

August 2020

The candidate confirms that the work submitted is his/her/they own and that appropriate credit has been given where reference has been made to the work of others.

Acknowledgements

Firstly, I would like to say thank you to my supervisor, Prof Andrew Bayly, for giving me this opportunity and for his assistance throughout the past three years.

I would like to extend my thanks to Prof Phil Threlfall-Holmes and Prof Nik Kapur for providing me with the monodisperse nozzles, which are essential parts of my experimental equipment. Thank you to Prof Phil Threlfall-Holmes for providing me training on droplets generation at the beginning of my PhD, which made my start smother. Prof Phil Threlfall-Holmes was always available to answer my technical questions and provide advice. The thanks are also extended to Mr Gurdev Bhogal for his help in the mechanical and the electrical work during the rig development.

A big thank you to my parents who have been morally and financially supporting me. I would like to dedicate what I have achieved in this work to them. Also, I would like to thank my little family for being patient and supportive during my PhD.

I would like to show my appreciation to all the past and present colleagues from Prof Bayly's research group and the droplet research society in Leeds for their helpful inputs throughout the past three years.

The work was supported by the EPSRC project: "Evaporative Drying of Droplets and the Formation of Micro-structured and Functional Particles and Films" (Grant No. EP/N025245/1) and the University of Leeds.

Publications

Al-Dirawi, K.H. and Bayly, A.E., 2019. **A new model for the bouncing regime boundary in binary droplet collisions**. *Physics of Fluids*, *31*(2), p.027105.

Al-Dirawi, K.H. and Bayly, A.E., 2020**. An experimental study of binary collisions of miscible droplets with non-identical viscosities**. Experiments in Fluids, 61(2), p.50.

Al-Dirawi, K.H. and Bayly, A.E., 2019. **The role of the size and the size ratio in binary droplet collisions**. In progress.

Al-Dirawi, K.H. and Bayly, A.E., 2019. **A new model for the reflexive separation regime boundary in binary droplet collisions**. In progress.

Al-Dirawi, K.H. and Bayly, A.E., 2019. **An experimental study of binary collisions of unequal-size droplets with non-identical viscosities**. In progress.

Al-Dirawi, K.H., Al-Ghaithi K., Bayly, A.E., 2019**. A model for the post-collision trajectories of binary droplet collisions in the bouncing regime.** In progress

Conferences and Workshops

1. Droplets 2019, Durham (20 min talk);
2. 10th International Conference on Multiphase Flow 2019, Rio de Janeiro (10 min oral presentation delivered by my supervisor);
3. UK Fluids Networks Drop Dynamics SIG, Oxford 2020 (20 min oral presentation);
4. UK Fluids Networks Drop Dynamics SIG, Leeds 2019 (20 min oral presentation);
5. The 71st Annual Meeting of the American Physical Society's Division of Fluid Dynamics (10 min oral presentation);
6. International Advanced Course on Liquid, Interfaces, Drops and Sprays, 2018;
7. Summer school of multiphase flow 2017, Nottingham (flash presentation);
8. Spray drying course, Leeds, 2017;
9. ChemEng Day UK 2018, Leeds: Molecules to Manufacturing (poster);
10. Workshop on Droplet Coalescence, Durham 2017;
11. Spray Drying and Atomisation of Formulations course, Leeds 2017.

Prizes and Awards

1. Aerosol Society Doctoral Student Award (C. N. Davies);
2. Best poster at the school of chemical engineering internal research exchange, 2019, Leeds.

Abstract

Understanding the outcomes of binary droplet collisions is important to many areas of physics and technology. For a given system, the collision outcomes can be mapped, in the parameter space of impact parameter (offset between the droplets centres) and Weber number, with clear regimes boundaries. As Weber number increases, the collision outcomes are bouncing, coalescence, stretching separation at high offset and reflexive separation. This work, in collisions of miscible droplets, experimentally and theoretically investigates the role of the viscosity, viscosity difference, size and size ratio as they have impacts on the collisions' outcomes and hence the position of the regime boundaries in the regime map.

Increasing the viscosity, decreasing the size and decreasing the size ratio (d_s/d_l), qualitatively, have the same impact on the collisions outcomes, as both enhance the coalescence regime by suppressing the other regimes.

Collisions of droplets with non-identical viscosities show the following behaviours. The bouncing boundary shows an intermediate position compared to the identical viscosity cases, however, at high viscosity difference, a new regime was observed, namely, partial bouncing which is bouncing with a very thin ligament between the droplets. Likewise, in equal-size collisions, and in unequal size collisions where the large droplet has the higher viscosity, the boundary of reflexive separation regime shows an intermediate position. However, in unequal-size collisions, if the larger droplet has the lower viscosity the boundary remains similar to the identical viscosity case of the low viscosity droplet. Finally, stretching separation always shows a boundary similar to that of the identical viscosity case of the low viscosity droplet.

New models for the boundaries of the bouncing and the reflexive separation regimes were developed to consider the effects of the viscosity, the impact parameter and the size ratio.

Table of Contents

List of Tables

List of Figures

Nomenclature

Latin Characters

B	Impact parameter	-
d	Droplet diameter	m
m	Mass	kg
Oh	Ohnesorge number	-
R	Droplet radius	m
r	Spherical cap radius	m
Re	Reynolds number	-
S	Surface area	m^2
u	Velocity	$m\ s^{-1}$
V	Volume	m^3
We	Weber number	-
X	Volume ratio of interaction regions	-

Greek Characters

ρ	Density	$kg\ m^3$
μ	Viscosity	Pa s
σ	Surface tension	$N\ m^{-1}$
α	Viscous loss to kinetic energy	-
Δ	Size ratio (small/large)	-
ϕ	Shape factor	-

Subscripts

c	Critical
B/FC	Bouncing to fast coalescence at B = 0
FC/RS	Fast coalescence to reflexive separation at B = 0
l	Large droplet
s	Small droplet
r	relative

Chapter 1: Introduction

1.1 Background and motivation

Droplet collisions, apart from being classical problems in fluid mechanics, are ubiquitous in natural phenomena and many spray applications. In meteorology, raindrops are formed by coalescence-collisions of many extremely small droplets in the clouds that lead to larger droplets that cannot be sustained on the air current (Low et al., 1982; Saffman and Turner, 1956). In spray applications, such as spray painting, spray coating of pharmaceutical and food products (Hilton et al., 2013), spray combustion (Gavaises et al., 1996; Wang et al., 2003) and spray drying (Verdurmen et al., 2004), droplet collisions can change the spray structure and leads to wanted or unwanted consequences. Therefore, understanding and predicting the outcome of droplet collisions are crucial in these areas.

In many of the aforementioned areas, the droplet collisions occur between droplets of different properties. For example, in spray drying, particulate products are produced by spraying solutions or slurries into hot, turbulent air in a spray drying tower. During the drying process, droplets' properties change. Typically, the droplets undergo size reduction, due to solvent evaporation, and viscosity increase due to solute concentration increase caused by the solvent evaporation. Because of the change in the droplets' properties in addition to an initial droplet size distribution and circulations by the turbulent air, identical and non-identical droplet collisions can occur between miscible droplets of different sizes and viscosities (Southwell and Langrish, 2000). These collisions and their outcomes can have significant effects on the process operation and on the powder properties, such as the size distribution and morphology (Verdurmen et al., 2004; Mezhericher et al., 2008). Understanding the impact of the viscosity, size, and size ratio on the outcomes of collisions of identical and non-identical droplets is, therefore, of great interest in this and other areas.

In the previous studies, binary droplet collisions were considered experimentally and theoretically (Orme, 1997; Krishnan and Loth, 2015; Sommerfeld and Pasternak, 2019). In regime maps, using the Weber number (represents the ratio of kinetic energy to

surface energy) and the offset between the droplets as parameter space, five different collision outcomes were reported, namely slow coalescence, bouncing, fast coalescence, stretching separation and reflexive separation. these regimes have well-defined boundaries. These boundaries quantitatively change with viscosity and size-ratio as these two variables are not captured in the Weber number. Therefore, many studies were conducted to study the role of the viscosity and fewer to study the role of the size ratio. However, the majority of these studies are for collisions of droplets from the same liquid.

Experimental studies were reported regarding collisions of droplets from non-identical liquids. However, the majority of these studies is on the collisions of immiscible droplets. In collisions of miscible droplets, only the role of the surface tension difference was considered. Thus, although studies of collisions of equal-size and unequal-size of miscible droplets with non-identical viscosities are of great industrial relevance, they remain as a knowledge gap in the literature.

To predict the collision outcomes, many studies reported empirical and theoretical models to predict the regimes' boundaries (Krishnan and Loth, 2015; Sommerfeld and Pasternak, 2019). However, the reported models, apart from being designed for collisions of droplets from the same fluid only, either have limitations due to missing underlying physics or lack generality due to not considering factors such as the size ratio, the offset (i.e. models of head-on collisions only) and the viscosity.

1.2 Aims and objectives

In this work, the effects of the viscosity, size and size ratio on the collision outcomes will be investigated in collisions of miscible droplets with identical and non-identical viscosities. Moreover, the performance and the applicability of the existing models to such collisions will be assessed, and new models will be developed. This will be achieved through the following objectives:

- Design and develop a rig to conduct binary droplet collisions experiments;
- Conduct experiments of binary collisions of identical droplets at different viscosities to provide a comparative basis for non-identical viscosity collisions;

- Conduct experiments of binary collisions between miscible droplets with different viscosities to be compared against the collisions of identical droplets to study the role of the viscosity difference;
- Conduct a systematic study to investigate the role of the size and the size ratio at different viscosities in collisions between droplets from the same liquid;
- Investigate the role of the size ratio in collisions of miscible droplets with non-identical viscosities;
- Assess the performance of the existing models of the regimes' boundaries against the conducted experiments of the collisions between droplets from the same liquid;
- Examine the applicability of the existing models in the prediction of the regime boundaries of collisions between miscible droplets with non-identical viscosities;
- Define the limitations of the existing models and any missing underlying physics that can be crucial for the collisions' behaviours;
- Develop new, general and accurate models to predict the regime boundaries by extending the existing models to consider the missing underlying physics.

1.3 Thesis structure

The outline of the thesis is given as follows:

Chapter 2 reviews the relevant literature work and highlights the knowledge gaps. It starts with a general background then reviews experimental work of the collisions of droplets of identical liquid. Chapter 2 then covers collisions of droplets from non-identical liquids including immiscible droplets and miscible droplets. Finally, the existing models of the regimes' boundaries are reviewed, and their limitations are discussed. The chapter is closed by a conclusion that highlights the current gaps in the literature that motivates this project.

Chapter 3 covers the experimental methodology used in this thesis. This includes design and development of a rig to conduct binary droplet collisions experiments. The rig capabilities are explained. Then, a description of an image processing algorithm to track the droplets is given. Finally, the conducted experiments are described, and an assessment of experimental errors is provided

Chapter 4 investigates the role of the viscosity difference in collisions of equal-size droplets. The chapter starts with an investigation to the effect of the viscosity in collisions of identical droplets. Then, the role of the viscosity is investigated in experiments of collisions of droplets with non-identical viscosities by the comparison against the collisions of droplets with identical viscosities. Finally, the performance of the existing models of the regimes' boundaries is assessed and their applicability in collisions of non-identical viscosities is discussed.

Chapter 5 studies the role of the size and the size ratio in collisions of droplets with identical viscosities, and the role of the size ratio in collisions of droplets with non-identical viscosities. The chapter starts with experiments of collisions of identical droplets for two different sizes at two different viscosities to study the role of the size at different viscosities. These experiments are compared to collisions of unequal-size droplets to investigate the influence of the size ratio. In this chapter, the dynamics of collisions of unequal-size droplets with non-identical viscosities are investigated as well. Finally, the chapter assesses the performance of the existing models in predicting the regime boundaries of the provided experiments.

Chapter 6 proposes a model for the reflexive separation regime boundary. The chapter starts with a discussion of the limitations of the existing models of the reflexive separation regime boundary that were defined in the literature and chapters 4 and 5. Then, novel experimental observations to the dynamics of the collision are made to address the crucial underlying physics that needs to be considered to generate an accurate and general model. Finally, a new model is proposed and its performance is compared against experiments reported in the literature and chapters 4 and 5.

Chapter 7 proposes a model for the bouncing regime boundary. The chapter starts by discussing the existing models and their assumptions. An analysis of the missing underlying physics is provided by making observations from the dynamics of the collision and the comparison of the existing models against the experimental boundaries. Finally, the missing underlying physics are considered and a new model is provided.

Chapter 8 provides a summary of the main conclusions from this work followed by future work.

Chapter 2: Literature review

2.1 Introduction

Binary droplet collisions have received increasing attention in the last few decades due to their relevant importance for many atmospheric phenomena (Ochs III et al., 1995) and industrial applications, such as spray drying (Francia et al., 2017; Francia et al., 2016; Verdurmen et al., 2006). In most of the spray applications, to model and simulate the process, it is crucial to predict the collisions' outcomes (Pawar et al., 2015, Almohammed and Breuer, 2019, Finotello et al., 2019a, Finotello et al., 2019b, Ko and Ryou, 2005). In such simulations, the collisions' outcomes are predicted using empirical/theoretical models, which need negligible computational effort (sub-models). Therefore, to understand the underlying physics of the collisions and generate these models, many experimental studies of binary droplet collisions were conducted to construct regime maps for the outcomes of the collisions based on the impact details (i.e. the kinetic details and the physical properties of the droplets) (Sommerfeld and Pasternak, 2019; Orme, 1997).

Across the regime maps of different systems, the boundaries between the regimes are non-identical. With this in mind, depending on the application, many cases of binary droplet collisions can occur, such as collisions between droplets from identical liquid or from different liquids, which can be miscible or immiscible. These types of collisions also might occur in different cases as they can be at different scales, size ratios, and wetting and rheological properties. However, the reported studies are for limited cases and consequently, the provided models, based on these experiments, lack generality.

In this chapter, the literature of binary droplet collisions is reviewed with the main focus on experimental studies. It starts with the theory of binary droplet collisions, which includes the types of collision outcomes and the regime maps. Then, the reported findings regarding the role of the size, size ratio and viscosity will be reviewed for collisions of droplets from identical and non-identical liquids. Finally, models of the boundaries between the collisions outcomes regimes are reviewed, and their limitations

will be highlighted. This chapter is concluded by a summary of the review in which the knowledge gaps that motivates this thesis will be highlighted.

2.2 Theory

2.2.1 Dimensionless groups

Dimensionless groups are usually used to quantify the physics that dominate the dynamics of droplet collisions. As the surface tension and the viscosity become very important at the scale of droplets, the most important dimensionless groups are:

- Weber number (We): the ratio of the kinetic energy to the surface energy, given by Eq. (2.1).
- Reynolds number (Re): the ratio of the inertia to the viscous forces, given by Eq. (2.2).
- Ohnesorge number (Oh): the ratio of the viscous forces to the inertial and the surface tension forces, given by Eq. (2.3).

Table 2.1 Different definitions for some important dimensionless groups.

Weber number	$\mathrm{We} = \frac{\rho d u_r^2}{\sigma}$	$\mathrm{We} = (\mathrm{Oh}\,\mathrm{Re})^2$	(2.1)
Reynolds number	$\mathrm{Re} = \frac{\rho u_r d}{\mu}$	$\mathrm{Re} = \frac{\sqrt{\mathrm{We}}}{\mathrm{Oh}}$	(2.2)
Ohnesorge number	$\mathrm{Oh} = \frac{\mu}{\sqrt{\rho d \boldsymbol{\sigma}}}$	$\mathrm{Oh} = \frac{\sqrt{\mathrm{We}}}{\mathrm{Re}}$	(2.3)

Where ρ, u_r, d and μ are density, relative velocity, droplet diameter and droplet viscosity, respectively.

2.2.2 Collisions outcomes and regime maps

In the literature of binary collisions, five distinct collision outcomes were observed: slow coalescence, bouncing, fast coalescence, reflexive separation and stretching separation (Qian and Law, 1997). These regimes are typically mapped in the parameter space of the impact parameter (B) and the Weber number, as shown in Figure 2.1. The impact

parameter represents the offset between the colliding droplets. It is defined by the normal distance (b) from the centre of one of the colliding droplets to the vector of the relative velocity (u_r), which is plotted from the centre of the other droplet, normalized by the sum of the two droplets radii, Eq. (2.5), as sketched in Figure 2.2. Therefore, B has a value between 1 and 0, where 1 indicates a grazing collision and 0 a head-on collision.

$$\mathrm{B} = \frac{2b}{d_s + d_l}, \tag{2.4}$$

d_s and d_l are the small and the large droplet diameters, respectively, in case of any size ratio between the colliding droplets. Note that, We is defined using d_s in the case of unequal-size droplet collisions (Ashgriz and Poo, 1990).

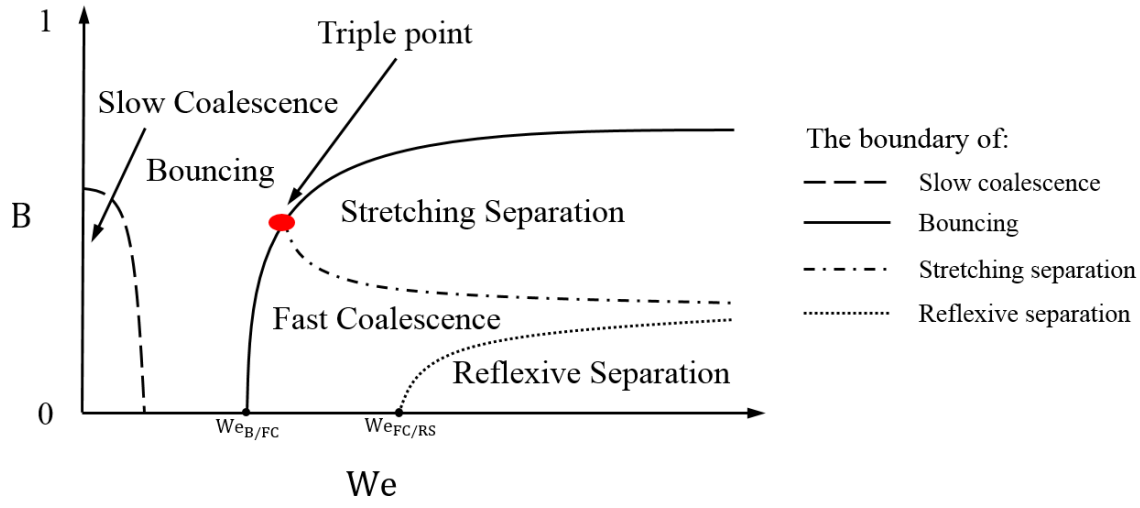

Figure 2.1 A schematic illustration of a typical regime map.

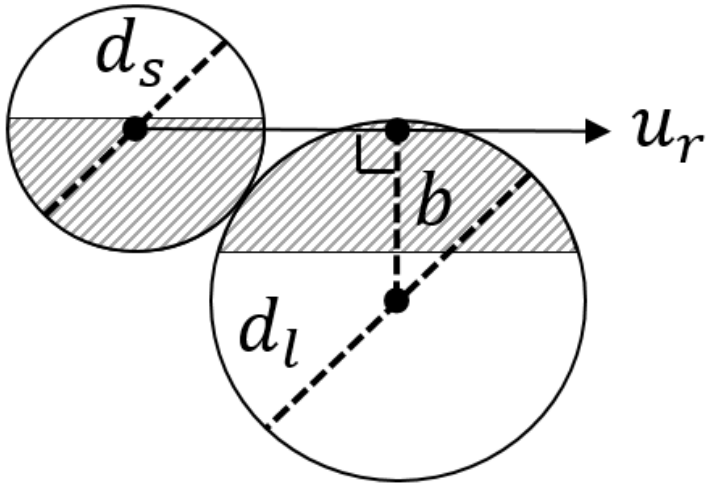

Figure 2.2 Schematic of the droplet collision geometry that shows the definition of the impact parameter.

The five distinct collisions outcomes are shown in Fig 2.3 and are characterized as follows:

- Slow coalescence: occurs when the two droplets approach each other at low We, so the gas between the droplets has a sufficient time to drain and the interfaces merge without significant deformation prior to the coalescence (Qian and Law, 1997), as shown in Figure 2.3a.
- Bouncing: occurs at a higher We than slow coalescence, in this case, an air film is trapped between the two colliding droplets. This prevents the interfaces from being close enough to each other to allow the intermolecular forces to merge the droplets (Qian and Law, 1997). As a result, the droplets deform on impact and their kinetic energy is converted to viscous loss and surface energy. Then, as the droplets tend to recover to their equilibrium spherical shape, the increase of the surface energy at the maximum deformation is converted back to viscous loss and the kinetic energy of the rebounding droplet, as shown in Figure 2.3b.
- Fast coalescence: with increasing We, the intervening air film thins to a point where coalescence occurs with significant deformation prior to the coalescence (Qian and Law, 1997), as shown in Figure 2.3c.
- Reflexive separation: occurs at low B (or at near head-on collisions) at We higher than that of fast coalescence. The droplets first merge forming a rimmed lamellar

disc shape, and then by the effect of the surface tension, a reflexive internal flow is induced. The flow driven by the shrinking rimmed lamellar disc is strong enough to make a cylindrical droplet that eventually breaks up into two or more droplets, as shown in Figure 2.3d. At the onset of the reflexive separation, the break-up of the cylinder results in two droplets that have about the same volume of the initial droplets and a small satellite droplet (Huang et al, 2019). However, by increasing the impact velocity, the size of this satellite droplet increases (Ashgriz and Poo, 1990).

- Stretching separation: starts at We slightly higher than that of the fast coalescence but at a moderate B. The two droplets partially interact and because of the momentum of the non-interacted regions the merged area is stretched forming a ligament between the two colliding droplets that eventually breaks up into satellite droplets, as shown in Figure 2.3e. The number of satellite droplets increases by increasing We and it also increases by increasing B for a certain limit then it starts decreasing by further increasing B (Brenn et al., 2001).

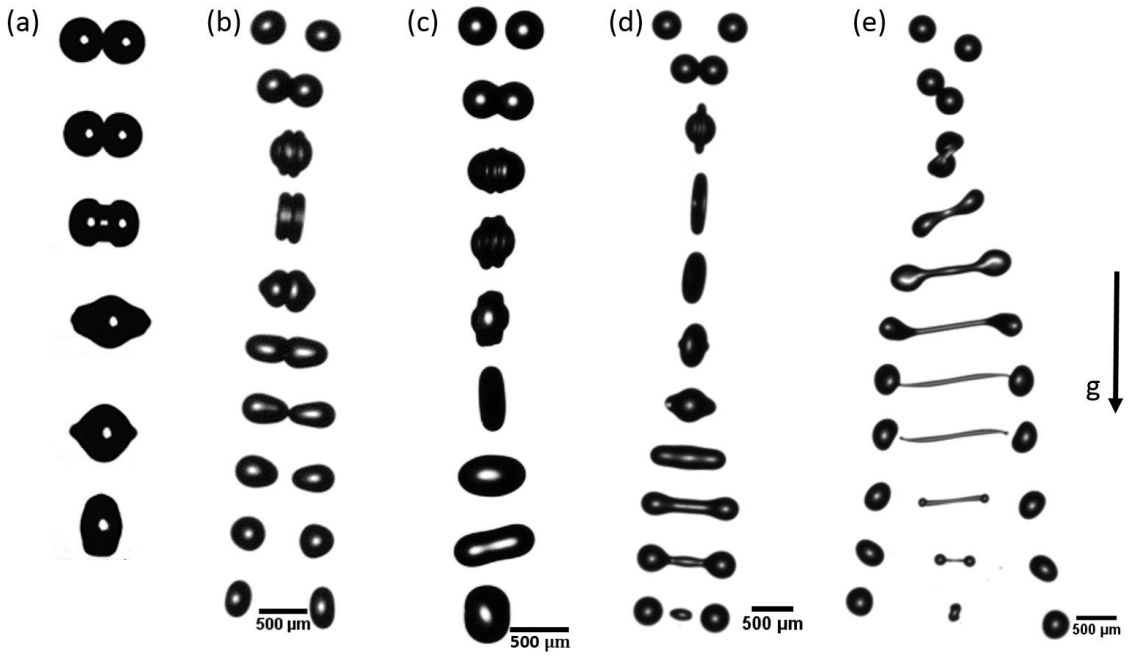

Figure 2.3 The collision outcomes: (a) slow coalescence of water droplets adapted from (Pan et al., 2016); (b) bouncing of 2% HPMC droplets; (c) fast coalescence of 2% HPMC droplets; (d) reflexive separation of 2% HPMC droplets; (e) stretching separation of 2% HPMC droplets. HPMC stands for Hydroxypropyl Methylcellulose and more details about it will be given in section 3.6.

2.3 Collisions of droplets with identical liquids

The majority of the conducted experiments are for collisions of droplets from the same liquid (Orme, 1997; Krishnan and Loth, 2015; Sommerfeld and Pasternak, 2019). Generally, these experiments are either to study the role of the viscosity or the role of the size ratio, see Table 2.2. Some of these studies also involve investigating some of the other factors such as the type and the pressure of the surrounding gas (Qian and Law, 1997) and the effect of the surfactants (Pan et al., 2016). In this section, the main findings of these studies will be reviewed.

2.3.1 The role of the viscosity

The early studies in the field of binary droplet collisions used water droplets where the viscosity effect is negligible, such as Adam et al. (1968), Brazier-Smith et al. (1972), Ashgriz and Poo (1990b). Water droplet collisions in these studies show only three collision outcomes: fast coalescence, reflexive separation, and stretching separation. Later on, Jiang et al. (1992) and Qian and Law (1997) used n-alkanes droplets ($\mu < 3.5\ \mathrm{mPa\ s}$), which show the five distinct collision outcomes regimes, reported in section (2.2.2). The different outcomes regimes between water and n-alkanes were attributed to the difference in rheological properties.

Due to the importance of understanding collisions at a higher viscosity range in applications like spray drying, more recent studies have considered viscosities up to 100 mPa s (Willis and Orme, 2003, Gotaas et al., 2007b, Kuschel and Sommerfeld, 2013, Sommerfeld and Kuschel, 2016, Finotello, 2019, Finotello et al., 2018a, Finotello et al., 2018b, Finotello et al., 2017). It was reported that elevating the viscosity shifts the boundary of reflexive separation towards high Weber numbers while shifting the boundary of stretching separation to higher impact parameters. This was attributed to more viscous loss that promotes the coalescence regime.

Unlike the regimes of reflexive separation and stretching separation, the role of the viscosity in the bouncing regime has received less attention. This might be due to the limited number of studies that show a clear transition from the bouncing regime to the fast coalescence regime at head-on collisions ($\mathrm{We}_{\mathrm{B/FC}}$). The absence of a bouncing to fast coalescence transition at head-on collisions could be attributed to the droplets' fluid

properties, as some fluids do not show bouncing at low B, such as water (Qian and Law, 1997) and ethanol (Estrade et al., 1999), or they do not show any bouncing at the entire range of B, such as milk (Finotello et al., 2018b).

However, Krishnan and Loth (2015) suggested based on a literature survey that for head-on collisions, the regime boundary $\mathrm{We}_{\mathrm{B/FC}}$ would be expected to increase with increasing viscosity. However, the basis of this claim is based on extrapolation of data from high B to low B, for fluids which are not seen to bounce at B = 0, rather than direct collision data.

Pan et al. (2016) also showed that the addition of glycerol to water, to increase the viscosity, enlarges the bouncing regime compared to pure water droplets. The propensity of the droplets to coalescence or bounce depends on the drainage rate of the air trapped between the droplets, which determines if the two interfaces are close enough to coalesce or not before the bouncing off. The drainage of the gas is associated with surface mobility (Pan et al., 2016). Thus, Pan et al. (2016) argued that increasing the viscosity reduces the surface mobility and hence reduces the rate of the air film drainage, which consequently promotes the bouncing regime.

2.3.2 The role of the size

The discussion of the role of the size, in collisions of equal-size droplets, is rare in the literature. Adam et al. (1968) reported two regime maps, in the parameter space of the impact parameter and the impact velocity, for water droplets of two different diameters 150 μm and 600 μm. Orme (1997) recast these regime maps in terms of B and We. The modified regime maps show that increasing the size promotes the coalescence regime by shifting the boundary of the reflexive separation regime towards higher We and the boundary of the stretching separation regime towards higher B. On the other hand, according to Orme (1997), Ashgriz and Poo (1990) showed that the size of the water droplets does not affect the regime maps. Thus, the lack of studies on the effect of size and the difference in the findings between Adam et al. (1968) and Ashgriz and Poo (1990) highlights the need for further studies to understand the role of the size in binary droplet collisions of equal-size droplets.

2.3.3 The role of the size ratio

Collisions of droplets with non-identical size have received less attention than those of identical size. Ashgriz and Poo (1990) was one of the first studies that conducted collisions of unequal-size droplets. The study focused on collisions of water droplets at different size ratios (0.5, 0.75, and 1), where, the size ratio is given by

$$\Delta = \frac{d_s}{d_l} \tag{2.5}$$

The author reported that decreasing the size ratio enlarges the coalescence regime by shifting the reflexive separation regime boundary to higher We while the boundary of the stretching separation regime is shifted to higher B. it should be mentioned that Ashgriz and Poo (1990) suggested that in case of collisions of non-identical size, the diameter of the smaller drop is used in We. The above findings of Ashgriz and Poo (1990) show that the conventional regime maps, in the space parameter of We and B, are not universal in terms of size ratio.

Rabe et al. (2010) tried to provide another way of representing We, in case of collisions of droplets with non-identical size, by which, a universal regime map can be constructed. The authors suggested using symmetric Weber number ($\mathrm{We_s}$), given by Eq. (2.6), instead of using the small droplet diameter in the conventional We. The symmetric Weber number represents the sum of kinetic energies on the sum of surface energies of the two droplets. The use of $\mathrm{We_s}$ shows that the boundaries of the stretching separation and the reflexive separation, of regime maps with size ratios of 1, 0.75, and 0.5, collapse on each other as shown in Figure 2.4.

$$\mathrm{We_s} = \frac{E_{k,l} + E_{k,s}}{E_{\sigma,l} + E_{\sigma,s}} = \mathrm{We}\frac{\Delta^2}{12(1+\Delta^3)(1+\Delta^2)} \tag{2.6}$$

Where $E_{k,l}$, $E_{k,s}$, $E_{\sigma,l}$ and $E_{\sigma,s}$ are the kinetic energies in the zero frame reference and the surface energies of the large and the small droplets, respectively.

It should be noted that neither Ashgriz and Poo (1990) nor Rabe et al. (2010) reported any bouncing data. Tang et al. (2012) also conducted experiments of collisions of unequal-size droplets using decane and tetradecane droplets, where bouncing data was reported. However, the study was limited to head-on collisions. Therefore, regime maps

were possible to be constructed in the parameter space of Δ and We, as shown in Figure 2.5. In addition to the bouncing regime, the regimes that were reported in these maps are fast coalescence and reflexive separation. The effect of the size ratio on the reflexive separation regime boundary in Tang et al. (2012) agrees qualitatively with the findings of Ashgriz and Poo (1990) and Rabe et al. (2010). However, the bouncing regime shows weak dependence on the size ratio, as can be seen in Figure 2.5.

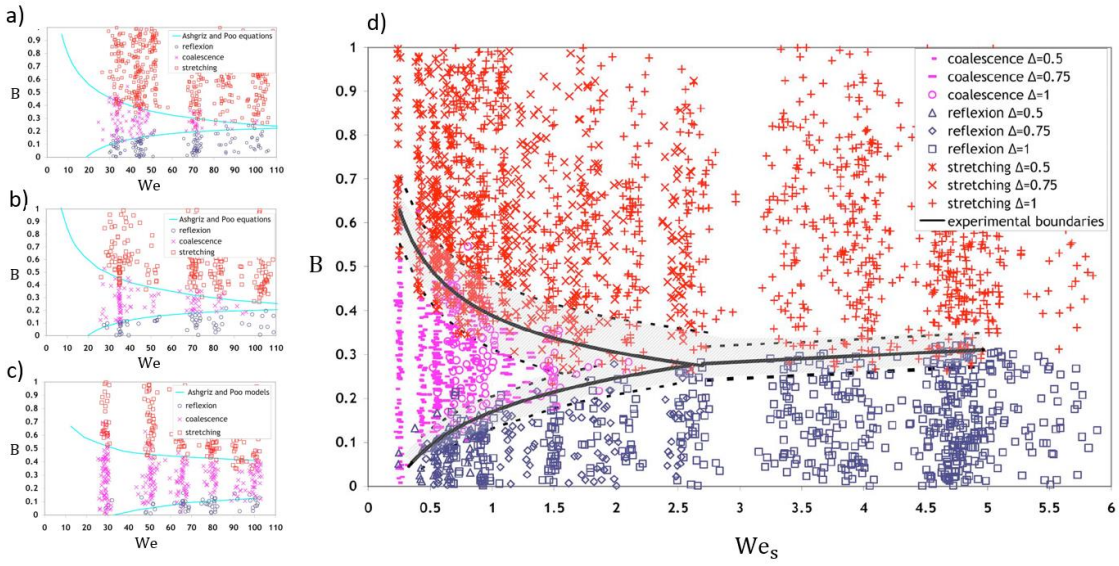

Figure 2.4 Water droplets collisions outcomes regime maps adapted from Rabe et al. (2010). a, b and c are conventional regime maps for $\Delta = 1$, $\Delta = 0.75$, and $\Delta = 0.5$, respectively; d) is the universal regime map that combines all data of a, b and c using the symmetric Weber umber.

Collisions of unequal-size droplets were also considered in other studies. Estrade et al. (1999) constructed conventional regime maps for ethanol droplets collisions with size ratios 1 and 0.5. These regime maps show for regimes: bouncing only at high impact parameter (B > 0.3), fast coalescence, reflexive separation, and stretching separation. Estrade et al. (1999) findings are consistence with findings of Ashgriz and Poo (1990) and Tang et al. (2012).

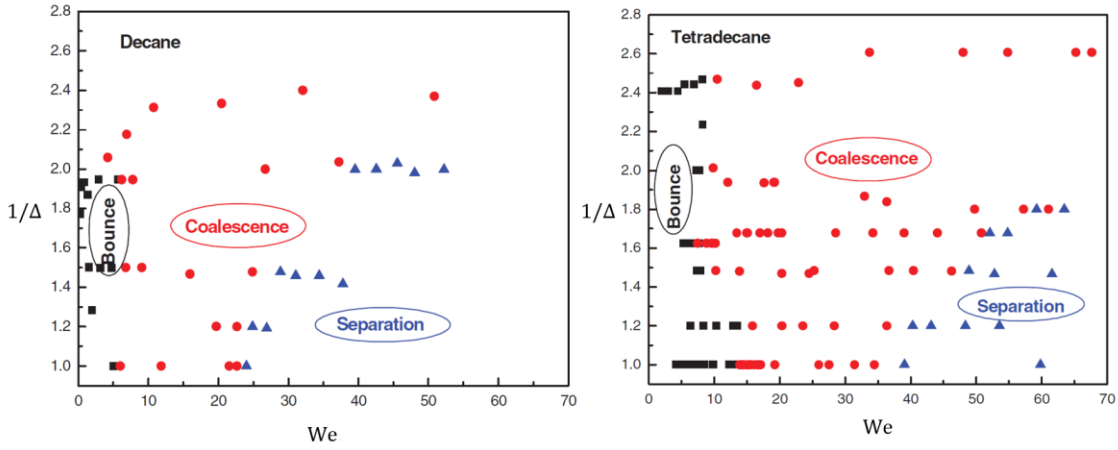

Figure 2.5 Head-on regime maps in the parameter space of the size ratio and Weber number adapted from Tang et al., (2012)

Sommerfeld and Pasternak (2019) considered collisions of unequal-size droplets at relatively higher viscosities compared to the already mentioned studies. The liquids that were considered are sunflower oil and PVP K17 (polymer aqueous solution). Conventional regime maps in term of We and B were constructed showing bouncing, fast coalescence, reflexive separation and stretching separation. The data shows that reducing the size ratio down to 0.34 remarkably suppresses the stretching separation regime by shifting its boundary towards higher B, as shown in Figure 2.6.

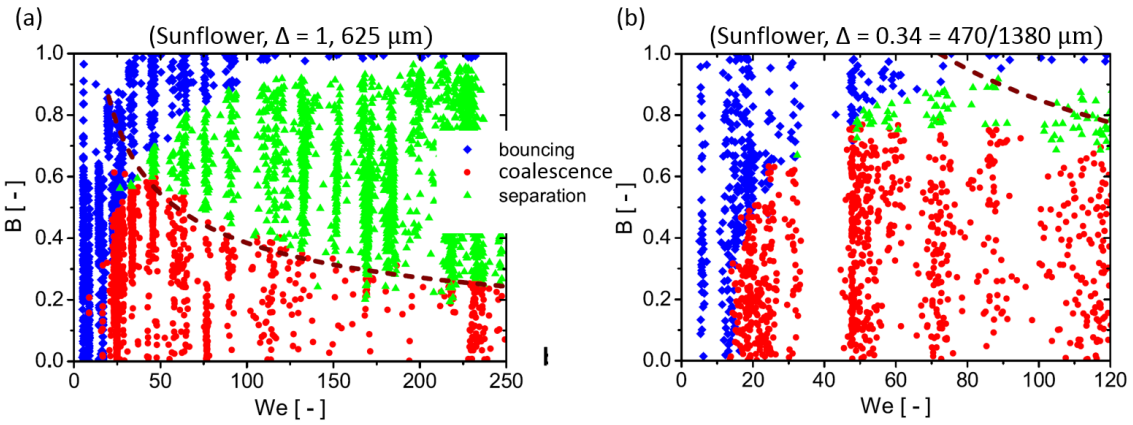

Figure 2.6 Regime maps showing the effect of the size ratio on the boundary of the stretching separation, adapted from Sommerfeld and Pasternak (2019).

Another recent study that considers the role of the size ratio, in head-on reflexive separation collisions, was by Huang et al. (2019). The study confirms the findings of Tang et al. (2012), which shows that decreasing the size ratio shifts the reflexive separation

regime towards higher Weber numbers. In addition, Huang et al. (2019) report that decreasing the size ratio supresses the formation of satellite droplets in reflexive separation.

However, although the role of the size ratio was studied in the literature, there is no systematic study that compares the unequal-size case to the equal-size cases of the same droplets scale. For example, none of the sizes used in Figure 2.6b is equal to the size used in Figure 2.6a. This is probably due to the assumption that the regime maps of collisions of equal-size droplets of a given liquid are universal regardless of the droplet size. Moreover, there is still no clear explanation of why the size ratio promotes coalescence by suppressing the separation regimes. Thus, further investigations are required.

2.3.4 The role of the surrounding gas

Qian and Law (1997) reported that increasing the pressure and/or density of the surrounding gas increases the size of the bouncing regime. The authors also reported that increasing the vapour content of the droplets fluid in the surrounding gas suppresses the bouncing regime. However, changing the gas properties has no pronounced influence on the other separation regimes.

2.3.5 The role of the addition of surfactants

Pan et al. (2016) showed that adding a surfactant to water droplets can enhance the bouncing regime significantly. This was attributed to the fact that as the droplets deform before the coalescence, the concentration of the surfactant on the deformed interface will be decreased. This will create a surface tension gradient, with its highest value at the deformed interfaces. Thus, Marangoni stress will occur and induce a flow toward the deformed interfaces, which in turn induces a drag force against the gas drainage flow and hence enhances the bouncing.

2.4 Collisions of droplets with non-identical liquids

Collisions between droplets with non-identical physical properties have also been studied but received less attention than the collisions of droplets from the same liquid.

These studies can be divided into two categories: collisions between immiscible droplets and collisions between miscible droplets.

2.4.1 Collisions of immiscible droplets

Immiscible droplet collisions were studied experimentally and theoretically. Chen and Chen (2006) experimentally studied collisions between water and diesel droplets. Collisions between silicone oil and glycerol aqueous solutions were experimentally studied by Planchette et al. (2010) and Planchette et al. (2011) and theoretically by Roisman et al. (2012), Planchette et al. (2012), and Planchette et al. (2017).

Chen and Chen (2006) reported regime maps in the parameter space of We and B. However, as water and diesel have different surface tension and densities, the author suggested using the physical properties of the lower surface tension droplet in We. This was attributed to the fact that the collisions' outcomes are controlled by the lower surface tension droplet. On the other hand, Planchette et al. (2010) and Planchette et al. (2011) constructed regime maps in the parameter space of the impact velocity and the impact parameter. Four distinct regimes were reported namely bouncing (only by Chen and Chen (2006)), encapsulation, stretching separation and different types of reflexive separation depending on the properties of the droplets. The regime maps are qualitatively similar to that of identical droplet collisions, where the encapsulation regime is equivalent to the coalescence regime.

Chen and Chen (2006) reported that, in the bouncing regime, the different surface tension between the water and the diesel oil droplet leads to different extent of deformation. The diesel oil droplet deforms more than the water droplet due to the lower surface tension (σ = 0.028 N m^{-1}), as shown in Figure 2.7a.

In the encapsulation regime, the lower surface tension droplet covers the high surface tension droplet (Chen and Chen, 2006; Planchette et al., 2010; Planchette et al., 2011), as shown in Figure 2.7b.

In the stretching separation regime, the ligament is from the encapsulating droplet, as shown in Figure 2.7c, and hence its viscosity has an influence on the regime boundary while the viscosity of the encapsulated droplet has no influence. Increasing the viscosity

of the encapsulating droplet shifts the boundary of the stretching separation regime to a higher B.

The reflexive separation regime is more complicated than the other regimes as three types were reported namely cross separation, single reflexive separation and reflexive separation (Planchette et al., 2011). Cross separation occurs If the viscosity of the encapsulating droplet is lower than the encapsulated one (Planchette et al., 2010; Planchette et al., 2011). The encapsulating drop flows around the encapsulated one and stretches from the other side and separates resulting in an encapsulated droplet and a pure droplet from the encapsulating fluid, as shown in Figure 2.7d. Single reflexive separation occurs if the viscosity of the encapsulating droplet is close to or greater than that of the encapsulated droplet (Chen and Chen, 2006; Planchette et al., 2011). The encapsulating droplet stretches the encapsulated one during its flow around it, consequently, the separation results in two encapsulated droplets, as shown in Figure 2.7e. Finally, if the density of the encapsulating droplet is sufficiently higher than the encapsulated droplet reflexive separation occurs (Planchette et al., 2011). However, this reflexive separation is not quite similar to that of the identical droplets, as a large amount of the encapsulating droplet flows around the encapsulated one, while the rest of the droplet shows a reflexive flow away from the encapsulated system until separation as shown in Figure 2.7f.

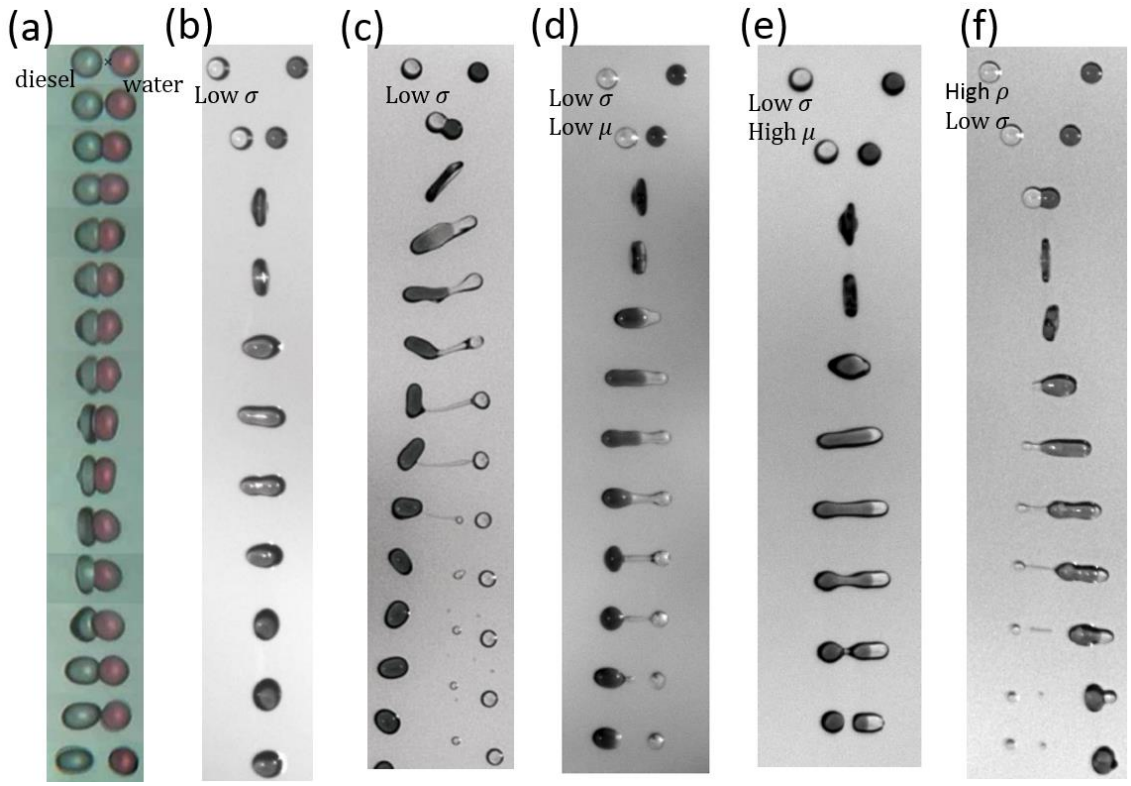

Figure 2.7 Collisions of immiscible droplets. (a) bouncing adapted from Chen and Chen (2006); (b) encapsulation (50% glycerol-water solution (dark) with silicone oil mixture M5); (c) stretching separation (50% glycerol-water solution (dark) with silicone oil mixture M5) adapted from Planchette et al. (2012 (d) crossing separations (50% glycerol-water solution (dark) with silicone oil mixture M5); (e) single-reflex separation (50% glycerol-water solution (dark) with silicone oil mixture M5/M10); (f) reflexive separation in collisions of droplets with a significant difference in density (50% glycerol-water solution vs. fluorodecaline). The columns b, d-f adapted from Planchette et al. (2011).

2.4.2 Collisions of miscible droplets

Studies of collisions of miscible droplets from unlike fluids are relatively scarce, as summarized in Table 2.2. Gao et al. (2005) studied collisions between water and ethanol droplets, and Chen (2007) experimentally investigated collisions between ethanol and diesel droplets. Both studies discuss the role of the surface tension differences. In both studies, regime maps were constructed using the parameter space of B and We, where the lower surface tension was used to define We.

Chen (2006) reported that the reflexive separation of diesel-ethanol collisions occurs at lower We than diesel-diesel droplet collisions. This was attributed to the non-uniform ligament before the separation, as it has more necking near the ethanol droplet than

the diesel droplet, which accelerates the separation, as shown in Figure 2.8a. However, the stretching separation of diesel-ethanol collisions occurs at higher B than diesel-diesel droplet collisions. The author attributed this to the spreading of ethanol to the ligament because of the difference in the surface tension ($\sigma_d = 0.028 > \sigma_e = 0.023$ N m^{-1}), which makes the ligament thicker and hence harder to break, as shown in Figure 2.8b.

Gao et al. (2005) studied collisions between water and ethanol which have a significant difference in their surface tension ($\sigma_w = 0.072 > \sigma_e = 0.023$ N m^{-1}). The large difference in surface tension leads to unbalanced surface forces (Marangoni effects) which cause liquids fingers at the higher surface tension droplets that produce satellite droplets as shown in the stretching separation in Figure 2.8c and the reflexive separation in Figure 2.8d. Note that, the liquid finger was also seen in the coalescence regime.

Finally, although collisions of miscible droplets from unlike fluids were studied by Gao et al. (2005) and Chen (2006), these studies are limited to low viscosity range (1–3.16 mPa s). There was another attempt to study higher viscosity ranges by Focke et al. (2013) who conducted a detailed numerical and experimental study of collisions with a high viscosity ratio (2.6 vs. 60 mPa s), however, their study was limited to the coalescence regime with a fixed We of 26 and no regime maps were constructed. Moreover, the bouncing regime was not discussed in the reported studies. Thus, more systematic studies are required, especially at high viscosity difference due to their industrial relevance, such as in spray drying.

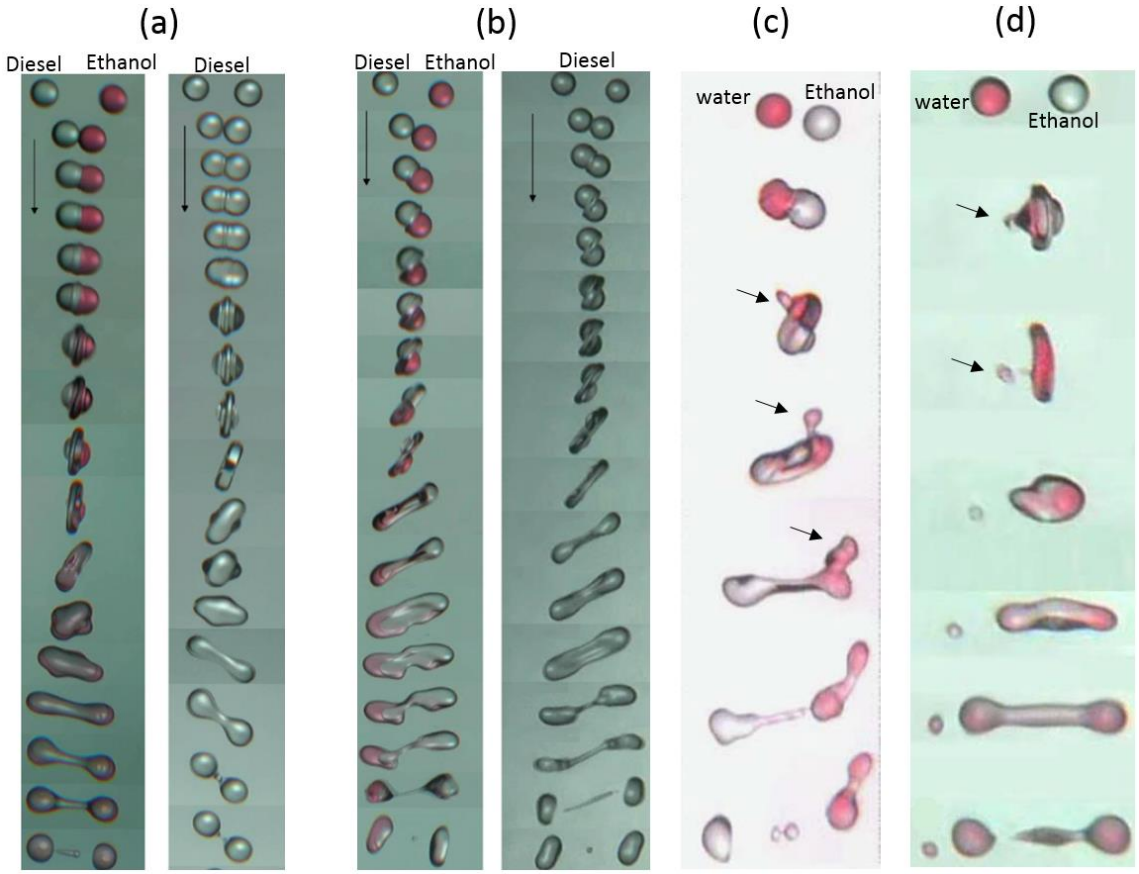

Figure 2.8 (a) Reflexive separation at We = 40 and B = 0.15; (b) stretching separation at We = 71 and B = 0.41; (c) stretching separation with liquid finger (pointed by black arrows) at We = 38 and B = 0.70; (d) reflexive separation with liquid finger (pointed by black arrows) at We = 38.5 and B = 0.02. (a and B) adapted from Chen (2006) and (c and d) from Gao et al. (2005).

Table 2.2 Summary of the reported experiments of binary droplet collisions.

Reference	d_s μm	Δ	B	Liquid	ρ kg m^{-3}	μ mPa s	σ mN m^{-1}
(Qian and Law, 1997)	300	1	0-1	Water	1000	1	73
	300	1	0-1	Tetradecane	773	2.3	27
(Estrade et al., 1999)	200	0.5,1	0-1	Ethanol	789	1.166	22
(Rabe et al., 2010b)	200	0.5-1	0-1	Water	1000	1	73
(Ashgriz and Poo, 1990a)	300	0.5-1	0-1	Water	1000	1.002	73
(Jiang et al., 1992)	300	1	0-1	Heptane	680	0.4	21
	300	1	0-1	Decane	726	0.9	24
	300	1	0-1	Dodecane	755	1.45	25
	300	1	0-1	Tetradecane	773	2.3	27
	300	1	0-1	Hexadecane	780	3.35	27
(Tang et al., 2012b)	100	0.43-1	0	Tetradecane	773	2.3	26.5
	100	0.4-1	0	Decane	730	0.92	23.8
	100	0.47-1	0	Water	1000	1	72.9

(Gotaas et al., 2007b, Gotaas et al., 2007a)	350-356	1	0-1	Monoethyleneglycol	1113	2.181	51
	351-364	1	0-1	Diethyleneglycol	1118	3.826	50
	357-375	1	0-1	Triethyleneglycol	1125	4.794	47
(Kuschel and Sommerfeld, 2013, Sommerfeld and Kuschel, 2016)	3701	1	0-1	Water	1000	1	73
	370	1	0-1	Ethanol	790	1.166	22
	370	1	0-1	Propanol	803	2	24
	370	1	0-1	Hexanol	814	4.3	26
	370	1	0-1	Heptanol	820	7.4	27
	370	1	0-1	Nonanol	828	12.9	28
	370	1	0-1	Dodecylalcohol	831	15.9	30
	370	1	0-1	Oil FVAI at 100 °C	803.7	3.04	22.6
	370	1	0-1	Oil FVAI at 90 °C	810.8	3.6	23.9
	370	1	0-1	Oil FVAI at 70 °C	825	5.3	26.2
	370	1	0-1	Oil FVAI at 60 °C	832.2	6.7	27.2
	370	1	0-1	Oil FVAI at 45 °C	842.9	14.5	28.1
	370	1	0-1	Oil FVAI at 23 °C	858.5	28.2	30.3
(Kuschel and Sommerfeld, 2013)	380	1	0-1	Saccharose-20%	1080.9	2	73.7
	380	1	0-1	Saccharose-40%	1176.5	6	75.1
	380	1	0-1	Saccharose-50%	1229.7	15.5	76
	380	1	0-1	Saccharose-54%	1252	19.4	76.4
	380	1	0-1	Saccharose-58%	1274.9	42.2	76.9
	380	1	0-1	Saccharose-60%	1286.6	57.3	77.1
	380	1	0-1	PVP K30-5%	1009.8	2.6	70.5
	380	1	0-1	PVP K30-10%	1021.5	5.7	69.7
	380	1	0-1	PVP K30-15%	1033.1	12.5	68.9
	380	1	0-1	PVP K30-20%	1044	27.4	68
	380	1	0-1	PVP K30-23%	1051.7	43.9	67.5
	380	1	0-1	PVP K30-25%	1056.3	60	67.2
	380	1	0-1	PVP K17-5%	1009.8	1.45	69.7
	380	1	0-1	PVP K17-10%	1021.4	2.5	69.1
	380	1	0-1	PVP K17-20%	1044.6	7.6	67.4
	380	1	0-1	PVP K17-30%	1063.2	22.7	66.3
	380	1	0-1	PVP K17-35%	1067.9	39.4	64.8
(Sommerfeld and Pasternak, 2019)	574	1	0-1	PVP K17 20%	1043	5.5	62.2
	583	0.86	0-1	PVP K17 20%	1043	5.5	62.2
	455	0.67	0-1	PVP K17 20%	1043	5.5	62.2
	522	0.35	0-1	PVP K17 20%	1043	5.5	62.2
	625	0.99	0-1	Sunflower – Oil	919.7	66.2	33.8
	727	0.91	0-1	Sunflower – Oil	919.7	66.2	33.8
	568	0.71	0-1	Sunflower – Oil	919.7	66.2	33.8
	470	0.34	0-1	Sunflower – Oil	919.7	66.2	33.8
(Finotello et al., 2018b)	620-770	1	0-1	Milk 20% TS content	1041	4.3	46.8
	620-770	1	0-1	Milk 30% TS content	1061	8.8	46.1
	620-770	1	0-1	Milk 46% TS content	1094	83	46.9
	620-770	1	0-1	40% glycerol	1104	5.01	68.5
	620-770	1	0-1	60% glycerol	1158	15.5	67.9
	620-770	1	0-1	80% glycerol	1211	88.8	65.1
(Finotello et al., 2018a)	1000	1	0-1	Xanthan 500 ppm	1000	3.8	72.2
(Pan et al., 2016)	280-440	1	0-1	Water	998	1.02	

	300	1	0-1	0.1% surfactant S11 1n in water	998	1.02	32
	300	1	0-1	0.3% surfactant S11 1n in water	998	1.02	21
	300	1	0-1	1% surfactant S11 1n in water	998	1.02	17
	300	1	0-1	0.005% surfactant S386 in water	998	1.02	32
	300	1	0-1	1% surfactant S386 in water	998	1.02	21
	440	1	0-1	30% glycerol in water	1069	2.83	72
	440	1	0-1	30% glycerol plus 1% surfactant S11 1n in water	1069	2.83	17
	450			Ethanol	789	1.2	22
(Chen, 2007)	700-800	1	0-1	diesel	817	3.16	28.3
	700-800	1	0-1	Ethanol vs. diesel	801 vs. 817	1.19 vs 3.16	22.1 vs. 28.3
(Gao et al., 2005)	400-600	1	0-1	Water vs. ethanol	1000 vs. 794	1 vs. 1.19	72.8 vs. 22.6
(Chen and Chen, 2006)	700-800	1	0-1	Water vs. diesel	1000 vs. 817	1 vs. 3.16	72.7 vs. 28.3
(Planchette et al., 2010)	200	1	0-1	50% glycerol vs. silicon oil M5	1126 vs. 913.4	6.00 vs. 4.56	68.6 vs. 19
	200	1	0-1	50% glycerol vs. silicon oil M3	1126 vs. 892.2	6.00 vs. 2.68	68.6 vs. 19
	200	1	0-1	55% glycerol vs. silicon oil M3	1139 vs. 892.2	7.80 vs. 2.68	68.1 vs. 19
	200	1	0-1	40% glycerol vs silicon oil M3	1099 vs. 982.2	3.72 vs. 2.68	69.5 vs. 19
	200	1	0-1	30% glycerol vs silicon oil M3	1073 vs. 892.2	2.50 vs. 2.68	70.3 vs. 19
	200	1	0-1	20% glycerol vs silicon oil M3	1047.9 vs. 892.2	1.76 vs. 2.68	70.7 vs. 19

2.5 Modelling the regimes' boundaries of collisions' outcomes

2.5.1 Bouncing boundary

Estrade et al. (1999) were the first to model the boundary of the bouncing regime for both collisions of equal-size and unequal-size droplets, Eq. (2.7). The model is based on an energy balance for inviscid droplets. To set the bouncing criteria it is assumed that

bouncing occurs if the impact kinetic energy does not cause a droplet deformation that exceeds a critical deformation limit. Assuming the droplet geometry at the maximum deformation is a spherical cap, as shown in Figure 2.9, the deformation limit is set through a shape factor (ϕ'), which is a function of ϕ as given by Eq. (2.11). The latter is defined as the ratio h_s/r_s or h_l/r_l, where h_s, r_s, h_l and r_l are defined in Figure 2.9. However, Estrade et al. (1999) do not suggest any correlation or approach to quantify ϕ, it is rather used as a fitting parameter. This is because, in addition to the wetting properties and the physical properties of the droplets, ϕ depends on the impact energy at the transitional point from bouncing to fast coalescence and this point is quite hard to quantify due to the complex dynamics of the intervening air layer and the interfaces of the droplets that control this transitional point (Pan et al., 2008; Pan et al., 2016)

$$\mathrm{We_c} = \frac{12\Delta(1+\Delta^2)(\phi'-1)}{X_l(1-\mathrm{B}^2)}, \tag{2.7}$$

Where X_l is the interaction region of the large droplet, as shown in the shaded area in Figure 2.2, which was firstly reported by Ashgriz and Poo (1990) and it is given by

$$X_l = \begin{cases} 1-\frac{1}{4}(2-\tau)^2(1+\tau) & \text{for } h > \frac{d_l}{2} \\ \frac{1}{4}\tau^2(3-\tau) & \text{for } h \le \frac{d_l}{2} \end{cases}, \tag{2.8}$$

τ and h is defined by

$$\tau = (1-\mathrm{B})(1+\Delta), \tag{2.9}$$

$$h = \tfrac{1}{2}(d_l + d_s)(1-\mathrm{B}). \tag{2.10}$$

and

$$\phi' = \frac{2}{3}\left(\frac{3}{\phi^2}+1\right)^{-\frac{2}{3}} + \frac{1}{3}\left(\frac{3}{\phi^2}+1\right)^{\frac{1}{3}}. \tag{2.11}$$

It should be noted that Estrade et al. (1999) validated the model against data of ethanol droplets collisions of two size ratios, 1 and 0.5. In both cases the shape factor value was $\phi' = 1.12$.

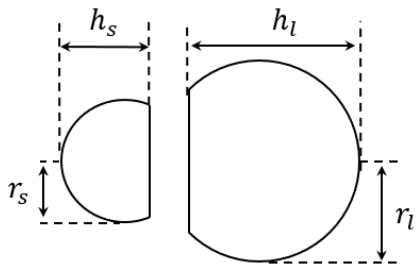

Figure 2.9 Droplet shape at the maximum deformation according to Estrade et al. (1999).

Hu et al., (2017) extended the model of Estrade et al. (1999) by adding a fitting parameter (α_2) to consider the viscous loss. α_2 represents the ratio of the viscous loss to the initial kinetic energy. The model is given by Eq. (2.12).

$$\mathrm{We_c} = \frac{12(1+\Delta^3)(1+\Delta^2)(\phi'-1)}{\Delta^2(1-\alpha_2)(1-\mathrm{B}^2)}. \tag{2.12}$$

The model of Estrade et al. (1999) has been widely used in the literature, however, it was reported in many studies that it is not accurate especially in predicting the bouncing boundary below the triple point (Kuschel and Sommerfeld, 2013, Sommerfeld and Kuschel, 2016, Finotello et al., 2018a, Finotello et al., 2018b). On the other hand, the model of Hu et al. (2017) was only fitted to numerical data of alumina droplets (Oh = 0.1151) using $\alpha_2 = 0.5$, based on numerical estimation, and using a shape factor that fits the model to the data. The authors do not propose a correlation or an approach to quantify the viscous loss in systems different than the alumina droplets. Thus, the modelling of the lower boundary of the bouncing regime still requires more investigation.

2.5.2 Reflexive separation boundary

The modelling of the reflexive separation has received more attention than that of bouncing. Many attempts to produce semi-theoretical or fully empirical models to predict the reflexive separation boundary were reported. These models can be divided

into two groups: models for the entire boundary of the regime, at B $\geq$ 0, and models only for the head-on transitional point, $\mathrm{We}_{\mathrm{FC/RS}}$, as summarized in Table 2.3.

Table 2.3 Summary of the existing models of the reflexive separation regime. ✓ and X mean considered and not considered, respectively.

Author	B	Δ	Viscous loss	Comments
Ashgriz and Poo (1990)	✓	✓	X	Empirical criteria to fit the boundary in water droplets.
Hu et al. (2017)	✓	✓	✓	No correlation for the viscous loss.
Qian and Law (1997)	X	X	✓	Shows poor performance at high Oh (Gotaas et al., 2007b).
Gotaas et al. (2007b)	X	X	✓	Empirical correlations.
Tang et al. (2012)	X	✓	✓	Has not been examined in high Oh systems.
Planchette et al. (2017)	X	X	✓	Has been examined for a wide range of Oh.

Ashgriz and Poo (1990) have reported an inviscid model to predict the entire boundary of reflexive separation. The model was developed based on an energy balance. The criterion of the model is that reflexive separation occurs if the reflexive kinetic energy, based on an elastic collision of the two droplets, is greater than 75% of the surface energy of the nominal droplet that would be produced by the coalescence of the colliding droplets. The model is given by

$$\mathrm{We_c} = 3\left[7(1+\Delta^3)^{\frac{2}{3}} - 4(1+\Delta^2)\right]\frac{\Delta(1+\Delta^3)^2}{\Delta^6 ¥_1 + ¥_2} \tag{2.13}$$

Where,

$$¥_1 = 2\left(1-\left(0.5\mathrm{B}(1+\Delta)\right)\right)^2\left(1-\left(0.5\mathrm{B}(1+\Delta)\right)^2\right)^{\frac{1}{2}} - 1, \tag{2.14}$$

and

$$¥_2 = 2\left(\Delta-\left(0.5\mathrm{B}(1+\Delta)\right)\right)^2\left(\Delta^2-\left(0.5\mathrm{B}(1+\Delta)\right)^2\right)^{\frac{1}{2}} - \Delta^3. \tag{2.15}$$

The above model is only valid for inviscid fluids as the viscous loss is not considered, and it has been shown to give good agreement for water and similar Oh droplets (Sommerfeld and Kuschel, 2016).

Hu et al. (2017) used the same approach as Ashgriz and Poo (1990) but with a different definition of impact kinetic energy for $B > 0$. They used a spherical cap geometry to define the interaction volume rather than a prolate volume used by Ashgriz and Poo. They also introduced a viscous loss factor α_3, defined as the ratio of the viscously dissipated energy to the collisional kinetic energy. This factor is used as a fitting parameter to fit the model with the experimental data. The model is given by

$$\mathrm{We_c} = \frac{3\left(7(1+\Delta^3)^{\frac{2}{3}} - 4(1+\Delta^2)\right)(1+\Delta^3)^2}{\Delta^2\left((2-\alpha_3)(\Delta^3 X_l + X_s) - (1+\Delta^3)\right)}. \tag{2.16}$$

Where, X_l and X_s are given by Eq. (2.8) and Eq. (2.17), respectively.

$$X_s = \begin{cases} \left(1 - \frac{1}{4\Delta^3}(2\Delta-\tau)^2(\Delta+\tau)\right) & \text{for } h > \frac{d_s}{2} \\ \frac{1}{4\Delta^3}\tau^2(3\Delta-\tau) & \text{for } h \le \frac{d_s}{2} \end{cases}. \tag{2.17}$$

In the modelling of the head-on transitional point, $\mathrm{We_{FC/RS}}$, Jiang et al. (1992), based on energy balance, reported that $\mathrm{We_{Fc/Rs}}$ can be linearly correlated with μ/σ. Later, Qian and Law (1997) extended the work of Jiang et al. (1992), by more detailed energy analysis, used droplets of water and hydrocarbons to prove that $\mathrm{We_{Fc/Rs}}$ has a linear relationship with Oh, given by $We_{FC/RS} = 17 + 510\,\mathrm{Oh}$. The Ohnesorge number is often a valuable group for capturing the physics governing the breakup of viscous threads (Ohnesorge, 1936; McKinley, 2005; Castrejon-Pita et al., 2012; Notz and Basaran, 2004), and the mechanism which governs reflexive separation. This encouraged more studies to produce empirical correlations ($\mathrm{We_{Fc/Rs}} = f(\mathrm{Oh})$) to define the onset of reflexive separation at head-on collision for systems with different rheological properties than those of Jiang et al. (1992) and Qian and Law (1997). Gotaas et al. (2007b), based on empirical analysis, reported that at $\mathrm{Oh} > 0.04$ the correlation is not linear and proposed two correlations, $\mathrm{We_{FC/RS}} = 14.8 + 643.1\mathrm{Oh}$ for $\mathrm{Oh} < 0.04$ and $\mathrm{We_{FC/RS}} = 9309\mathrm{Oh}^{1.7056}$ for Oh > 0.04. Finotello et al. (2018a) reported that in the viscoelastic fluids, the extensional $\mathrm{Oh}_E = \mathrm{Oh}\frac{\mathrm{Tr}}{3}$ need to be used instead of the conventional Oh, where Tr is the Trouton ratio (extensional viscosity to shear viscosity).

Recent studies used those Oh correlations to shift the curve of the model of Ashgriz and Poo (1990), Eq. (2.13), toward higher We (Sommerfeld and Kuschel, 2016, Finotello et al., 2018b, Finotello et al., 2018a). However, this approach is not always accurate as the fittings of $We_{FC/RS} = f(Oh)$ correlations show considerable scatter (Sommerfeld and Kuschel, 2016, Finotello et al., 2018b).

Planchette et al. (2017) developed a model to predict the onset of the reflexive separation regime at head-on collisions using energy balance. The criterion used for the separation threshold (called fragmentation by the authors) is based on a Rayleigh-like analysis of the break-up of the cylinder (eighth image in the reflexive separation sequence of Figure 2.3) formed on the contraction of the rimmed lamellar disc. The critical aspect ratio of the cylinder above which separation occurs was determined from experimental data to be $\zeta_{crit} \geq 3$, for Oh < 0.1. Two viscous losses are considered by the model, a loss in the compression period and a loss in the relaxation period. The loss in the compression period is characterised by a loss factor a, which is the ratio of the viscous loss in the compression period to the initial kinetic energy of the droplets ($\rho\pi d^3 u_r^2/24$). For a wide range of Oh (0.02 – 0.15), the loss factor $\alpha \sim 0.65$, however, for Oh < 0.02, α is lower and for Oh > 0.15, α is higher. In the relaxation period, a factor, q, is proposed to allow for losses. The proposed model of the critical collision velocity is given by

$$u_r^{theo} = 2\zeta_{crit}\sqrt{\frac{24\sqrt{2}/\pi}{(1-\alpha-q/(\mathrm{We}_{\mathrm{FC/RS}}^{0.5}Oh)}}\sqrt{\frac{\mu}{\rho t_{oscill}}}. \tag{2.18}$$

Where, t_{oscill} is a characteristic droplet oscillation time given by $t_{oscill} = \sqrt{\rho d^3/\sigma}$. The model was shown to give excellent agreement with experimental results for Oh < 0.1, and with the loss factor, q, adjusted to $q = 0.025(1-a)$.

The Oh correlations and the model of Planchette are for collisions of equal-size droplets. Tang et al. (2012) extended the work of Qian and Law (1997) to consider the role of the size ratio. The extended model is given by

$$\mathrm{We}_{\mathrm{FC/RS}} = \beta \mathrm{Oh}_{\mathrm{s}} + \gamma \tag{2.19}$$

Where β is a geometrical parameter given by Eq. (2.20) and γ is a scale of residual surface energy, given by Eq. (2.21), which represents the difference in the surface energy

between that of the initial droplets and of the after-separation droplets. The value of γ was found by Tang and Qian to be ~ 11 and it weakly depends on the size ratio.

$$\beta = \frac{2\sqrt{2}(1+\Delta^3)}{(1-\alpha)}\left[\frac{\tilde{a}^{0.5}}{\sqrt{2}\,\tilde{b}^2}\sqrt{1+\frac{\tilde{a}}{\tilde{b}}}\left(\frac{2(1+\Delta^3)}{\Delta^3}-\tilde{c}^3\right)+\tilde{c}^{\frac{3}{2}} + \frac{2\tilde{f}^3}{(1+\Delta^3)}\left(\frac{1}{\Delta^3\tilde{d}^{\frac{5}{2}}}+\frac{\Delta}{\tilde{e}^{\frac{5}{2}}}\right)\right], \tag{2.20}$$

where α represents the ratio of the viscous loss to the initial kinetic energy for the period from the beginning of the collision up to the maximum deformation of the disc (fourth image in the reflexive separation sequence of Figure 2.3c). α in the model of Tang et al. (2012) is similar to that of the model of Planchette et al. (2017), however, the former reported lower values than the latter ($\alpha \sim 0.55 \pm 0.05$). The parameters $\tilde{a}$, $\tilde{b}$, $\tilde{c}$, $\tilde{d}$, $\tilde{e}$ and $\tilde{f}$ are geometrical parameters and given by polynomial correlations as a function of Δ, as listed in Table 2.4. These polynomials were produced by fitting experimental measurements in collisions of tetradecane droplets for a wide range of Δ and assumed to be universal.

$$\gamma = \frac{3\left(S_f - S_o\right)(1+\Delta^3\,)}{(1-\alpha)\pi R_s^2} \sim 11, \tag{2.21}$$

where, S_o and S_f are the initial and after-separation surface area, respectively.

The model of Tang et al. (2012) was validated using relatively low viscosity systems, water, decane and tetradecane. Moreover, to the best of the author's knowledge, the validity of the model has not been examined against higher Oh systems in other studies.

Table 2.4 Fitting coefficients of the geometrical parameters in the model of Tang et al (2012).

$f(\Delta) = A_o + \frac{A_1}{\Delta} + \frac{A_2}{\Delta^2}$	A_o	A_1	A_2
$\tilde{a}$	1.556	0.6032	− 0.0314
$\tilde{b}$	0.47506	−0.00508	−0.01025
$\tilde{c}$	−3.30844	4.12313	0.80968
$\tilde{d}$	−0.01747	0.91154	−0.02622
$\tilde{e}$	0.87656	0.06067	−0.04016
$\tilde{f}$	3.09374	0.95754	0.502
$\tilde{S}_f - \tilde{S}_o$	1.13341	−0.09298	0.01724

Note that, generally, the difference between the approach of Planchette et al. (2017) and that of Qian and Law (1997) and Tang et al. (2012) is the method of estimating the viscous loss in the relaxation period (shown in the images 6-5 in the reflexive separation sequence of Figure 2.3c). Planchette et al. (2017) used the analogy between the dynamics of reflexive separation and the compression and relaxation process of liquid springs, and hence the oscillation time is used to evaluate the velocity gradient of the internal flow from which the viscous loss is estimated. However, Qian and Law (1997) and Tang et al. (2012) local curvatures to evaluate the local capillary pressure and hence the velocities in the internal flow.

Overall, there was a good number of attempts to produce models to predict the boundary of the reflexive separation, as listed in table 2.4. However, these models lack for generality as they are either inviscid (Ashgriz and Poo, 1990), poorly consider the viscous loss (Hu et al., 2017), do not consider the effect of B (Tang et al., 2012), or do not consider Δ and B (Qian and Law, 1997; Gotaas et al., 2007b; Planchette et al., 2017). Thus, there is a need for more work to produce a general model that considers the viscous loss, B and Δ.

2.5.3 Stretching separation boundary

The modelling of the boundary of the stretching separation regime was considered by many studies (Park 1970; Brazier-Smith et al., 1972; Arkhipov et al., 1983; Ashgriz and Poo, 1990; Jiang et al., 1992; Planchette et al., 2012). Jiang et al. (1992) and Planchette et al. (2012) considered the viscous loss whereas the others are inviscid models.

The model of Park (1970), Eq. (2.21), is based on a competition between the angular momentum and the surface tension in the regions of the interaction. The model considers the effect of the size ratio, however, the viscous loss is not considered, as it was developed for water droplets collisions.

$$\mathrm{B} = \left(\frac{12}{\pi}\right)^{0.5} \frac{(\Delta^2 - \Delta + 1)^{0.5}}{\Delta \mathrm{We}^{0.5}} \left[\frac{(1+\Delta^5)(\Delta^2 - \Delta + 1)}{5\Delta^3} + \frac{1+\Delta}{2}\right]\left[4 - \left[\mathrm{B}(1+\Delta) - \frac{1-\Delta}{\mathrm{B}}\right]^2\right]^{0.25} \tag{2.22}$$

The model of Brazier-Smith et al. (1972) was developed based on a competition between the rotational energy and the surface energy assuming that if the rotational energy is greater than the additional surface energy required to reform the initial drops from the coalesced droplets. The model is given by

$$\mathrm{B} = \frac{2.191}{\mathrm{We}^{0.5}}\left(\left(\frac{1}{\Delta}\right)^3 - 2.4\left(\frac{1}{\Delta}\right)^2 + 2.7\left(\frac{1}{\Delta}\right)\right)^{0.5} \tag{2.23}$$

Arkhipov et al. (1983) used competition between the rotational energy, which is based on the angular velocity and the moment of inertia, and the surface energy of the regions of non-interaction. The model is given by

$$\mathrm{B} = \frac{1}{\Delta^3}\left(\frac{6(1+\Delta^3)}{\mathrm{We}}\right)^{0.5} \tag{2.24}$$

The performance of the above three models was examined by Ashgriz and Poo (1990) against experimental data of water droplets collisions with different size ratios (1, 0.75 and 0.5). The models of Park (1970) and Arkhipov et al. (1983) show over-predictions of the boundary. Whereas the model of Brazier-Smith et al. (1972) performs well for size ratios of 1 and 0.75 while it shows an over-prediction at Δ=0.5. Ashgriz and poo (1990) argued that the criteria of these models, which is based on the comparison of the rotational energy with surface energy, is not physically observed. This because it had been observed that the separation happens before the development of any significant rotation. Therefore, Ashgriz and Poo (1990) proposed a new criterion stating that separation occurs if effective kinetic energy exceeds the surface energy in the regions of interactions. The effective kinetic energy is defined by the kinetic energy of the non-interaction regions in addition to that obtained from the regions of interactions using only the component of the drop velocities in the separating direction. The developed model shows good performance in all the size ratios, and it is given by

$$\mathrm{We} = \frac{4(1+\Delta^3)^2[3(1+\Delta)(1-\mathrm{B})(\Delta^3 X_s + X_l)]^{0.5}}{\Delta^2[(1+\Delta^3)-(1-\mathrm{B}^2)(X_s+\Delta^3 X_l)]}, \tag{2.25}$$

where X_l and X_s are given by Eq. (2.8) and Eq. (2.17), respectively.

As all the aforementioned models are inviscid, Jiang et al. (1992) developed a model in which the viscous loss is considered. The model of Jiang et al. (1992) was developed based on momentum conservation, assuming that the coalesced droplets behave as two circular plates that are sliding on each other. The sliding velocity is the component of the relative velocity that is perpendicular to the line between the two droplets centres; while the other component is responsible for the deformation. The resistance to the sliding velocity is the surface tension forces along the circumference of the plates and the viscous loss due to the shearing flow layer between the sliding plates (i.e., the droplets). The model is given by

$$\mathrm{B} = \frac{1}{\mathrm{We}^{0.5}}\left[1 + C\frac{\mu}{\sigma}\left(\frac{\rho d}{\sigma}\right)^{0.5}\right], \tag{2.26}$$

where *C* is a constant that can be used to fit the model to the experimental data. However, the model was widely used with two fitting parameters, C_a and C_b, as in Eq. (2.27), and showed to perform very well in a wide range of data (Kuschel and Sommerfeld, 2013, Sommerfeld and Kuschel, 2016, Gotaas et al., 2007b, Finotello et al., 2018a, Finotello et al., 2018b, Finotello et al., 2017). It should be noted that k in Eq. (2.26) and C_b in Eq. (2.27) are not dimensionless parameters and have a unit of ($m^2\ s^{-2}$), while C_a is a dimensionless parameter.

$$\mathrm{B} = \frac{C_a}{\mathrm{We}^{0.5}}\left[1 + C_b\frac{\mu}{\sigma}\left(\frac{\rho d}{\sigma}\right)^{0.5}\right]. \tag{2.27}$$

Sommerfeld and Pasternak (2019) reported that C_b can be fixed and changing only C_a can fit the model to experiments. The authors used a wide range of experiments to correlate the optimum C_a with Oh by fixing C_b = 1 $m^2\ s^{-2}$. Two polynomial correlations ($C_a = f(Oh)$) were reported, one for pure liquids, and the other for solutions. The latter is applicable to this study, as HPMC solutions are used, which is given by

$$C_a = 2.63 - 7.20\ Oh + 7.86\ Oh^2 + 1.40\ Oh^3 \tag{2.28}$$

Another approach to predict the boundary of stretching separation was reported by Planchette et al. (2012). The authors discussed that if part of the kinetic energy is converted into rotational energy as reported by Brazier-Smith et al. (1972), there is a

need for an effective impact parameter, B_{eff}. This is because the droplets suffer strong distortion when undergoing off-centre collisions. The set criteria to estimate B_{eff} are that B_{eff} tends to B when We tends to 0 and/or B tends to 1, whereas $(B_{eff} - \mathrm{B})$ increases with We when B tends to 0. Based on these criteria, B_{eff} is given by

$$B_{eff} = \mathrm{B} + (1 - \mathrm{B})\frac{u_r}{U^*}, \tag{2.29}$$

where, U^* is a fitting parameter.

Planchette et al. (2012) showed that taking a stretching separation boundary for high viscosity droplets collisions as a reference boundary for B_{eff}, leads to the boundaries of the lower viscosity droplets collapsing on that boundary by using B_{eff}. Hence, a unified boundary can be used to represent systems with different viscosities. However, the authors do not propose a scaling law to the fitting parameter U^*, which makes the model of Jiang et al. (1992) preferable.

Although the model of Jiang et al. (1992) can be applied to viscous systems, it does not consider the effect of the size ratio. Sommerfeld and Pasternak (2019) proposed combining the model of Brazier-Smith et al. (1972), which considers Δ, with the model of Jiang et al. (1992) to produce a general model that accounts for the size ratio and the viscous loss. This by multiplying the model of Jiang et al. (1992), Eq. (2.27), by the term between the brackets in the model of Brazier-Smith et al. (1972), Eq. (2.23), normalized by its value when Δ = 1. The modified model of Jiang et al (1992) is therefore given by

$$\mathrm{B} = \frac{\mathrm{C_a}}{1.14\mathrm{We}^{0.5}}\left[1 + \frac{\mu}{\sigma}\left(\frac{\rho d}{\sigma}\right)^{0.5}\right]\left[\left(\frac{1}{\Delta}\right)^3 - 2.4\left(\frac{1}{\Delta}\right)^2 + 2.7\left(\frac{1}{\Delta}\right)\right]^{0.5}, \tag{2.30}$$

where $\mathrm{C_a}$ is assumed to be evaluated Eq (2.28) using Oh of the small droplet ($\mathrm{Oh_s}$) in case of Δ < 1.

The performance of the modified model of Jiang et al (1992) in Eq. (2.23) was examined by Sommerfeld and Pasternak (2019) using a wide range of size ratio (1, 0.91, 0.86, 0.71, 0.67, 0.35) for a wide range of $\mathrm{Oh_s}$ range of 0.0282-0.547. The model shows good performance Except in very low size ratios it fails to predict the boundary of the stretching separation regime.

Ultimately, although the modelling of the stretching separation regime has been studied by many authors, it still requires more investigation to make a better understanding of the roles of the size ratio and the viscous loss.

2.6 Conclusions

This chapter provided a detailed review of the main findings of the studies of binary droplet collisions. The previous studies provided experimental data to study the outcomes of binary droplet collisions. Five distinct regimes were reported, in the parameter space of We and B, namely slow coalescence, bouncing, fast coalescence, stretching separation and reflexive separation. These regimes show clear boundaries. However, the reported experiments quantitatively show that these boundaries are not universal as they change for example with viscosity, size, size ratio, surrounding air pressure and additives such as surfactants. Thus, efforts were made to use the experimental observations to develop models to predict the regime boundaries based on the physical properties of the droplets. Nevertheless, the reported experiments do not cover all the possible scenarios and the developed models lack generality.

- In collisions of droplets from the same liquid, there was a special focus on the role of the viscosity. It was shown that increasing the viscosity promotes the coalescence regime by suppressing the stretching and the reflexive separation regimes. However, there was no systematic study that clearly shows the role of the viscosity in the bouncing regime. One the other hand, it was reported that the size ratio has a qualitative effect similar to that of viscosity. However, there are no systematic studies that compare the collisions of unequal-size droplets to the cases of equal-size droplets (i.e., of the small and the large droplets). Moreover, studies show the roles of the size were scarce, especially in collisions of viscous droplets.
- Collisions of non-identical liquid were also studied. More attention has been given to collisions of immiscible droplets than that of the miscible droplets. The latter was only studied for low viscosity liquids < 4 mPa s, as the main interest was the effect of the difference in the surface tension between the droplets. Thus, more experimental investigations are required to understand the role of the viscosity difference in collisions of miscible droplets. Moreover, in non-

identical liquid collisions of both immiscible and miscible droplets, the role of the size ratio has not been investigated.

Many studies considered the modelling of the regimes' boundaries and many models were produced, at least more than one for each boundary. Most of these models are based on energy balance plus empirical criteria. However, these models lack generality.

- The model of Estrade et al. (1999), in addition to its failure in predicting the boundary of the bouncing regime below the triple point it includes a fitting shape factor, without a scaling law to quantify it. On the other hand, its modified version by Hu et al. (2017) includes an extra fitting parameter, viscous loss factor, which is also without a scaling law; moreover, the model was not tested against experimental data. Thus, more research is required to assess the existing models, look again in the underlying physics and provide scaling laws for the fitting parameters if required.
- The reported models of the boundary of reflexive separation lack generality as they are either inviscid (Ashgriz and Poo, 1990), poorly consider the viscous loss (Hu et al., 2017), do not consider the effect of B (Tang et al., 2012), or do not consider Δ and B (Qian and Law, 1997; Gotaas et al., 2007b; Planchette et al., 2017). Thus, there is a need for more work to produce a general model that considers the viscous loss, B and Δ.
- The modelling of the stretching separation regime has been studied by many authors. From the consequent studies in the literature, the model of Jiang et al. (1992) shows the best performance among the existing models in fitting the boundaries of viscous systems. However, more investigations, to validate the model and to make a better understanding of the role of the viscous loss in collisions of unequal-size droplets, are still required.
- Finally, the existing models were not designed or applied in collisions of droplets from different fluids.

Chapter 3: Rig Development and Quantification

3.1 Introduction

This chapter starts with providing a description of a rig that was designed and developed from scratch to conduct experiments of binary droplet collisions. The rig provides images/videos of the dynamics of the collisions. Therefore, after a description of the rig, an image analysis algorithm, that was developed to extract the quantitative data from the videos, is described. Finally, the characterisation of the selected liquids to generate the droplets will be covered, and the conducted experiments will be described.

3.2 The apparatus

The experimental setup is schematically illustrated in Figure 3.1 and shown in Figure 3.2. It consists of two systems: the droplet generation system and the imaging system.

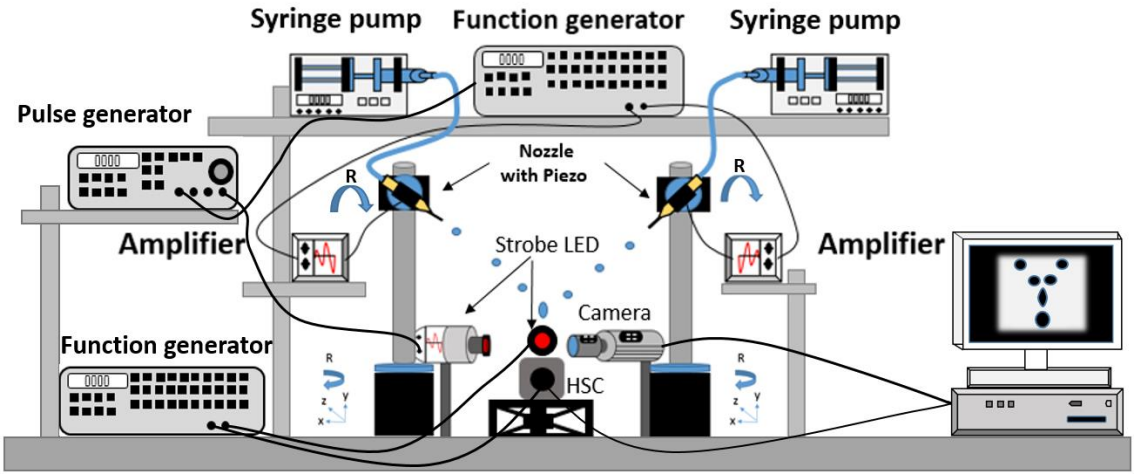

Figure 3.1 Schematic of the experimental setup. HSC: high-speed camera.

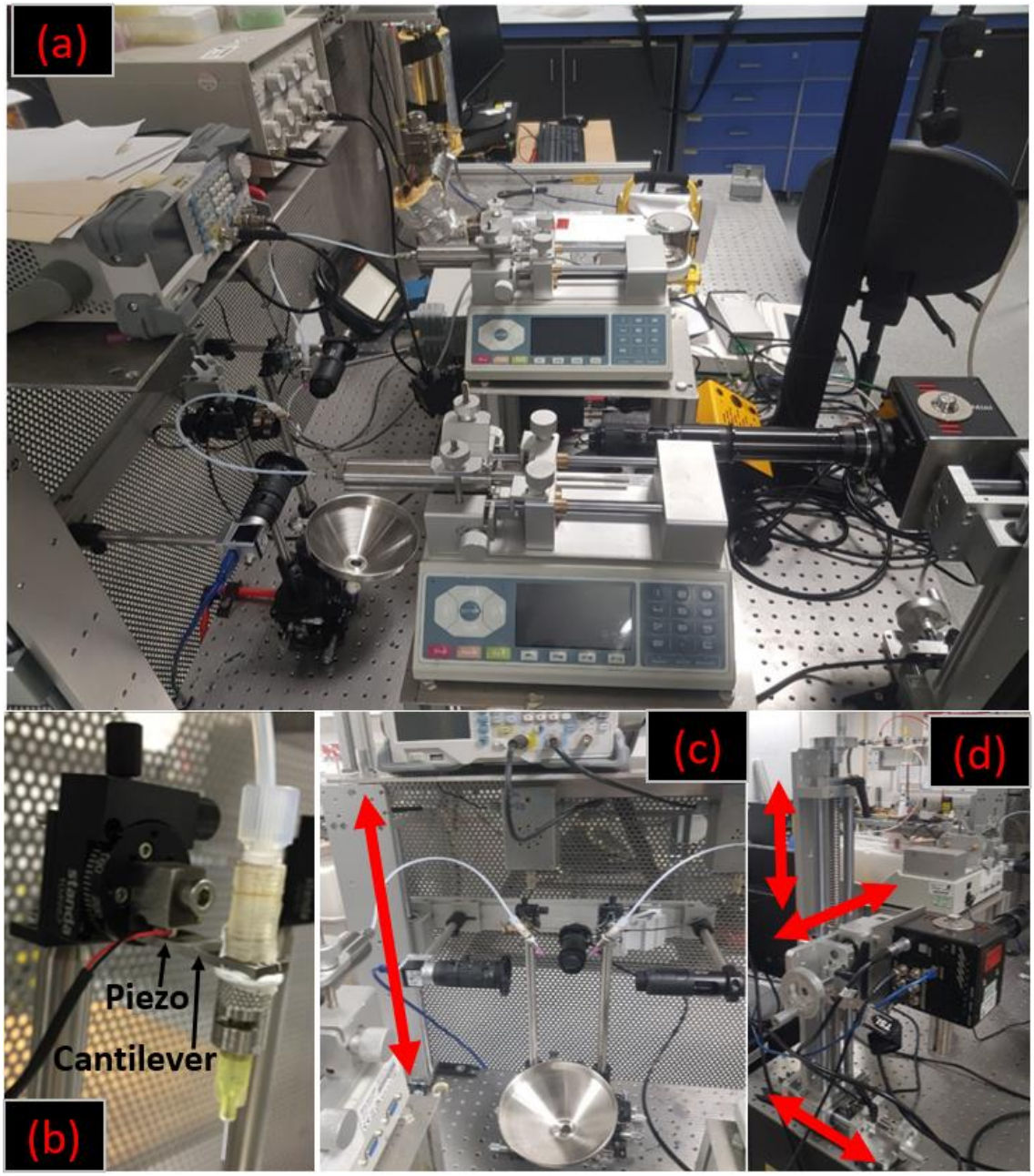

Figure 3.2 Images showing the main components of the binary droplet collisions rig. (a) the rig; (b) the nozzle; (c) the imaging alignment system; (d) the high-speed camera and its alignment system.

3.2.1 Droplet generation

The droplets are generated by exploiting the well-known theory of Plateau–Rayleigh instability (Plateau, 1873; Rayleigh, 1892). A liquid jet can be broken-up into monodisperse droplets if a certain frequency and amplitude of perturbation are applied to excite it. The applied frequency of the perturbation needs to match the frequency of the wave of the fastest growth rate, which is developed on the jet surface due to the

shear between the jet and the surrounded gas. Therefore, the frequency depends on the jet properties including its physical properties, diameter and speed. Extensive details can be found in Lefebvre et al. (2017).

To generate the jet, the liquid is driven by high-pressure syringe pump (Nexus 6000) to a custom-made nozzle to create a continuous jet. After the jet is generated, it is excited using piezoelectric chips (THORLABS, PA4JEW) which are attached to the nozzles/tubing via spring steel cantilevers, which act as clips, as shown in Figure 3.2b. Note that the use of spring steel cantilevers is to avoid fatigue that was seen when using stainless steel cantilevers which weakens the press on the piezo and thereby losing the vibration at the nozzles. To modulate the frequency and the amplitude of the Piezo, it is connected to a function generator whose signals are amplified using 20X amplifier (PiezoDrive PDu150CL). By using square signals and searching for the right frequency, the droplets were generated in a reproducible manner, as shown in Figure 3.3.

To perform droplets collisions experiments, two nozzles are used. These nozzles are mounted on micro rotation stages (a compact 360° rotation platform: STANDA, 7R128) so they can be directed towards each other at a controlled angle to make the collisions happen. The micro rotation stages are mounted on 30 cm optical posts which are mounted on XYZR micro traversers, which are used to allow for the side-alignment of the two droplets streams.

It should be mentioned that the nozzles' size can be controlled via disposable dispensing tips, as shown in Figure 3.2b. Therefore, the droplets' size can be varied, so collisions at different sizes and size ratios can be achieved.

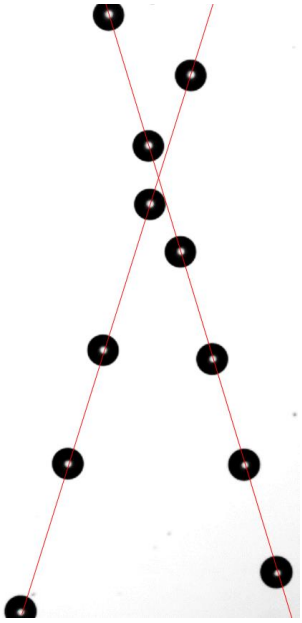

Figure 3.3 Image showing the reproducibility of the droplets and their defined trajectory.

3.2.2 The imaging system

Two imaging techniques are used to capture the dynamics of the collisions from two orthogonal directions. A strobe imaging from the side for alignment of the droplet collisions and a high-speed camera from the front to capture the dynamics.

The strobe imaging technique is used to capture the two streams of droplets from the side and to make sure that they collide in the same plane (no offset from the side). This was achieved by using a low frame rate camera, < 200 fps, (acA1300-200um - Basler ace) attached to a macro zoom lens (MLH-3XMP) and a custom-made strobe light to backlight the droplets. The light is driven by a pulse generator. The strobe imaging is used to freeze the droplets movements and hence the alignment of the collisions can be seen. This is done by synchronizing the pulse generator with the function generator, used to generate the droplets and selecting short exposure time. Once the movements of the two droplet streams are frozen their alignment becomes quite easy via the XYZR micro traversers. Figure 3.4 shows examples of the alignment captured by the side strobe imaging.

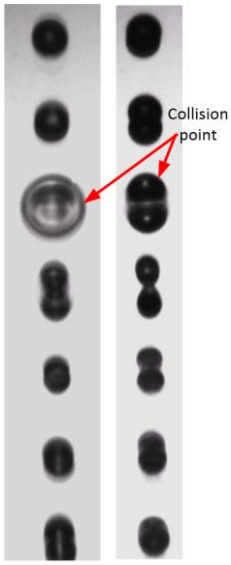

Figure 3.4 Images showing the alignment of the two droplets stream using the side imaging system.

After the alignment of the two droplets streams, the collision outcomes are recorded at 30,000 fps using a high-speed camera (Photron, FASTCAM Mini AX100 540K M3) attached to a long-distance microscope zoom lens (Navitar 12x with 12mm fine focus) and another strobe light used to backlight the droplets. The frame rate of the high-speed camera is synchronized with the strobe light through a function generator. This puts more control on the exposure time as the strobe light can provide 10 ns pulse duration while the best of the high-speed camera is 1 µs. However, 3 µs of light pulse duration was sufficient to obtain sharp images for the speeds of droplets used in this work.

The use of 30,000 fps in the high-speed camera allows for 256 x 384 pixel in the field of view. The size of the pixel depends on the applied zooming in the lens. However, although we can decrease the number of microns per pixel by zooming in, this would reduce the field of view so not all the collision dynamics are captured. Therefore, 13-20 µm/pixel was selected as a balance between the resolution and the field of view. Based on this resolution and the range of droplets' sizes considered in this work (220-450 µm), the measurements of the droplets' dimeter have an uncertainty of ± 6-3%.

3.3 The variation of Weber number and the impact parameter

To construct a regime map for the outcomes of the collisions, the size of the droplets was kept the same for all data points. Weber number is varied by changing the collision

relative velocity, u_r, by changing the angle between the two droplets streams, θ_4, as given by

$$u_r^2 = u_l^2 + u_s^2 - 2u_l u_s \cos\theta_4 \tag{3.1}$$

where, $u_l$and u_s are the velocities of the two streams, as shown in Figure 3.5.

Note that, by changing the angle between the two droplets streams, the height at which the collision point occurs change and the imaging system need to be repositioned to capture the dynamics. Thus, the side imaging system and the light of the high-speed camera are mounted on a rail that is mounted on a vertical traverser, as shown in Figure 3.2c. This ensures keeping the alignment of the imaging system when it moves up or down. The high-speed camera is mounted on an xyz traverse system, as shown in Figure 3.2d, that helps to position and focus the high-speed camera.

The impact parameter (offset) is varied by applying a delay or a frequency shift between the two signals of the droplets' generators (Gotaas et al., 2007a).

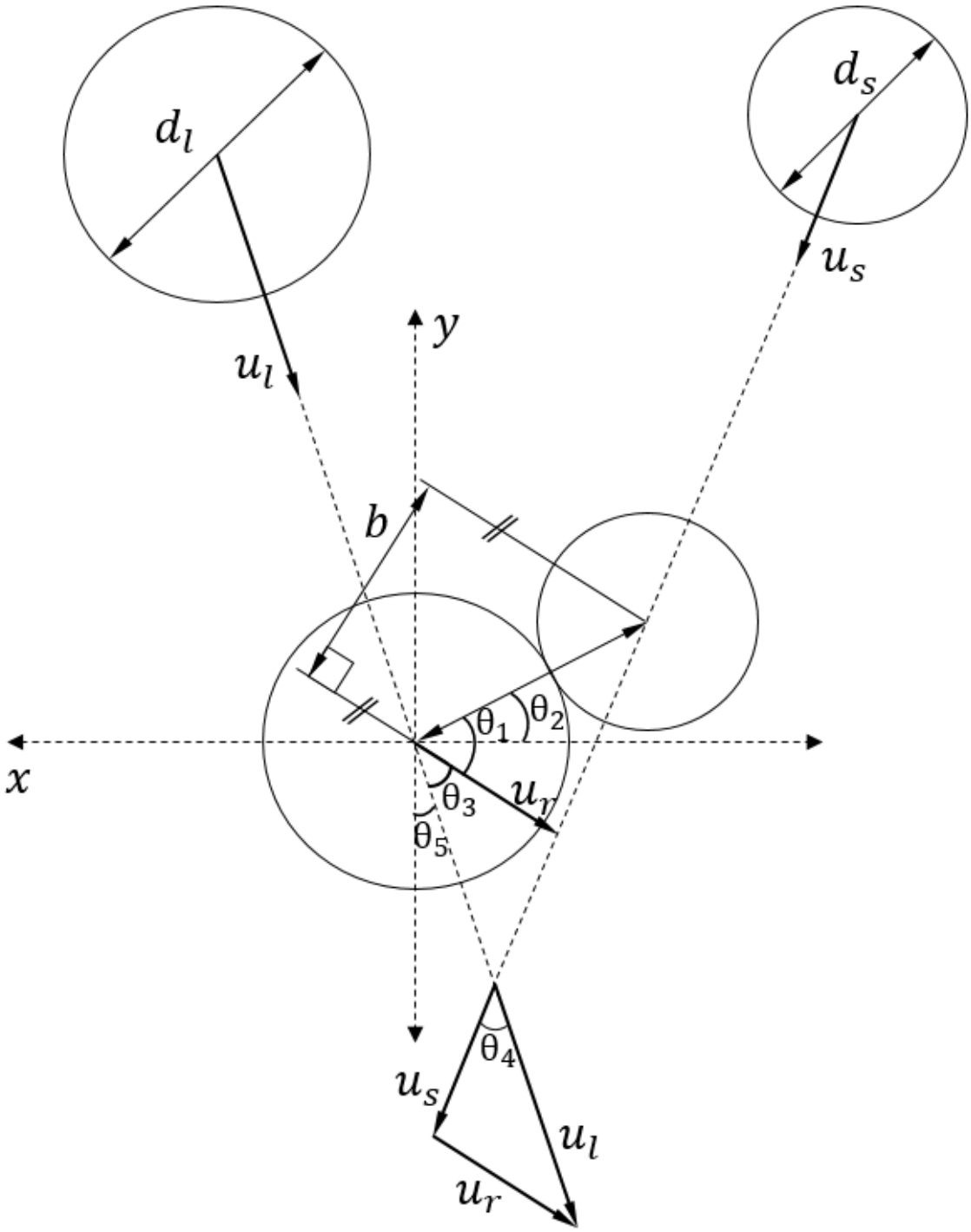

Figure 3.5 Schematic of the geometry of droplet collisions.

3.3.1 Frequency delay method to control the impact parameter

To achieve collisions with designed impact parameter, a frequency delay between the two signals of the droplet's generators can be applied. For example, if the collision for

identical droplets needs to be head-on, the signals of the two droplet generators must be synchronised, as in Figure 3.6a, so the droplets are generated and arrive at the collision point at the same time. However, if the collision needs to have an impact parameter of 0.5, for example, then a delay of a quarter the wavelength between the two generators needs to be applied, as shown in Figure 3.6b. Therefore, this method can be used to achieve a given B.

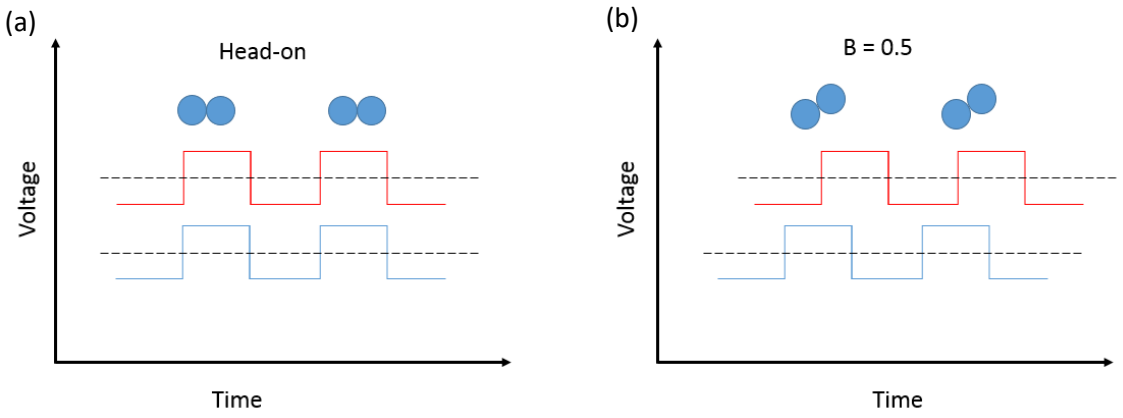

Figure 3.6. The effect of frequency delay on the impact parameter. The blue line is the signal of the first drop generator while the red is of the other generator.

3.3.2 Frequency shift method to control the impact parameter

By applying two slightly different frequencies between the two droplets generators, the impact parameter will keep changing periodically between 0 and 1, as shown in Figure 3.7. The difference in the frequency is negligible to affect the breakup process. The shift is often in the range of 0.001-0.002 KHz while the droplets generator frequency is often in the order of few KHz. The advantage of this method is that collisions with different impact parameters can be filmed in one video (Gotaas et al., 2007a).

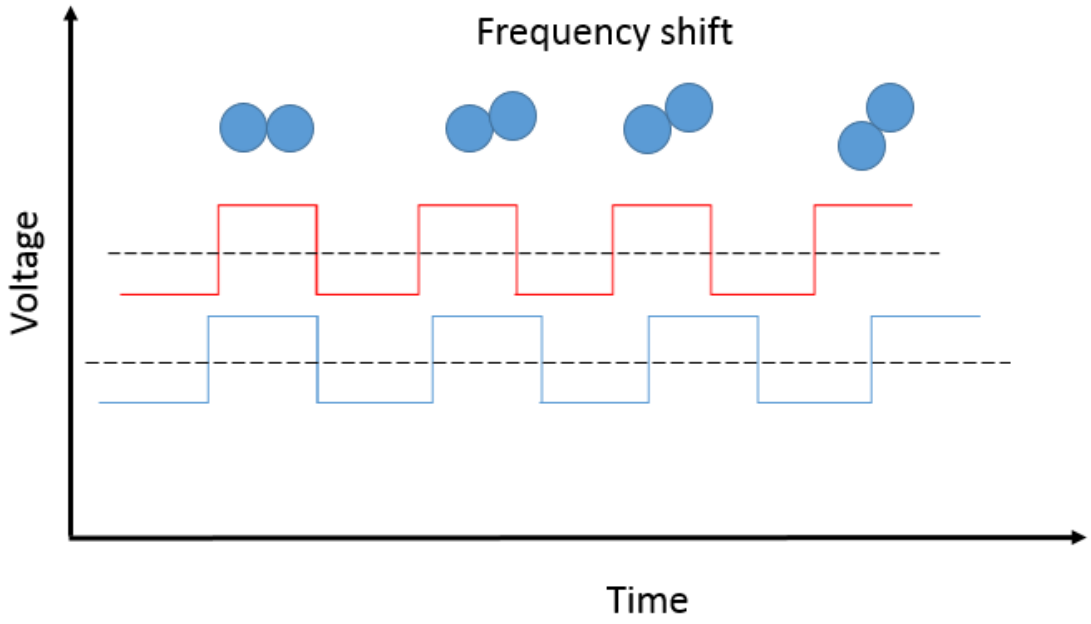

Figure 3.7 The frequency shift to vary the impact parameter. The blue signal is the first droplet generator while red is of the other

3.4 Tracking methodology

A tracking algorithm was developed to obtain the impact details from the recorded videos. The tracking algorithm is implemented by using a MATLAB based tracking software, called Droplet Morphometry and Velocimetry (DMV) that was developed by Basu (2013), to track droplets before the collision point. The interface of DMV is shown in Figure 3.8. For each droplet, DMV provides the (x, y) position of the droplet's centre, (x, y) velocities, equivalent diameter, time, frame number, and droplet ID (as a number). Based on this data provided by DMV, the impact details are then extended with very small increments to the exact collision point using a MATLAB code that was developed for this purpose. The impact parameter and We are then evaluated at the collision point. The advantage of this method is to avoid cases when the exact collision point does not appear in the recording (i.e. occurred in an instance between two consequent frames), especially at high We. It should be noted that the use of the MATLAB code alongside with DMV is essential because the latter is not designed to estimate the impact parameter.

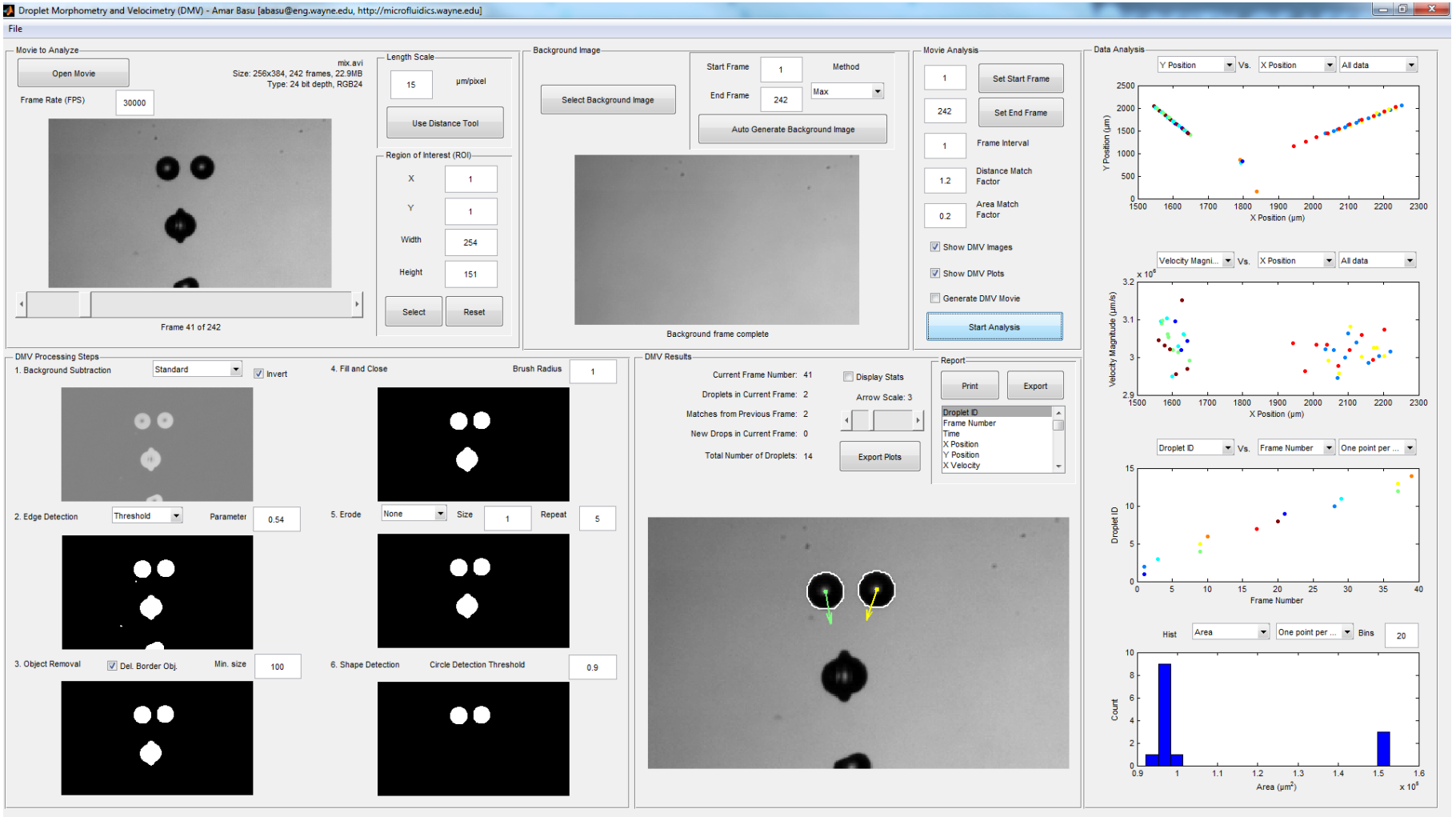

Figure 3.8 The interface of DMV.

The tracking starts by uploading the high frame rate video into DMV. In DMV, the frames are cut for the region before collision point, as shown in Figure 3.9. In each frame, DMV evaluates time (t), diameter (d), and the centre position (x, y) for each droplet. Every droplet is given an ID number to enable the tracking of each droplet through different frames. From every two successive frames, DMV evaluates the velocity in x and y direction for each droplet; details on DMV can be found in Basu (2013). This data is saved in an Excel sheet, which is then loaded into MATLAB. In MATLAB the positions of the droplets are extended along their trajectories to the collision point. The extension procedure is as follow:

1. The (x, y) position of the tracked droplets, in frame 4 in Figure 3.9, is extended with a very small increment of time (Δt) to become (x + $\vec{u}_x \Delta t$, y + $\vec{u}_y \Delta t$). The increment of the time selected in this study is
$$\Delta t = \frac{d_l}{500} u_l; \tag{3.2}$$
2. At the new position, the time is updated by adding Δt;
3. When the newly calculated (x, y) positions of droplets satisfy the condition in Eq. (3.3), the impact parameter is estimated using $\mathbf{B = \sin \theta_1}$.
$$\sqrt{(x_s - x_l)^2 + (y_l - y_s)^2} - ((d_l + d_s)/2) < 0.0001 d_l \text{ at } t = t_l = t_s, \tag{3.3}$$
where, θ_1 is the angle between the vector of the relative velocity and the line between the centres of the two droplets as shown in Figure 3.5. the times t_l and t_s represent the time of the large and the small tracked droplets.

The angle θ_1 is a function of (x, y) positions of the droplets l and s and can be estimated using the following procedure considering that the frame of reference is on the centre of the large droplet, as shown in Figure 3.5:

1. Evaluation of the angle between the two streams of droplets using
$$\theta_4 = \tan^{-1}(\vec{u}_{xl}/\vec{u}_{yl}) + \tan^{-1}(\vec{u}_{xs}/\vec{u}_{ys}); \tag{3.4}$$
2. Evaluation of the angle between the x-axis and the line that connects the centres of the colliding droplets at the collision point using
$$\theta_2 = \tan^{-1}((y_l - y_s)/(x_s - x_l)); \tag{3.5}$$
3. Evaluation of the relative velocity from Eq. (3.1);

4. Evaluation of the angle between the relative velocity vector and the trajectory of the large droplet using

$$\theta_3 = \sin^{-1}\left(\frac{\|\vec{u}_s\|}{\|\vec{u}_r\|}\sin\theta_4\right); \tag{3.6}$$

5. Evaluation of the angle between the large droplet trajectory and the y-axis, θ_5, using

$$\theta_5 = \tan^{-1}\left(\frac{\vec{u}_{xl}}{\vec{u}_{yl}}\right); \tag{3.7}$$

6. Finally, the angle θ_1 is estimated using

$$\theta_1 = 90 - \theta_5 - \theta_3 + \theta_2. \tag{3.8}$$

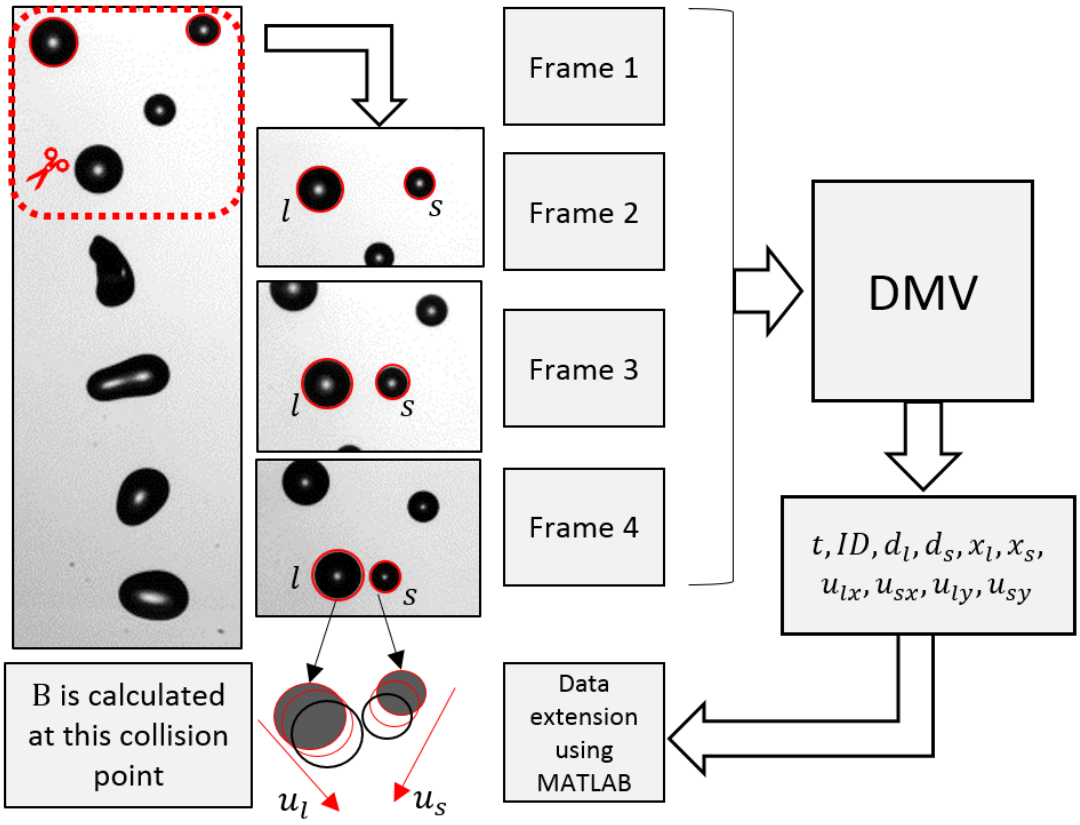

Figure 3.9 Tracking methodology to estimate the collision point and hence the impact parameter.

3.5 Droplet fluids

Four different concentrations, 2%, 6%, 4%, and 8%, of Hydroxypropyl Methylcellulose grade 603 Shin-Etsu Chemical's PHARMACOAT® (HPMC) solutions, in deionised water,

were used for this study. HPMC was selected due to its industrial relevance as it is widely used in many spray applications, where droplet collisions are relevant, such as in pharmaceutical tablets coating (Sangalli et al., 2004), food products coating (Andrade et al., 2012) and spray drying (Karim et al., 2016; Alanazi et al., 2006; Li et al., 2015). The viscosities of the solutions were measured in a rheometer (Anton Paar, Physica MCR 301) using a cone and plate geometry (75 mm, Angle 1°, and gap 0.149 mm) and a linear shear sweep from 1 to 1000 s^{-1} over 410 s at 20 °C. The solutions exhibit Newtonian behaviour within the applied shear rate, as shown in Figure 3.10. The surface tension was measured using a pendant drop in an optical tensiometer (KSV CAM 200). The density was measured by weighing 50 ml of the solution using an analytical balance. Table 3.1 illustrates the physical properties of the three solutions. The measured values agree with the values that have been reported in the literature (Parker et al., 1991; Kokubo and Obara, 2008). All collision experiments and measurements were carried at atmospheric conditions and room temperature 20 °C.

Table 3.1 Physical properties of the three HPMC systems that are used in this work.

Liquid	ρ (kg m^{-3})	σ (mN m^{-1})	μ (mPa s)
2% HPMC	998	46	2.8
4% HPMC	998	46	8.2
6% HPMC	998	46	17.7
8% HPMC	997	46	28.4

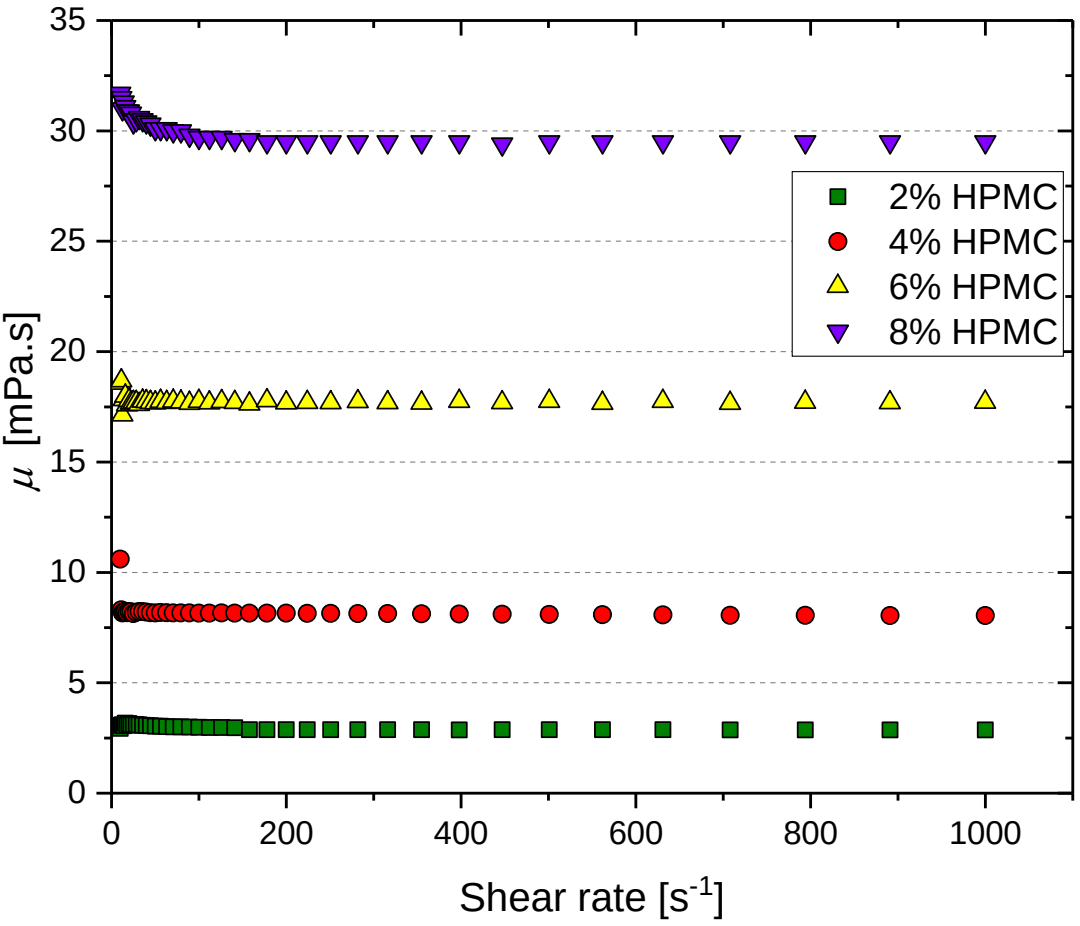

Figure 3.10 The shear viscosity versus the shear rate of the four HPMC solution used in this work.

3.6 The conducted experiments

In this work, three different sizes of the dispensing tips were used to generate the droplets, gauges 32, 30, and 27. Using these nozzles and the HPMC solutions in table 3.1, 15 regime maps were generated, as listed in table 3.2, to study the role of the viscosity and the viscosity difference in collisions of equal-size and non-equal-size droplets.

Note that, in addition to these experiments, some coloured images were obtained to help in understanding the dynamics of the collisions of non-identical viscosities. This was done by adding ~ 300 ppm of Nigrosin water-soluble dye to the higher viscosity droplet to make it black while keeping the low viscosity droplet transparent. To distinguish between the colours of the two droplets, the droplets were lit using a front light and a

white background was used. The light was positioned at an angle of ~ 45° compared to the high-speed camera to obtain a good colour contrast.

Table 3.2 The conducted experiments. For all the listed cases Regime maps were constructed in the parameter space of B and We.

HPMC	Δ (-)	Nozzle (Gauge)	Nozzle inner diameter (μm)	Droplet diameter (μm)
2%	1	30	159	365
	1	27	210	400
	1	32	108	230
	0.58	32 vs. 27	108 vs. 210	230 vs. 400
4%	1	30	159	380
	1	32	108	230
	0.58	32 vs. 27	108 vs. 210	400 vs. 230
6%	1	27	210	400
	1	32	108	230
8%	1	30	159	385
2% vs. 4%	1	30	159	370
	0.58	27 vs. 32	210 vs. 108	400 vs. 230
	0.58	32 vs. 27	108 vs. 210	230 vs. 400
2% vs. 8%	1	30	210	370
4% vs. 8%	1	30	210	370

3.7 Experimental error assessment

There are many potential sources of experimental uncertainties in the experimental methodology used in this thesis. One of the potential sources is the resolution of the images which can affect the measurements of the size and the velocity. Another

potential source of uncertainty is the oscillation of the droplets before they collide. Due to the breakup of the jet into droplets, the droplets oscillate for a short time before they reach their equilibrium. Moreover, the air drag might also affect the droplets' shape before they collide. Therefore, it is important to make sure that the droplets have a good degree of sphericity at the collision point to avoid any complexity that might be introduced to the dynamics by the effect of the initial droplet shape. On the other hand, the size of the droplets can be affected by the applied frequency shift that is used to change the impact parameter. Therefore, in the following, the uncertainties arise form these sources will be assessed.

3.7.1 Errors due to resolution

The selected resolution for the various experiments that were conducted in this thesis keeps the uncertainty in the droplet diameter in the order of $\pm\ 0.05d$ in identical size collisions and $\pm\ 0.05d_s$ in unequal-size collisions. This leads to errors in the measured diameters and velocities. Therefore, an error propagation analysis needs to be conducted when evaluating values that depend on the diameter and/or velocity, such as in evaluating We and Oh.

The general formula for the error propagation in Weber number ($\delta\mathrm{We}$) is given by

$$\delta\mathrm{We} = \pm\sqrt{\left(\frac{\partial\mathrm{We}}{\partial d}\delta d\right)^2 + \left(\frac{\partial\mathrm{We}}{\partial u_r}\delta u_r\right)^2}, \tag{3.9}$$

where, δd is the uncertainty of the dimeter of the droplet and δu_r is the uncertainty of the relative velocity of the colliding droplets and it is given by $\delta u_r = \pm\ 0.05d$.

Simplifying Eq. (3.9), $\delta\mathrm{We}$ is given by

$$\delta\mathrm{We} = \pm\sqrt{\left(\frac{0.05\rho u_r^2 d}{\sigma}\right)^2 + \left(\frac{0.1\rho d^2 u_r}{\sigma}\right)^2} \tag{3.10}$$

Due to the large values of velocity ($1 - 5\ \mathrm{ms}^{-1}$) compared to the diameter (four orders of magnitude), $\left(\frac{0.1\rho d^2 u_r}{\sigma}\right)^2 \ll \left(\frac{0.05\rho u_r^2 d}{\sigma}\right)^2$, hence errors associated with the velocity are negligible. On the other hand, we anticipate that the uncertainty in the relative velocity, and hence in We, arises from the uncertainty in the trajectories/angles due to the resolution is also negligible compared to that of the diameter. This is because the fact

that the trajectories were measured over a distance that is significantly longer than the diameter of the droplet (about 10 times), so the uncertainty of $\pm\ 0.05d$ has a negligible effect. Therefore, the main uncertainty in We due to the resolution is that due to the uncertainty of the droplet diameter. This uncertainty of We is, after simplifying Eq. (3.10), in order of

$$\delta\mathrm{We} = \pm 0.05\mathrm{We}. \tag{3.11}$$

Similarly, the uncertainty of Ohnesorge number ($\delta\mathrm{Oh}$), due to the uncertainty of the droplet diameter, is given by

$$\delta\mathrm{Oh} = \pm\sqrt{\left(\frac{\partial\mathrm{Oh}}{\partial d}\delta d\right)^2} = \pm\ 0.025\mathrm{Oh}, \tag{3.12}$$

However, due to that the used diameter in We and Oh is an average of measurements in a number of frames before the collision point, the believed uncertainty due to the resolution is smaller than the estimates of Eqs. (3.11) and (3.12).

In many cases, as will be seen in the next chapters, critical values of We need to be evaluated experimentally. This evaluation is done by finding two close successive experimental points that belong to two different regimes, so the critical value is selected as the average of them ($\mathrm{We_{av}}$). If the uncertainty due to a lack of data between these two successive points (δ_{lack}) is considerably large, it should be added to uncertainty from the resolution in Eq. (3.11). Thus, the total uncertainty of the critical value is then given by

$$\delta\mathrm{We_c} = \pm\frac{\delta\left(\mathrm{We_{av}} - \frac{\delta_{lack}}{2}\right) + \delta\left(\mathrm{We_{av}} + \frac{\delta_{lack}}{2}\right) + \delta_{lack}}{2}. \tag{3.13}$$

Simplifying Eq. (3.13) gives

$$\delta\mathrm{We_c} = \pm\left(\delta\mathrm{We_{av}} + \frac{\delta_{lack}}{2}\right), \tag{3.14}$$

where $\delta\mathrm{We_{av}} = \pm 0.05\mathrm{We_{av}}$ according to Eq. (3.11).

3.7.2 Droplet sphericity assessment prior to the collisions

The collisions were considered in the regime maps by making sure that the droplets are spherical. The small size of the droplets ensures high capillary pressure which alongside with the viscosity reduce the deformability of the droplets. A sample of data for three different solutions is given in Figure 3.11. The figure shows the ratio of the minor axis length (minor droplet diameter) to the major axis length (major droplet diameter) as a function of the droplet Y position. It can be seen that all the tracked data fall in the range between 1 and 0.96, which means the droplets have negligible deformation before the collision point.

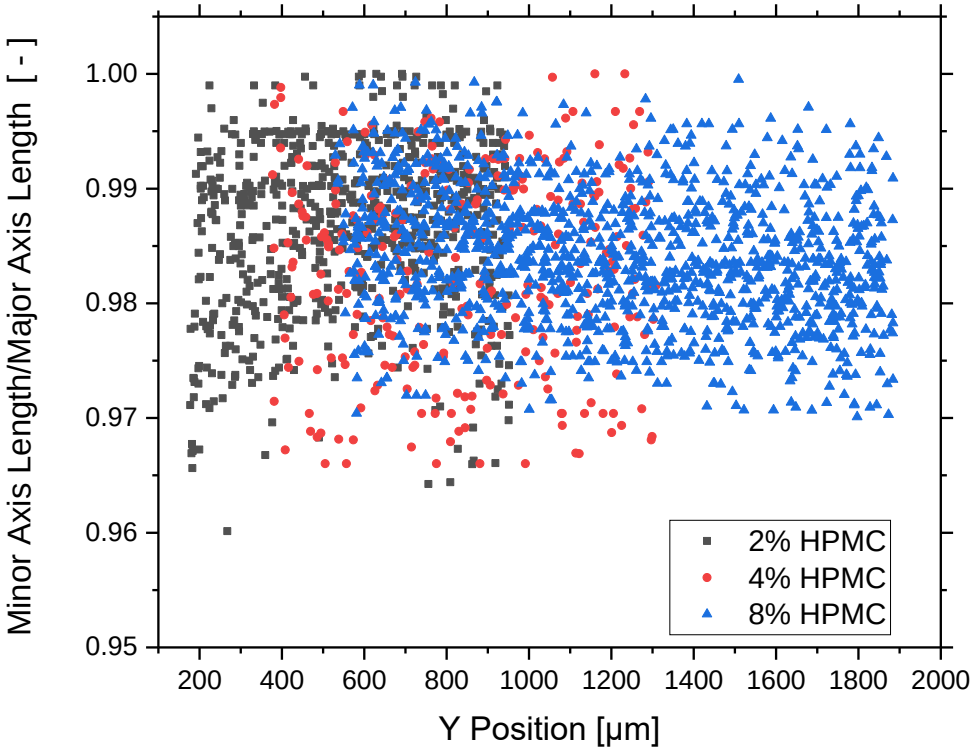

Figure 3.11 A sphericity assessment for 3 samples of droplets tracked before the collisions' points for a Weber number range from 60 to 80. The three samples are 48 droplets of 2% HPMC, 16 droplets of 4% HPMC and 55 droplets of 8% HPMC.

3.7.3 Size variation assessment

Figure 3.12 shows the size variation of the colliding droplets in both nozzles for three HPMC solutions 2%, 4%, and 8%. The variation in the size is negligible, within the regime, and it is always below 8 µm.

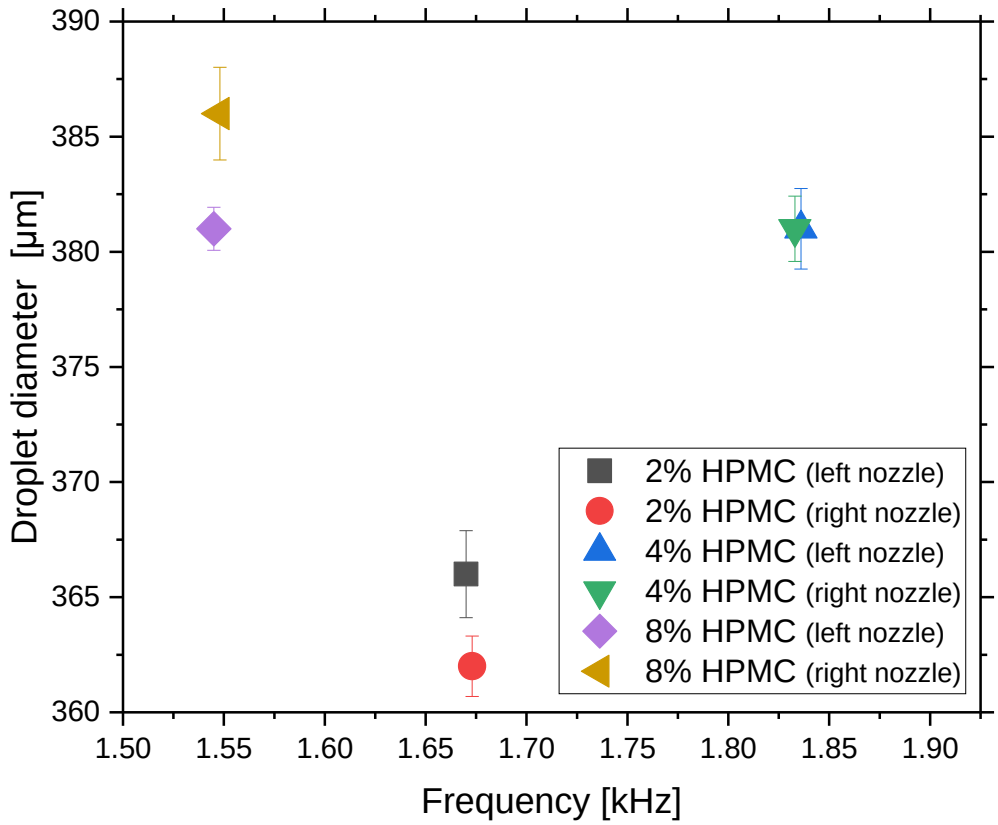

Figure 3.12 The size variation of the droplets for three HPMC solutions, 2% 4% and 8%. The error bars represent the standard deviation.

3.7.4 Zero-momentum frame reference

It also should be noted that it was ensured that the zero-momentum frame reference has no/negligible movement along the x-axis. This is by making sure that the dynamics of the colliding droplets stay below the collision point, as shown in the example in Figure 3.13. This ensures that all the relative velocity contributes in the deformation of the droplets and hence the calculated We is the effective impact We.

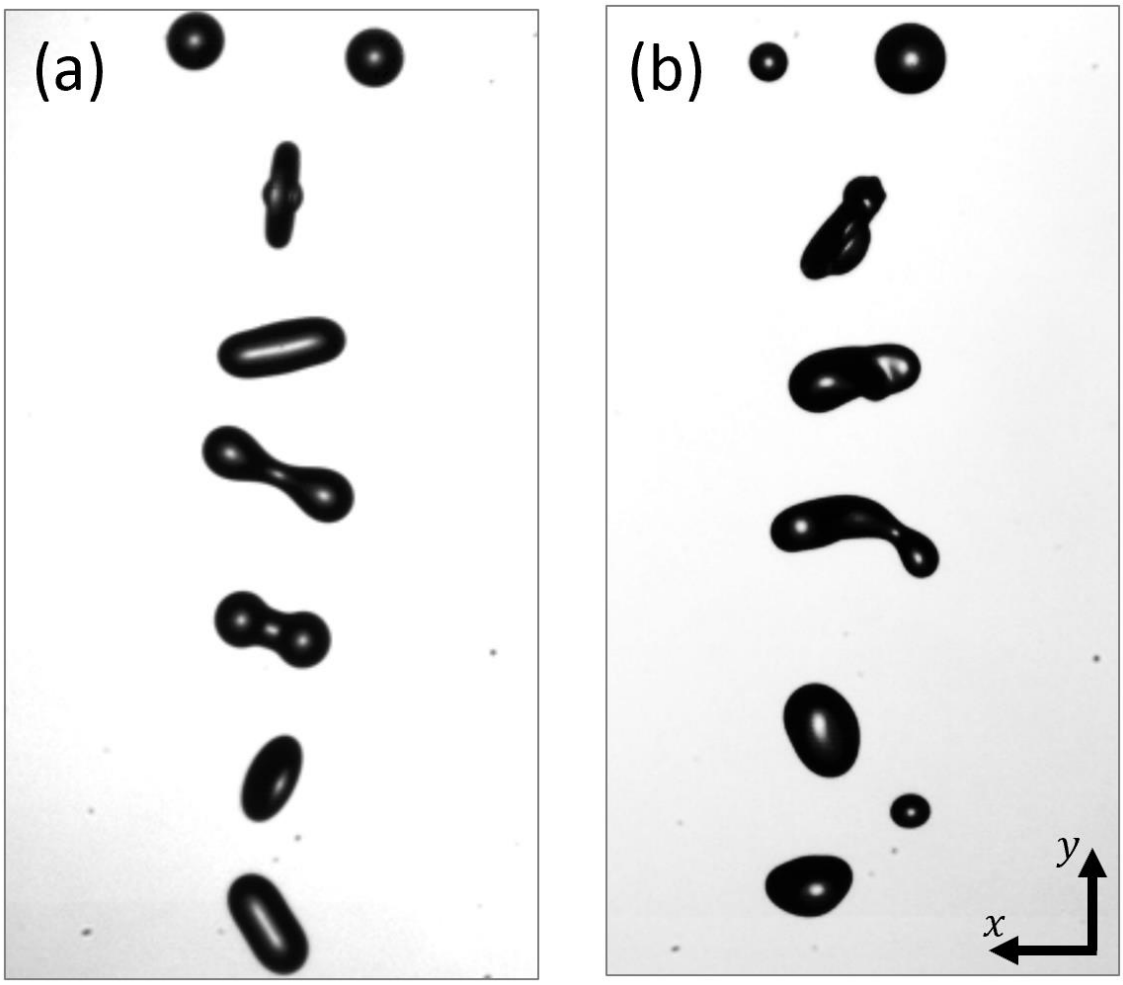

Figure 3.13 Images showing that the coalesced droplets has negligible movement in the x-axis: (a) 2% HPMC 360 um equal-size collisions (We = 35); (b) 2% HPMC unequal-size droplet collisions Δ = 0.58 (We = 53).

3.8 Conclusion

This chapter provided a description of a rig that was developed from scratch to conduct binary droplet collisions. The rig generates droplets based on the theory of Plateau–Rayleigh instability and the collisions are captured using high-speed imaging techniques. The rig can produce a wide range of droplet sizes by using the required dispensing gauge, velocities and viscosities. An image processing algorithm to extract the collisions details from the videos was developed using MATLAB. Newtonian aqueous solutions of HPMC, 2%, 4%, 6% and 8%, were used to generate the droplets. The characteristics of the HPMC solutions and the characterization methods were described. Finally, the conducted experiments were listed, and error analysis provided by making sure that the droplets

are spherical before the collisions, have consistent sizes in the whole regime map, and the zero-momentum frame reference has a negligible movement that can affect the collisions' outcomes.

Chapter 4: An experimental study of binary collisions of miscible droplets with non-identical viscosities.

This chapter reports experiments of equal-size binary droplet collisions at different viscosities. These collisions include collisions of droplets of identical viscosities to study the roles of the viscosity and collisions of non-identical viscosities to study the role of the viscosity difference.

4.1 Introduction

Droplet collisions are important to many areas of physics and technology, such as atmospheric studies, combustion science and spray drying (Ashgriz and Poo, 1990, Qian and Law, 1997, Francia et al., 2016, Post and Abraham, 2002). In many of these areas, the droplet collisions occur between droplets of different properties. For example, in spray drying, particulate products are produced by spraying solutions or slurries into hot, turbulent air in a spray drying tower. During the drying process droplet collisions can occur between droplets of different extents of drying (Southwell and Langrish, 2000). These collisions and their outcomes can have a significant effect on the process operation and on the powder properties, such as the size distribution and morphology (Verdurmen et al., 2004). Understanding, and predicting the outcome, of droplet collisions of non-identical droplets is therefore of great interest in this and other areas.

As mentioned in Chapter two, In the literature, the majority of the work is for collisions of droplets with identical physical properties. Whilst more limited, collisions between droplets with non-identical physical properties have also been studied. These studies can be divided into two categories: collisions between immiscible droplets and collisions between miscible droplets. The experimental and theoretical studies of immiscible droplet collisions with non-identical viscosity are more numerous, e.g. (Chen and Chen, 2006, Planchette et al., 2011, Planchette et al., 2010, Tsuru et al., 2010, Planchette et al., 2012, Planchette et al., 2017). However, studies of collisions of miscible droplets from unlike fluids are relatively scarce. Chen (2007) and Gao *et al.* (2005) experimentally investigated water, ethanol and diesel collisions; this limited their viscosities to a low range at relatively low viscosities (1 –

3.16 mPa s). Focke et al. (2013) made a detailed numerical and experimental study of collisions with a high viscosity ratio (2.6 vs. 60 mPa s), however, their study was limited to the coalescence regime with a fixed We of 26 and no regime maps were constructed.

In this work, the role of the viscosity difference between the colliding droplets will be experimentally studied, with collision conditions covering the whole regime map, for miscible fluids at viscosity range of 2.8 - 29 mPa s. This chapter is structured as follows. In Section 4.2, the regime maps will be presented and discussed. In section 4.2.1, the effects of the viscosity on the regime boundaries will be discussed and justified using observations of the dynamics from the high-speed images. In section 4.2.2, the applicability of the existing models, presented in chapter 2, to collisions of droplets with non-identical viscosities will be examined. Finally, a conclusion, will be drawn in section 4.3.

4.2 Regime maps

The standard regime maps of droplet collisions, with droplets that have identical physical properties, are commonly plotted in the parameter space of We and B. However, for collisions of droplets with different physical properties, We is not unique as it can have different values depending on the physical properties chosen. Gao et al. (2005) suggested that in the case of droplets of two different miscible liquids, We should be based on the properties of the droplet that has lower surface tension. This was attributed to the belief that the lower surface tension controls whether the collision outcome is coalescence or separation. However, this is only valid for collisions of low viscosity droplets because of the predominance of the viscosity effect in determining the collision outcome in viscous collisions (Kuschel and Sommerfeld, 2013). Therefore, in some studies of collisions with non-identical fluids, the use of We in the regime maps is avoided and the relative velocity is used instead, such as in Planchette et al., (2010).

In this work, HPMC solutions show a negligible variation in surface tension and density, as seen in Table 1. We is therefore independent of solution concentration and allows the regime maps to be constructed based on We. Moreover, the similar values of surface tension and the density, see Table 1, isolate the effect of the viscosity on the collision outcome.

To allow comparison and further analysis, three HPMC solutions, 2%, 4%, and 8%, were used to construct six regime maps, three for collisions of identical droplets as shown in Figure 4.1, while the other three for collisions of droplets with non-identical viscosities, as shown in Figure 4.2. Noticeably, the regime maps of the non-identical solutions show defined regime boundaries that are qualitatively comparable to those of identical solutions.

In the following sections, the effect of the viscosity on the regime maps and the dynamics of the collisions will be discussed by comparing the role of the viscosity on collisions of droplets with identical viscosities with its role on non-identical collisions. Finally, the applicability of the existing models of the regimes' boundaries, on both types of collisions (i.e. of identical and non-identical viscosities), will be discussed.

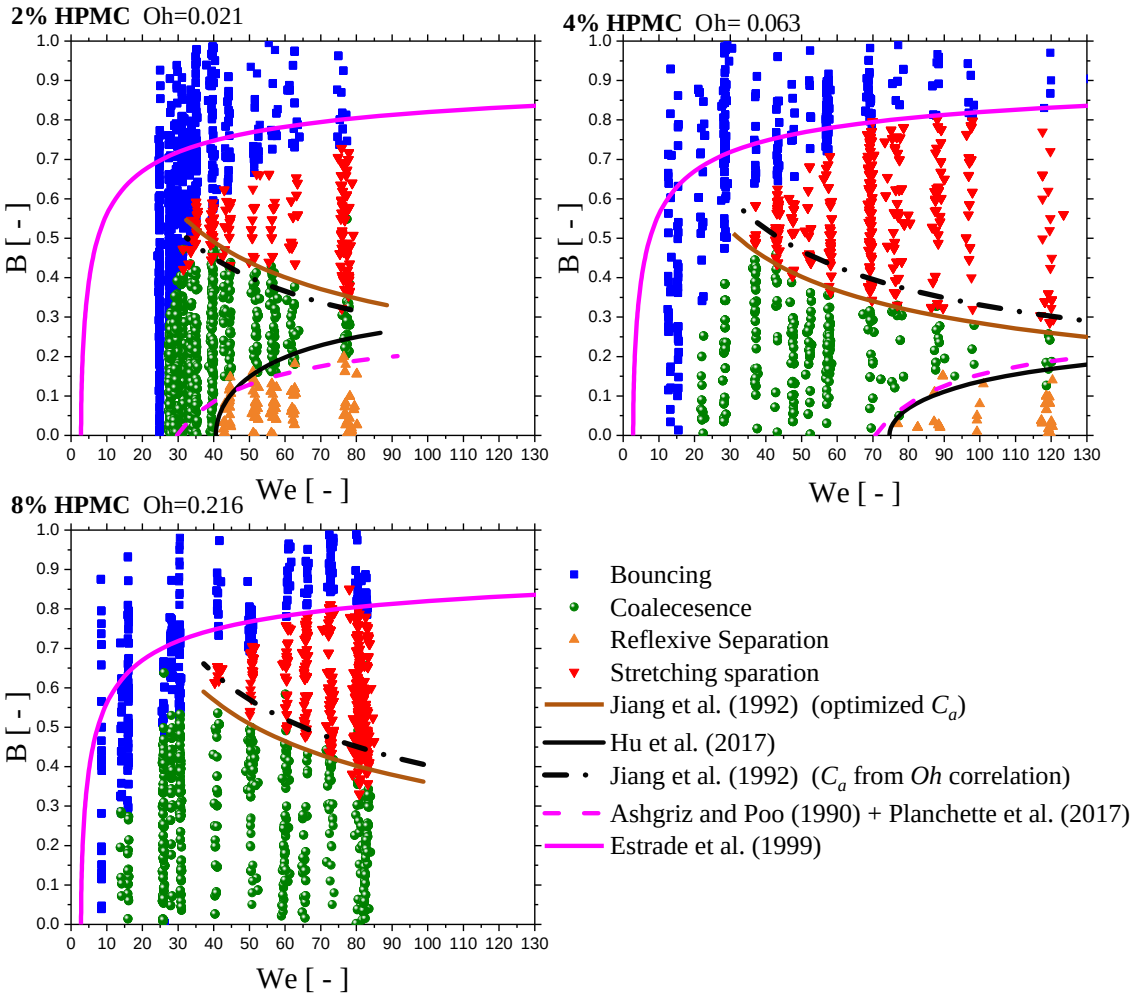

Figure 4.1 Regime maps of binary droplet collisions with droplets that have identical viscosities, and the performance of the existing models in predicting the regimes' boundaries.

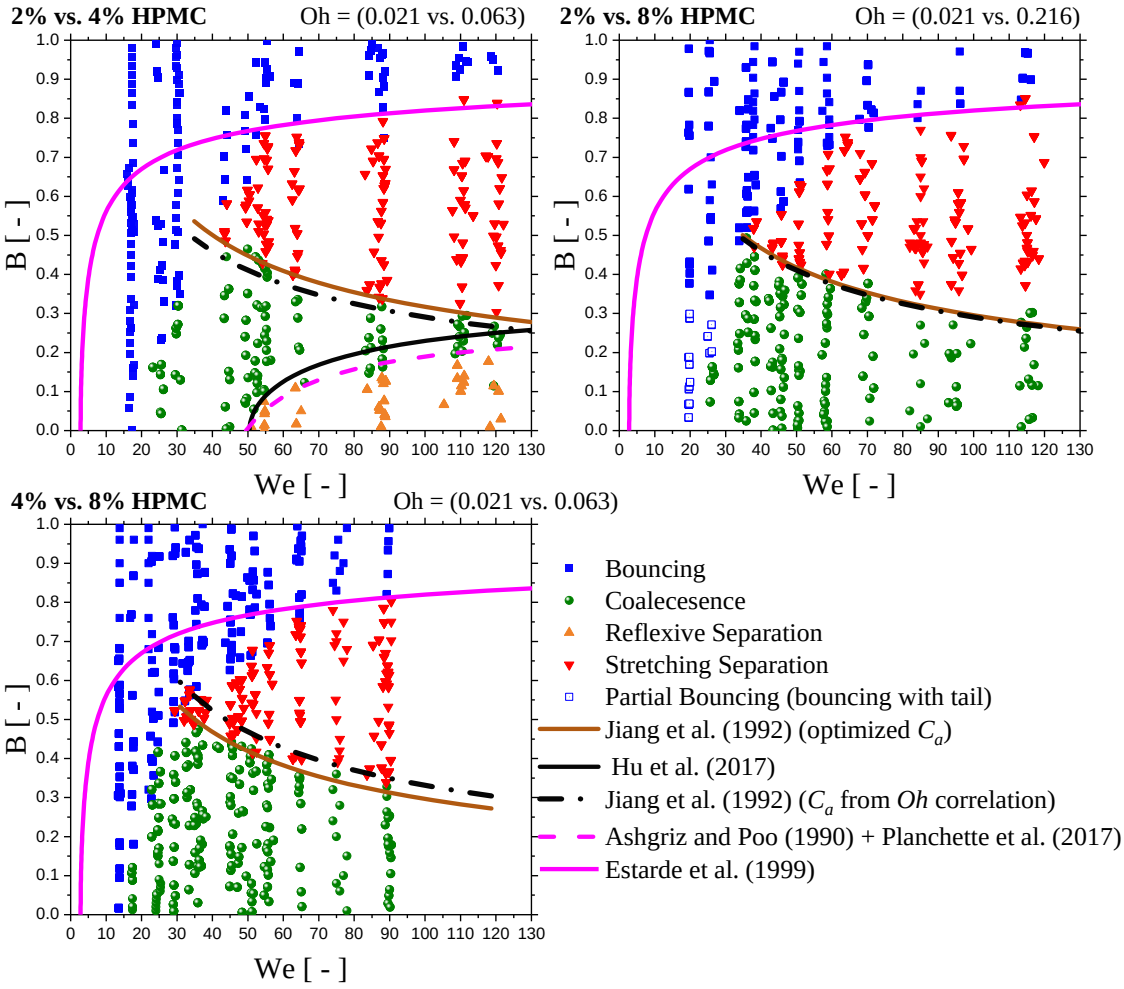

Figure 4.2 Regime maps of binary droplet collisions with droplets that have non-identical viscosities, and the performance of the existing models in predicting the regimes' boundaries.

4.2.1 Comparison of the identical and the non-identical collisions

4.2.1.1 Bouncing

Although the role of the viscosity on collisions of identical droplets has been widely investigated, its effect on the bouncing regime boundary has scarcely been studied. This might be due to the limited number of studies that show a clear transition from the bouncing regime to the fast coalescence regime at head-on collisions ($\mathrm{We}_{\mathrm{B/FC}}$). The absence of a bouncing to fast coalescence transition at head-on collisions could be attributed to the droplets' fluid properties, as some fluids do not show bouncing at low B, such as water (Qian and Law, 1997) and ethanol (Estrade et al., 1999), or they do not show any bouncing at the entire range of B, such as milk (Finotello et al., 2018b). Krishnan and Loth (2015) suggested based on a literature survey that for head-on collisions, $\mathrm{We}_{\mathrm{B/FC}}$ value would be expected to increase with increasing viscosity. However, the basis of this claim is based on extrapolation of data from high B to low B, for fluids which are not seen to bounce at B = 0, rather than direct collision data. Pan et al. (2016) also showed that a 30% aqueous glycerol solution, with a viscosity three times that of pure water, promotes bouncing compared to pure water droplets. The authors attributed this to less surface mobility in the case of higher viscosity droplets that suppresses the air drainage and hence bouncing is promoted.

The above hypothesis of surface mobility by Pan et al. (2016) is based on the observed phenomenon that when the droplets' interfaces approach each other the trapped air experiences high-pressure build-up at the centre of the gap, which causes indentation to the interfaces. Because of this indentation, a rim is formed on the surface and hence the minimum clearance between the droplets takes a ring shape. Therefore, to discharge the trapped air, this rim is pushed away from its centre. This dynamic is called surface mobility. Therefore, at higher viscosity the rim will have less mobility which resists the air drainage and consequently bouncing occurs. It should be noted that the surface mobility was numerically and experimentally observed in droplets coalescence on surfaces (Hicks and Purvis, 2010; Weitz and Mahadevan, 2012), while in binary droplet collisions it is only observed in numerical studies (Pan et al., 2008; Pan et al., 2016).

In this study, the regime maps of all viscosity combinations show a bouncing to fast coalescence transition at head-on collisions, as shown in Figures 4.1 and 4.2. For collisions between droplets of identical fluid, $\mathrm{We}_{\mathrm{B/FC}}$ decreases with increasing viscosity. This is contrary to the aforementioned observations of Krishnan and Loth (2015) and Pan et al. (2016). This might be due to the higher viscosity range in this work compared to those in the previous studies, which are up to 4.3 mPa s in Krishnan and Loth (2015) and up to 2.8 mPa s in Pan et al. (2016). At high viscosity, the pressure build-up of the trapped air might not be sufficient to cause a significant surface indentation (Langley et al., 2017) and hence bouncing might be controlled by a different mechanism. By accepting this hypothesis, the resistance of the gas drainage is therefore determined by the area of surface flattening, which is expected to decrease by increasing the viscosity, as shown in the schematic in Figure 4.3. Therefore, the bouncing might be enhanced by increasing the viscosity, according to the mechanism of the surface mobility, up to a certain limit after which the flattening mechanism takes over and hence increasing the viscosity further suppresses the bouncing. This can be a possible explanation for the suppression of bouncing when the droplet viscosity is increased in our study.

Figure 4.4 shows the bouncing dynamics of the three HPMC systems. The viscosity of 2% HPMC is within the range reported by Krishnan and Loth (2015) and Pan et al. (2016), therefore it is expected to have some surface indentation. This also can be expected by noticing the distorted shape of the droplet, at time 0.17 ms and 0.27 ms in Figure 4.4, which seems to have a rim development. However, in cases of 4% and 8% HPMC the droplets do not show clear distortions and seem to have nearly flat interfaces (or negligible indentation). Thus, in 2% HPMC we assume there is a rim mobility mechanism that controls the air drainage, whereas it is controlled by the flattening mechanism in 4% and 8% HPMC. However, more experimental and numerical efforts are required to validate the hypotheses of the mechanism change with sufficient increase in the viscosity of the droplets.

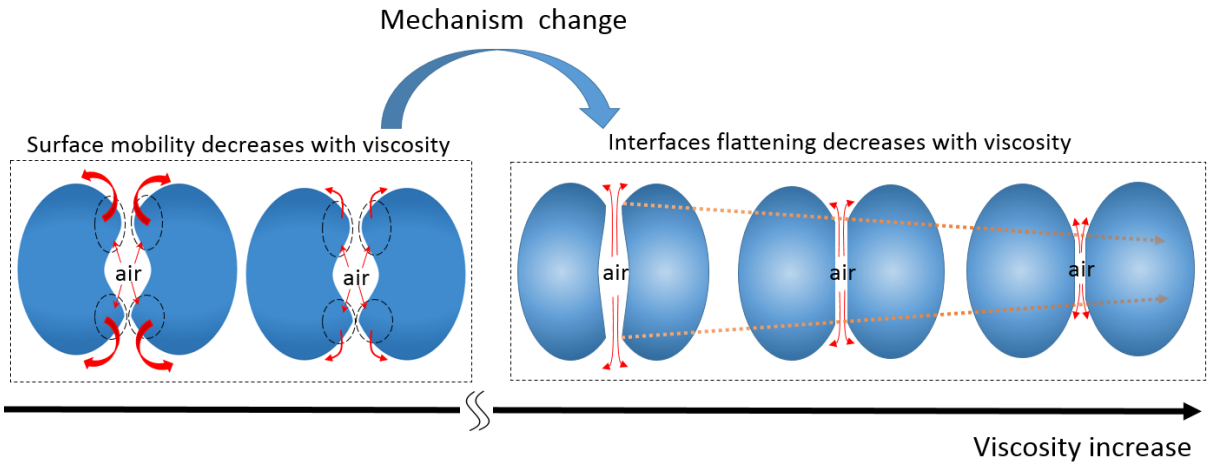

Figure 4.3 A schematic showing the expected change in the mechanism of the interfaces' deformation and the air drainage process by increasing the viscosity.

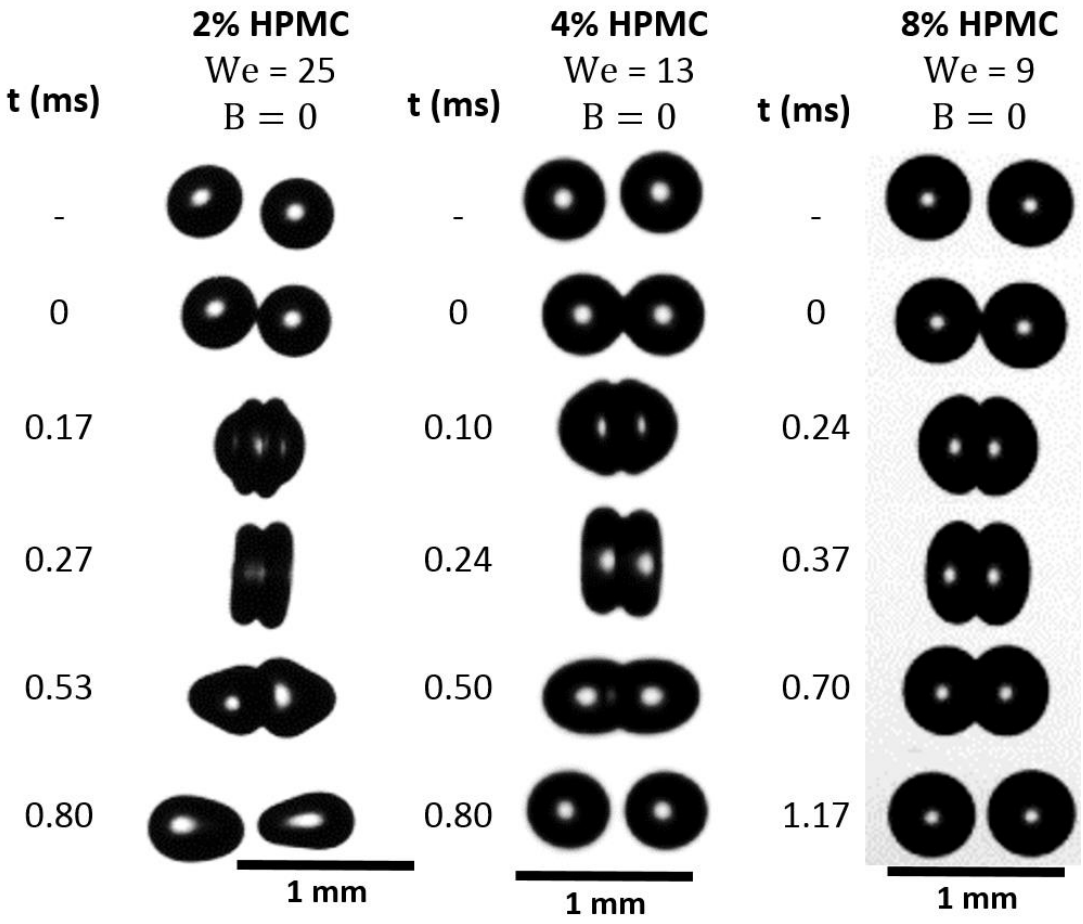

Figure 4.4 The effect of the viscosity on the dynamics of the head-on bouncing collision, at the transitional Weber numbers between bouncing and coalescence $We_{B/FC}$, for droplets that have identical viscosities. The higher droplets viscosity the lower $We_{B/FC}$ and deformation.

Table 4.1 Bouncing/fast coalescence boundary for head-on droplet collisions.

% HPMC	*2%*	*2 vs. 4%*	*4%*	*4 vs. 8%*	*8%*
$\mathrm{We}_{\mathrm{B/FC}}$	26 ±1	22 ±2	18 ±2	15 ±1	11 ±2
% HPMC	2 vs. 8%				
$\mathrm{We}_{\mathrm{B/FC}}$	21 ±2				

In the case of collisions between miscible droplets that have different viscosities, $\mathrm{We}_{\mathrm{B/FC}}$ has an intermediate value between the values of the identical cases, see Table 4.1. The bouncing dynamic in cases of head-on identical collisions is symmetric to the impact plane, as shown in Figure 4.4. However, bouncing in cases of non-identical viscosities shows asymmetric dynamics as the lower viscosity droplet is deformed more than the higher viscosity droplet. This deformation difference increases as the viscosity ratio increases, as shown in Figure 4.5. This change in deformation leads to a higher drainage rate of the trapped air between the colliding droplets than that of the equivalent case of the lower viscosity droplet, and a drainage rate lower than that of the equivalent case of higher viscosity droplets. Thus, the intermediate values of $\mathrm{We}_{\mathrm{B/FC}}$ are expected.

A new collision regime has also been identified in case of non-identical viscosities at high viscosity ratio (i.e. 2% vs. 8% HPMC), where a relatively significant asymmetry in dynamics due to the differences in viscosity is observed. In this case, bouncing is accompanied by a temporary partial coalescence and a thin ligament (tail) between the two droplets is observed. This ligament breaks rapidly at the surface of the high viscosity droplet and retracts back to the lower viscosity droplet, as shown in Figure 4.5. This type of bouncing is named partial bouncing on the regime map in Figure 4.2. The exact mechanisms that lead to the partial bouncing are not clear due to the complexities of surface deformation, air drainage and surface contact involved in determining the droplet dynamics in this region of the regime map.

It is interesting to notice that the dynamics of bouncing in case of non-identical viscosities is very similar to the bouncing dynamics of the collisions of low viscosities droplets that have large surface tension difference, such as the bouncing collision between a water droplet and a diesel oil droplet, see Figure 9 in Chen and Chen (2006). In this case, the droplet with lower surface tension, diesel oil, suffers larger deformation than that of the water droplet. This is because the higher surface tension leads to higher capillary pressure ($2\sigma/d$), which makes the droplet more resistible to the deformation, and vice versa.

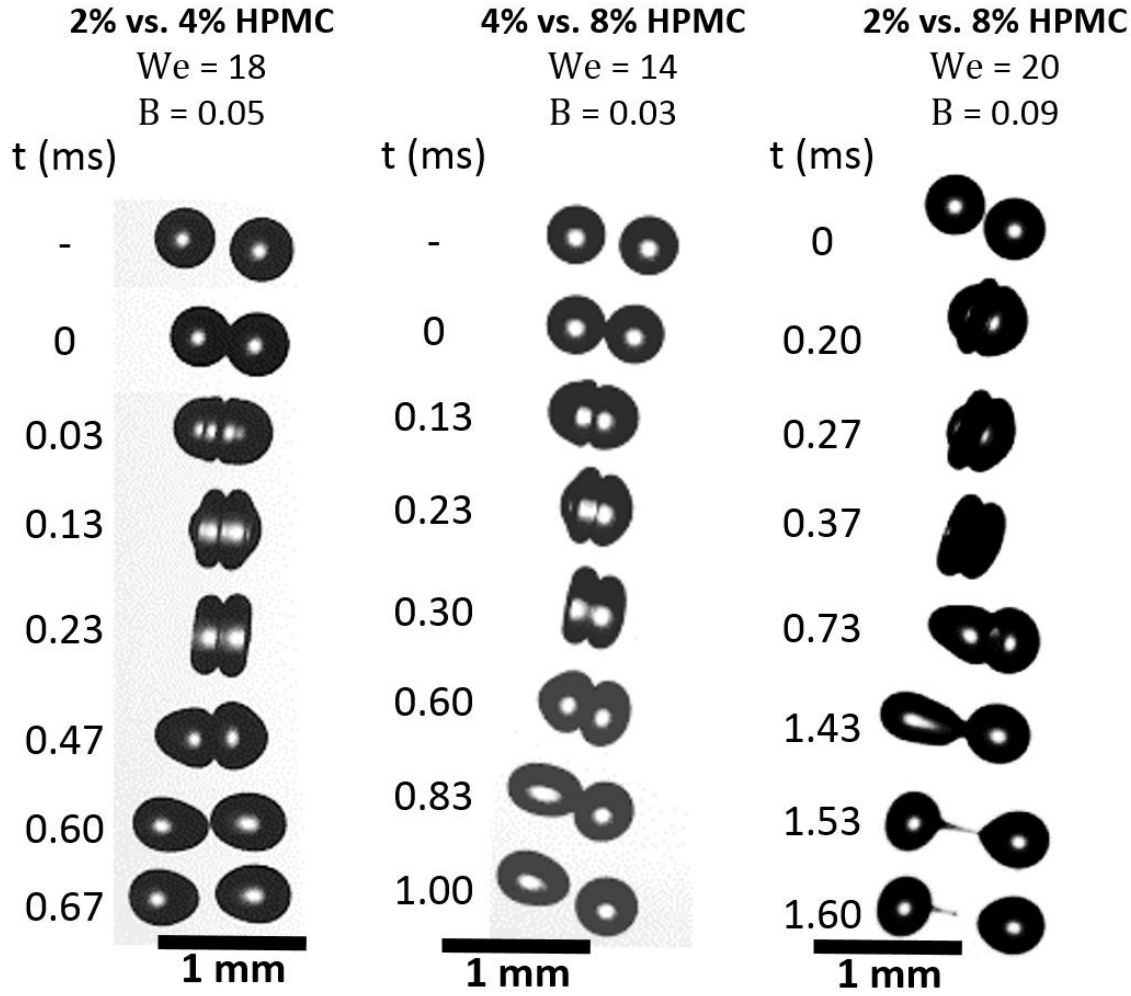

Figure 4.5 The effect of the viscosity on the dynamics of the head on bouncing collisions of droplets that have different viscosities. High viscosity (right droplet) low viscosity (left droplet). Partial bouncing is seen at high viscosity ratio (2% vs 8% HPMC).

4.2.1.2 Stretching separation

Kuschel and Sommerfeld (2013) observed that increasing the viscosity in identical droplet collisions would shift the boundary of the stretching separation toward higher B values. The regime maps of the identical cases in this study show the same trend, when HPMC concentration is increased from 4% to 8%, as shown in Figure 4.6a. However, the boundary of 2% shows slightly higher B values compared to 4% HPMC, see Figure 4.6a. This trend (the boundary of the lower viscosity collisions occurring at higher B was also observed in Kuschel and Sommerfeld (2013) in case of comparing the regime maps of 20% and 40% saccharose. A possible hypothesis explaining this will be given in the following discussion.

In the three non-identical systems studied, the boundary of the stretching separation regime is nearly superimposed (with slightly higher B) on the boundaries of the identical viscosity cases of the lower viscosity droplet, as shown in Figure 4.6b, c, and d. This can be clearly seen in case of 4% vs. 8% HPMC, where its boundary closer to the identical case of 4% HPMC than the identical case of 8% HPMC, as shown in Figure 4.6c. Similar behaviours can be seen in cases of 2% vs. 4% HPMC and 2% vs. 8% HPMC as their stretching separation boundaries are closer to the cases of the identical viscosity collisions of the lower viscosity (i.e. 2% HPMC in both cases), as shown in Figure 4.6b and d. Ultimately, this means increasing the viscosity of one of the colliding droplets has a negligible effect on the boundary of the stretching separation regime.

It is interesting to note that both 2% and 2% vs. 4% HPMC boundaries lie at higher B values than 4% HPMC, see Figure 4.6b, which is contrary to the other aforementioned cases. This may be due to the dominance of surface tension, $\mathrm{Oh} < 0.1$, in controlling collision outcome in these conditions. A slight increase in the viscosity (from 2.8 mPa s in 2%HPMC to 8.2 mPa s in 4% HPMC) might reduce this effect before entering an area where viscosity plays a dominant role in governing behaviour. In Figure 4.6a, 8% HPMC the boundary occurs at higher B than the lower viscosity cases, $\mathrm{Oh} = 0.216$, which suggests that viscosity will have a dominant effect. It is interesting to note that Planchette et al. (2016) also reported similar Oh boundary for head-on collisions, as at $\mathrm{Oh} < 0.1$ the compression period show different deformation and have less viscous loss

ratio a, which is attributed to the insufficient time in low Oh to form viscous boundary layers. However, a full understanding of these observations requires a systematic study for the viscosity effect for solutions that have $\mathrm{Oh} < 0.1$, which is out of the scope of this research.

In cases of collisions between droplets that have identical viscosities, a uniform ligament is formed between the droplets during the stretching process, as shown in Figure 4.7. However, in case of non-identical viscosities, the ligament is thicker on the side of the higher viscosity droplet and the breakup happens at the thinner side of the ligament, near the low viscosity droplet, as shown in Figure 4.8. Consequently, it is of interest to visualise and understand the mixing between the two droplets that occurs during the stretching separation process. As this is not possible from the shadow images in Figure 4.8 an alternative imaging set-up was developed where one droplet was coloured and the collisions were lit from the front.

Colour images of stretching separation of the three viscosity ratios are shown in Figure 4.9. During the early stages of the stretching process, a steep colour, and consequently viscosity, gradient is seen in the ligament near the higher viscosity droplet. This explains the non-uniform ligament in Figure 4.8 and reveals that the breakup occurs in the lower viscosity region of the filament close to the low viscosity droplet. Thus, in these non-identical cases the stretching separation is controlled by viscosity of the lower viscosity droplet, which explains the near superposition of the stretching separation boundary of the non-identical droplets with the boundary seen for identical, lower viscosity droplets. Moreover, from Figure 4.9, it also can be noticed that the separated droplets have no significant mixing, as they keep their original colour and no significant size change is observed, while the satellite droplets seem to have some mixing as their colour is in-between of the original droplets.

For completeness, It should be noted that in collisions of immiscible droplets with different viscosities, Planchette et al. (2012) also found that the ligament is formed from the low viscosity droplet (the encapsulating droplet).

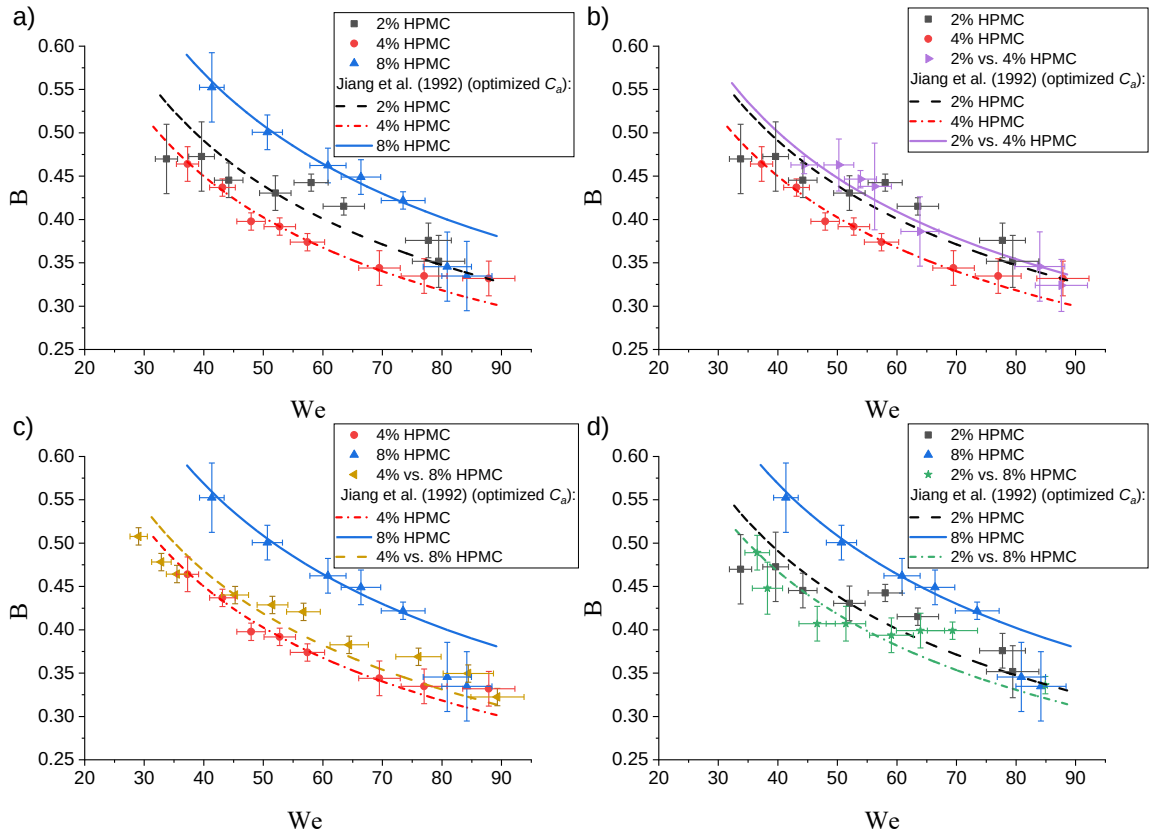

Figure 4.6 Comparisons of the stretching separation boundaries of the identical droplets collisions at different viscosities, as well as the non-identical droplets collisions vs. the identical droplets collisions. The vertical error bars represent the uncertainty due to the gaps between the data points in Figures 4.1 and 4.2. The horizontal error bars represent the uncertainty in We raised from the resolution as discussed in chapter 3. The lines represent the model of Jiang et al. (1992) with C_b =1 and C_a is optimized based on the minimum MAE.

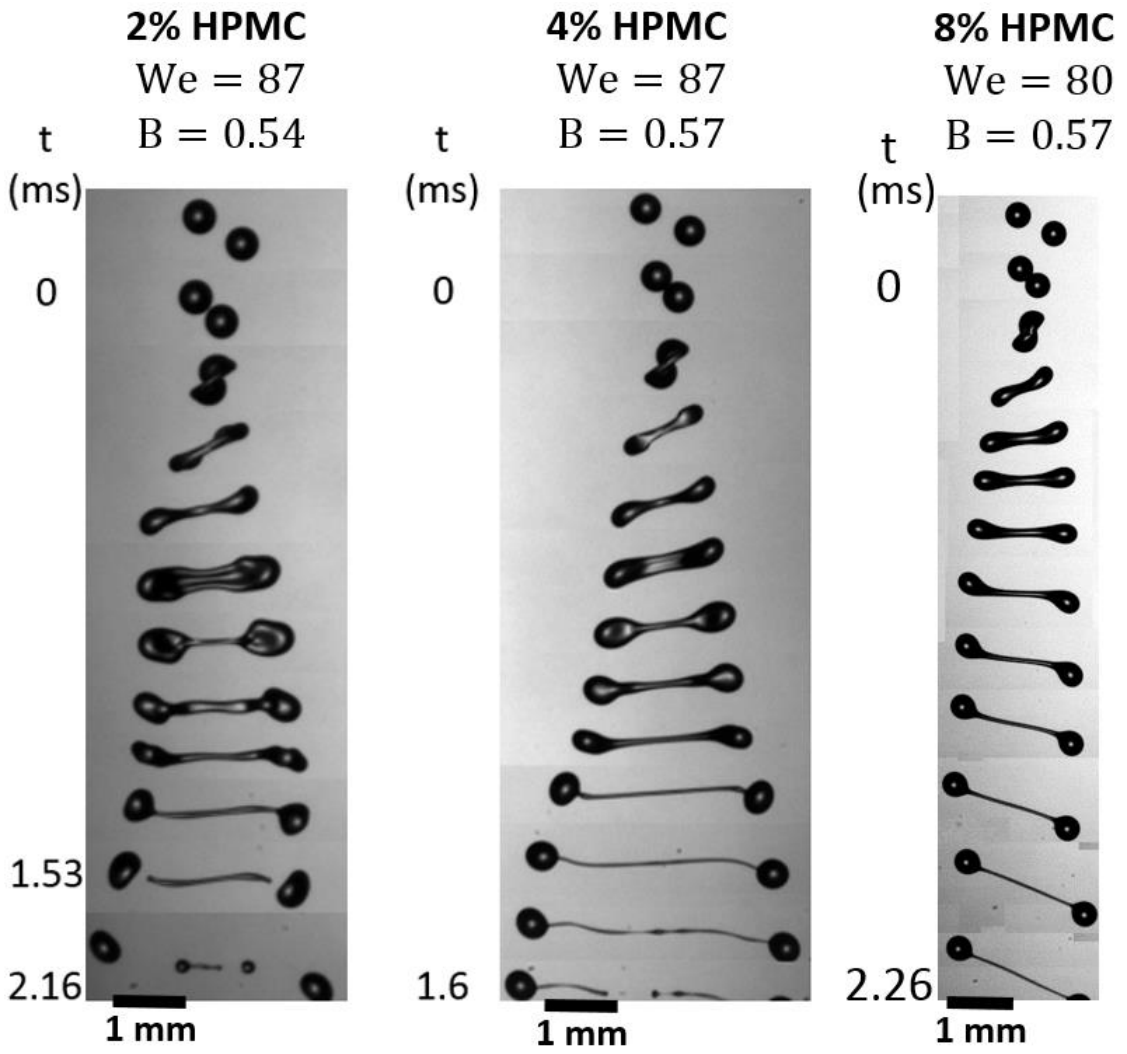

Figure 4.7 Shadow images showing the effect of the viscosity on the dynamics of the stretching separation in collisions of droplets with identical viscosities. The higher viscosity droplet the longer ligament. In 8% HPMC, the ligament is expected to become longer before it breaks up, however, this takes a relatively long time to happen and hence occurs out of the field of view.

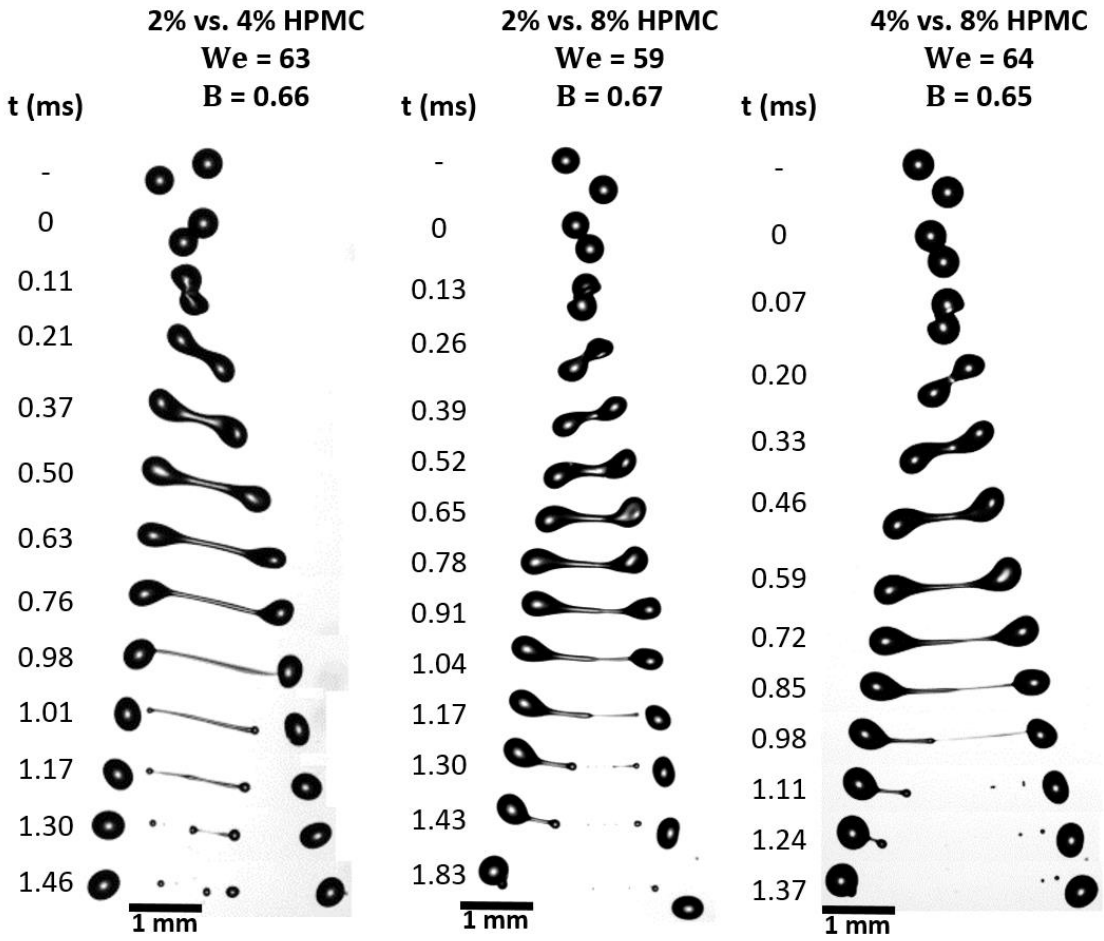

Figure 4.8 Shadow images showing the effect of the viscosity difference on the dynamics of the stretching separation collisions of droplets that have non-identical viscosities. The high viscosity droplet coming from the right (on the top) and stretching to the left (from the middle to the bottom of the images).

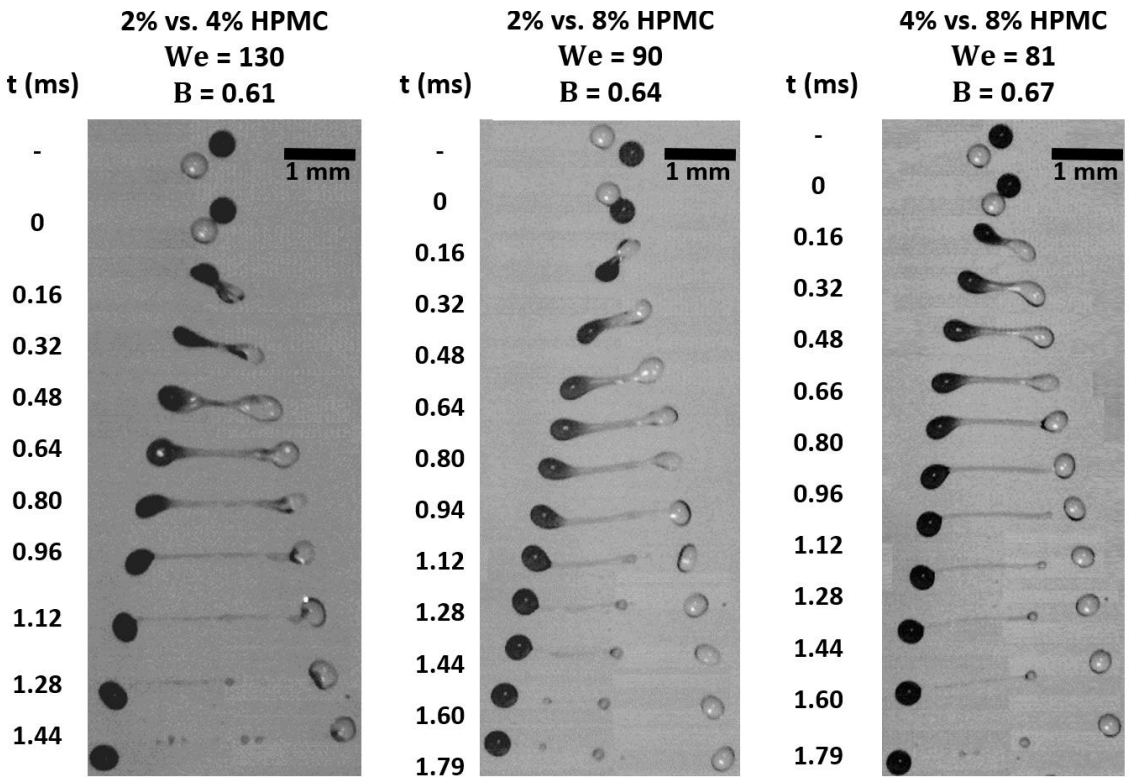

Figure 4.9 Coloured time-resolved images showing that ligament is drawn from the low viscosity droplet. The transparent droplets are the lower viscosity, and the dark droplets are the higher viscosity.

4.2.1.3 Reflexive separation

It is known from the previous studies of identical droplet collisions that increasing the viscosity shifts the onset of the reflexive separation $\mathrm{We}_{\mathrm{FC/RS}}$ towards higher We (Kuschel and Sommerfeld, 2013, Finotello et al., 2018b, Finotello et al., 2018a, Gotaas et al., 2007). The collisions of identical viscosity droplets show the same trend in this study. For example, changing the concentration of HPMC from 2% to 4% shifts $\mathrm{We}_{\mathrm{FC/RS}}$ from 41 ±1 to 75 ±2 and increasing the viscosity further in 8% HPMC returns with no reflexive separation for the investigated range up to $\mathrm{We}_{\mathrm{Max}} = 84$.

Unlike stretching separation, increasing the viscosity of one of the colliding droplets noticeably shifts the boundary of the reflexive separation towards higher We. However, this shift is less significant than that of increasing the viscosity of both of the colliding droplets. For example, $\mathrm{We}_{\mathrm{FC/RS}}$ of the collision of 2% HPMC droplet with 4% HPMC droplet is 48 ±2, while it is 41 ±1 and 75 ±2 for identical viscosity collisions of 2% and 4%, respectively, see Figures 4.1 and 4.2. Interestingly, on further increasing the viscosity of

the high viscosity droplet, 2% vs. 8% HPMC, no reflexive separation is observed within the investigated range of We. Similarly, in 4% vs. 8% HPMC, no reflexive separation is observed, see Figure 4.2.

In the case of head-on collisions of identical droplets, the droplets initially form a rimmed lamellar disc, whereby the impact kinetic energy is completely converted into viscous loss and surface energy. Then, by the action of surface tension, the edges of the formed disc retract toward the centre of the mass. This retraction causes a reflexive internal flow inside the combined droplet which leads to the formation of a cylindrical shape aligned along the original axis of collision. At high enough We, this continues to extend symmetrically until separation occurs. When the impact We is relatively low, the separation leads to formation of two equal-size droplets that have equivalent size to the mother droplets, However, at higher We a large satellite type droplet can form between the two droplets separating droplets. The size of this satellite droplet is proportional to We (Ashgriz and Poo, 1990). Figure 4.10 shows the dynamics of reflexive separation at relatively high We for 2% and 4% HPMC solutions.

In the case of non-identical viscosity collisions, a similar rimmed lamellar disc is still observed, however, on retraction the internal reflexive flow shows non-symmetrical behaviour. In these cases, the lower viscosity fluid starts separating faster and forms a *baseball-bat* shape. The subsequent ligament breaks near the end of the low viscosity region forming a droplet. The remaining extended ligament then retracts towards the high viscosity end forming a single droplet with a larger size than the lower viscosity droplet. The coloured droplet images help to understand this behaviour. Interestingly, some partial mixing is seen between the colliding droplets in the earlier stages of the collision. This leads to a viscosity gradient along the ligament and consequently the break-up occurs at the lower viscosity end of the ligament, closest to the low viscosity droplet. At the collision conditions at the last set of images shown in Figure 4.10, the remaining ligament retracts and forms a single large droplet. This large droplet will be more diluted than the initial droplet due to the partial mixing at the retracted ligament, however the small droplet has a concentration similar to that of the lower viscosity.

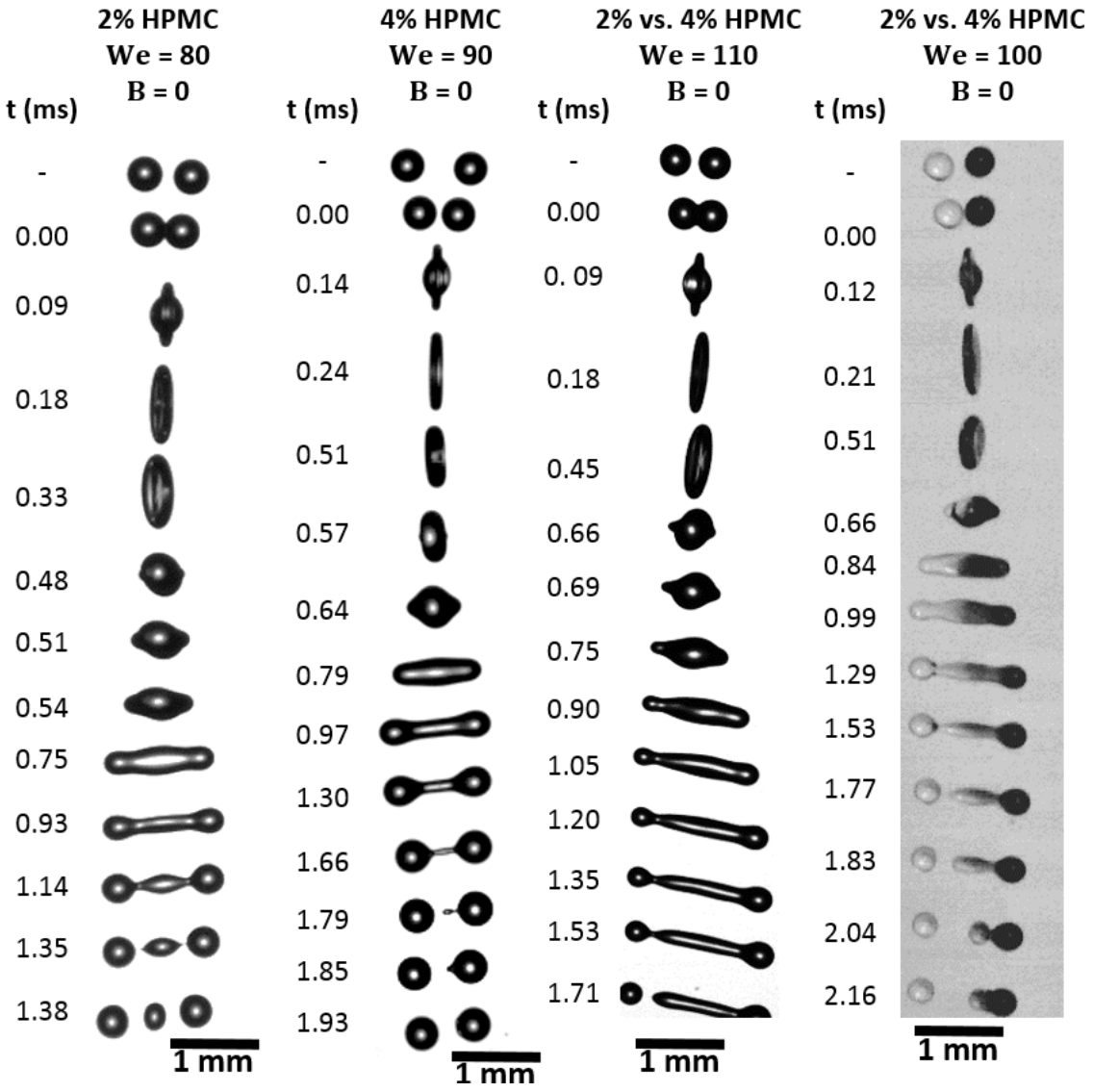

Figure 4.10 Dynamics of reflexive separation collisions for droplets that have identical and non-identical viscosities. In the case of the collision of 2% vs. 4% HPMC in the shadow images, the low viscosity droplet is located on the left). In the coloured images, the dark droplet is the higher viscosity (4% HPMC).

4.2.2 Boundaries Modelling

Modelling the regime boundaries of binary droplet collisions has received substantial attention. However, the majority of these studies deal with collisions of droplets that have identical fluids (e.g. Ashgriz and Poo, 1990; Jiang et al., 1992; Estrade et al., 1999). In addition, a few studies have been conducted to model the boundaries of the separation regimes in collisions of immiscible droplets (Planchette et al., 2012). To the

best knowledge of the author, the regime boundaries of non-identical, miscible fluid, droplet collisions have not been considered in the literature. In this section, the applicability of the existing models, in section 2, for the boundaries of the regimes for both identical and non-identical viscosity droplet collisions, of this study, will be examined.

4.2.2.1 Bouncing boundary

Estrade et al. (1999) developed the first model to predict the bouncing regime boundary, Eq. (2.7). This model includes a shape factor, ϕ', which is reported to have a value of 1.12. Generally, this model shows poor performance, as can be seen in Figures 4.1 and 4.2. Its poor performance has been frequently reported in the literature (Kuschel and Sommerfeld, 2013, Sommerfeld and Kuschel, 2016, Sommerfeld and Pasternak, 2019, Finotello et al., 2018a, Finotello et al., 2018b). Therefore, this model and the modelling of bouncing, in general, will be discussed in great detail in Chapter 7.

4.2.2.2 Stretching separation boundary

The boundary of the stretching separation regime, in case of non-identical viscosities, is comparable to that of the identical case of the lower viscosity droplet. Therefore, the model of Jiang et al. (1992), Eq. (2.27), can be used to fit the boundaries in both identical and non-identical collisions. In the case of collisions of droplets with non-identical viscosities, the lower viscosity is used in the model. This is based on our aforementioned observation that the ligament between the droplets is mainly composed of the lower viscosity fluid and the break up occurs near the lower viscosity droplet. Figure 4.1 and 4.2 show that the model of Jiang et al. (1992) captures the shape of the boundary very well for both the identical and non-identical cases. Also shown in these figures is a comparison of a fit with an optimised empirical parameter, C_a, with the fit using the $C_a = f(\mathrm{Oh})$ correlation of Sommerfeld and Pasternak (2019), Eq (2.28). In both cases $C_b = 1$, and the optimisation was done by minimising the MAE, using Eq. (4.1) and the data points shown in Figure 4.6.

$$\mathrm{MAE} = \frac{1}{n}\sum_{i=1}^{n} \mid \mathrm{B}_{model} - \mathrm{B}_{exp.} \mid_i . \tag{4.1}$$

As can be seen in the case of the optimised empirical factor, the model of Jiang et al. (1992) gives a very good fit in all cases. However, the fit using the correlation in Eq. (2.28) (Oh for the lower viscosity droplet is used) gives a slight offset in most cases, though interestingly in the case of the non-identical collisions this offset in, B, is small < 0.05.

Figure 4.11 details and quantitatively compares the values C_a used to define the curves in these plots. Noticeably, the optimised C_a values of the non-identical collisions are close to the values of the identical collisions of the droplet of the lower viscosity. Comparing optimised C_a values with the C_a values calculated using Eq. (2.28) a reasonable agreement is seen, however, there is a little scatter. Ultimately, the model of Jiang et al. (1992), with the single empirical parameter, C_a, can be used to accurately describe the stretching separation boundary for collisions of non-identical viscosities by using the lower viscosity and C_b=1. The correlation of Sommerfeld and Pasternak (2019) provides a reasonable estimate for C_a, whilst an optimised value of C_a gives an excellent fit of B across a wide range of We.

The excellent agreement with the model of Jiang et al. (1992) for the boundary in all the systems studied, suggests that the impact parameter modifications proposed by Planchette et al. (2012), Eq. 2.29, are not necessary, even though some droplet distortion and rotation was observed. However, it is also of interest to see if this alternative approach provides a good fit to the data, consequently, it was evaluated. The effective impact parameter B_{eff}, was calculated using the 8% HPMC boundary as a reference boundary based on the assumption that these droplets experience negligible distortions compared to the lower viscosity cases. The empirical parameter *U** was determined for both the identical and non-identical data sets by minimising the MAE between B_{eff} describing each boundary and the reference boundary. Using these fitted values of *U** to calculate B_{eff} for the experimentally determined boundary values (Figure 4.12a), shows a reasonable collapse on to a single curve, Figure 4.12b, which can be approximated by the model of Jiang et al. (1992). For completeness, as the model of Jiang et al. (1992) was fitted to this single curve, the empirical parameter $\mathrm{C_a}$ is dependent on the viscosity of the system, see Figure 4.11. As all points collapsed on a

single line, C_a values of 2% and 2% vs. 4% and 2% vs. 8% HPMC were collapsed in a single value that is larger than the optimised values, similarly in case of 4% HPMC and 4% vs 8% HPMC.

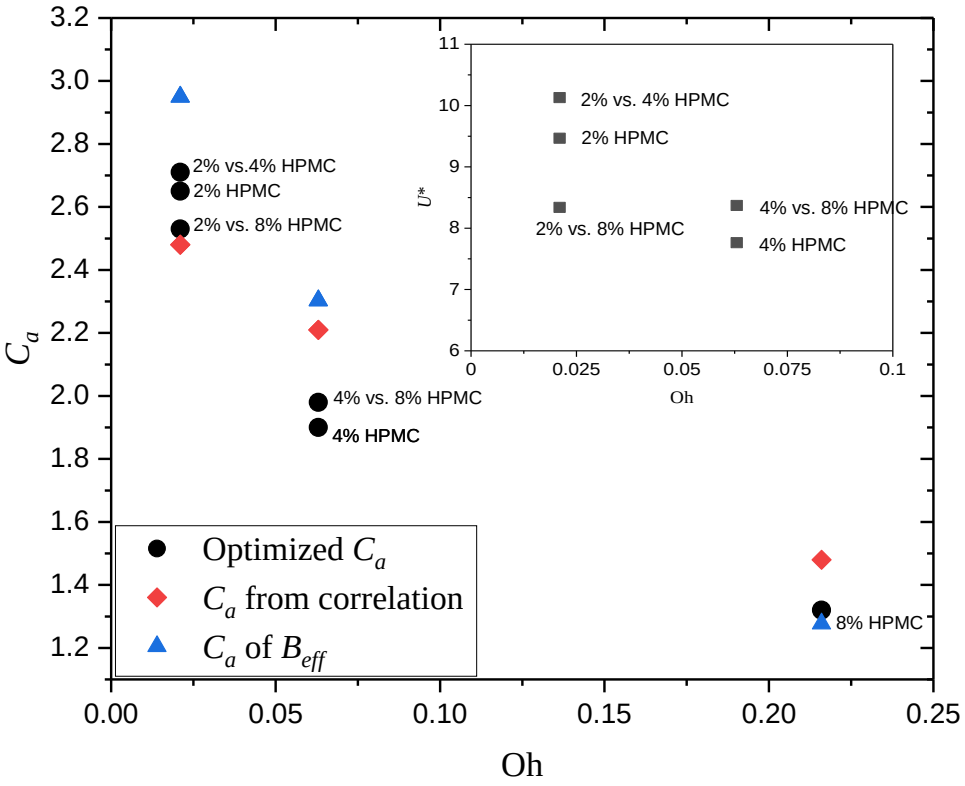

Figure 4.11 The evaluation of the parameter C_a in the modified model of Jiang et al. (1992), Eq. (2.27), for the six systems that are used in this study using different methods, where $C_b = 1$. Circles are direct fittings based on the minimum MAE; diamonds are the values from the correlation of Sommerfeld and Pasternak (2019), Eq. (2.28); triangles are based on the effective impact parameter estimated from the model of Planchette et al. (2012). The inset figure shows the evaluation of the constant U* in the model of Planchette et al. (2012). Oh of the non-identical collisions is taken for the lower viscosity droplet.

The *U** determined for each system are shown in the inset graph in Figure 4.11. They correlate with the off-sets in the boundaries seen in Figure 4.6. As the 8% HPMC case is significantly off-set from the other curves, the values are relatively similar. These contrast with the findings of Planchette et al. (2012), who, for immiscible systems, reported higher absolute levels of *U** and saw *U** with increase monotonically with the

viscosity of the more deformable component. Consequently, whilst this modelling approach can be used to approximate the boundary observed in these systems, the lack of a clear trend in *U** makes the approach of Jiang et al. (1992) preferable.

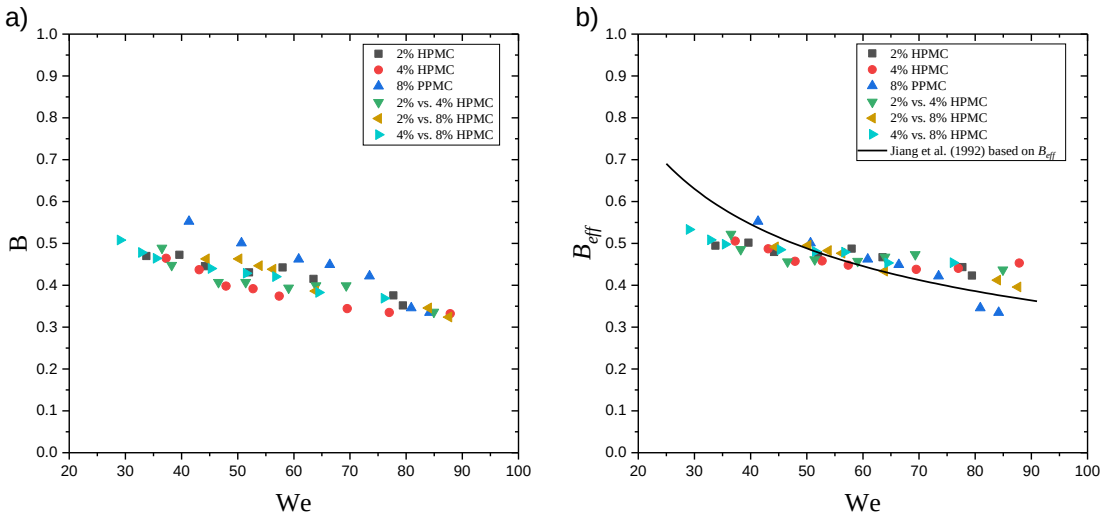

Figure 4.12 The application of the model of Planchette et al. (2012) on the experimental data of the boundary of the stretching separation regime. Applying the model shows that the data collapse on the boundary of the 8% HPMC (the reference boundary). a) is the original experimental data; b) is the data plotted versus the effective impact parameter B_{eff} using the approach of Planchette et al. (2012), Eq. (2.29).

4.2.2.3 Reflexive separation boundary

The boundary of the reflexive separation regime is widely predicted by shifting the model of Ashgriz and Poo (1990), Eq. (2.13), towards higher We using Oh correlations (Sommerfeld and Pasternak, 2019). The shifted model of Ashgriz and Poo (1990) is given by

$$\mathrm{We_c} = \left(\mathrm{We_{FC/RS\,(}}_{f(\mathrm{Oh}))} - \mathrm{We_{FC/RS\,(water)}}\right) + 3\left[7(1+\Delta^3)^{\frac{2}{3}} - 4(1+\Delta^2)\right]\frac{\Delta(1+\Delta^3)^2}{\Delta^6 ¥_1 + ¥_2}. \tag{4.2}$$

Where $\mathrm{We_{FC/RS\,(}}_{f(\mathrm{Oh})}$ is the onset of the reflexive separation regime predicted by Oh correlations detailed in section 2.5.2, and given by Eqs. (4.3 and 4.4), and $\mathrm{We_{FC/RS\,(water)}}$

is the onset of the reflexive separation of water which is equal to $6\left[7(2)^{\frac{2}{3}}-8\right]$ at $B=0$ from Eq. (2.13). ¥$_1$, and ¥$_2$ are defined in Eqs. (2.14 and 2.15).

$$\mathrm{We_{FC/RS}} = 14.8 + 643.1\mathrm{Oh} \text{ for } \mathrm{Oh} < 0.04 \text{ and} \tag{4.3}$$

$$\mathrm{We_{FC/RS}} = 9309\mathrm{Oh}^{1.7056} \text{ for } \mathrm{Oh} > 0.04. \tag{4.4}$$

However, the more detailed model, of Planchette et al. (2017), Eq. (2.18) can be used as an alternative to the Oh correlations and a comparison of the two approaches will be made (i.e. the model Planchette et al. (2017) vs. Oh correlations in Eqs. (4.3 and 4.4)). Before implementing any model, it should be noted that in the case of collisions between droplets with different viscosities an Oh based on the arithmetic mean viscosity will be used. This is attributed to the observed intermediate value of $\mathrm{We_{FC/RS}}$ in the non-identical viscosity collisions compared to the identical collisions, in section 4.2.3.

The model of Planchette et al. (2017), Eq. (2.18), can be written in terms of We and Oh,

$$\mathrm{We_{FC/RS}} = (0.8p\zeta_{crit})^2 \frac{24\sqrt{2}/\pi}{(1-\alpha-q/(\mathrm{We_{FC/RS}}^{0.5}\mathrm{Oh})}\mathrm{Oh}. \tag{4.5}$$

The model has three adjustable parameters ζ_{crit}, α and q. The loss ratio α was experimentally determined for the three systems, using the same procedure used in Planchette et al. (2017). It was confirmed to be independent of the initial velocity, and the system viscosity, see Appendix A. Its measured values agree very well with those reported by Planchette et al. (2017) ($\alpha \backsim 0.67 \pm 0.02$). ζ_{crit}, the critical aspect ratio for the break-up, was also set at 3 as in Planchette et al. (2017) breakage criteria. The model was used with $q = 0.025(1-\alpha) = 0.00825$ and a pre-factor $p = 2.38$ as in Planchette et al. (2017).

Figure 4.13 compares the $\mathrm{We_{FC/RS}}$ predictions of the two alternative models against each other and against the experimentally observed values. Similar trends are seen in both models, however at higher Oh values, the gradient of the model of Planchette et al. (2017), Eq. (4.3), is lower and an improved prediction is seen versus the correlations of Gotaas et al. (2007), Eqs. (2.17 and 2.18), which have some significant error. This

error attributed to the noticeable scattering of the data when the Oh correlation was produced, the reader is referred to the review of Sommerfeld and Pasternak (2019). Both models show under-prediction in case of 2% HPMC, the reason behind this is unclear and further investigations for low concentration HPMC droplets would be of value especially for $\mathrm{Oh} < 0.04$.

Based on the above, the model of Planchette shows promising performance in predicting the onset of reflexive separation for head-on collisions for both identical and non-identical viscosity cases. It is therefore used as an alternative to the correlations of Gotaas et al. (2007) to predict the reflexive separation boundary using Eq. (4.2). The boundaries predicted by this approach are shown in Figures. 4.1 and 4.2.

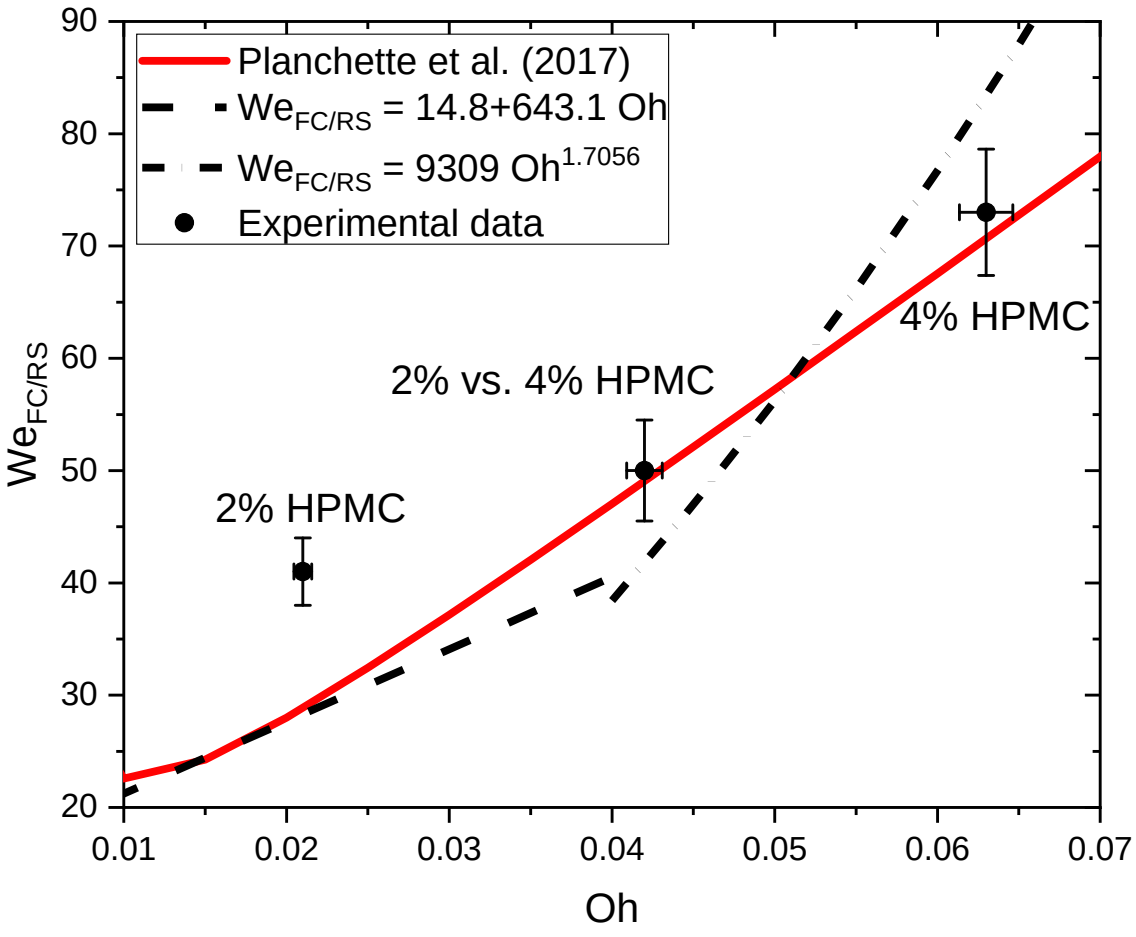

Figure 4.13 Performance comparison between the model of Planchette et al. (2017) and the Oh correlations in predicting the onset of the reflexive separation regime at head-on collisions. The vertical error bars are estimated using Eq. (3.14), while the horizontals by Eq. (3.12).

An alternative model that can be applied to predict the reflexive separation regime boundary is the model of Hu et al. (2017), Eq. (2.16). This model uses a fitting parameter α_3 to represent the ratio of the entire viscous loss, to the impact kinetic energy. Therefore, in addition to the collisions of identical viscosities, this model can be implemented to predict the reflexive separation regime boundary for the collisions of droplets with non-identical viscosities. This is done by setting α_3 to fit the predicted $\mathrm{We}_{\mathrm{FC/RS}}$ to the experimentally measured boundary for the head-on collision. The fitted viscous loss parameters α_3, in the case of collisions of identical droplets, increase as the viscosity increases. It is 0.55 for 2% HPMC, and 0.75 for 4% HPMC. However, contrary to the stretching separation, the non-identical viscosity system 2% vs. 4% HPMC shows an intermediate viscous loss parameter, α_3= 0.63, compared to the identical droplets systems. This is consistent with the mixing between the colliding droplets as shown at the last set of images in Figure 4.10.

The ratio of the viscous loss to the kinetic energy is expected to not change noticeably by changing the droplet viscosity. This is because at the onset of the reflexive separation, of identical droplets collisions, the separated droplets have a similar surface area to the initial droplets and possess negligible kinetic energy compared to the initial droplets. This is to say almost all kinetic energy has been lost. This also was evident by Planchette et al. (2017). Therefore, the ratio of the total viscous loss to the initial kinetic energy is expected to be close to unity and higher than those of the model of Hu et al. (2017) and to not vary significantly by changing the viscosity of the droplets. This raises a need for more investigation into the assumptions of Hu et al. (2017), which is out of the scope of this thesis.

Although the model of Hu et al. (2017) shows unphysical α_3 values, it is still interesting to be used and compared with the shifted model of Ashgriz and Poo (1990). At $\mathrm{B} > 0$ both models show good agreement with the experimental data for the identical droplets 4% HPMC, as shown in Figure 4.1. However, the model of Hu et al. (2017) slightly over-predicts B in case of 2% HPMC and 2% vs. 4% HPMC, whereas, the model of Ashgriz and Poo (1990) shows good agreement in both cases as shown in Figures 4.1 and 4.2. This

requires more investigation into the role of the impact parameter and its implementation in the modelling of the boundary of the reflexive separation regime.

4.3 Conclusions

Viscosity is an important factor in determining the collision behaviour of droplets. This work has extended the understanding of the effects of viscosity by investigating collisions between miscible droplets of non-identical viscosity in which only the viscosity was significantly different. In addition to regime maps of non-identical viscosities collisions, identical collision regime maps were also structured to provide a comparative basis for the non-identical viscosity collisions. For the range of viscosities studied we found similar behaviours to the identical droplets, with the same regimes identified in the We, B space and clear boundaries between regimes that were shifted versus the identical cases. The mechanisms involved in shifting the boundaries are slightly different in each case, and depend on the role of viscosity on the transfer of collision energy to deformation and then its effect on the subsequent separation mechanism. The following conclusions can be drawn for each boundary:

Bouncing transition - Increasing the viscosity promotes fast coalescence by suppressing the bouncing regime due to the higher viscosity decreasing the droplet deformation and allowing more rapid drainage of the air layer between the colliding droplets. The transition from bouncing to fast coalescence, therefore, occurs at lower We. In the non-identical case this transition occurs at an intermediate value between the transition We values of the two identical cases at the lower and higher viscosity. In comparison to identical collisions at the lower viscosity, the deformation is only reduced in one of the droplets, therefore the drainage of the air layer only benefits from half the change versus the collisions at the higher viscosity. A new phenomenon, partial bouncing, is also observed at high viscosity ratio, whereby a thin ligament between the bounced droplets is observed. This ligament separates from the higher viscosity droplet and retracts to the lower viscosity droplet. The model of Estrade et al. (1999) shows poor performance and required more investigations, which will be provided in Chapter 7.

Stretching separation transition - In identical collisions, at the higher Oh studied, increasing the viscosity shifts the boundary of the stretching separation regime to higher

B values this might be anticipated due to the increase in the viscous loss and the relative importance of the viscosity term in the Oh number. However, at low $\mathrm{Oh} < 0.1$ increasing the viscosity showed the opposite behaviour, this may be due to the increased role of surface tension and the physics change of impact. The reasons are not entirely clear and more investigation into this behaviour is required. In the case of non-identical collisions, we see the stretching separation regime boundaries remaining very similar to the identical case for lower viscosity droplets. This was shown to be due to the filament being drawn mainly from the lower viscosity droplet and consequently, its break up behaviour occurs at the low viscosity region and being similar to the low viscosity case. In addition, the satellite droplets produced from the breakup of the ligament during stretching separation, have a similar composition the lower viscosity with a small amount of mixing. Consequently, the adjustable parameters in the model of Jiang et al. (1992) were very similar to those of the lower viscosity case. The model of Planchette et al. (2012) was also evaluated and the use of an effective impact parameter allowed the collapse of the experimental data to a unified curve. However, its value was limited as no clear relationship between the *U** fitting parameter and the physical properties of the droplets was observed.

Reflexive separation transition - For identical droplets, the transition from fast coalescence to reflexive separation is shifted to higher We due to increased viscous loss in the stretching and reflexive motion of the droplets. For non-identical drops, a similar trend is seen, with the transition moving to intermediate values of We compared to the identical cases. Deformation is reduced and partial mixing is seen between the colliding droplets so there is both less energy in the reflexive separation and intermediate viscosity in the necking ligament. Interestingly because of the mixing, a concentration gradient is set-up and the lower viscosity droplet detaches at the low viscosity end of the ligament. This leads to a smaller low viscosity droplet and a larger droplet composed of both the higher viscosity fluid mixed with a little lower viscosity fluid. The application of the model of Ashgriz and Poo (1990), using an off-set based on a prediction of the head on boundary $\mathrm{We}_{\mathrm{FC/RS}}$ using the approach of Planchette et al. (2017) can be used for both the identical and the non-identical cases based on the average Oh. It was found to give slightly better predictions than the correlation proposed by Gotaas et al. (2007)

in the higher Oh systems tested. Neither model gave a good prediction of the onset of the reflexive separation at head-on for 2% HPMC, the lowest Oh system. The model of Hu et al. (2017) was found to give an approximate fit to the reflexive separation boundary of the non-identical case when an intermediate loss factor was used. However, at $B > 0$, the fit of this model was found to be poorer than that of the model of Ashgriz and Poo (1990). Moreover, the model of Hu et al. (2017) shows unphysical viscous loss factors. Therefore, further work is required to understand the model's assumptions related to the role of impact parameter and the viscously lost energy.

This work represents an initial step in characterising these non-identical collisions. Several phenomena have been observed and mechanistic insights obtained, however, there are clearly opportunities to learn more about these interesting, industrially relevant systems.

Chapter 5: The role of the size and the size ratio

In the previous chapter, the roles of the viscosity and the viscosity difference, in equal-size binary droplet collisions, were studied experimentally. In this chapter, the experimental work is extended to study the role of the size and the size ratio. The study of the size ratio covers collisions of identical viscosities and collisions of non-identical viscosities.

5.1 Introduction

In the previous chapter, the role of the viscosity was discussed for collisions of equal-size droplets with identical and non-identical viscosities. This chapter extends that considering the role of the size and the size ratio. The role of the size is considered in identical droplet collisions, whereas the role of the size ratio is considered in both collisions of droplets with identical viscosities and non-identical viscosities.

2% and 4% HPMC systems were used to construct regime maps in this chapter. For collisions of equal-size droplets, four regime maps were constructed considering two sizes 400 µm and 230 µm in each system, as will be shown in section 5.2 in Figure 5.1. A size ratio of $\backsim$0.6, from the combination of these two sizes, was selected to generate another four regime maps two for identical viscosities and the other two are for non-identical viscosities, as will be shown in section 5.3 in Figure 5.4.

Although the droplet size is taken into account in We, reducing the size of the colliding droplets, of equal-size droplet collisions, shows shifts in the positions of the regimes' boundaries. In addition, the collisions of the unequal-size droplets also show different positions to the regimes' boundaries compared to those of the equal-size droplets collisions. Moreover, changing the viscosity shows an impact on the way that the regimes' boundaries shift due to the change in the size and the size ratio. All these interesting behaviours will be discussed in the upcoming sections.

5.2 The role of the size

To study the role of the size, regime maps of equal-size droplet collisions of 2% HPMC and 4% HPMC were constructed for two different droplet size (400 μm and 230 μm). These regime maps are shown in Figure 5.1. The four regime maps show four distinct collision outcome regimes (bouncing, fast coalescence, stretching separation and reflexive separation). Noticeably, changing the size of the colliding droplets for a given system produces regime maps that quantitatively vary in the regime boundaries. This is despite that the droplet size is considered in the parameter space. Therefore, the effect of the size on each boundary will be discussed separately in the next sections.

5.2.1 Bouncing

In both of 2% and 4% HPMC reducing the size of the colliding droplets shifts the onset of the fast coalescence regime towards lower We, as shown in Fig 5.1 and detailed in Table 5.1. Moreover, bouncing disappeared at head-on collisions and at $\mathrm{B} < 0.05$, at the investigated range of We, for the collisions of small droplets of 4% HPMC, whereas it is seen at $\mathrm{B} = 0$ for the larger droplets.

Table 5.1 The onset of fast coalescence at head-on collisions.

	2% HPMC	4% HPMC
	$\mathrm{We}_{\mathrm{B/FC}}$	$\mathrm{We}_{\mathrm{B/FC}}$
$d = 400 \pm 20$ um	23 ± 1	20 ± 2
$d = 230 \pm 10$ um	11	<9
$\Delta \sim 230/400 \sim 0.6$	9 ± 3	-

The bouncing occurs due to the trap of an air film between the colliding droplets that prevent their merging. The air is trapped because the interface of the droplets gets indented or flattened at the maximum deformation, as explained in the previous chapter. However, at smaller droplets, the curvature of the droplet $(2/R)$ increases, which leads to easier air drainage before the droplets reach their maximum deformation, Moreover, increasing the curvature of the droplet increases the capillary pressure $(2\sigma/R)$ within the droplet and hence the colliding droplets have larger resistance to the deformation. Thereby the smaller droplets will have less indentation/flattened interface at the maximum deformation than that of the larger

droplets. This enhances the air film drainage process at the maximum deformation instant. Thus, the smaller droplets have higher chance to coalesce and hence $We_{B/FC}$ is lower compared to that of the larger droplet. Ultimately, reducing the size of the colliding droplets qualitatively plays a similar role as increasing the viscosity, which also suppresses bouncing as reported in Chapter 4.

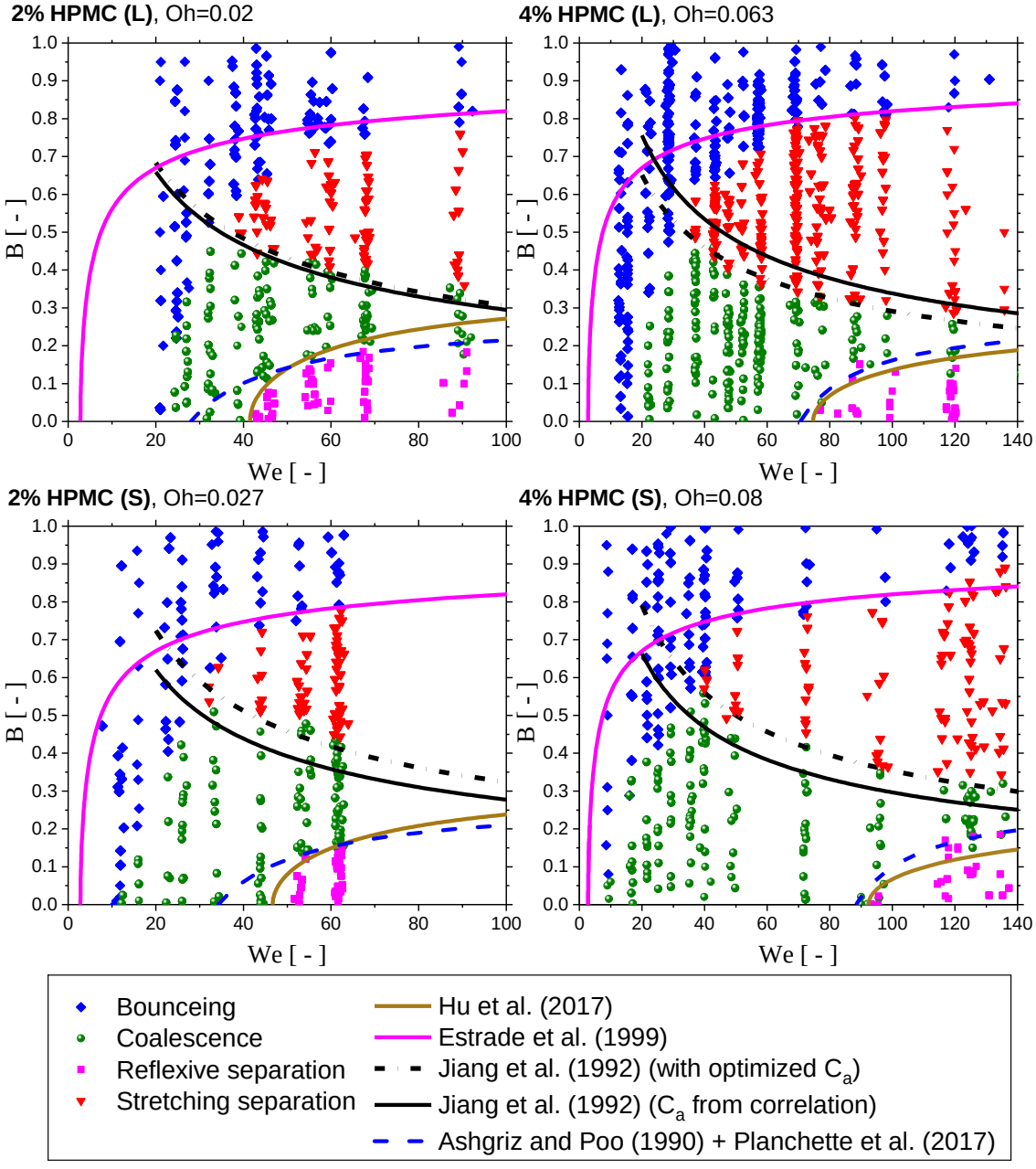

Figure 5.1 Regime maps for 2% HPMC and 4% HPMC. (L) means large droplets ($d = 400 \pm 20$ µm); (S) means small droplets ($d = 230 \pm 10$ µm).

5.2.2 Reflexive separation

Reducing the size of the colliding droplets causes an increase in the required We for the onset of reflexive separation. This can be clearly seen in both systems 2% and 4% HPMC, as shown in Fig 5.1. The onset of reflexive separation of 2% HPMC (L) occurs at We = 40, however, it occurs at We = 50 in 2% HPMC (L). Similar behaviour is seen in 4% HPMC as reducing the droplet size by 60% shifts the onset of reflexive separation from 72 to 90, as, see Table 5.2. Moreover, it can be noticed that the onset of reflexive separation in 4% HPMC is more sensitive to the size reduction than 2% HPMC, as the We difference is 20 in the former while it is 10 in the later.

The above observations are contrary to the findings of Adam et al. (1968) who reported that the size shifts the reflexive separation towards lower We. They also do not agree with Ashgriz and Poo (1990) who suggested that the regime maps are universal in terms of size. Therefore, the physics behind these observations and the disagreement with the literature need to be addressed.

The onset of the reflexive separation regime occurs if the cylindrical shape of the merged-reflexed droplets reaches a critical aspect ratio of ($\sim\pi$) (Planchette et al., 2017). However, this aspect ratio depends on the extent of the axial deformation of the cylinder, which depends on both We and Re according to a theoretical study of Roisman (2004). Therefore, to understand why the onset of the reflexive separation occurs at higher We when the size is reduced, it is important to examine the dependency of Re on the size for a given We. This can be achieved by keeping $u_r^2 d$ constant for a wide range of d, as this ensures a constant We. Therefore, Re can be determined for every d in the selected range using a u_r that keeps $u_r^2 d$ constant. Using this method, Fig 5.2 shows the evaluation of Re over *d* for a constant We for three systems: water, 2% HPMC, and 4%. In the three systems, it can be seen that Re decreases by decreasing the droplet size. This means that reducing the size for a given We results in more viscous loss that suppresses the axial extension of the cylinder and hence the separation is suppressed.

The onset of reflexive separation was also widely related to the Oh number. The We of onset of the reflexive separation regime increases by increasing Oh, this was experimentally proven, by comparing droplets with different viscosities, by many

authors (Qian and Law, 1997, Tang et al., 2012, Finotello et al., 2018a, Finotello et al., 2017, Gotaas et al., 2007, Sommerfeld and Kuschel, 2016). Therefore, it is interesting to see the sensitivity of Oh with d. Figure 5.2 shows the evaluation of Oh as a function of d for the three systems. Generally, the Ohnesorge number is inversely proportional to the square root of the droplet diameter, However, Oh sensitivity to this inverse proportionality is clearly affected by the viscosity of the droplet. As can be seen from the figure, Oh in 4% HPMC is more sensitive to d than in 2% and the latter is more sensitive to d than water, which shows negligible sensitivity. This explains the higher sensitivity of the onset we of reflexive separation regime with changing d in 4% HPMC than the in 2% HPMC. Moreover, the universal regime map in terms of d seen by Ashgriz and Poo (1990) is due to the negligible sensitivity of Oh with d.

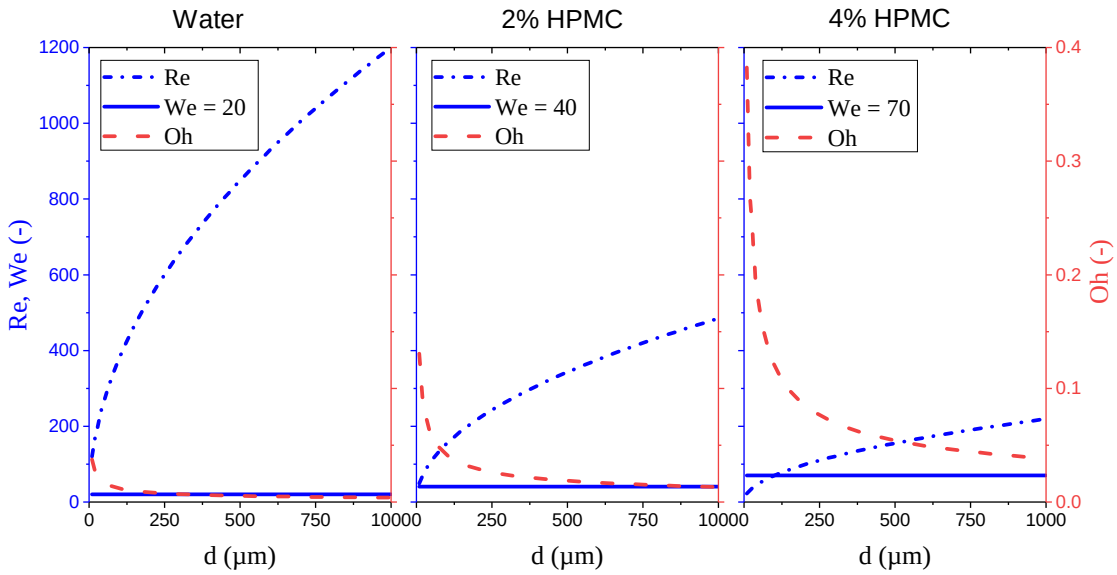

Figure 5.2 Oh and Re as a function of droplet size for a constant We for water, 2% HPMC, and 4% HPMC. The selected We is that of the onset of the reflexive separation regime for droplets size (400 ±20 um for HPMC systems, and 300 um of water).

5.2.3 Stretching separation

The boundary of the stretching separation regime also shows a dependency on the size of the droplet, as reducing the droplet size shifts the boundary towards higher B, as can be seen in Figure 5.3. This is also because the smaller droplet possesses higher Oh, which leads to more viscous loss. Therefore, to achieve separation the kinetic energy of the non-interaction regions needs to be higher. This can be achieved by increasing the offset

between the droplets, as this increases the mass of the non-interaction regions which in turn increases the stretching energy.

In Figure 5.3, it also can be seen that the boundary of the stretching separation regime is less sensitive to the size of the droplets in 2% HPMC than in 4% HPMC. This is again, as explained in the previous section, due to the fact that Oh of the higher viscosity droplets has higher sensitivity towards the droplet size, as shown in Figure 5.2.

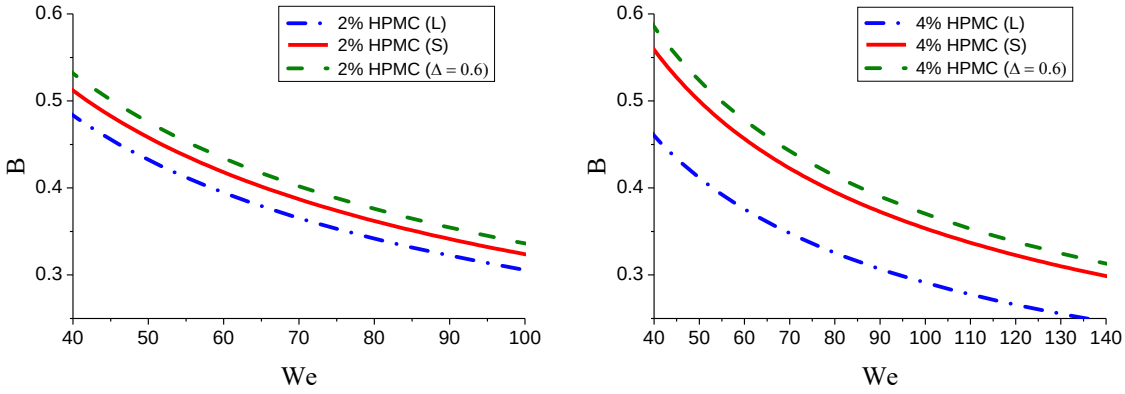

Figure 5.3 The boundary of the stretching separation regime represented by the optimized model of Jiang et al. (1992).

5.3 Role of the size ratio

In this section, data of unequal-size droplet collisions are provided. The size ratio of the colliding droplet is 0.6 and it is a combination of the sizes used in the previous section. Regime maps for collisions of droplets with identical viscosities were constructed for both 2% HPMC and 4% HPMC, as shown in Figure 5.4. In addition, regime maps for collisions of droplets with non-identical viscosities were constructed, also shown in Figure 5.4. These regime maps, quantitatively, are not identical to any of those of the identical cases. Therefore, it is important to understand the underlying physics that make the regime boundaries quantitatively different from identical cases.

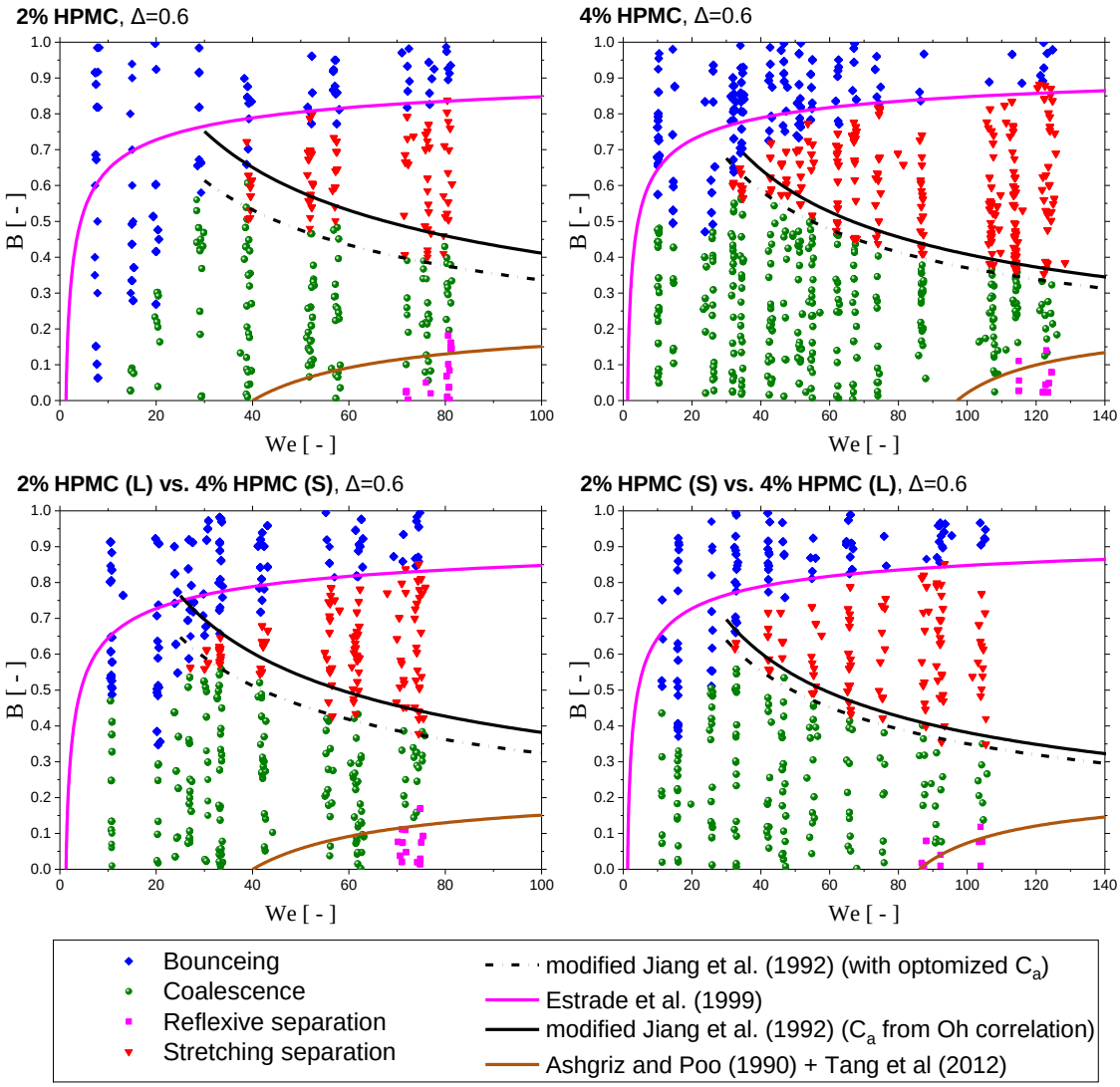

Figure 5.4 Regime maps for unequal-size droplet collisions with size ratio ($\Delta \sim 0.6$). The top row is for collisions of droplets with identical viscosities, while the bottom row is for collisions of droplets with non-identical viscosities.

5.3.1 Bouncing

It has been reported in the literature that the bouncing regime has a weak dependence on the size ratio (Tang et al., 2012). However, we showed that, in equal-size droplets collisions, reducing the droplets' size suppresses the bouncing regime. This raises the question that what droplets size, in equal-size droplets collisions, shows a comparable bouncing regime boundary to that of the collisions of unequal-size droplets? In 2% HPMC head-on collisions, the unequal-size droplet collisions show a comparable onset of the fast coalescence regime to that of the equal-size droplet collisions of the small

droplet, as detailed in Table 5.1. However, the unequal-size droplet collisions of 4% HPMC show no bouncing at head-on collisions despite that it shows near head-on bouncing in the case of equal-size collisions of the small droplet. Therefore, the bouncing dependency on the size ratio depends on the viscosity of the droplets.

Figure 5.5 shows the head-on collisions' dynamics of both the bouncing, at $\mathrm{We} = 9$, and the coalescence, at $\mathrm{We} = 20$, of 2% HPMC. The figure also shows the coalescence dynamics of head-on collisions for comparable Weber numbers of 4% HPMC. In the bouncing of 2% HPMC, it can be seen that the small droplet reaches its maximum deformation before the large droplet and makes a successful bouncing. Whereas in the coalescence dynamics of 2% HPMC at $\mathrm{We} = 20$, the droplets' interfaces coalesce at the maximum deformation of the small droplet ($\mathrm{t} = 0.17$ ms). Similar dynamics can be observed in the case of 4% HPMC at $\mathrm{We} = 24$ as the interfaces coalesce at $\mathrm{t} \sim 0.1$ ms. However, in the case of 4% HPMC at $\mathrm{We} = 10$, the coalescence does not occur immediately after the collision. The small droplet reaches its maximum deformation without coalescence, see $\mathrm{t} = 0.16$ ms, and as it tries to bounce by recovering its spherical shape, the coalescence occurs, see $\mathrm{t} = 0.63$ ms. Therefore, it is interesting to understand the underlying physics behind the observed differences between 2% HPMC and 4% HPMC.

In equal-size droplets collisions, both droplets reach the maximum deformation and start bouncing-off at the same time. This means that the minimum air film thickness is reached at an instant close to the instant of the maximum deformation. If that film thickness is larger than the effective range of the intermolecular forces, the bouncing occurs. However, in case of unequal-size droplets collisions, the small droplet reaches the maximum deformation quicker than the larger droplet due to the shorter oscillation time. Hence, the air film thickness reaches its minimum at an instant close to the instant of the maximum deformation of the small droplet. If that thickness is larger than the effect of the intermolecular forces, the smaller droplet starts bouncing before the larger droplet reaches its maximum deformation. In this case, the centre of mass of the large droplet might still have kinetic energy towards the small droplet. Moreover, as the small droplet starts bouncing the large droplet tries to recover the spherical shape, consequently, that the interface follows the small droplet faster than the centre of mass.

This might lead to various dynamics scenarios depending on the viscosities of the colliding droplets, as it will be shown in the following.

If the viscosity of the colliding droplet is low, more air will be trapped at the instant of the maximum deformation of the small droplet due to the indentation in the droplets, see Figure 5.6a in the 2% HPMC case. In addition, the small droplet will experience higher deformation compare to higher viscosity droplets, which means more energy is stored as surface energy that is converted to kinetic energy for the bouncing. Thus, droplets with low viscosities will have relatively far interfaces from each other and the small droplet bounces in a velocity faster than the higher viscosity droplets which give more chance for the small droplet to escape from the large droplet and hence bouncing occurs.

Unlike low viscosity droplets, when the viscosity is relatively high the indentation in the droplet is less and hence less air is trapped between the droplets, as depicted in Figure 5.6b. In addition, the small droplet will suffer less deformation than the lower viscosity case due to the more viscous loss, and hence less surface energy is converted to the kinetic energy of the bouncing. Therefore, the closer interfaces between the colliding droplets and the slow bouncing velocity of the small droplet give more chance for the large droplet to capture it and hence coalescence occurs.

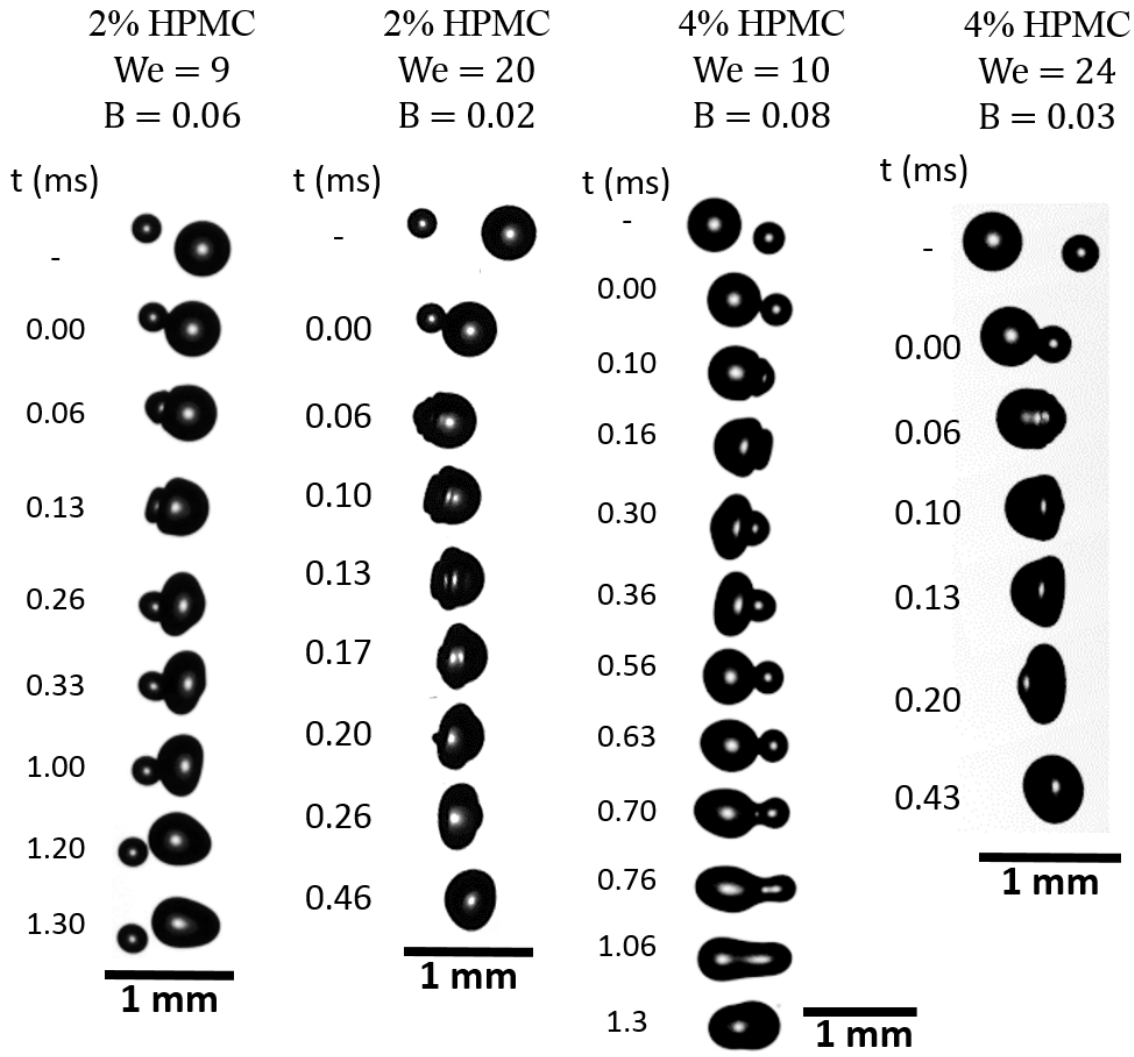

Figure 5.5 The effect of the viscosity on the bouncing and the coalescence dynamics of the collisions of unequal-size droplets with identical viscosities. At low viscosity and We, a successful bouncing occurs, however, at higher viscosity the small droplet tries to bounce but a late coalescence occurs.

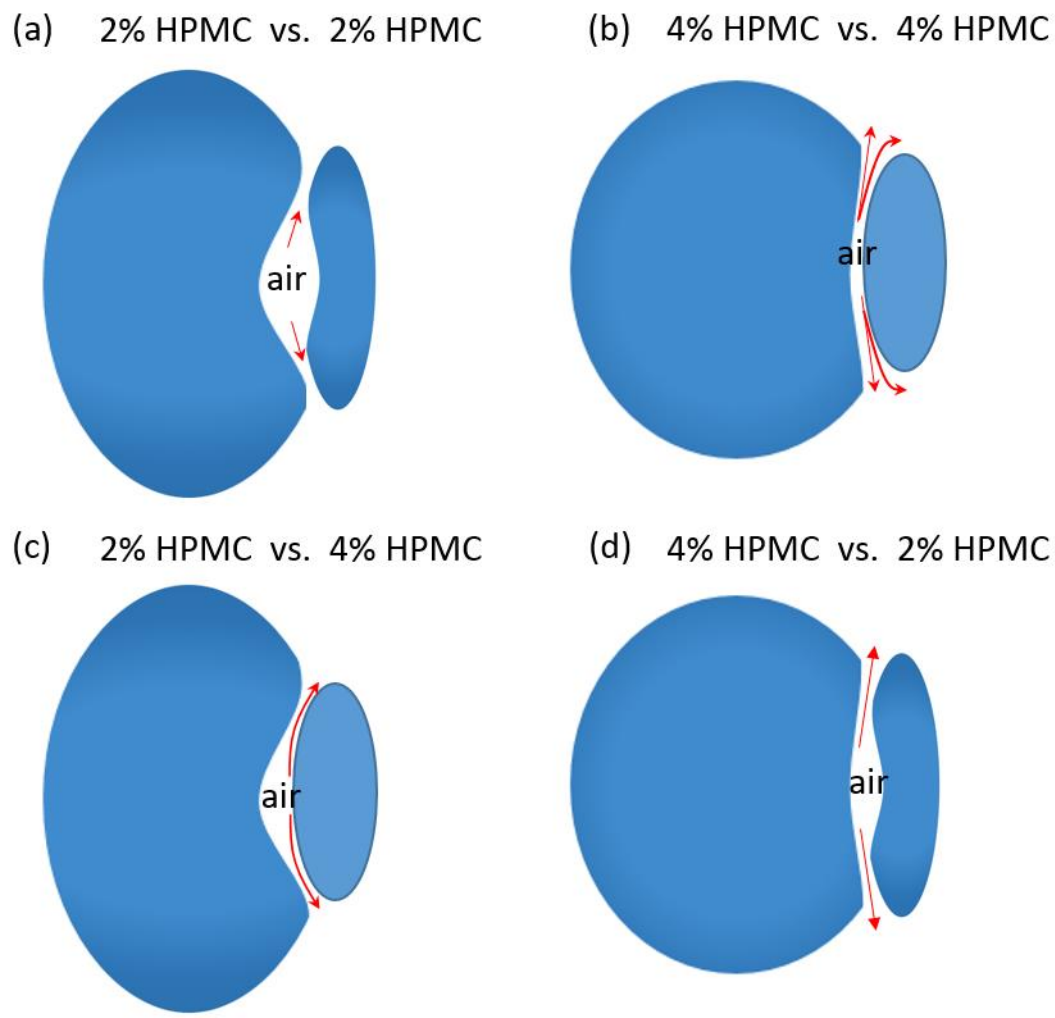

Figure 5.6 The deformation of the interfaces of the droplet at the maximum deformation of the small droplet.

In collisions of non-identical viscosities, both cases (i.e. 2% (L) vs. 4% (S) HPMC and 2% (S) vs. 4% (L) HPMC) do not show bouncing at head-on collisions, as shown in Figure 5.4. Both cases show similar dynamics to that of the identical viscosity case of 4% HPMC, as shown in Figure 5.7. At We=11 the small droplet tries to bounce by recovering the spherical shape, but late coalescence occurs. However, at We = 20, the interfaces coalesce at the maximum deformation of the small droplet. the underlying physics that prefer the coalescence in these cases, will be explained by comparing with the identical cases in Figure 5.6(a and b).

In the identical viscosities, the air is expected to make less indentation in the small droplet due to its higher capillary pressure that resists the deformation, as depicted in

Figure 5.6 (a and b). However, if the small droplet has a higher viscosity, it becomes even more resistant to the deformation. Therefore, although the air makes a significant indentation in the large droplet, the air drainage process will be easier at the side of the small droplet, as in Figure 5.6c, than the case of identical viscosity case of 2% HPMC in Figure 5.6a. This means closer interfaces at the maximum deformation of the small droplet. In addition, the viscous loss in the small droplet will reduce its bouncing velocity compared to that in the identical viscosity case of 2% HPMC. Thus, the large droplet will have a higher chance to capture it, due to the remaining kinetic energy and the moving interface towards the small droplet, than the identical viscosity case of 2% HPMC.

If the large droplet has a higher viscosity, the air indentation in the large droplet is smaller than the case of the identical viscosity of 2% HPMC, as depicted in Figure 5.6d. Therefore, the air drainage process will be easier than the case of identical viscosity case of 2% HPMC in Figure 5.6a, which means closer interface at the maximum deformation of the small droplet. Thus, the large droplet will have a higher chance to capture the small droplet, due to the remaining kinetic energy and the moving interface towards the small droplet, than the identical viscosity case of 2% HPMC.

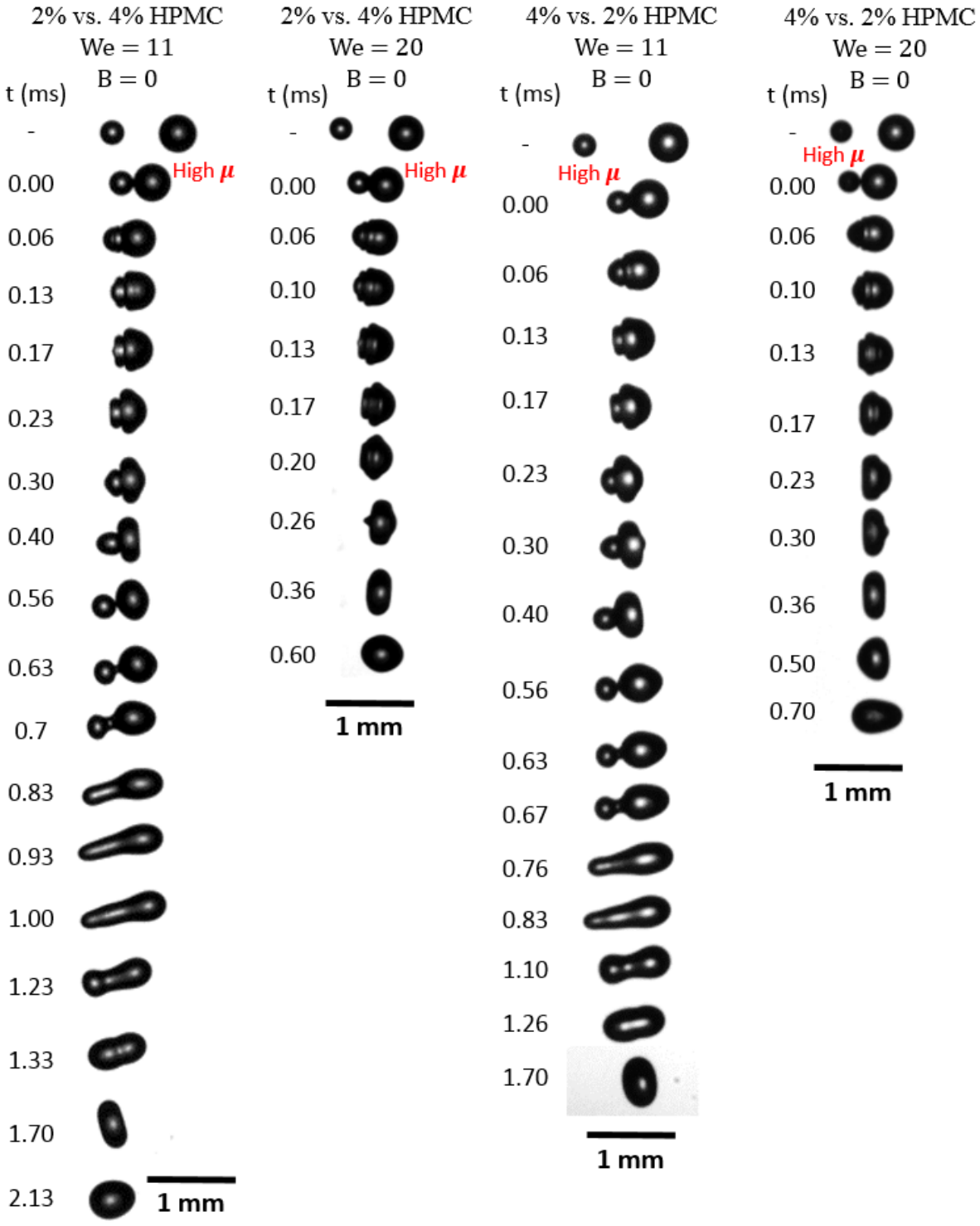

Figure 5.7 The coalescence dynamics of the collisions of unequal-size droplets with non-identical viscosities. At relatively high We the droplets coalesce at an early stage, while at lower We the small droplet tries to bounce but a late coalescence occurs.

5.3.2 Stretching separation

The unequal-size collisions have different dynamics of stretching separation than the equal-size collisions, as shown in Figure 5.8. In the equal-size collisions, due to the

symmetry, the ligament between the droplets has a uniform thickness and the necking happens at the centre until it breaks up. However, in the unequal-size collisions, the ligament between the droplets is thicker at the large droplet side and the necking happens at the small droplet side until it breaks up. This is due to the curvature difference between the unequal-size droplets.

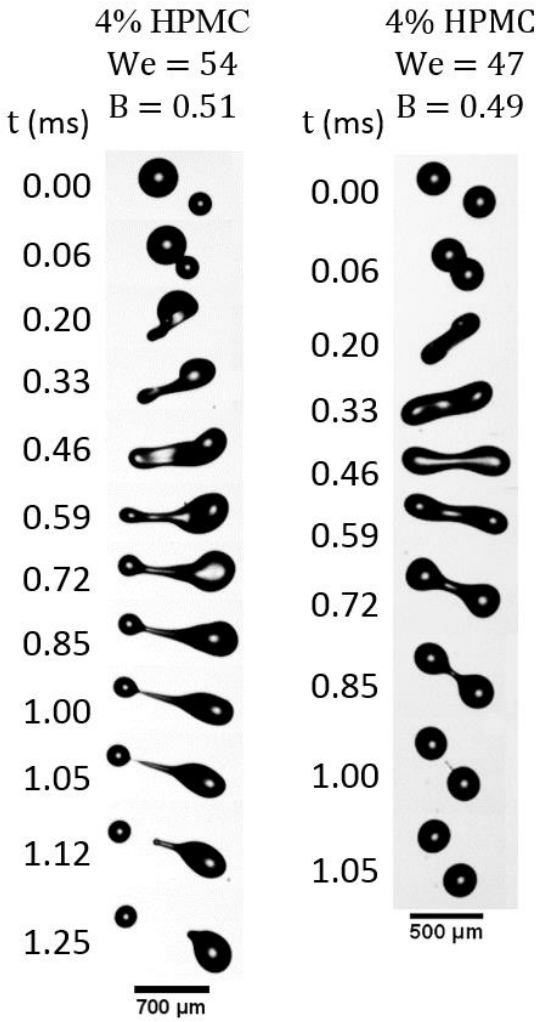

Figure 5.8 The dynamics of stretching separation regime in collisions of equal-size droplets and unequal-size droplets.

The boundary of the stretching separation regime of unequal-size droplet collisions has higher B values than collisions of the identical size droplets. This behaviour is already observed by Ashgriz and Poo (1990) and Rabe et al. (2010). However, the comparison, in these studies, is made between the unequal-size droplet collisions and the identical size collisions of the large droplet. In this study, it is observed that although reducing the

size of equal-size collisions shifts the stretching separation boundary upwards, collisions of unequal-size droplets still show a boundary with higher B, as shown in Figure 5.3.

The reason for the upward shifting of the boundary of the stretching separation regime has not clearly been justified in the previous studies. Ashgriz and Poo (1990), briefly justified this by saying that the momentum of the smaller droplet cannot overcome the inertia and the surface force of the interaction region. Therefore, it is interesting to explore the underlying physics.

It is important to notice that, in unequal-size collisions, the small droplet is the controlling droplet in the stretching process. This is because if its region of non-interaction does not have enough momentum to stretch the ligament until the breakup, the retraction forces at the stretched ligament would retract it back to the large droplet. This is because the small droplet has less inertia than the large droplet. Whereas, in the equal-size collisions both droplets control the stretching process, due to the symmetry. Therefore, if the non-interaction regions do not have enough momentum to reach breakup, the retraction forces in the ligament will retract both droplets towards the centre of the mass, which is at the centre of the ligament.

Figure 5.9 is a schematic for a side view of droplet collisions at three size ratios, from left to right, 1, 0.5, and 0.35. All three cases have the same impact parameter (B=0.5). It can be seen that although the impact parameter is fixed in all cases, reducing the size ratio reduces the region of the non-interaction of the small droplet. Consequently, stretching kinetic energy decreases. Thus, to achieve stretching separation for collisions with size ratio, a higher impact parameter is needed than that of the equal-size collisions.

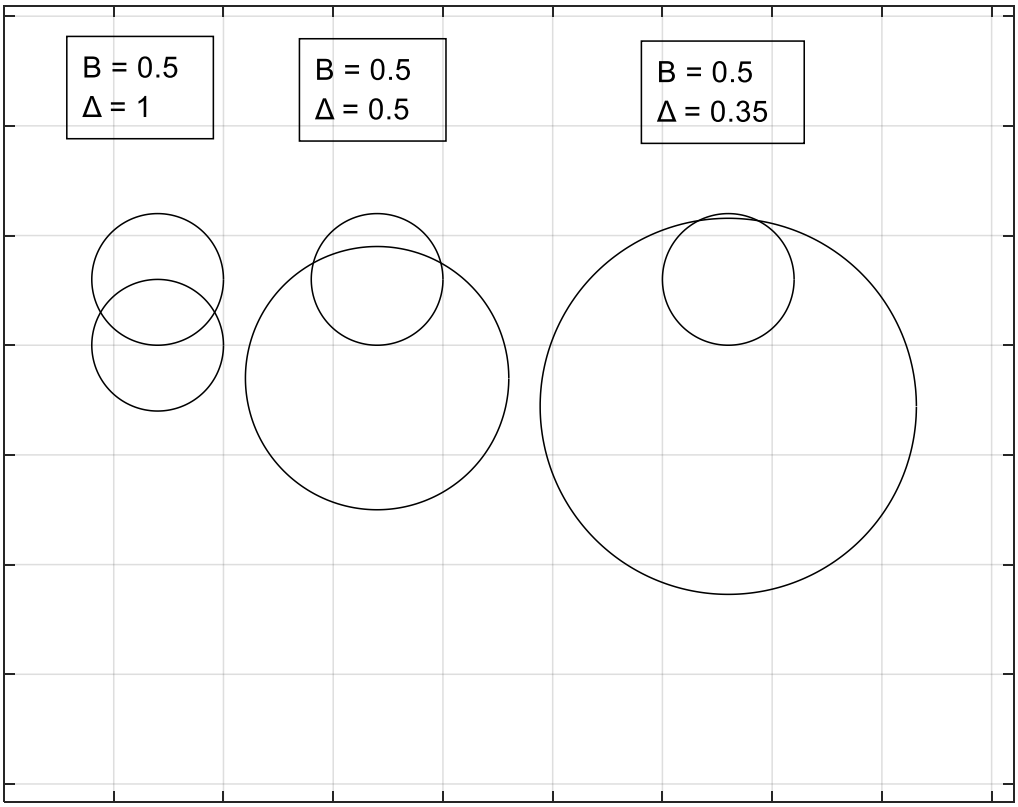

Figure 5.9 A schematic showing the effect of the size ratio on the non-interaction region of the small droplet at a constant offset.

In both cases of non-identical viscosities (i.e. 2% (S) vs. 4% (L) HPMC, and 2% (L) vs. 4% (S) HPMC), the stretched filament is mainly from the low viscosity droplet, 2% HPMC, as can be seen in the coloured images in Figure 5.10. Therefore, the boundaries of stretching separation of the non-identical viscosities are comparable to the unequal-size droplet collisions of the 2% HPMC, and below the boundary of the identical viscosity collisions of the unequal-size droplets of 4% HPMC, as shown in Fig 5.11. However, the boundary of stretching separation of 2% (S) vs. 4% (L) HPMC has higher B values compared to 2% (L) vs. 4% (S) HPMC. This because of the small 2% HPMC droplet in the case of 2% (S) vs. 4% (L) HPMC has higher Oh than that of the large 2% HPMC droplet in the case of 2% (L) vs. 4% (S) HPMC. Therefore, 2% (S) vs. 4% (L) HPMC requires higher B to achieve separation, as the ligament in both cases is drawn from the 2% HPMC droplet and Oh is a measure of the ligament breakup resistant.

The dynamics of the two cases of non-identical viscosities are shown in both coloured and shadow images in Figure 5.10. The separated small droplet in 2% (L) vs. 4% (S) HPMC

has some mixing, as can be seen at t = 1.17 ms in the first column in Figure 5.10. However, the separated small droplet in 2% (S) vs. 4% (L) HPMC has no noticeable mixing, see the second column in Figure 5.10. The large droplet, in both cases, shows no mixing. Moreover, from the shadow images, the ligament in the 2% (S) vs. 4% (L) HPMC is longer compared to the other case, and it breaks first at the side of the low viscosity droplet (the small one). However, in the 2% (L) vs. 4% (S) HPMC, the ligament breaks from both sides at the same time as can be seen at t=1.07 ms. This is because the large droplet of 4% HPMC has a higher Re compared to the small droplet 4% HPMC in the other case and hence more tendency for stretching. This leads to a viscosity gradient in the ligament near the large droplet as can be seen in the second coloured column at t=70 ms.

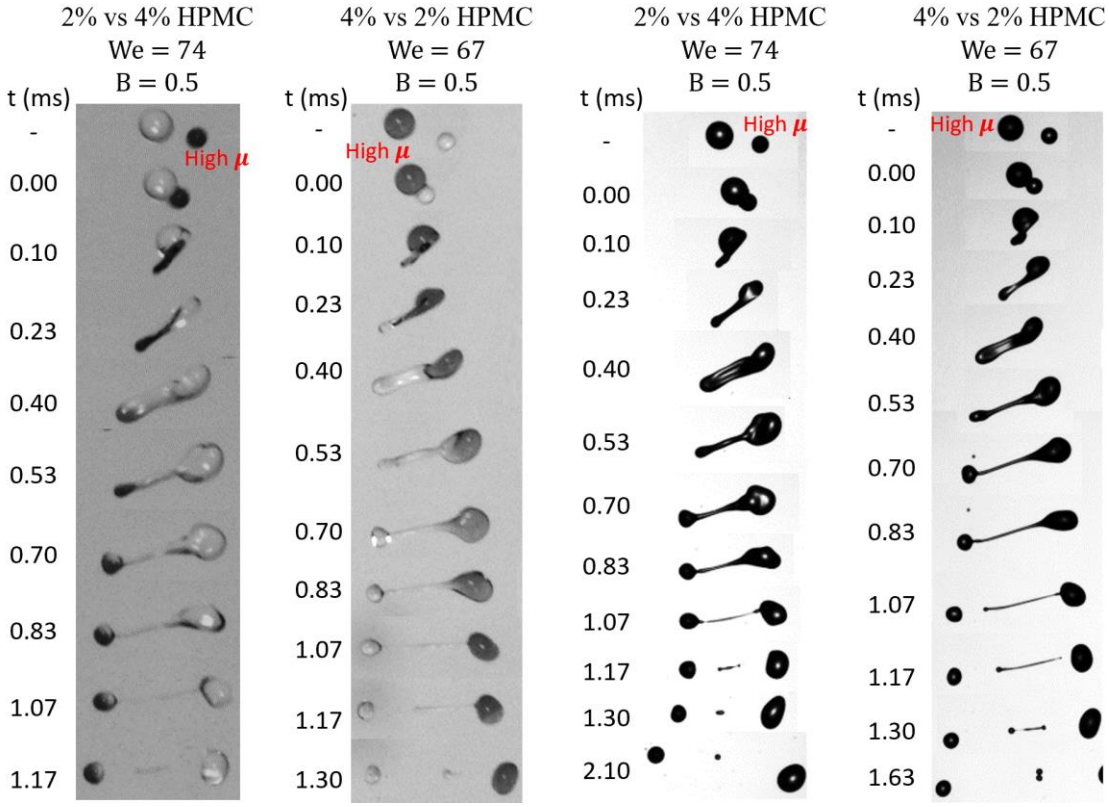

Figure 5.10 The dynamics of the stretching separation in the collisions of unequal-size droplets with non-identical viscosities. The first two columns (on the left) are front-lit with dyeing the high viscosity droplets while the last two columns are for the same collisions but with shadow imaging.

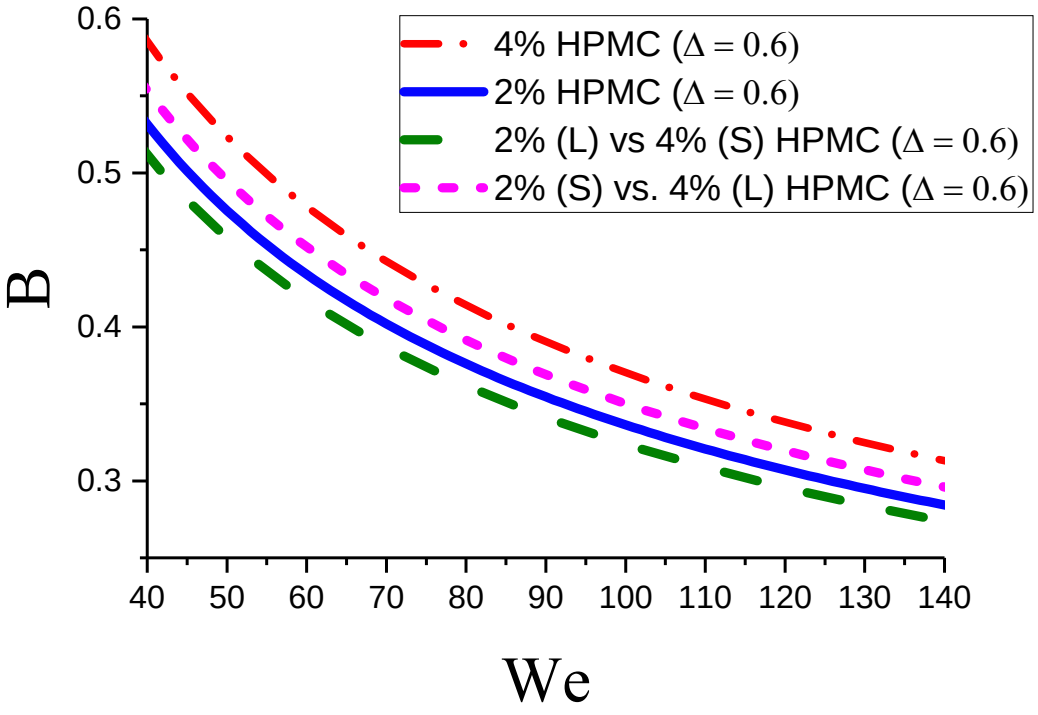

Figure 5.11 The boundaries of the stretching separation of the collisions of the unequal-size droplets for both of the identical and non-identical viscosities. The boundaries are represented by the modified model of Jiang et al. (1992) with optimizedC_a.

5.3.3 Reflexive separation

In the equal-size collisions, reducing the size shifts the onset of the reflexive separation towards higher We. However, in collisions of unequal-size droplets, the onset of the reflexive separation regime moves even farther, as detailed in Table 5.2. This is due to the difference in the dynamics between the collisions of equal-size droplets and those of the unequal-size droplets, as shown in Figure 5.12.

Table 5.2 The onset of the reflexive separation regime at head-on collisions

HPMC	2%	2% (L) vs 4% (S)	2% (S) vs 4% (L)	4%
	$\mathrm{We_{Fc/RS}}$	$\mathrm{We_{Fc/RS}}$	$\mathrm{We_{Fc/RS}}$	$\mathrm{We_{FC/RS}}$
$d = 410 \pm 20$ um	40 ± 1	-	-	72 ± 2
$d = 240 \pm 30$ um	49 ± 3	-	-	90
$\Delta = 240/41 = 0.56$	65 ± 5	67 ± 3	82 ± 5	112 ± 2

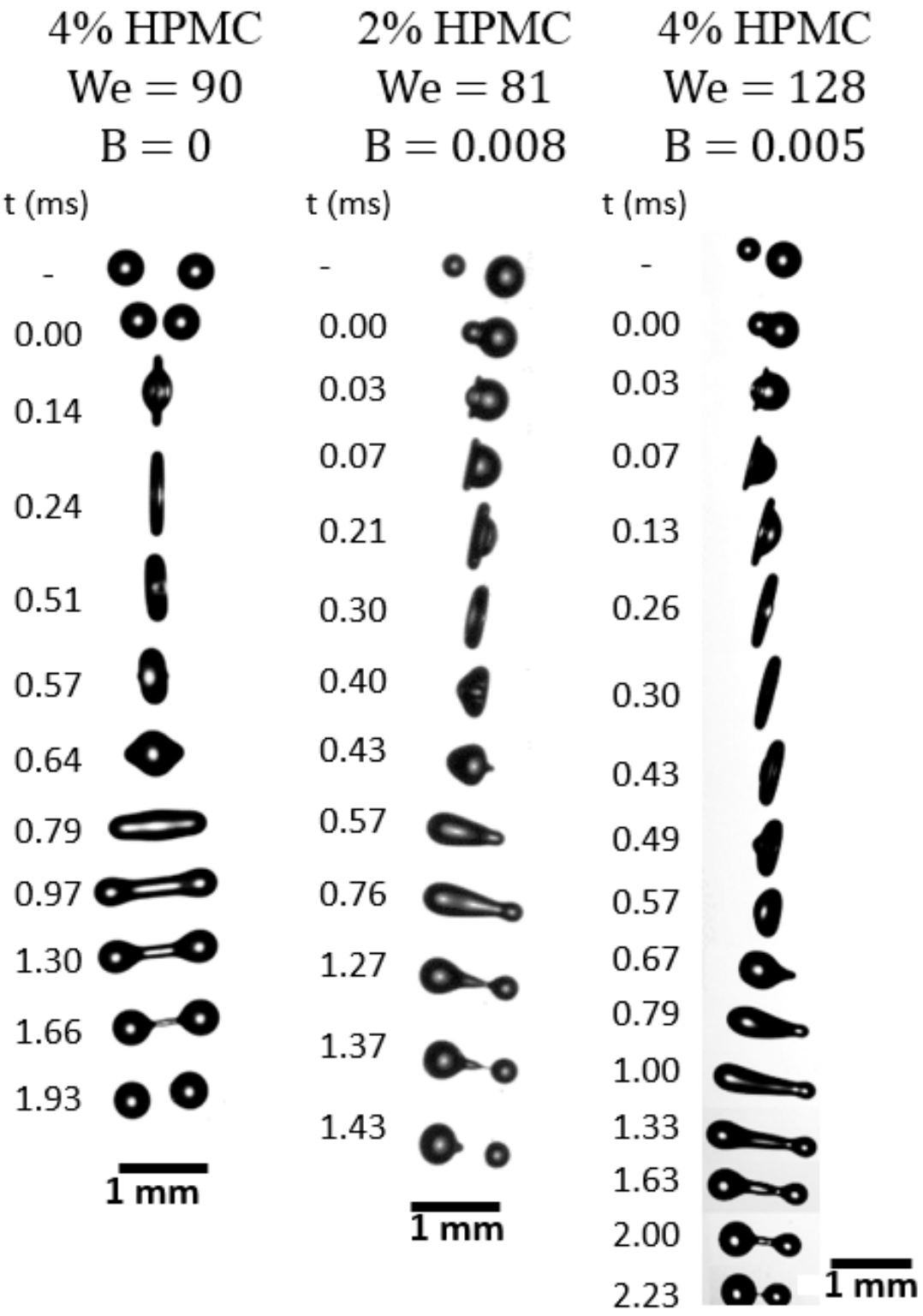

Figure 5.12 The dynamics of reflexives separation regime in collisions of equal-size droplets and unequal-size droplets.

In equal-size droplet collisions, the droplets collide forming a rimmed lamellar disc shaped droplet, which is a circular lamella bounded by a toroidal rim at its highest

deformation, as shown in stage 3 Figure 5.13. The droplet after stage 3 tends to minimize the surface energy, hence the rim starts shrinking and gets thicker until it meets at the centre of the lamella, stages 4-5. The collapse of the rim induces reflexive flows in the opposite directions to the colliding droplets, initially by forming protrusions, as can be seen in stage 5. These protrusions expand away from each other until the whole droplet is converted into a cylindrical shape that eventually breaks up into two droplets.

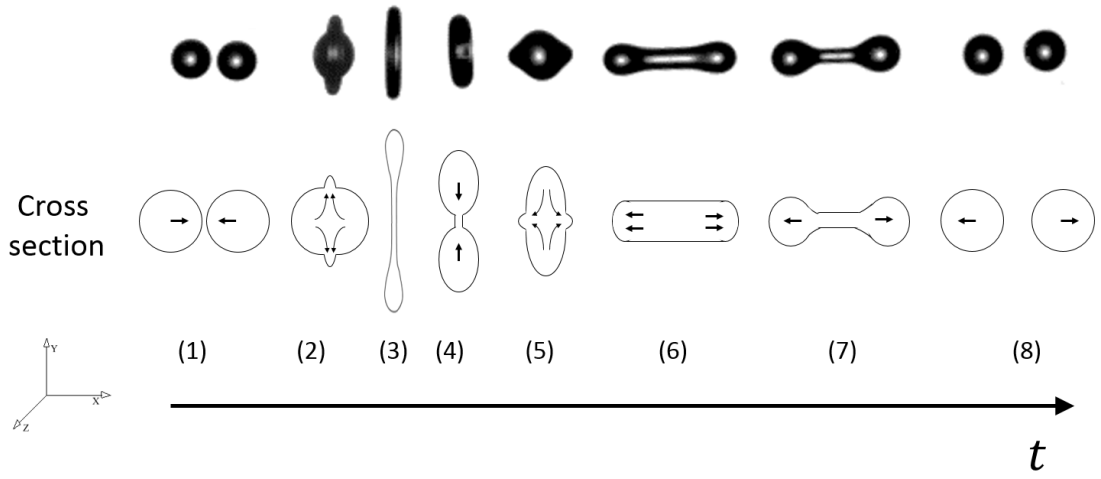

Figure 5.13 Schismatic of the reflexive separation process of equal-size droplet collisions.

In collisions of unequal-size droplets, as the small droplet starts penetrating the large droplet a thin rim (corona like) emerges on the surface of the large droplet as can be seen in stage 2 Figure 5.14. As the small droplet dives into the large droplet, this corona gets thicker and converts into a rim that tries to move around on the surface of the non-deformed part of the large droplet. Because of this movement, the rim only faces one side, which is the side of the large droplet, as depicted in stage 4 in Figure 5.14. Once the rim reaches its maximum expanding, stage 4, it starts shrinking and getting thicker, as in stage 5. At the same time the flat side of the rim, in stage 4, gets curvy, as in stage 5. Then the one-sided rim globules merge and that leads to a jet bursting from the side of the large droplet, as shown in stage 6. This jet keeps growing until it eventually breaks forming a small droplet as in stage 8. This shows that the reflexive flow is from one side. Therefore, it is harder to achieve separation compared to the collisions of equal-size droplets where jets burst from both sides.

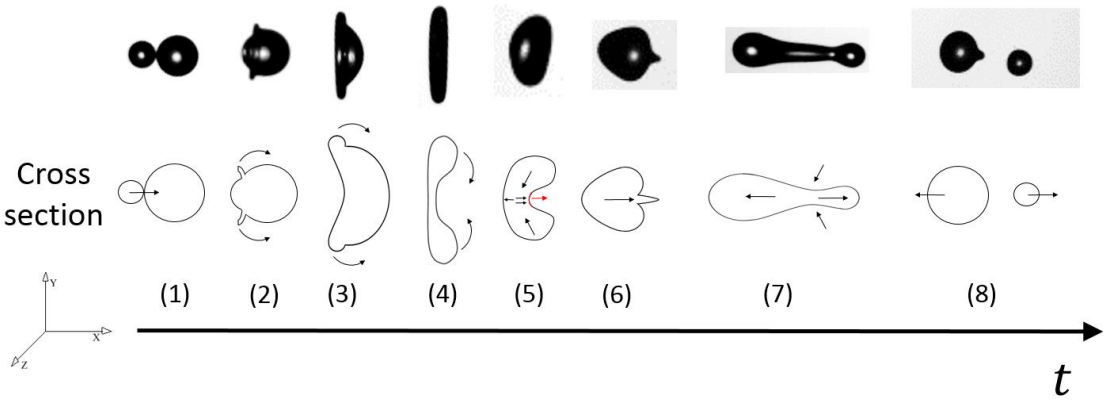

Figure 5.14 Schismatic of the dynamic of the reflexive separation in unequal-size droplet collision.

The collisions of unequal-size droplets with non-identical viscosities show defined reflexive separation regime that are qualitatively comparable to those of the identical viscosities, as shown in Figure 5.4 and detailed in Table 5.2. However, quantitatively, the onset of the reflexive separation regime depends how the viscosity is assigned to the size of the unequal-size droplets. In the case of 2% (L) vs. 4% (S) HPMC, the onset of reflexive separation is similar to that of the collisions of unequal-size droplets of 2% HPMC, as detailed in Table 5.2. On the other hand, the case of 2% (S) vs. 4% (L) HPMC has an onset of reflexive separation that sits on an intermediate $\mathrm{We}_{\mathrm{Fc/RS}}$ compared to those of the collisions of unequal-size droplets with identical viscosities of 2% HPMC and 4% HPMC, as detailed in Table 5.2.

Figure 5.15 shows the collisions' dynamics of the two cases of unequal-size droplets with non-identical viscosities. In the case of the 2% (L) vs. 4% (S) HPMC, there is no mixing at the developed rim, as can be seen at t=0.40 ms. Therefore, the jet that bursts from its collapse is from only the 2% HPMC droplet, see t=0.86 ms, and hence the separated small droplet has concentration similar to that of the initial large droplet (2% HPMC). This explains the similar onset of reflexive separation with the collisions of unequal-size droplets with identical viscosities of 2% HPMC. On the other hand, the collision of 2% (S) vs. 4% (L) HPMC shows clear mixing as can be seen from the images at t=1.30 and 1.70 ms in the second column in Figure 5.15. Therefore, the jet has an intermediate viscosity which consequently leads to an intermediate onset of reflexive separation compared to the cases of the identical viscosities.

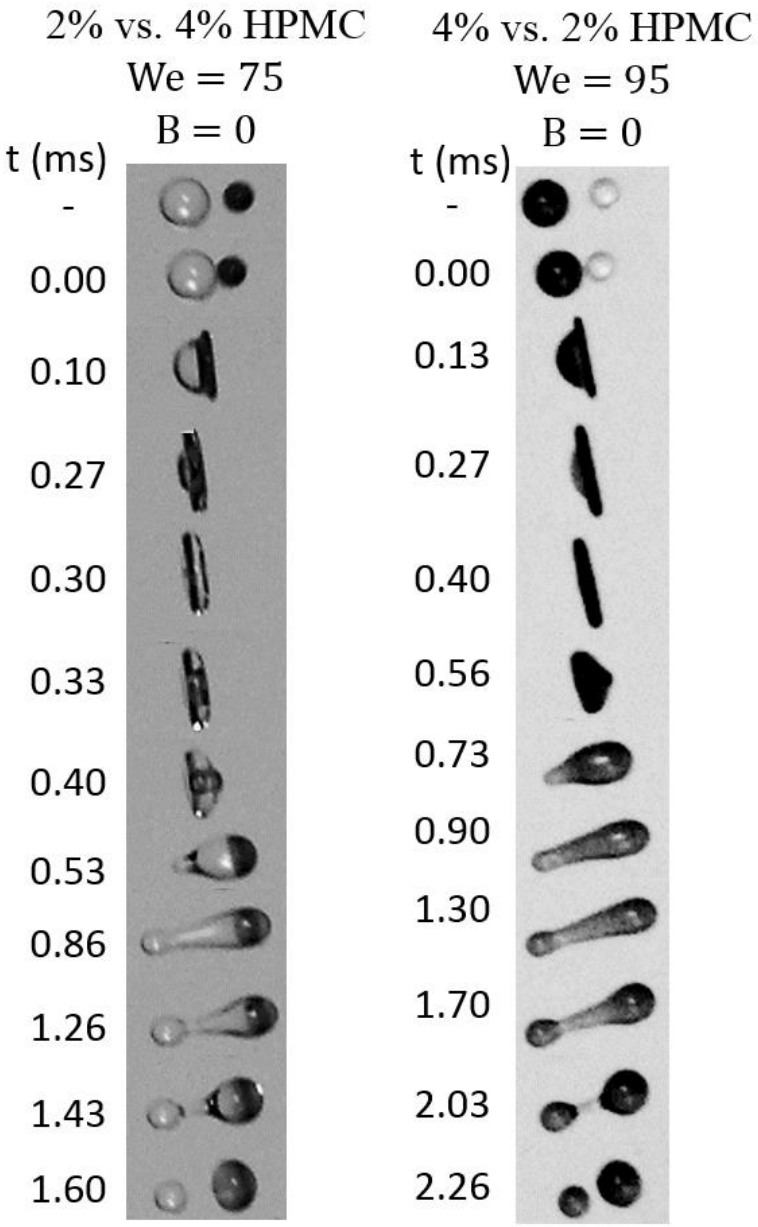

Figure 5.15 The dynamics of the reflexive separation of collisions of unequal-size droplets with non-identical viscosities.

5.4 Predicting regimes' boundaries

In the literature, models to predict the regimes' boundaries were reported. In this section, these existing models will be used to predict the regimes' boundaries of the regime maps reported in this chapter.

5.4.1 Bouncing

Estrade et al. (1999) developed the first model to predict the bouncing regime boundary, Eq. (2.7). This model includes a shape factor which is reported to have a value of 1.12.

Generally, this model shows poor performance, as can be seen in Figures 5.1 and 5.4. Its poor performance has been frequently reported in the literature (Kuschel and Sommerfeld, 2013, Sommerfeld and Kuschel, 2016, Sommerfeld and Pasternak, 2019, Finotello et al., 2018a, Finotello et al., 2018b). Therefore, the modelling of bouncing will be discussed in great details in Chapter 7.

5.4.2 Stretching separation

In the previous chapter, it has been shown that the model of Jiang et al. (1992) can reasonably fit the boundary of the stretching separation regime. Therefore, as the boundaries of the stretching separation regimes of the data presented in this chapter in Figures 5.1 and 5.4 have a quantitatively similar shape to those of the previous chapter, the model of Jiang et al. (1992) will be adopted in this chapter as well. The model in its original shape is only for collisions of identical droplets, Eq. (2.27). However, in this chapter, we have collisions of non-identical droplets, in terms of size and viscosity, in Figure 5.4 alongside collisions of identical droplets in Figure 5.1. Sommerfeld and Pasternak (2019) combined the model of Jiang et al. (1992) with the model of Brazier-Smith et al. (1972) to consider the effect of the size ratio, Eq. (2.30). Thus, this modified model will be used for the non-identical droplets' collisions.

In the identical droplet collisions, the empirical parameter in the model of Jiang et al. (1992), C_a, was first optimized for the best data fit, detailed in Table 5.3. The model shows very good fits, as can be seen from Figure 5.1. The optimization procedure of C_a is based on the minimum mean absolute error as explained in the previous chapter. The Oh correlation to predict C_a by Sommerfeld and Pasternak (2019), Eq. (2.28), was used as well, as detailed in Table 5.3, to compare with the performance of the optimized values of C_a. The use of the Oh correlation shows good prediction in case of collisions of the large droplets of 2% HPMC, while show scattering in the other systems, as shown in Figure 5.1. The average value of the scatter is $\backsim$0.05 in terms of the impact parameter B.

In the non-Identical droplet collisions, the empirical parameter C_a in the modified model of Jiang et al. (1992), by Sommerfeld and Pasternak (2019), was also optimized, as detailed in Table 5.3. As the droplet diameter and the viscosity are variables in the

model, they need to be assigned for the controlling droplet in the cases of non-identical droplet collisions. The diameter of the small droplet is used, as it is the controlling one. In the collisions of the unequal-size droplets with non-identical viscosities, the viscosity of the low viscosity droplet was used in the model. This is because the ligament is mainly composed of the low viscosity droplet, as shown in the coloured images in Figure 5.10. The model fits the boundary of the stretching separation very well, as shown in Figure 5.4. Although the Oh correlation was produced based on data of equal-size droplet collisions, Sommerfeld and Pasternak (2019) used it for collisions of unequal-size droplet collisions by taking Oh of the small droplet. This approach is also applied here. Generally, the use of the Oh correlation shows an over prediction of B, as shown in Figure 5.4. However, it has a reasonable prediction in the case of the collisions of unequal-size droplets of 4% HPMC and the case of 2%(S) vs. 4% (L) HPMC with an average scatter value of $\backsim$0.03 in terms of B. whereas, it shows poorer prediction in the case of the collisions of unequal-size droplets of 2% HPMC and the case of 2%(L) vs. 4% (S) HPMC with an average scatter value of $\backsim$0.07 in terms of B.

Ultimately, the model of Jiang et al. (1992), in both forms the original and the modified, can be used to accurately fit the boundary of the stretching separation if the fitting parameter, C_a, is accurately known. Generally, predicting C_a based on Oh by using the correlation of Sommerfeld and Pasternak (2019) shows scattering and that scattering has no defined trend, especially in the equal size droplet collisions. For example, in Figure 5.1, it shows a good prediction of B in 2% HPMC (L), an over-prediction of B in 4% HPMC (L), and under-predications in both 2% HPMC (S) and 4% HPMC (S). Such a random behaviour was also observed in the previous chapter as it shows under-prediction in 2% HPMC while over-prediction in 4% HPMC and 8% HPMC. This random performance across the data is due to that correlating C_a with Oh cannot produce a general correlation.

Based on the optimized fittings, $C_a$is inversely proportional to μ and d, as can be seen from Table 5.3. However, $\mathrm{Oh} \propto \frac{\mu}{d^{0.5}}$, which therefore means C_a cannot be correlated with Oh. it should be noted that the good fitting of C_a with Oh in Sommerfeld and Pasternak (2019) is due to the constant diameter across their experiments. Therefore,

another scaling law is required for C_a to make better use of the model of Jiang et al. (1992), which is out of the scope of this work.

Table 5.3 Parameters used in the model of Jiang et al. (1992).

	μ (mPa s)	Oh	C_a (from Oh correlation)	C_a (optimized)
2% HPMC (L)	2.8	0.020	2.49	2.58
2% HPMC (S)	2.8	0.027	2.44	2.85
4% HPMC (L)	8.2	0.063	2.21	1.90
4% HPMC (S)	8.2	0.080	2.11	2.51
2% HPMC (Δ=0.6)	2.8	0.027	2.44	2.15
4% HPMC (Δ=0.6)	8.2	0.080	2.11	2.91
2%(L) vs 4% (S) HPMC (Δ=0.6)	2.8	0.027	2.49	2.07
2%(S) vs 4% (L) HPMC (Δ=0.6)	2.8	0.027	2.44	2.24

5.4.3 Reflexive separation

In the previous chapter, it was shown that the shift of the model of Ashgriz and Poo (1990) by the model of Planchette et al. (2017), Eq. (2.18), is a promising approach to predict the boundary of the reflexive separation regime in collisions of equal-size droplets. Therefore, this approach will be applied to the equal-size droplet collisions in this chapter. The adjustable parameters in the model of Planchette et al. (2017) were kept the same as in the previous chapter. This approach shows good predictions at 4% HPMC systems while it under-predicts $\mathrm{We}_{\mathrm{Fc/RS}}$ of the 2% HPMC systems, as shown in Figure 5.1.

The performance of the model of Planchette et al. (2017), in predicting the onset of the reflexive separation regime at head-on collisions of the data of the previous chapter and this chapter, is summarised in Figure 5.16a. Generally, the model shows good agreements with the experimental data at Oh > 0.04, but it shows under-predictions at Oh < 0.04. In addition, the performance of the Oh correlations of Gotaas et al. (2007) also was examined in Figure 5.16a. These correlations fail in predicting the trend of $\mathrm{We}_{\mathrm{FC/RS}}$ with Oh of the HPMC systems. However, the data produce a linear Oh correlation with less scatter compared to the existing models, as shown in Figure 5.16b.

The model of Hu et al. (2017), Eq. (2.16), is also applied to the equal-size droplet collisions. The fitting parameter α_3 was used to fit the model to the onsets of the reflexive separation regimes at head-on collisions, as shown in Figure 5.1. α_3 represents the total viscous loss energy (i.e. from the instant of the collision until the separation) to the impact kinetic energy, hence α_3 is expected to be close to 100%. This is because, at the onset of the reflexive separation, the separated droplets have a similar surface area to the initial droplets and possess negligible kinetic energy compared to the initial droplets, as mentioned in the previous chapter. However, the fitted values of α_3 are noticeably lower than 100% and they increase with Oh as detailed in Table 5.4. This strange behaviour is due to the assumptions in the model of Hu et al. (2017), which will be discussed in detail in Chapter 6.

Table 5.4 The fitting values of the viscous loss parameter in the model of He et al. (2017).

	Oh	α_3
2% HPMC (L)	0.020	0.55
2% HPMC (S)	0.027	0.60
4% HPMC (L)	0.063	0.75
4% HPMC (S)	0.080	0.825

At B > 0, the model of Hu et al. (2017) shows over-prediction of B at the lowest Oh system, 2% HPMC (L), and under-prediction of B at the highest Oh system, 4% HPMC (S). whereas, good fits are shown at the moderates Oh systems. On the other hand, the model of Ashgriz and Poo (1990) shows good fits in all the systems. This requires more investigation in the assumptions of the impact parameter, which will be also provided in Chapter 6.

The modelling of collisions of viscous droplets with unequal size has received less attention compared to the equal-size droplet collisions. Tang et al. (2012) developed a model, Eq. (2.20), to predict the onset of the reflexive separation regime at head-on collisions for collisions of unequal-size droplets, which explicitly considers the viscous loss energy. Therefore, it can be used instead of the model of Planchette et al (2017) to shift the model of Ashgriz and Poo (1990) to fit the collisions of the unequal-size droplets. However, the model includes Oh of the small droplet which makes its application to the cases of the non-identical viscosities is not straightforward.

The viscosity term in the Oh in the model of Tang et at. (2012) comes from the flow induced by the rim shrinking and the jet bursting in the stages from 4 to 8 in Figure 5.14. whereas, the diameter of the small droplet in the Oh comes from the that all length scales are normalized by the radius of the small droplet in the model of Tang et al. (2012). In the case of 2% (L) vs 4% (S) HPMC, the rim and the emerging jet are from the low viscosity droplet, as shown in Figure 5.15. Therefore, the viscosity of the large droplet is used in the Oh in the model of Tang et at. (2012) while the diameter is kept for the small droplet. This results in a similar prediction, of the onset of reflexive separation regime, to that of the collisions of the unequal-size droplets with identical viscosities of 2% HPMC. This similarity is also seen in the experiments as mentioned earlier in section 5.3.3. On the other hand, mixing is seen in the dynamics of 2% (S) vs 4% (L) HPMC, as shown in Figure 5.15. Therefore, the viscosity is averaged by volume fraction using $(\Delta^3\mu_s + \mu_l)/(1 + \Delta^3)$.

Generally, the model of Tang et al. (2012) shows under prediction except in the case of 2% (S) vs 4% (L) HPMC where the onset of the reflexive separation is accurately predicted, as shown in Figure 5.4. On the other hand, the model of Ashgriz and Poo (1990) slightly under predicts the boundary of the reflexive separation regime in terms of B.

Another model that is supposed to be usable in collisions of unequal-size droplets is that of Hu et al. (2017), as it includes the effect of the size ratio and viscous loss. However, the model strangely returns in negative values when the size ratio is changed from 1 to 0.6.

Finally, the modelling of the boundary of the reflexive separation regime will receive special attention in Chapter 6 where all the raised issues from the use of the various models in this section will be discussed and justified.

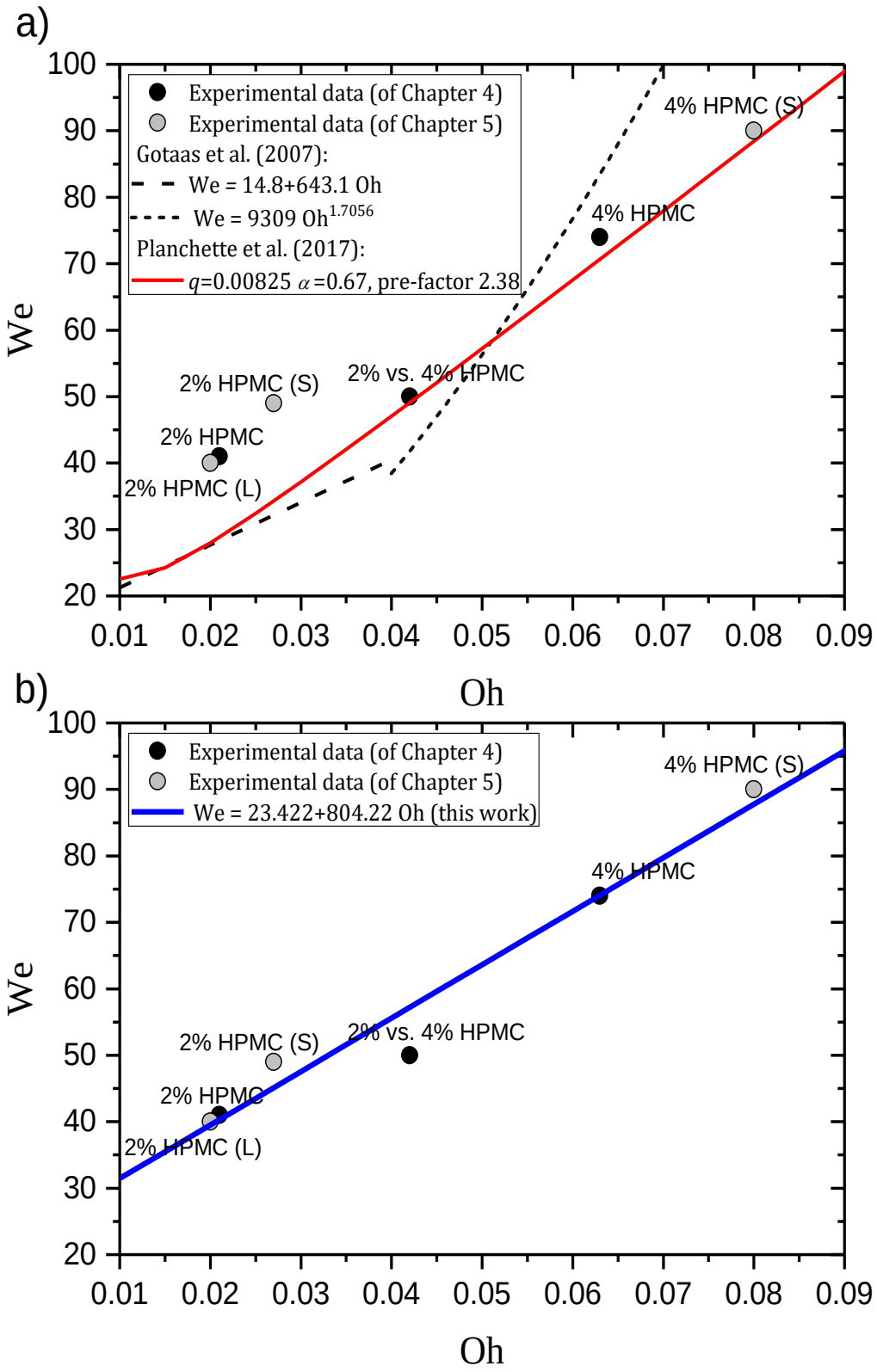

Figure 5.16 The onset of the reflexive separation regime at head-on collisions versus Oh for equal-size droplet collisions. a) the performance of the existing models against the experimental data; b) the fitting of the experimental data ($R^2 = 0.9644$).

5.5 Conclusion

In this chapter, a novel data is reported to explore the role of the size and the size ratio in binary droplet collisions. Two solutions, 2% and 4% HPMC, were used to generate droplets of two sizes ~400 μm and ~230 μm. Four regime maps were constructed for collisions of identical droplets using the two solutions and the two sizes. Another four regime maps were also constructed but for unequal-size collisions, of which two are for collisions of droplets of identical viscosities and the other two are for non-identical viscosities by swapping the solution over the sizes.

For collisions of equal-size droplets, the size has an impact on the location of the regimes' boundaries, despite it being considered in the parameter space.

- *Bouncing regime:* the bouncing regime moves to a lower We by reducing the size. This is attributed to the higher curvature and capillary pressure, which enhance the air film drainage between the colliding droplets and that consequently promotes the coalescence.
- *Separation regimes:* by reducing the size, the boundary of the reflexive separation regime moves to a higher We and the boundary of the stretching separation regime to a higher B. This is because the smaller droplets have higher Oh. However, the sensitivity of these boundaries' shifts depends on the viscosity of the droplets as Oh of the low viscosity droplets is less sensitive to the droplet size.

Generally, reducing the droplet size promotes the coalescence regime. However, farther promotion is seen in the collisions of the unequal-size droplets with identical viscosities.

- *Bouncing regime:* the low viscosity droplets, 2% HPMC, show similar bouncing regime to that of the identical size collisions of the small droplet size. However, higher viscosity droplets show less bouncing compared to the identical size collisions of the small droplet. This is attributed to that the small droplet starts bouncing off before the large droplet, which still moves towards it. Therefore, the low viscosity small droplets bounce in a faster velocity than those of higher viscosity, due to the less viscous loss, and hence more chance to escape from the large droplet.

- *Reflexive separation regime:* by reducing the size ratio, the boundary of the reflexive separation regime moves to a higher We. This is due to the loss of the symmetry that leads to a one side reflexive flow.
- *Stretching separation regime:* reducing the size ratio shifts the boundary of the stretching separation regime towards higher B. This is because, for a given B, the non-interaction region of the small droplet, which is the main contributor in the stretching energy, gets smaller by reducing the size ratio.

For collisions of unequal size droplets with non-identical viscosities:

- *Bouncing regime:* both cases of non-identical viscosities, 2% (L) vs 4% (S) HPMC, and 2% (S) vs 4% (L) HPMC, show no bouncing at head-on collisions. This is due to the less air indentation in the high viscosity droplet that consequently enhances the air film drainage. Consequently, when the small droplet starts bouncing, the large droplet has a high chance to catch it and hence late coalescence occurs.
- *Reflexive separation regime:* if the large droplet is the lower viscosity, 2% (L) vs 4% (S) HPMC, the reflexive jet is from the low viscosity and no significant mixing occurs. Consequently, the onset of the reflexive separation has similar We to that of the collisions of the unequal-size droplets with identical viscosities of 2% HPMC. In addition, the separated droplets are small low viscosity droplet and large mixed droplet. On the other hand, if the large droplet is the higher viscosity, 2% (S) vs 4% (L) HPMC, a significant mixing occurs. Consequently, the onset of the reflexive separation has an intermediate We between those of the collisions of unequal-size droplets with identical viscosities of 2% HPMC and 4% HPMC.
- *Stretching separation regime:* in both cases of non-identical viscosities, 2% (L) vs 4% (S) HPMC, and 2% (S) vs 4% (L) HPMC, the stretched ligament is from the low viscosity droplet. Thus, the boundary of the stretching separation regime is comparable to that of the collisions of the unequal-size droplets with identical viscosities of 2% HPMC.

The existing models were also used to predict the regimes' boundaries. The model of Estrade et al. (1990) shows poor prediction to all systems in this chapter. Thus, the bouncing modelling will be discussed in more details in Chapter 7. On the other hand, the model of Jiang et al. (1992) can predict the shape of the stretching separation boundary if its adjustable parameter C_a is known. Moreover, it was found that C_a cannot be correlated with Oh as C_a scales differently with the change of Oh by changing μ than that by changing d, and hence another scale law is required. Finally, the models of the reflexive separation were also applied in this chapter and they found to have issues in predicting the boundary. Therefore, the modelling of the reflexive separation regime will be discussed in detail in Chapter 6.

5.6 The Significance of the findings

The above findings are very important for studies of sprays, as although the parameter space of the regime maps accounts for the drop size, the regime maps are not universal in terms of the drop size. Thus, care must be taken when these regime maps are used, as most of the spray applications have droplets with a mean size of 50 μm while most of the published regime maps are for drop sizes >200 μm, as shown in table 2.2.

Chapter 6: Modelling of the boundary of the reflexive separation regime

The previous chapters, 4 and 5, represent the experimental part of this thesis where experiments of binary droplet collisions were conducted to study the roles of the viscosity, size and size ratio. The upcoming chapters, 6 and 7, represent the modelling part of this thesis. In this chapter, the modelling of the boundary of the reflexive separation regime will be discussed in great details and a model will be suggested. Then in chapter 7, the modelling of the bouncing regime boundary will be discussed.

6.1 Introduction

In the previous chapter, it was shown that there are issues associated with the existing models of the reflexive separation regime. Apart from the model of Hu et al. (2017), there is no general model that considers the size ratio, the impact parameter and viscous loss together. However, it was mentioned in the previous chapter that the model of Hu et al. (2017) gives unphysical values (negative values of We) when $\Delta < 1$. Therefore, there is a need for a model that can predict the whole boundary of the reflexive separation regime for various viscosities and size ratios.

The existing models can be divided into two main types: models for the whole boundary of the reflexive separation (Ashgriz and Poo, 1990, Hu et al., 2017), and models only for the onset of the reflexive separation regime at head-on collisions (Planchette et al., 2017, Tang et al., 2012). The model of Ashgriz and Poo (1990) considers the impact parameter and the size ratio but does not consider the viscous loss. Hu et al. (2017) modified the model of Ashgriz and Poo (2017) to consider the viscous loss but it was seen in the previous chapter that it returns with negative values for collisions of unequal-size droplets. On the other hand, in the head-on collisions' models, both models consider the viscous loss but the model of Planchette et al. (2017) is only for the equal-size droplet collisions while the model of Tang et al. (2012) considers the role of the size ratio. In this chapter, these models will be discussed in detail, their weakness addressed and then a new model that considers the size ratio, the impact parameter and viscous

loss will be proposed. This will be done by looking into the assumptions and comparing them against experimental observations and looking for any crucial underlying physics that still need to be considered.

6.2 The existing models that consider the effect of the impact parameter

The first attempt to model the boundary of the reflexive separation regime was by Ashgriz and Poo (1990). To derive the model, the authors suggested that the energy of the reflexive flow (E_{re}), in stage 6 in Figure 6.1, can be evaluated from the energy balance for the period from the instant of the collision until the maximum deformation of the rimmed lamellar disc, as given by Eq. (6.1). Ashgriz and Poo (1990), with the help of the linear theory of Rayleigh (1945), suggested that separation occurs if E_{re} is greater than 0.75 of the surface energy of a nominal droplet that would be formed from the merge of the colliding droplets, Eq. (6.2). To perform the energy balance and consequently developing the model, a set of assumptions were used, listed in Table 6.1.

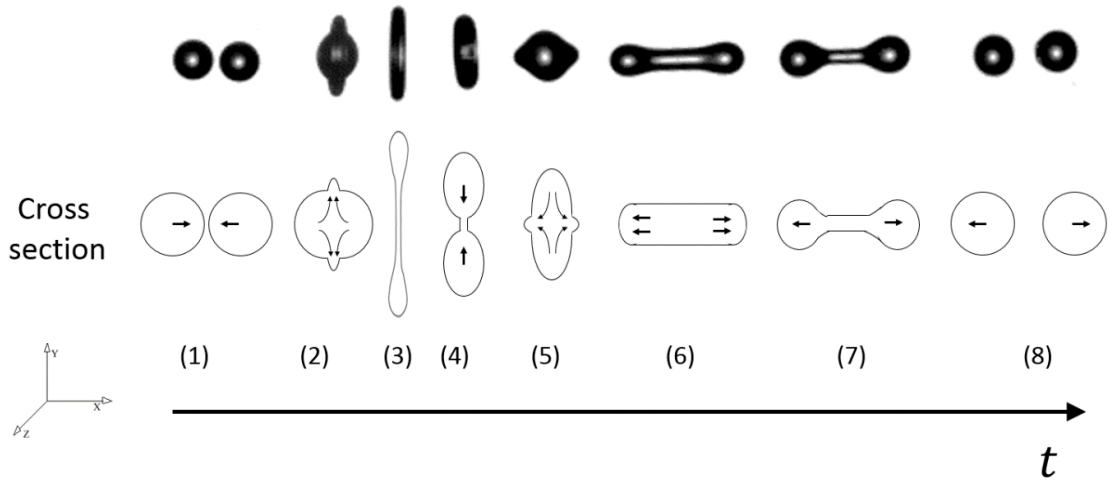

Figure 6.1 The dynamics of reflexive separation of a head-on collision.

$$E_{k,ini,cont} + E_{\Delta\sigma} - E_{K,ini,str} = E_{re} \tag{6.1}$$

$$E_{re} \geq 0.75\sigma\pi(d_l^3 + d_s^3)^{\frac{2}{3}} \tag{6.2}$$

Where, $E_{k,ini,cont}$, $E_{\Delta\sigma}$ and $E_{K,ini,str}$ are the initial kinetic energy of the interaction regions, the excess-surface energy, which is the difference between the energy of the

initial droplets and that of nominal spherical droplet that would be formed by the merge of the colliding droplets, and the stretching energy, respectively. They are given by

Table 6.1 The assumptions that were applied by Ashgriz and Poo (1990) to develop a model for the boundary of the reflexive separation regime.

Assumptions	Justifications
1. No viscous loss is considered.	The model developed based on experiments of water droplets collisions.
2. At B > 0, only the kinetic energy of the prolate interaction region contributes to the reflexive flow energy (E_{re}), see Figure 6.3a.	The reflexive flow is generated by the portions of drops which directly oppose each other.
3. The kinetic energy of the non-interaction regions is considered as stretching energy ($E_{K,ini,str}$) that resists E_{re}.	The non-interaction regions have kinetic energy in the opposite direction to the reflexive flow, as shown in the schematic in Figure 6.2 at stage 4.
4. Separation occurs if the reflexive energy (E_{re}) $\geq$ 0.75 of the surface energy of the spherical droplet that would be formed by the merge of the colliding droplets.	Experimental observations with the help of the linear theory of Rayleigh (1945).

$$E_{k,ini,cont} = \frac{\pi}{12}\rho d_s^3 \left(\frac{u_r}{1+\Delta^3}\right)^2 \left(\Delta^3 X_{pl} + X_{ps}\right), \tag{6.3}$$

Where X_{ps} and X_{pl} are the ratio of the prolate interaction regions and given by Eq. (6.7) and Eq. (6.8) and represented by the shaded areas in Figure 6.3a.

$$E_{\Delta\sigma} = \frac{\pi}{\Delta^2}\sigma d_s^2 \left((1+\Delta^2) - (1+\Delta^3)^{\frac{2}{3}}\right) \tag{6.4}$$

and

$$E_{K,ini,str} = \frac{\pi}{12}\rho d_s^3 \left(\frac{u_r}{1+\Delta^3}\right)^2 \left((1+\Delta^3) - (\Delta^3 X_l + X_s)\right) \tag{6.5}$$

Substituting Eqs. (6.1, 6.3, 6.4, and 6.5) in Eq. (6.2) gives the model of Ashgriz and Poo (1990) which is given in chapter 2 in Eq. (2.13) and rewritten in this chapter in terms of X_{pl} and X_{ps} as in Eq. (6.6).

$$\mathrm{We_c} = \frac{3\left(7(1+\Delta^3)^{\frac{2}{3}} - 4(1+\Delta^2)\right)(1+\Delta^3)^2}{\Delta^2\left(2(\Delta^3 X_{Pl} + X_{Ps}) - (1+\Delta^3)\right)} \tag{6.6}$$

$$X_{ps} = \frac{1}{\Delta^3}\left(\Delta - 0.5\mathrm{B}(1+\Delta)\right)^2\left(\Delta^2 - \left(0.5\mathrm{B}(1+\Delta)\right)^2\right)^{0.5} \tag{6.7}$$

$$X_{pl} = \left(1 - 0.5\mathrm{B}(1+\Delta)\right)^2\left(1 - \left(0.5\mathrm{B}(1+\Delta)\right)^2\right)^{0.5} \tag{6.8}$$

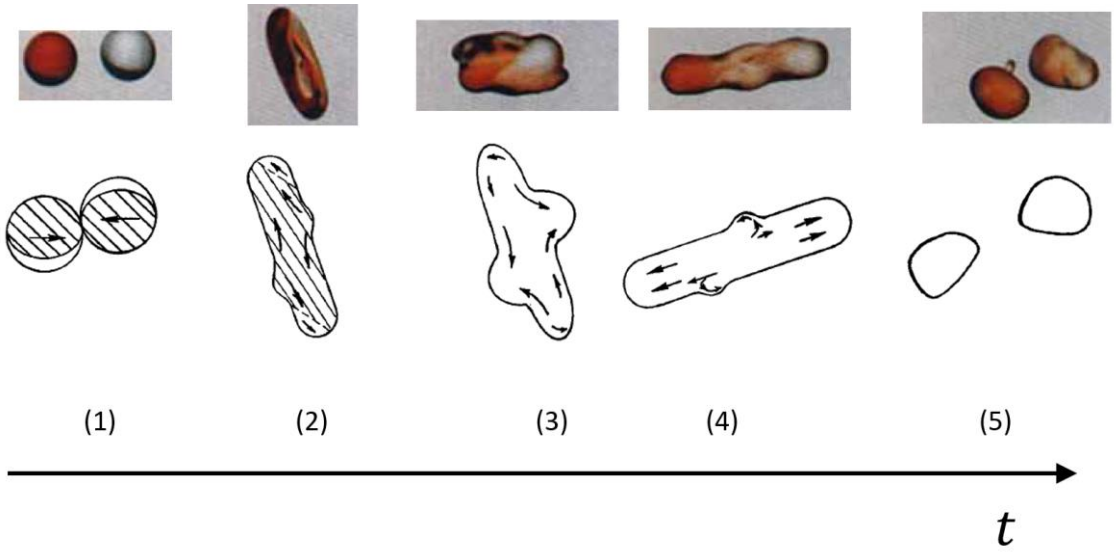

Figure 6.2 The dynamics of the off-centre reflexive separation adapted from (Ashgriz and Poo, 1990).

Hu et al. (2017) have extended the model of Ashgriz and Poo (1990) to consider the viscous loss by introducing a viscous loss factor, α_3, which represents the ratio of the viscous loss energy to the kinetic energy of the interaction regions, assuming that there is no viscous loss at the non-interaction regions. Therefore, the energy balance is given by Eq. (1.9), which leads to the model in Eq. (6.10). Moreover, Hu et al. (2017) used spherical cap interaction regions, given by X_s and X_l, instead of the prolate interaction regions, as in Figure 6.3b. It should be noted that, the equations of the ratios of spherical caps interaction regions used by Hu et al. (2017), Eq. (6.11) and Eq. (6.12), were first reported by Ashgriz and Poo (1990) to be used in the model of the stretching separation regime boundary Eq. (2.25).

$$(1-\alpha_2)E_{k,ini,cont} + E_{\Delta\sigma} - E_{K,ini,setr} = E_{re} \tag{6.9}$$

$$We_c = \frac{3\left(7(1+\Delta)^{\frac{2}{3}} - 4(1+\Delta^2)\right)(1+\Delta^3)^2}{\Delta^2\left((2-\alpha_3)(\Delta^3 X_l + X_s) - (1+\Delta^3)\right)}. \tag{6.10}$$

$$X_s = \begin{cases} \left(1 - \frac{1}{4\Delta^3}(2\Delta-\tau)^2(\Delta+\tau)\right) & \text{for } h > \frac{d_s}{2} \\ \frac{1}{4\Delta^3}\tau^2(3\Delta-\tau) & \text{for } h \le \frac{d_s}{2} \end{cases} \tag{6.11}$$

and

$$X_l = \begin{cases} 1 - \frac{1}{4}(2-\tau)^2(1+\tau) & \text{for } h > \frac{d_l}{2} \\ \frac{1}{4}\tau^2(3-\tau) & \text{for } h \le \frac{d_l}{2} \end{cases}, \tag{6.12}$$

where

$$\tau = (1-B)(1+\Delta), \tag{6.13}$$

and

$$h = \frac{1}{2}(d_l + d_s)(1-B) \tag{6.14}$$

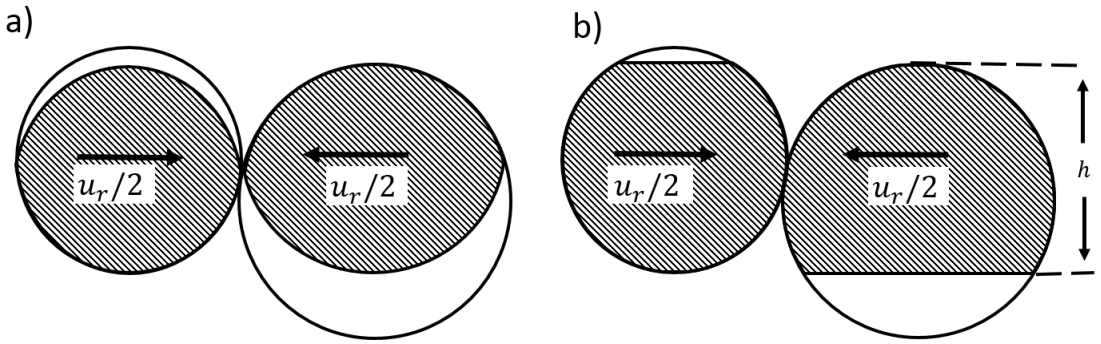

Figure 6.3 Schematic shows the difference in the interaction regions used by a) Ashgriz and Poo (1990), b) Hu et al. (2017).

6.2.1 The role of the impact parameter

In the previous chapter, the model of Hu et al. (2017) was reported to give negative values at Δ = 0.6. The model of Hu et al. (2017) utilizes the same assumptions of Ashgriz

and Poo (1990) except the viscous loss factor and the geometry of interaction regions. Therefore, if the viscous loss factor is 0 that means the only difference between the two models is the type of interaction regions. For head-on collision, at $\alpha_3 = 0$, the model of Hu et al. (2017) still gives negative values, when $\Delta \leq 0.56$ whereas the model of Ashgriz and Poo (1990) gives positive values. Therefore, the source of the error is expected to come from the formulas of the interaction regions, Eq. (6.11) and Eq. (6.12). Thus, in the next section, the validity of the mathematical expressions of the interaction regions will be investigated.

6.2.2 The interaction regions' ratios

In this section, it will be shown that the existing mathematical expressions of the spherical cap interaction regions, in Eq. (6.11) and Eq. (6.12), and those of the prolate, in Eq. (6.7) and Eq. (6.8), have issues. Therefore, correct mathematical expressions of spherical cap will be proposed to be used instead.

The mathematical expressions of the ratio of the interaction regions, Eq. (6.11) and Eq. (6.12), are plotted in Figure 6.4a. At $\mathrm{B} = 0$, X_s is expected to be 1, however, the mathematical expressions show that it is less than 1 and for $\Delta \leq 0.6$, $X_s = 0$ at $\mathrm{B} = 0$. On the other hand, at B = 0 of $\Delta = 0.1$, X_l is ~0.6, which is obviously over-predicted. Moreover, Ashgriz and Poo (1990) reported two formulas for X_s and another two for X_l depending on the value of h, see Eq. (6.11) and Eq. (6.12), however, the two formulas of each X are identical as can be seen in Figure 6.4a. Thus, the formulas in Eq. (6.11) and Eq. (6.12) have many issues and are not valid for non-identical size collisions.

The formulas of the prolate interaction regions by Ashgriz and Poo (1990) in Eq. (6.7) and Eq. (6.8) were also examined in this study, See Figure 6.4b. The formulas show unexpected trends. For example, for $\Delta < 1$, X_{pl} is expected to be less than 1 at B = 0, however $X_{pl} = 1$ even for very small size ratios. The derivation of these formulas was not reported by Ashgriz and Poo (1990), which makes finding the source of the error difficult. Thus, there is a need for new mathematical expressions that correctly describe the geometry to be implemented in the modelling of the reflexive separation regime to consider the effect of B.

A new mathematically derived expression for the ratio of the interaction regions was developed for spherical cap geometry and given by Eq. (6.15) and Eq. (6.16), see Appendix B for the full derivation. The spherical cap geometry was chosen for simplicity and it is also believed that there is no clear reason yet that makes one geometry more suitable than the other. The performance of the new mathematical expressions is shown in Figure 6.4c.

$$X'_l = \begin{cases} \frac{1}{4}\tau^2(3-\tau) & \text{for B} > \frac{d_l - d_s}{d_l + d_s} \\ 1 - \left(\frac{2h_1^2\left(\frac{2}{3}d_l - h_1\right)}{d_l^3}\right) - \left(\frac{2h_2^2\left(\frac{2}{3}d_l - h_2\right)}{d_l^3}\right) & \text{for B} \leq \frac{d_l - d_s}{d_l + d_s} \end{cases}, \quad (6.15)$$

and,

$$X'_s = \begin{cases} \frac{\tau^2(3\Delta - \tau)}{4\Delta^3} & \text{for B} > \frac{d_l - d_s}{d_l + d_s} \\ 1 & \text{for B} \leq \frac{d_l - d_s}{d_l + d_s} \end{cases}. \quad (6.16)$$

Where τ is given by Eq. (6.13), and $h1$ and $h2$ are given by

$$h_1 = \frac{d_l - ds}{2} + \frac{\text{B}(d_l + d_s)}{2} \quad (6.17)$$

$$h_2 = \frac{d_l - ds}{2} - \frac{\text{B}(d_l + d_s)}{2} \quad (6.18)$$

The new expression shows that at size ratio < 1, the ratio of the interaction region of the small droplet stays at 1 for a certain B range depending on Δ then it drops down. In addition, the interaction region of the large droplet is reasonably predicted. It should be noted that the new formulas, Eq. (6.15) and Eq. (6.16), show identical performance to that of the formulas in Eq. (6.11) and Eq. (6.12) at collisions of equal-size droplets. Ultimately, implementing the new mathematical expressions Eq. (6.15) and Eq. (6.16) in the model of Hu et al (2017), instead of Eq. (6.11) and Eq. (6.12), returns with positive values of We for Δ ≤ 0.56.

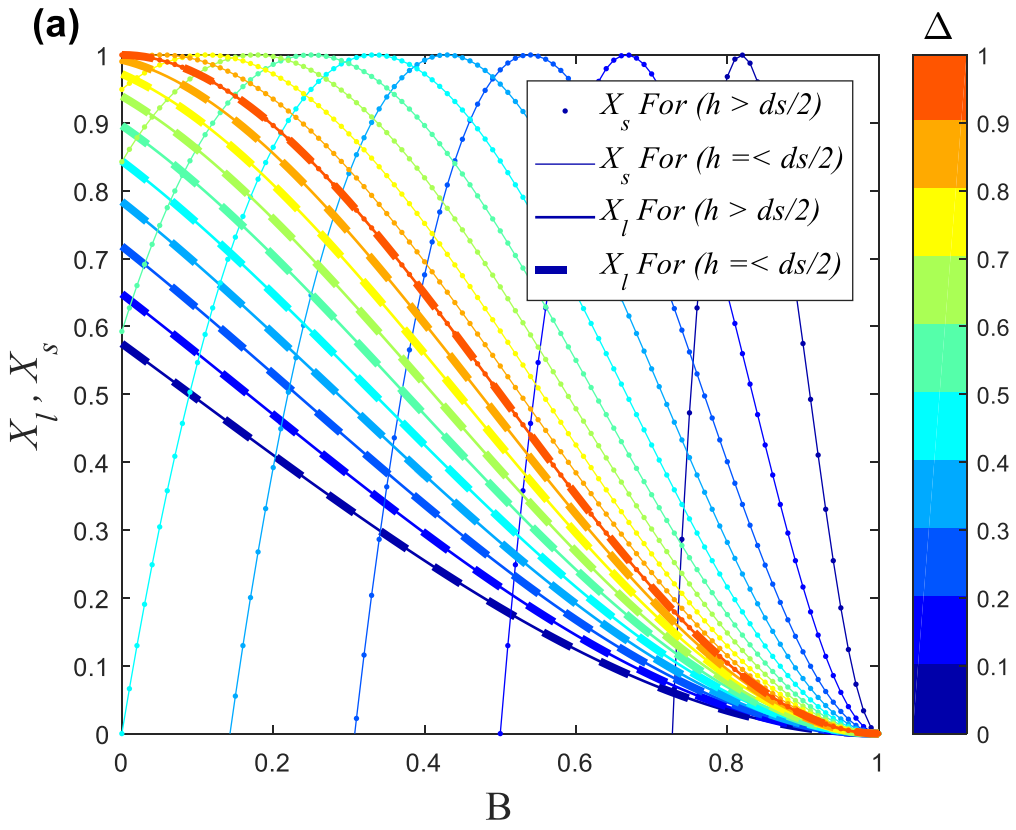
(a)
Δ
X_s For (h > ds/2)
X_s For (h =< ds/2)
X_l For (h > ds/2)
X_l For (h =< ds/2)
X_l , X_s
B

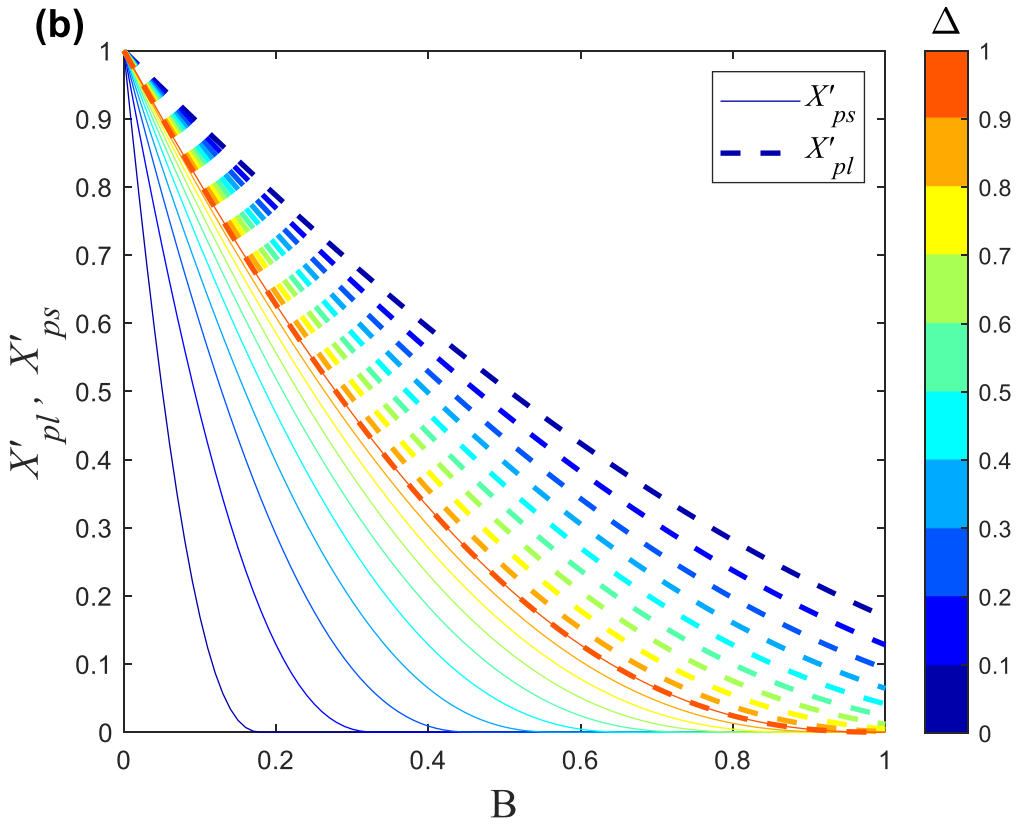
(b)
Δ
X'_{ps}
X'_{pl}
X'_{pl} , X'_{ps}
B

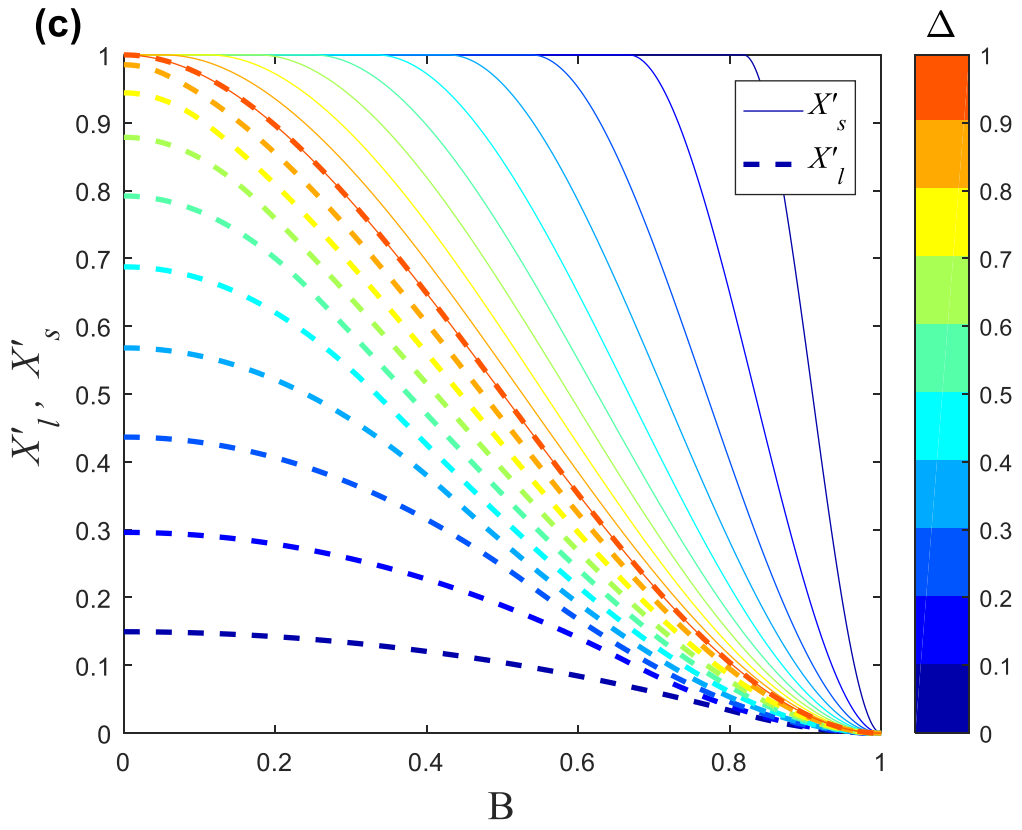

Figure 6.4 The ratio of the interaction region as a function of the impact parameter for different Δ. (a) spherical cap interaction regions reported by Ashgriz and Poo (1990) and used in the model of Hu et al. (2017), given by Eq. (6.11) and Eq.(6.12); (b) prolate interaction regions used in the model of Ashgriz and Poo (1990), given by Eq. (6.7) and Eq. (6.8); (c) the new formulas for the spherical cap interaction regions, given by Eq. (6.15) and Eq. (6.16).

6.2.3 The viscous loss in the model of Hu et al. (2017)

It was mentioned in the previous chapters that the model of Hu et al. (2017) reflects unphysical values of the viscous loss factor α_3. The viscous loss factor increases by increasing the onset We of the reflexive separation, as shown in Figure 6.5. The viscous loss factor in the model of Hu et al. (2017) represents the ratio of total viscous loss to the kinetic energy. However, at the onset of the reflexive separation regime at head-on collisions, about 100% of the kinetic energy is lost (Planchette et al., 2017). This is because, at the onset of the reflexive separation regime, the separated droplets have negligible kinetic energy and they have the same surface energy as that of the colliding droplets. Therefore, the values of α_3 are unphysical.

The model of Hu et al. (2017) is based on a criterion that was empirically set by Ashgriz and Poo (1990) assuming there is no viscous loss in the water droplet collisions. However, the viscous loss in water droplet collisions was noticed by many researchers, such as Qian and Law (1997) and Tang et al. (2012). Therefore, the empirical criterion of the inviscid model of Ashgriz and Poo (1990) already involves 100% loss of water droplets kinetic energy at its onset of the reflexive separation regime ($\mathrm{We}_{\mathrm{FC/RS}} \backsim 19$). This can be proved by proving that adding the 100% loss of kinetic energy of water droplets to the viscous loss in α_3 of any onset $\mathrm{We}_{\mathrm{FC/RS}}$ from the model of Hu et al. (2019), makes the losses approaches 100% of the kinetic energy. This becomes $\alpha_3 + (19/\mathrm{We}_{\mathrm{FC/RS}})$, where $\mathrm{We}_{\mathrm{FC/RS}}$ is the onset of the reflexive separation regime from the model of Hu et al. (2017) as a function of α_3. Figure 6.5 shows that the addition of the 100% loss of water droplets kinetic energy to α_3, leads to ~100% of the kinetic energy is viscously lost.

The above shows that the criterion of Ashgriz and Poo (1990) is fundamentally wrong to be used in the modelling of viscous droplet collisions as it leads to under-estimation of viscous loss. Moreover, apart from the invalid criterion of Ashgriz and Poo (1990), the simple approach of Hu et al. (2017) to consider the effect of the viscosity, by introducing a factor that represents the ratio of the total viscous loss to the kinetic energy is not valid. This is because this ratio does not scale with the viscosity and it equals to ~100% at the onset of the reflexive separation regime boundary, as explained earlier in this section. Therefore, another approach is needed to consider the effect of viscosity on the boundary of the reflexive separation regime.

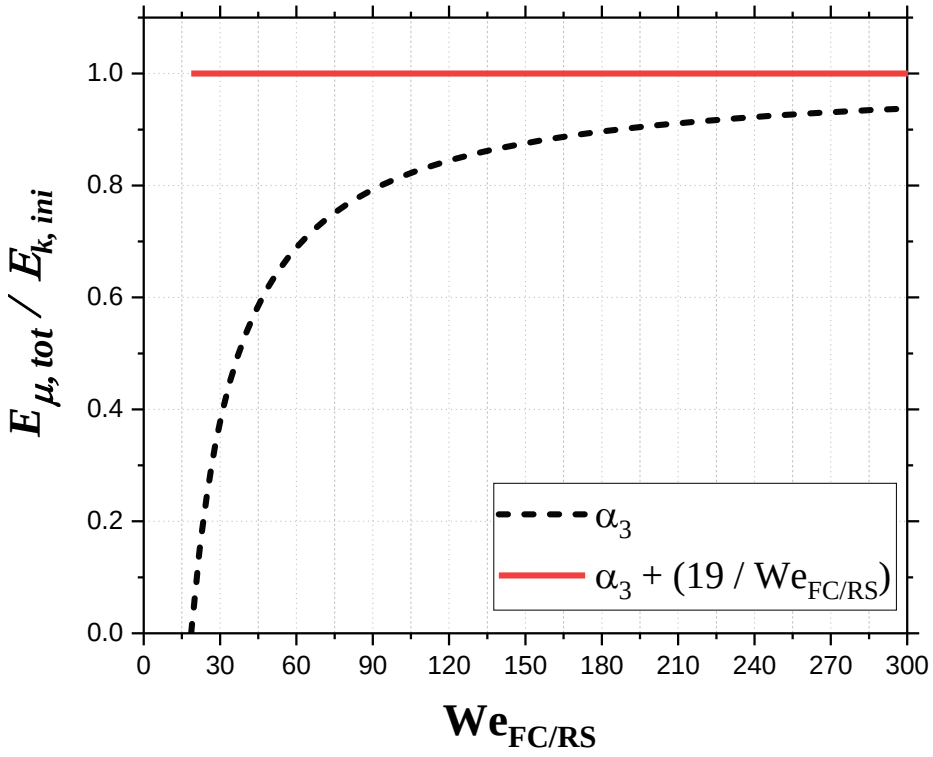

Figure 6.5 The ratio of the total viscous loss to the initial kinetic energy as a function of the onset We of the reflexive separation regime at head-on collisions. The dashed line represents this ratio, α_3, in the model of Hu et al. (2017). The solid line represents the same ratio plus the 100% loss of the water droplets collisions.

6.3 The existing models of head-on collisions

The head-on collision models of Planchette et al. (2017), Eq. (2.18), and Tang et al. (2012), Eq. (2.19), use a more precise approach than that of Hu et al. (2017) to consider the viscous loss. Considering the viscous loss in the dynamics of the reflexive separation is quite difficult. Therefore, both models, of Planchette et al. (2017), and Tang et al. (2012), aimed to estimate the viscous loss into sub-periods within the dynamics of the reflexive separation. Therefore, it is useful to use this approach to develop a complete model for the boundary of the reflexive separation regime. However, the model of Planchette et al. (2017) does not consider the effect of the size ratio. On the other hand, the size ratio is taken into account in the model of Tang et al. (2012). Thus, for generality, the approach of Tang et al. (2012) will be used in the next sections to develop a model that accounts for the viscous loss, size ratio and the impact parameter.

6.3.1 The model of Tang et al. (2012)

Tang et al. (2012) divided the process of the reflexive separation into three stages as schematically illustrated in Figure 6.6. The first stage is the compression period from the instant of collisions until the maximum deformation. The second stage is from the start of contraction of the rim until the start of the jet bursting in instant 4 in stage 2. The third sub-period is from the instant of jets bursting until the maximum elongation of the cylindrical droplet.

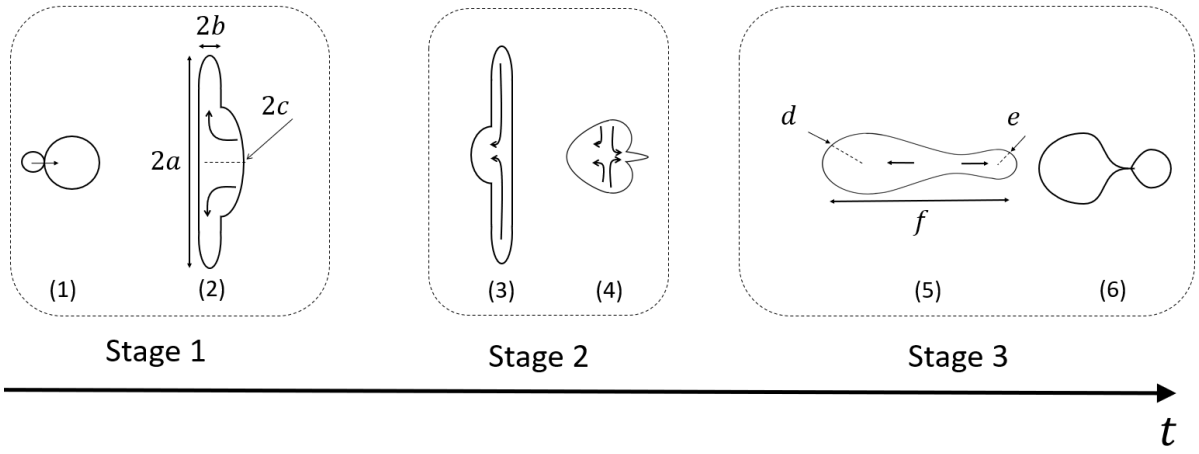

Figure 6.6 A schematic shows the stages of the dynamics of the reflexive separation of unequal-size droplet collisions.

Tang et al. (2012) applied energy conservation on the process, described in Figure 6.6, which is given by

$$E_{K,ini} + E_{\sigma,ini} = E_{\mu,1} + E_{\mu,2} + E_{\mu,3} + E_{k,fin} + E_{\sigma,fin} \tag{6.19}$$

Where, $E_{K,ini}$ is given by Eq. (6.20) and $E_{k,fin}$ is the kinetic energy of the droplets at the separation, in instant 6 in Figure 6.6, which is assumed to equal to 0. This due to the observation that at the instant of the reflexive separation regime the separated droplets have negligible velocity. $E_{\mu,1}, E_{\mu,2}$ and $E_{\mu,3}$ are the viscous loss of the stages in Figure 6.6. $E_{\sigma,ini}$ and $E_{\sigma_{fin}}$ are the initial and the final surface energy of the droplets, respectively. The initial surface energy is given by $E_{\sigma,ini} = 4\pi\sigma(R_s^2 + R_l^2)$, while the droplets at the separation in instant 6 have some deformation and hence $E_{\sigma_{fin}} > E_{\sigma,ini}$.

$$E_{K,ini} = \frac{1}{2}\pi\left(\frac{1}{3}R_s^3\rho u_r^2 + \frac{1}{3}R_l^3\rho u_r^2\right) \tag{6.20}$$

Qian and Law (1997) reported that for equal-size droplets collisions of water and hydrocarbons $\alpha = \frac{E_{\mu,1}}{E_{K,ini}} = 0.5$ and this value is independent of the droplet viscosity. This is by using an empirical approach based on volume conservation to estimate the surface area at the maximum rimmed lamellar disc deformation with the help of the images, and hence the surface energy. Planchette et al. (2017) has applied this approach and found that for a wide range of Oh (0.02 – 0.15), the loss factor $\alpha \sim 0.65$, however, for Oh < 0.02, α is lower and for Oh > 0.15, α is higher. On the other hand, Tang et al. (2012) for collisions of unequal-size droplets of water and hydrocarbon reported that α has a weak dependence on the size ratio and its value is in the range of $\alpha \sim 0.55 \pm 0.05$. Thus, $E_{\mu,1} \sim 0.55\, E_{K,ini}$.

The viscous loss in stage 2 is due to the capillary pressure-driven flow starting from instant 2 in stage 1. Which can be estimated from the general form of the viscous dissipation in Eq. (6.21), reported by Qian and Law (1997).

$$E_{\mu,i} = \mu \int \int \frac{1}{2}\left(\frac{\partial v_i}{\partial x_j} + \frac{\partial v_j}{\partial x_i}\right)^2 \mathrm{d}t\, \mathrm{d}x^3 \tag{6.21}$$

The viscous loss in stage two is due to the flow in the rimmed lamellar disc ($E_{\mu,2'}$), in addition to the flow in the bulging portion of the droplet ($E_{\mu,2''}$) at instant 2 in Figure 6.6. Tang et al (2012) simplified Eq. (6.21) to estimate $E_{\mu,2'}$ and $E_{\mu,2''}$ in Eq. (6.22) and Eq. (6.23), respectively.

$$E_{\mu,2'} \sim \frac{1}{2}\mu \left(\frac{v_{2'}}{b}\right)^2 \left(\frac{a}{v_{2'}}\right)\left(V_{tot} - \frac{2}{3}\pi c^3\right), \tag{6.22}$$

where, V_{tot} is the total volume of the combined droplets.

$$E_{\mu,2''} \sim \frac{1}{2}\mu \left(\frac{v_{2''}}{c}\right)^2 \left(\frac{c}{v_{2''}}\right)\left(\frac{2}{3}\pi c^3\right). \tag{6.23}$$

The characteristic velocities $v_{2'}$ and $v_{2''}$ can be approximated from the capillary pressure $\frac{1}{2}\rho v_{2'}^2 = \sigma(\frac{1}{a} + \frac{1}{b})$, and $\frac{1}{2}\rho v_{2''}^2 = \frac{2\sigma}{c}$, respectively. Therefore, $E_{\mu,2} = E_{\mu,2'} + E_{\mu,2''}$ is given by

$$E_{\mu,2} \sim \frac{1}{3}\pi\mu R_s^{\frac{3}{2}}\sqrt{\frac{\sigma}{\rho}}\left(\sqrt{2}\frac{\tilde{a}^{0.5}}{\tilde{b}^2}\sqrt{1+\frac{\tilde{a}}{\tilde{b}}}\left[2\left(1+\frac{1}{\Delta^3}\right)-\tilde{c}^3\right]+2\tilde{c}^{\frac{3}{2}}\right), \quad (6.24)$$

where, $\tilde{a}=\frac{a}{R_s}, \tilde{b}=\frac{b}{R_s}\ and\ \tilde{c}=\frac{c}{R_S}$.

In the same way, Tang et al. (2012) derives $E_{\mu,3}$ using the geometry in instant 5 in stage 3, in Figure 6.6. The characteristic flows in instant 5 are driven by the curvatures at the ends, which are given by $v_{3'}=2\sqrt{\frac{\sigma}{\rho d}}$ and $v_{3''}=2\sqrt{\frac{\sigma}{\rho e}}$. The characteristic flow lengths of these two flows depend on the size ratio and given by $\frac{f}{v_{3'}(1+\Delta)}$ and $\frac{\Delta f}{v_{3''}(1+\Delta)}$. Therefore, $E_{\mu,3}=\ E_{\mu,3'}+E_{\mu,3''}$, which is given by Eq. (6.25).

$$E_{\mu,3} \sim \frac{4\pi\mu\tilde{f}R_s^{\frac{3}{2}}}{3\left(1+\frac{1}{\Delta}\right)}\sqrt{\frac{\sigma}{\rho}}\left(\frac{1}{\Delta^4\tilde{d}^{\frac{5}{2}}}+\frac{1}{\tilde{e}^{\frac{5}{2}}}\right), \quad (6.25)$$

where, $\tilde{d}=\frac{d}{R_s}, \tilde{e}=\frac{e}{R_s}\ and\ \tilde{f}=\frac{f}{R_S}$.

Plugging the viscous loss equations in the energy balance and normalizing all the energy terms by the initial surface energy, $E_{\sigma,ini}$, gives the model of Tang et al. (2012), given in Eq. (2.19) which is also rewritten here in Eq. (6.26). However, the model contains geometrical parameters, defined in Figure 6.6. These parameters were measured for a wide range of size ratios for collisions of tetradecane droplets and correlated by Tang et al (2012) in the polynomial correlations, given in table 6.2, and they were assumed to be universal.

$$We_{FC/RS}=\beta \mathrm{Oh_s}+\gamma \quad (6.26)$$

where β is a geometrical factor and γ is the residual surface energy, from the surface area difference between instant 1 and 6 in figure 6.6, and its value was found by Tang and Qian to be $\sim$ 11 and it weakly depends on the size ratio.

$$\beta = \frac{2\sqrt{2}(1+\Delta^3)}{(1-\alpha)}\left[\frac{\tilde{a}^{0.5}}{\sqrt{2}\,\tilde{b}^2}\sqrt{1+\frac{\tilde{a}}{\tilde{b}}}\left(\frac{2(1+\Delta^3)}{\Delta^3}-\tilde{c}^3\right)+\tilde{c}^{\frac{3}{2}} + \frac{2\tilde{f}^3}{(1+\Delta^3)}\left(\frac{1}{\Delta^3\tilde{d}^{\frac{5}{2}}}+\frac{\Delta}{\tilde{e}^{\frac{5}{2}}}\right)\right] \tag{6.27}$$

$$\gamma = \frac{3\left(S_f - S_o\right)(1+\Delta^3\,)}{(1-\alpha)\pi R_s^2} \sim 11 \tag{6.28}$$

Where, S_o and S_f are the initial and final surface area, respectively.

Table 6.2 Fitting coefficients of the polynomials that fits the measured geometrical parameters in the model of Tang et al (2012).

$f(\Delta) = A_o + \frac{A_1}{\Delta} + \frac{A_2}{\Delta^2}$	A_o	A_1	A_2
$\tilde{a}$	1.556	0.6032	− 0.0314
$\tilde{b}$	0.47506	−0.00508	−0.01025
$\tilde{c}$	−3.30844	4.12313	0.80968
$\tilde{d}$	−0.01747	0.91154	−0.02622
$\tilde{e}$	0.87656	0.06067	−0.04016
$\tilde{f}$	3.09374	0.95754	0.502
$\tilde{S}_f - \tilde{S}_o$	1.13341	−0.09298	0.01724

6.3.2 The performance of the model of Tang et al. (2012)

For equal-size droplets collisions, the model of Tang et al. (2012) was only validated against data generated using water and hydrocarbons droplets, where Oh < 0.04. On the other hand, the model of Planchette et al. (2017) was validated using a wider range of Oh by using glycerol droplets, and it found to perform well for Oh up to 0.1. Therefore, comparing the performance of the two models is a good test for the performance of the model of Tang et al. (2012) for Oh > 0.04.

The geometrical parameters in Table 2 were measured for 200 µm tetradecane droplets (Oh = 0.034) and assumed to be universal (Tang et al., 2012). Therefore, before comparing the model of Tang et al. (2012) against Planchette et al. (2017), it is interesting to check if these geometrical parameters hold for higher Oh. Using the HPMC data of $\Delta = 1$ presented in the previous chapters, the geometrical parameters were

measured for a wide range of Oh up to 0.08, as shown in Figure 6.7a. The measured geometrical parameters show a weak dependence on Oh, and they show good agreement with measurements of Tang et al. (2012) in table 2, except $\tilde{f}$, which is under-predicted compared to the HPMC data.

In Figure 6.8, the model of Tang et al. (2012) is plotted for identical size collisions as a function of Oh and compared for two cases: using $\tilde{f}$ of Tang et al. (2012), in Table 6.2, and using the measured $\tilde{f}$ of HPMC data. The model shows weak sensitivity towards $\tilde{f}$. In Figure 6.8, the model of Planchette et al. (2017), Eq. (2.18) is also plotted to compare with the model of Tang et al. (2012). The performances of the two models are quite comparable with slightly higher prediction of $\mathrm{We}_{\mathrm{FC/RS}}$ (by ΔWe∼5) predicted by the approach of Tang et al. (2012). Moreover, Figure 6.8 also shows data collected from the literature for the onset of the reflexive separation for different material and Oh. Given the significant scatter in the experimental data, both models give a reasonable fit across the whole Oh tested.

For collisions of unequal size droplets, the geometrical parameters were also measured for the 2% and 4% HPMC data, as shown in Figure 6.7b. The measured geometrical parameters agree with the prediction of Tang et al. (2012) except $\tilde{f}$, which is under-predicted compared to the HPMC data, similar to the case of the equal-size droplet collisions.

In addition to the validation against the data of water and the hydrocarbon in Tang et al. (2012), the performance of the model in collisions of unequal size droplets is assessed against our 2% and 4% HPMC data as well as data of unequal-size droplet collisions reported by Sommerfeld and Pasternak (2019). The model shows reasonable performance in predicting the onset of the reflexive separation regime, as shown in Figure 6.9. In addition, Figure 6.9 shows that the model still shows weak sensitivity towards the value of $\tilde{f}$ even in collisions of unequal-size droplets.

It should be noted that in Figures 6.8 and 6.9 the value of α was kept equal to 0.65. This is based on the observations in the previous chapters and the observations of Planchette et al. (2017). This shows better performance in predicting the onset of the reflexive separation of the 2% and 4% HPMC compared to the use of $\alpha = 0.55$, proposed by Tang

et al. (2012), which leads to significant under-prediction in We, as shown in Figure 5.4 in the previous chapter. Ultimately, the model of Tang et al. (2012) shows comparable performance to the model of Planchette et al. (2012) at equal-size droplet collisions and shows good performance at unequal-size droplet collisions when $\alpha = 0.65$.

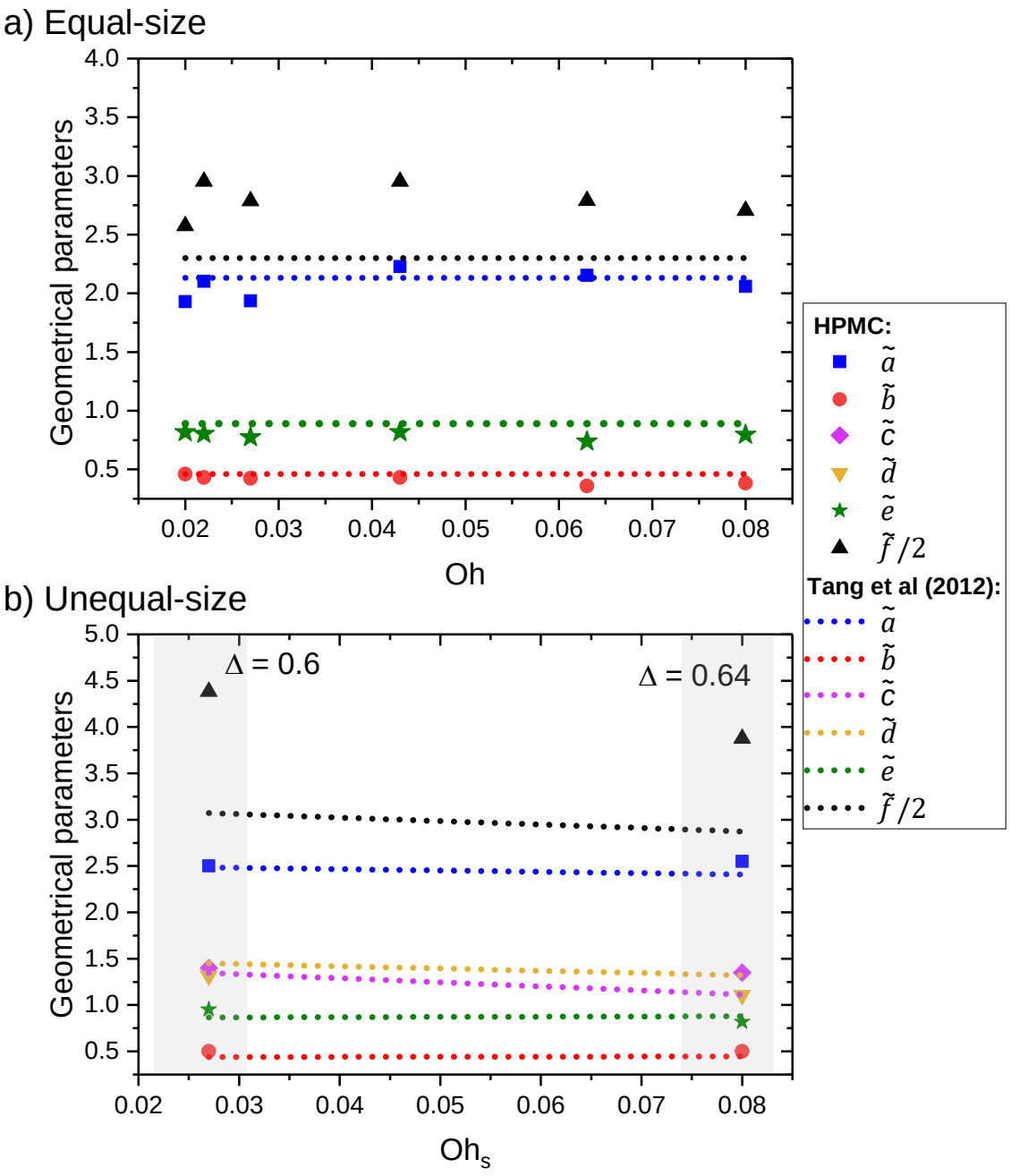

Figure 6.7 A comparison between the geometrical parameters reported by Tang et al. (2012) and measurements from the HPMC data. a) collisions of equal-size droplets; b) collisions of unequal size droplets.

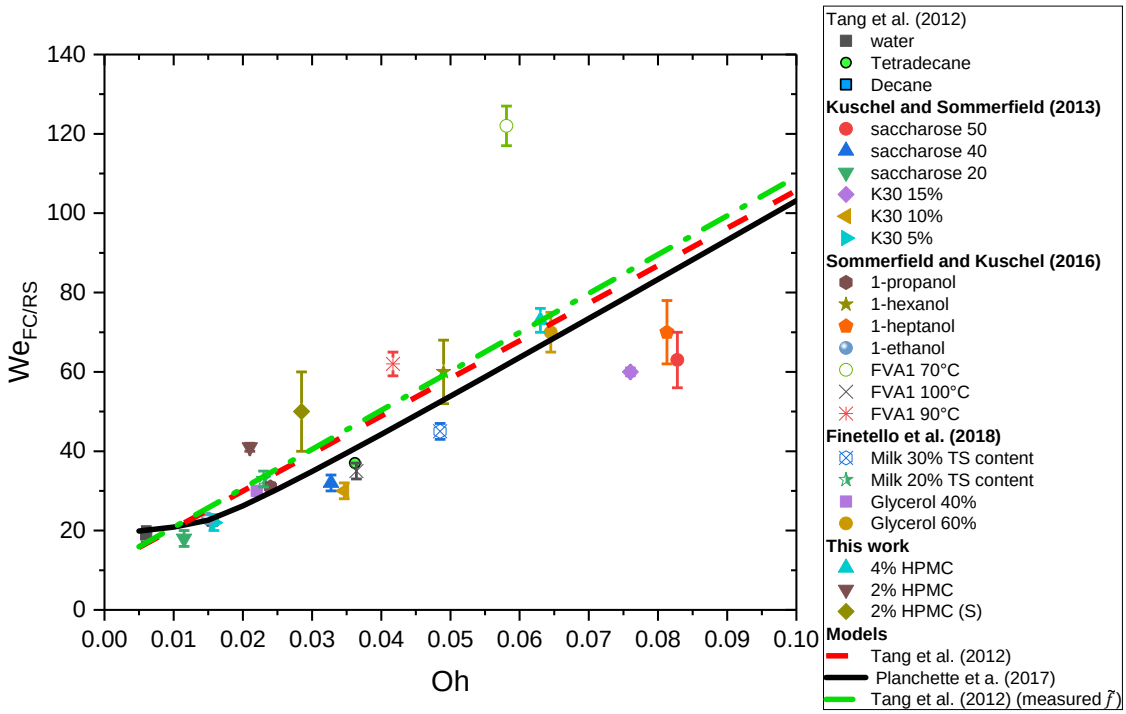

Figure 6.8 A comparison of the performance of the model of Tang et al. (2012) against the model of Planchette et al. (2017) against data points for the onset of the reflexive separation regime collected from the literature for equal-size droplet collisions. The error bars represent the uncertainty due to the gaps between the experimental data in the regime maps.

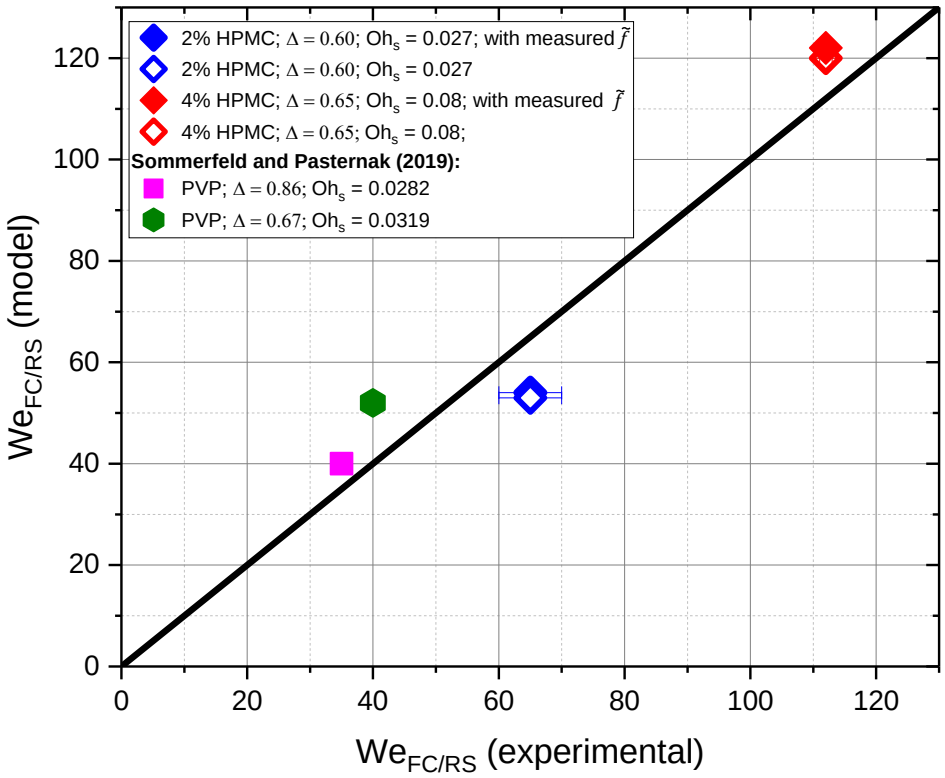

Figure 6.9 The performance of the model of Tang et al. (2012) against experimental data of unequal-size droplet collisions. The error bars represent the uncertainty due to the gaps between the experimental data in the regime maps.

6.4 Extending the model of Tang et al. (2012) to consider the impact parameter

The model of Tang et al. (2012) was derived for head-on collision and to extend it for collisions with $\mathrm{B} > 0$, it is useful to examine the shape of the reflexive separation regime boundary for different Oh and Δ, beforehand. For generality, in addition to our experimental data, a literature survey was conducted to see the trends of the boundary of the reflexive separation regime in various systems at $\mathrm{B} \geq 0$. The data of the reflexive separation that were reported in literature were reproduced in Figure 6.10. In equal-size droplet collisions, different systems in Figure 6.10a show a consistent trend that the boundary of reflexive separation regime eventually lies on $\mathrm{B} \sim 0.2$. Similarly, in Figure 6.10b for collisions of unequal-size droplets, it can be seen for different systems and Δ, the boundary lays on $\mathrm{B} \sim 0.2$. It should be noted that the reviewed boundary lines have various threshold $\mathrm{We_{FC/RS}}$ depending on Oh of the droplets, however, these lines were shifted to start at We = 19 using $\mathrm{We_C} + 19 - \mathrm{We_{FC/RS}}$ to facilitate the comparison

between them in terms of B. Any value can be used instead of 19, however, the value 19 was chosen because it is the value of the onset of the reflexive separation regime of water droplets (just as a reference value).

To consider the effect of the impact parameter, it is good to start by applying the approach of the interaction regions that were applied by Ashgriz and Poo (1990) and Hu et al. (2017) to the model of Tang et al. (2012). In this approach, at B > 0 , only the kinetic energy of the interaction regions contributes to the reflexive energy, whereas, the kinetic energy of the non-interaction regions acts as resistance to the reflexive flow, see assumption 3 in Table 6.1. Therefore, the energy balance of the model of Tang et al. (2012) becomes

$$E_{K,ini,cont} - E_{K,ini,set} + E_{\sigma,ini} = E_{\mu,1} + E_{\mu,2} + E_{\mu,3} + E_{\sigma,fin}. \quad (6.29)$$

Where, $E_{K,ini,cont}$ and $E_{K,ini,set}$ are given by Eq. (6.3) and Eq. (6.5), respectively. However, X_l and X_s in, Eq. (6.3) and Eq. (6.5), are given by the new formulas that derived in this work and given by Eq. (6.15) and Eq. (6.16), respectively. Note that, to conserve the momentum at head-on collisions in collisions of Δ < 1, X_l is normalized by its value at head-on collisions to ensure that its value equals to 1 when B = 0. This means that at head-on collisions of unequal-size collisions, although there are non-interaction regions, they do not act as stretching regions and hence the model of Tang et al. (2012) is reproduced.

Assuming that in stage 1 both $E_{K,ini,cont}$ and $E_{K,ini,set}$ are partially dissipated due to the viscous loss, thereby $E_{\mu,1}$ is given by

$$E_{\mu,1} = \alpha(E_{K,ini,cont} - E_{K,ini,set}) \quad (6.30)$$

Where α is assumed to have the same value of that at head-on collisions. For now, let us assume that $E_{\mu,2}$ and $E_{\mu,3}$ in Eq. (6.24) and Eq. (6.25) still hold for B > 0. Substituting Eq. (6.3), Eq. (6.5), Eq. (6.24), Eq. (6.25), Eq. (6.30) in Eq. (1.29) and normalizing all the energy terms by the initial surface energy, $E_{\sigma,ini} = 4\pi R^2(1 + \Delta^2)$, gives new forms of β and γ in the model of Tang et al. (2012) in which the impact parameter is considered. The newly derived β and γ are given by Eq. (6.31) and Eq. (6.32), respectively.

$$\beta = \frac{2\sqrt{2}(1+\Delta^3)^2}{(1-\alpha)\left(2\left(\Delta^3 \widetilde{X'}_l + X'_s\right) - (1+\Delta^3)\right)}\left[\frac{\tilde{a}^{0.5}}{\sqrt{2}\,\tilde{b}^2}\sqrt{1+\frac{\tilde{a}}{\tilde{b}}}\left(\frac{2(1+\Delta^3)}{\Delta^3} - \tilde{c}^3\right) + \tilde{c}^{\frac{3}{2}} + \frac{2\tilde{f}^3}{(1+\Delta^3)}\left(\frac{1}{\Delta^3 \tilde{d}^{\frac{5}{2}}} + \frac{\Delta}{\tilde{e}^{\frac{5}{2}}}\right)\right], \tag{6.31}$$

where $\widetilde{X'}_l$ is X'_l given by Eq. (6.15) after the normalization by its value at B = 0.

$$\gamma = \frac{3\left(S_f - S_o\right)(1+\Delta^3)^2}{(1-\alpha)\pi R_s^2\left(2(\Delta^3 X'_l + X'_s) - (1+\Delta^3)\right)} \sim \frac{(1+\Delta^3)11}{\left(2\left(\Delta^3 \widetilde{X'}_l + X'_s\right) - (1+\Delta^3)\right)} \tag{6.32}$$

To assess the performance of the new model in predicting the effect of B, it is compared with the experimental data that is presented in Figure 6.10. This is by applying the model for a wide range of Oh, from 0.01 to 0.1, and normalized to start at We = 19 at head-on collisions, as shown in Figure 6.11a for equal-size droplet collisions and in Figure 6.11b for unequal-size droplet collisions. In the unequal-size droplet collisions in Figure 6.11b, the model is applied for size ratio of 0.6, as the difference in the size ratio in Figure 6.11b do not show significant effect on the role of B. Generally, the model shows over-prediction in terms of B in both equal-size and unequal size collisions, which means that there are crucial underlying physics, relevant to the role of B, that have not been considered in the model of Ashgriz and Poo (1990) and will be explored in the next section. Not that the good performance of the model of Ashgriz and Poo in predicting the effect of B, as shown in Figure 6.11, is due to the unphysical values of X_{ps} and X_{pl} which give significant under-predictions of the interaction regions compared to the spherical cap geometry, as shown in Figure 6.4 (b and c).

a) Equal-size

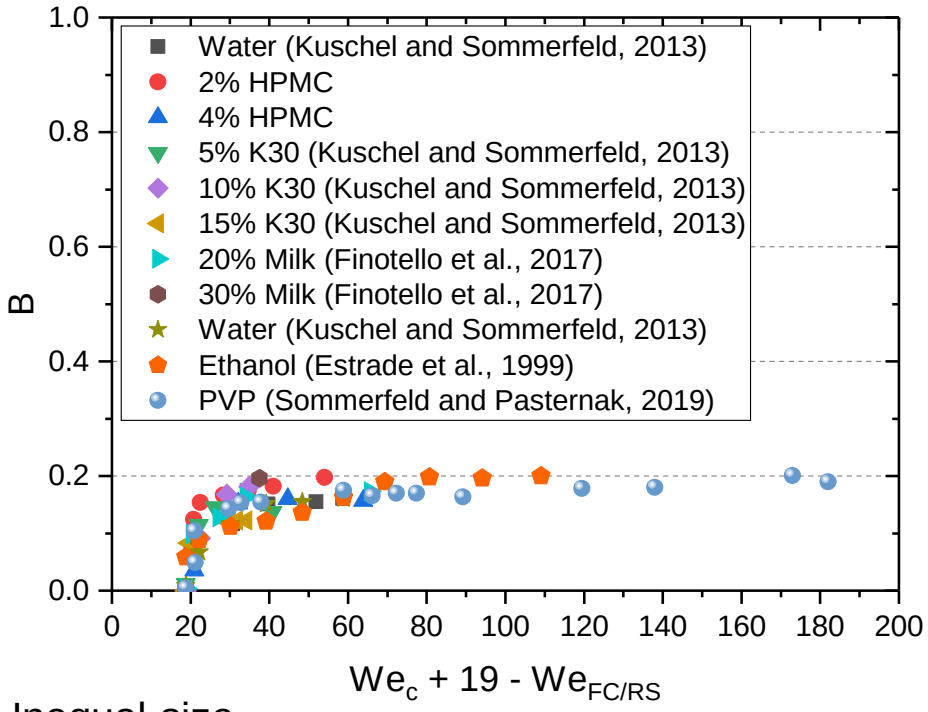

b) Unequal-size

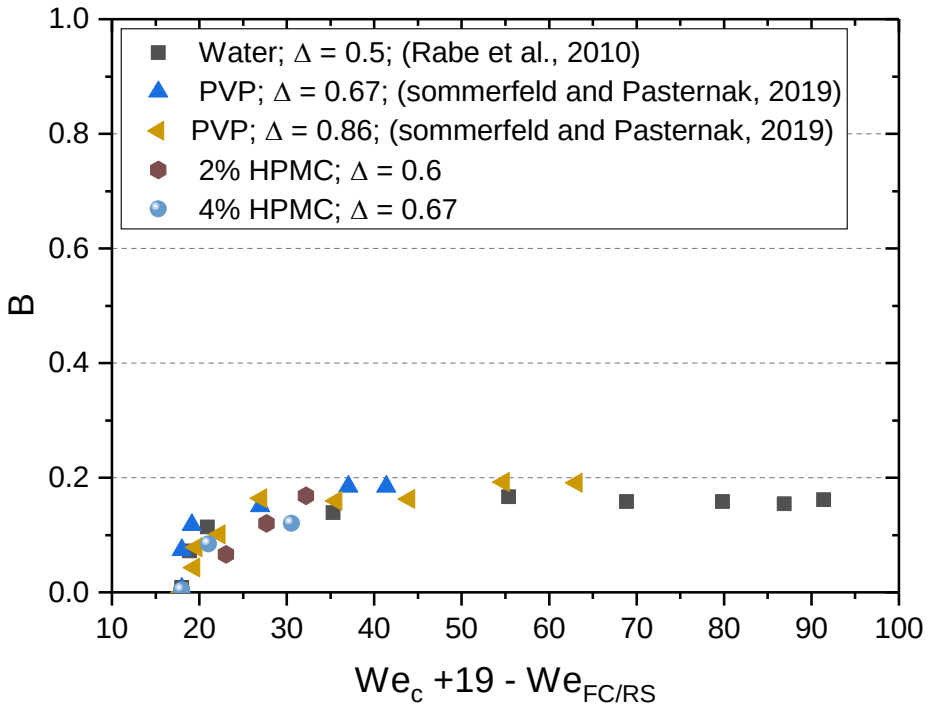

Figure 6.10 A literature survey of data showing the trend of the boundary of the reflexive separation regime. a) for equal-size collisions; b) for unequal-size collisions.

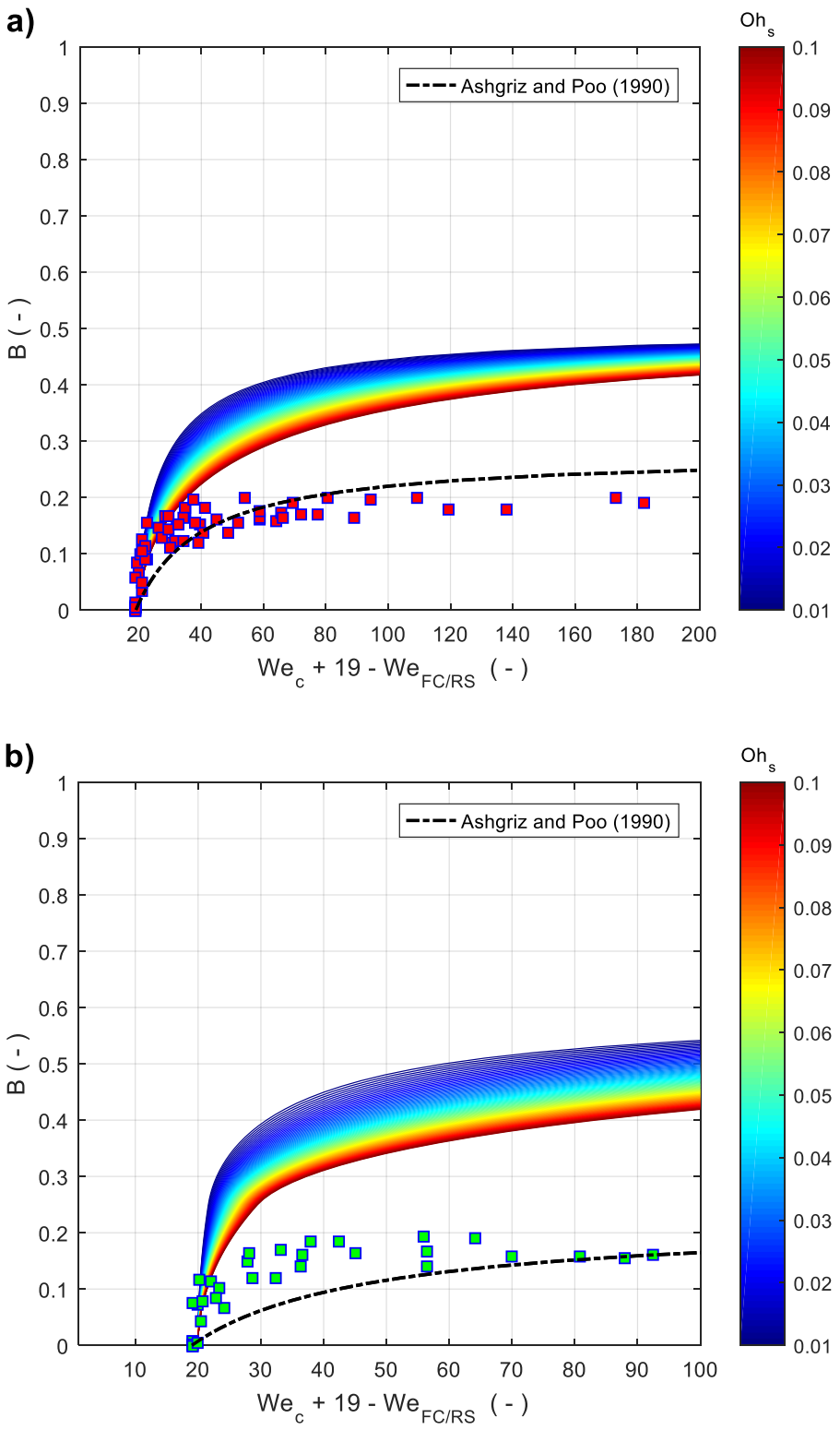

Figure 6.11 The performance of the extended model of Tang et al. (2012) using the interaction regions' assumptions. a) for equal-size collisions; b) unequal-size collisions and the model solved for Δ=0.6. The dashed line is the model of Ashgriz and Poo (1990). The data points are those detailed in Figure 6.10b.

6.4.1 Asymmetrical rim shrinking

As the approach of considering B by Ashgriz and Poo (1990) misses crucial underlying physics, this section will search of the mechanism that shape the boundary of the reflexive separation regime.

Applying the assumption of the interaction regions to consider the effect of B means that, for given droplets and B, if $(1-\alpha)(E_{K,ini,cont}-E_{K,ini,set})$ is equal to a critical value, reflexive separation occurs. This critical value is evaluated at head-on collisions and equal to $(1-\alpha)E_{K,ini}$. Therefore, this assumption suggests that the suppression of the reflexive separation regime by increasing B is due to the decrease in the kinetic energy of the interaction regions that leads to the formation of the rimmed lamellar disc geometry and the increase in the stretching energy that has opposite flow direction to the reflexive flow (Ashgriz and Poo, 1990). In reality, the stretching energy is not seen to affect the reflexive flow in the images in Figure 6.12. This because the rimmed lamellar disc at $\mathrm{B}=0.17$ case becomes very thin similar to the case of the head-on collision and stays for a while, which reveals that the stretching energy vanishes before any reflexive flow. However, during this time, rimmed lamellar disc rotation is seen, as shown by the change of the angle with time in the case of $\mathrm{B}=0.17$ in Figure 6.12. This is attributed to the energy of the non-interaction regions. Thus, the stretching energy, suggested by Ashgriz and Poo (1990), acts as rotational energy rather than stretching energy. It can be assumed that the rotational energy has a negligible effect on the dynamics of the reflexive flow and hence it can be ignored in the energy balance of the model.

If the stretching energy is removed from the derivation of the model, the model shows less response to B as it shows even more over-prediction in terms of B, as shown in Figure 6.13. This because now it is only the reduction in the interaction regions and thereby the kinetic energy that contributes to the formation of the rimmed lamellar disc that shapes the boundary of the reflexive separation regime. Thus, there must be more underlying physics in addition to the decrease in the interaction regions that need to be considered. The following searches for the underlying physics that shape the boundary of the reflexive separation regime.

By tracking the dynamics of the images in Figure 6.12, it can be seen that the dynamics of both cases are comparable up to the maximum deformation at $t = 0.23$ ms in the case of head-on collisions and $t = 0.26$ ms for $\mathrm{B} = 0.17$. Even the diameters of the rimmed lamellar discs are comparable $\backsim(2.4 \pm 0.2)$. However, differences are seen after the start of the rimmed lamellar disc shrinkage. Thus, side view high-speed imaging was performed for identical size collisions, to observe the dynamics in a 3D view and hence obtaining a better understanding of what happens.

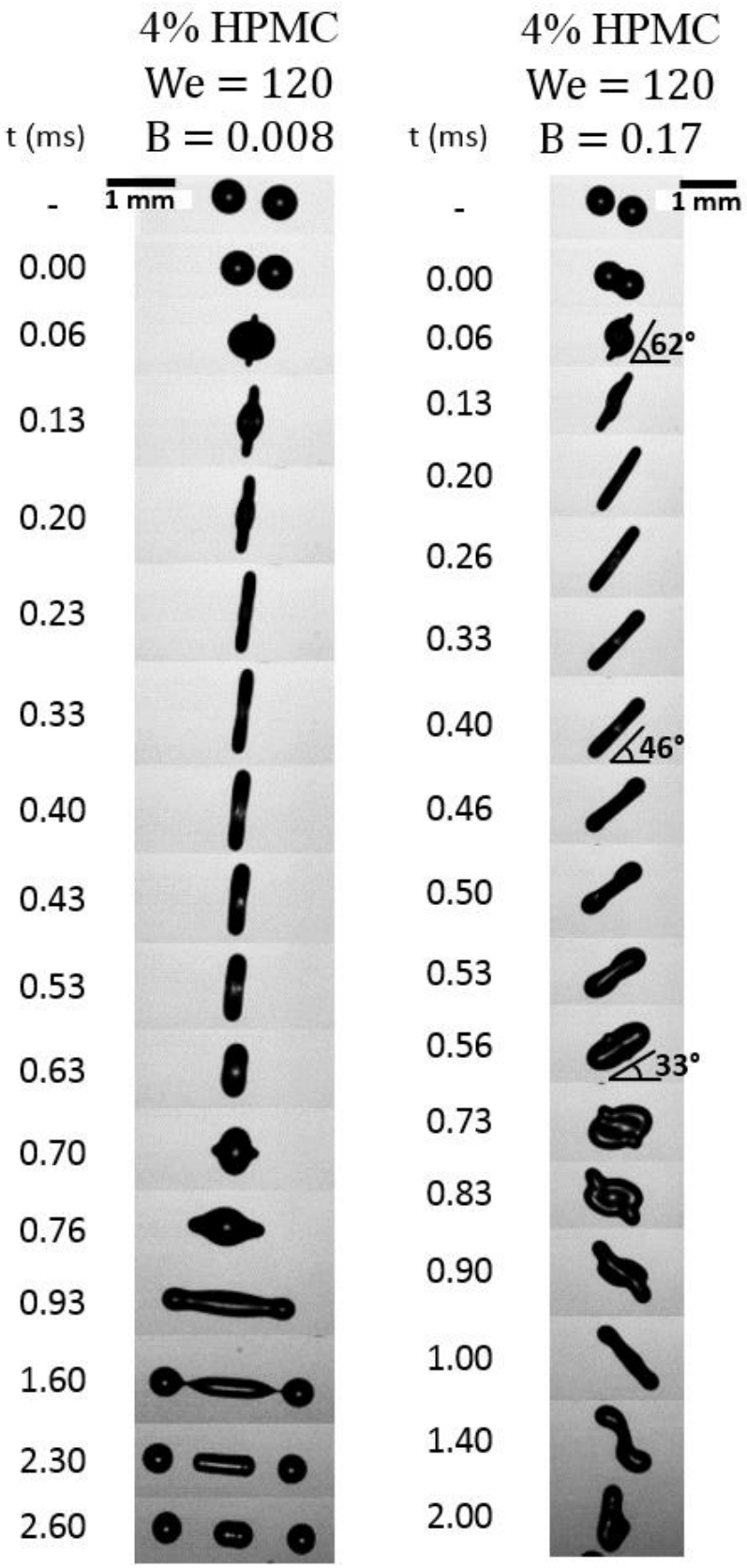

Figure 6.12 A front view comparison for the dynamics of the reflexive separation between head-on and off-centre reflexive separation.

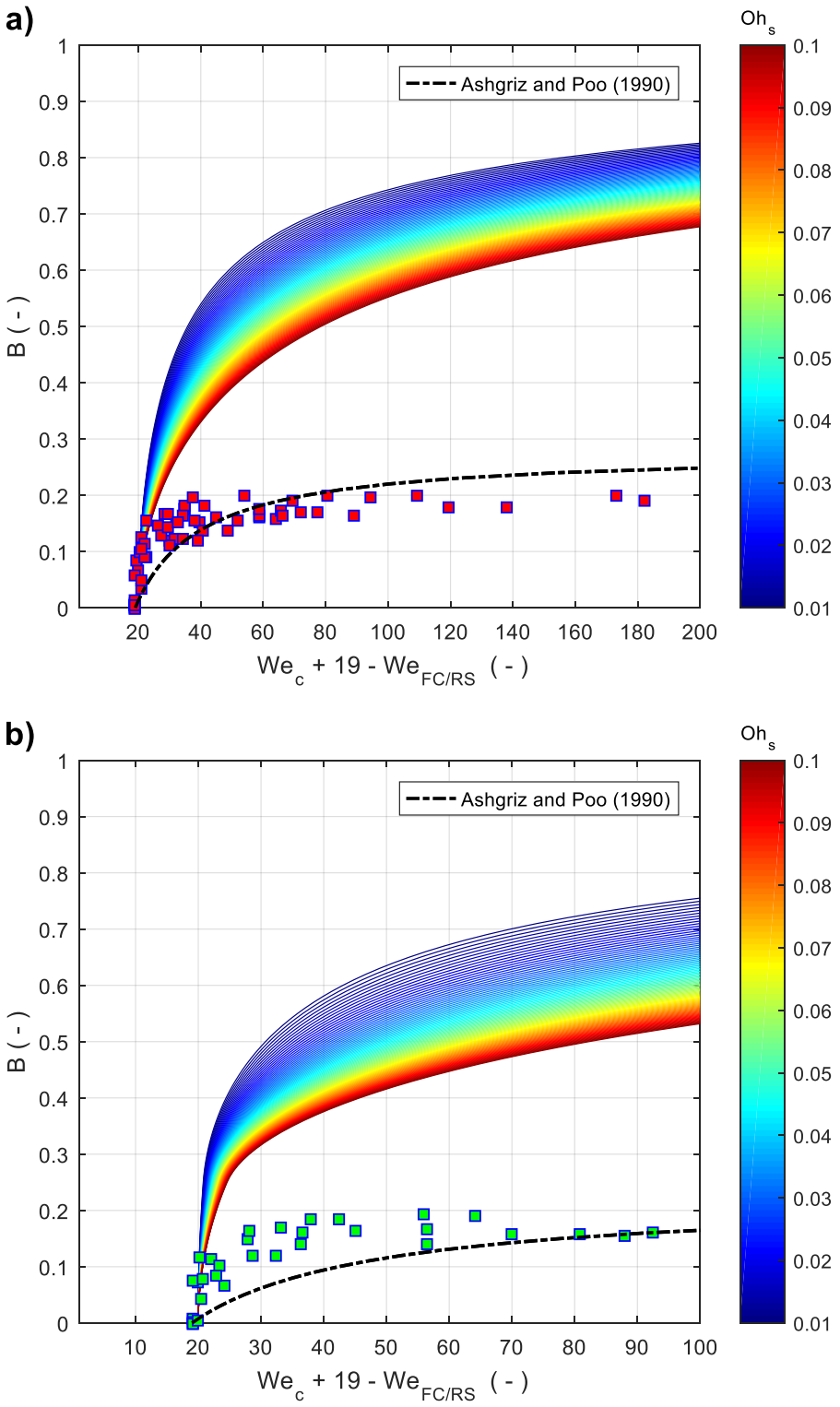

Figure 6.13 The performance of the extended model of Tang et al. (2012) by neglecting the stretching energy. a) for equal-size collisions; b) unequal-size collisions and the model solved for Δ=0.6

Figure 6.14 shows the side view of the cases in Figure 6.12. It can be seen that in the head-on collision case the colliding droplets form a circular rimmed lamellar disc that

consists of a lamella that is bounded by a uniform toroidal rim at the edge. This toroidal rim expands outwardly until it reaches its maximum at $t = 0.33$ ms. Once the rim reaches its maximum expansion, it retracts inwardly towards the centre of the lamella. This retraction is associated with a continuous increase in the rim thickness. At a given point, see $t = 0.63$ ms, the inner edges of the rim that bounds the lamella meet at the centre of the lamella. This leads to the reflexive flow, which is like jets burst in both sides, as shown in the head-on collision case in Figure 6.12 at $t = 0.70$ ms.

In off-centre collisions, although the colliding droplets form a thin disc, as shown in Figure 6.14 (e.g. see at $t = 0.20$ ms), the side view in Figure 6.14 shows that the formed rim is not uniform in comparison to the case of the head-on collision. The rim is not quite circular and it is thicker at the top and the bottom edges than the left and the right edges as can be seen at $t = 0.13$ ms in Figure 6.14. The non-uniform rim thickness makes the thinner edges retract inwardly faster than the thicker. This is because the retraction is driven by the capillary pressure of the rim which is inversely proportional to its thickness. The difference in the rim's edge retraction speeds causes the rim to take an elliptical shape rather than circular, as can be seen in the case of $\mathrm{B} = 0.17$ in Figure 6.14 at $t = 0.40$ ms. Consequently, the left and the right edges of the rim meet at the centre of the lamella before the top and the bottom edges, see $t = 0.53$ ms. This leads to the formation of attached droplets at the top and the bottom of the rim edges. However, the meeting of the left and the right edges of the rim induces jets in the orthogonal direction to the rim's retraction direction. These jets stretch the top and the bottom globules of the rim leading to form a butterfly shape in the front view, see $t = 0.73$ ms in Figure 6.12. The partial contribution of the rim in forming the jets and the contribution of the later in the stretching of the globules makes the jets in the off-centre collisions have less momentum than those of the head-on collisions. The stretched globules eventually retract towards each other. However, they have some offset in the way they face each other due to the initial collisions offset, see $t = 0.90$ ms in Figure 6.12, which leads to curvature in the jets upon the retraction, see $t = 1.40$ ms in Figure 6.12. This breaks the symmetry of the cylinder and the jets collapse instead of a successful separation.

Comparable dynamics to that of the equal-size collisions are seen in unequal-size droplet collisions at B > 0, as shown in Figure 6.15 in the case of B = 0.17 at $t = 0.70$ where the stretching of the globules by the single jet makes a stingray shape with a bulge on one of the wings. Consequently, the curvature in the cylinder also can be seen at $t = 1.03$ ms.

6.4.2 Considering the effect of the symmetry brakeage dynamics in the model

Based on the above, it is not valid to only assume that the reflexive separation occurs regardless of B value, once a certain value of kinetic energy is available, which is ensured via X'_l and X'_s. In addition to the reduction in the kinetic energy due to the reduction in the interaction regions, the effects of the asymmetrical shrinking of the rim need to be considered as well. However, explicitly considering such dynamics in the model is quite complicated. Therefore, for simplicity, the effects of the asymmetrical shrinking of the rim can be empirically considered.

As the asymmetrical retraction of the rim, after its maximum expansion, suppresses the process of the reflexive separation, more viscous loss can be introduced during this stage. This by introducing a weighting factor to $E_{\mu,2}$, named the asymmetrical shrinking factor (S_b). From observing the trends of the model without this factor in Figure 6.13, it can be seen that in both cases (i.e. the equal-size and unequal-size collisions) the model deviates from the experimental points at $\mathrm{B} \sim 0.15$ and this division increases exponentially with We. Thus, S_b needs to be a function of B through a power law.

A good qualitative fitting of the model to the experimental data can be achieved through the power law in Eq. (6.33), as shown in Figure 6.16. lines of different Oh collapse on each other and this power is assumed to be universal. The new model has the same form of Eq. (6.26) but with new β and γ which are given by Eq. (6.34) and Eq. (6.35), respectively.

$$S_b = 1 + 10^{10} B^{12.5} \tag{6.33}$$

$$\beta = \frac{2\sqrt{2}(1+\Delta^3)^2}{(1-\alpha)\left(\Delta^3 \widetilde{X'}_l + X'_s\right)}\left[S_b\left(\frac{\tilde{a}^{0.5}}{\sqrt{2}\,\tilde{b}^2}\sqrt{1+\frac{\tilde{a}}{\tilde{b}}}\left(\frac{2(1+\Delta^3)}{\Delta^3} - \tilde{c}^3\right) + \tilde{c}^{\frac{3}{2}}\right) + \frac{2\tilde{f}^3}{(1+\Delta^3)}\left(\frac{1}{\Delta^3 \tilde{d}^{\frac{5}{2}}} + \frac{\Delta}{\tilde{e}^{\frac{5}{2}}}\right)\right], \tag{6.34}$$

$$\gamma = \frac{3\left(S_f - S_o\right)(1+\Delta^3)^2}{(1-\alpha)\pi R_s^2\left(\Delta^3 \widetilde{X'}_l + X'_s\right)} \sim 11\frac{(1+\Delta^3)}{\left(\Delta^3 \widetilde{X'}_l + X'_s\right)}. \tag{6.35}$$

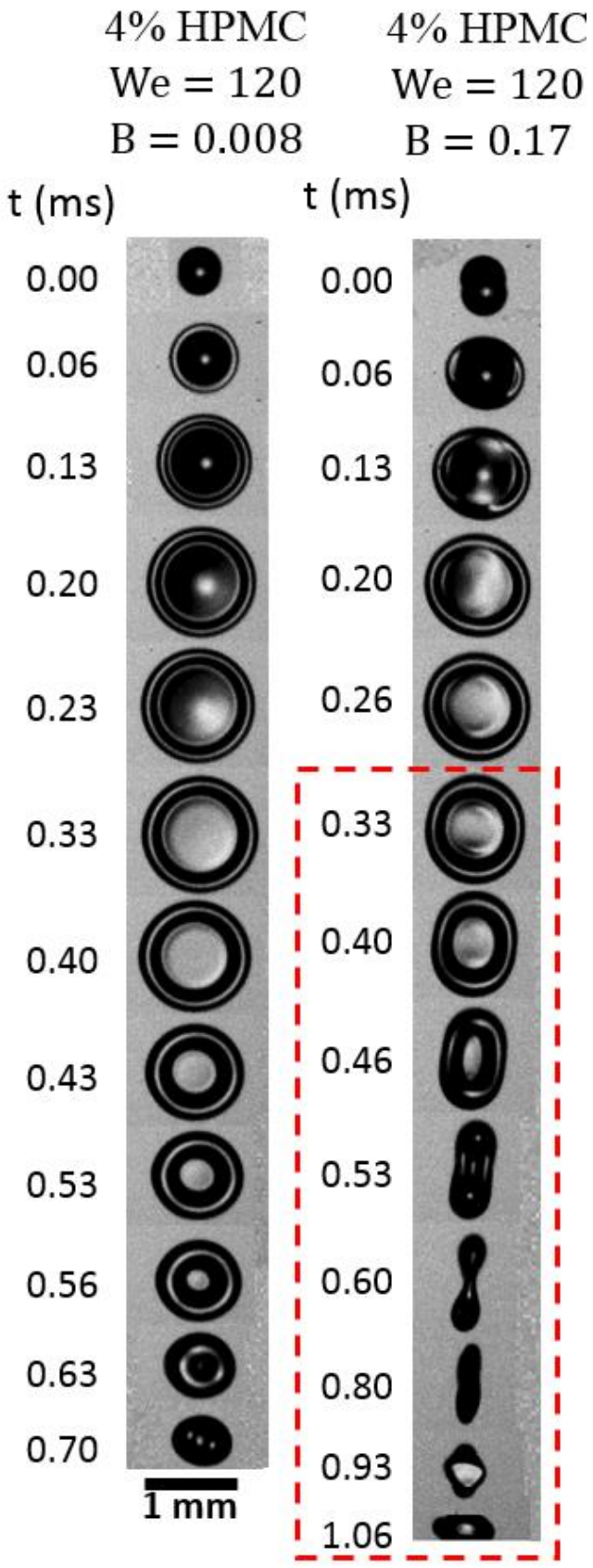

Figure 6.14 A side view showing the dynamics' differences between head-on and off-centre reflexive separation. The asymmetrical rim shrinking is surrounded by red.

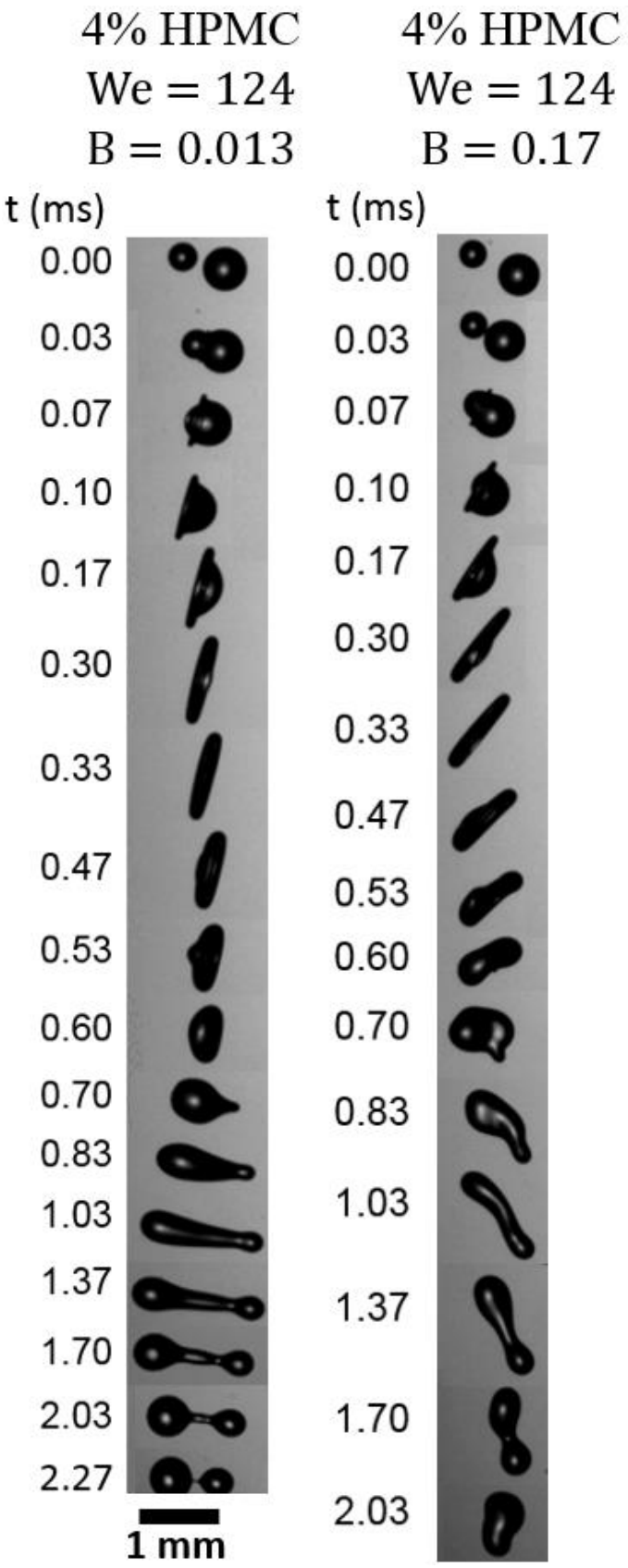

Figure 6.15 The dynamic difference between head-on and off-centre reflexive separation for Δ = 0.6.

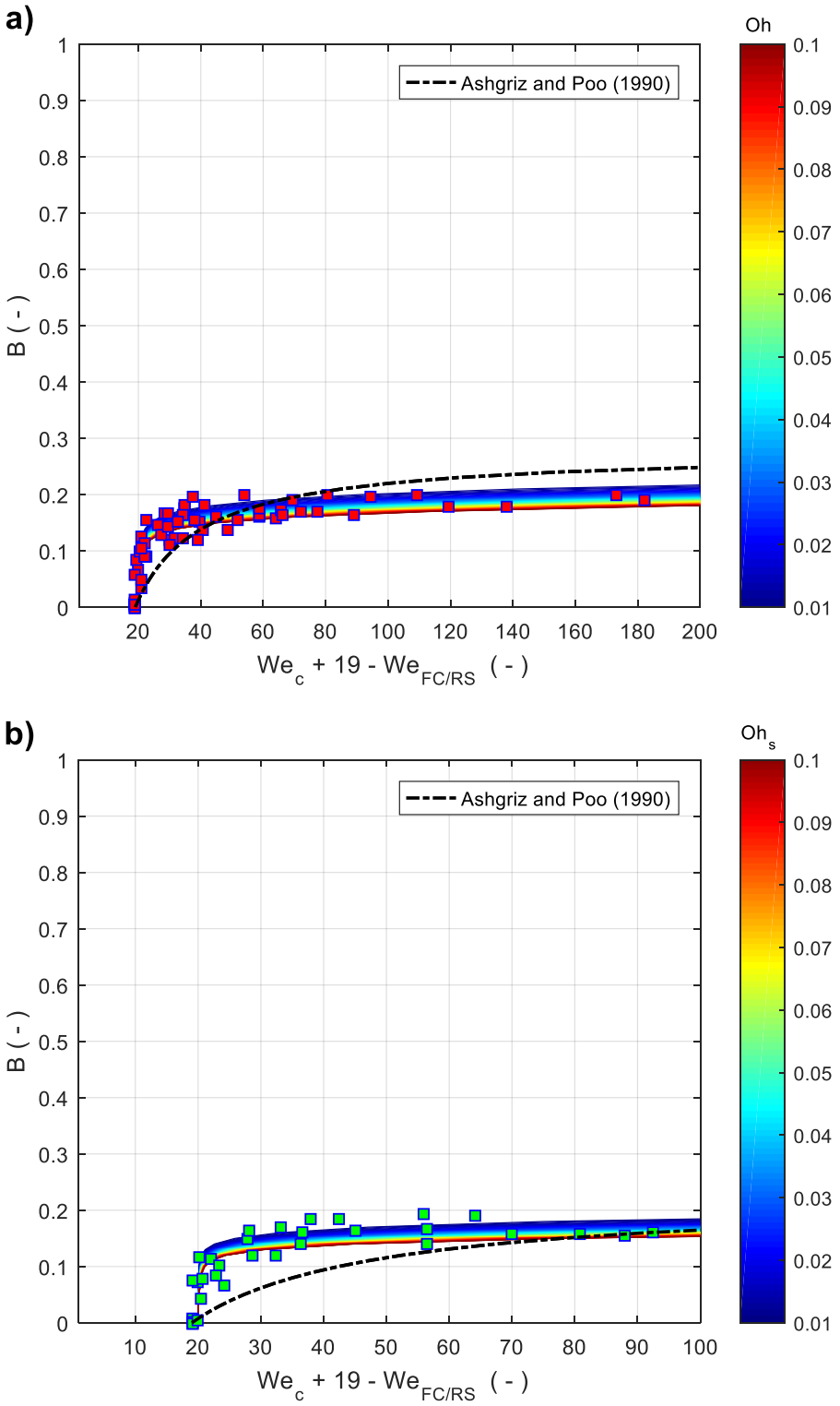

Figure 6.16 The performance of the extended model of Tang et al. (2012) with the asymmetrical shrinking factor. a) equal-size collisions; b) unequal-size collisions and the model applied for Δ=0.6.

6.5 Conclusion

Considering the effect of the impact parameter in the modelling of the reflexive separation regime has received limited attention in the literature. The existing models which consider the effect of the size ratio and B are the inviscid model of Ashgriz and Poo (1990) and the model of Hu et al. (2017), which is a modified version of the former by considering the viscous loss. However, it was found that these models having issues in the definition of the effects of B and the viscous loss.

In both models, it is believed that the trend of the boundary of the reflexive separation is shaped by the reduction in the interaction regions due to the increase of B. This reduction reduces the kinetic energy that contributes to the formation of the rimmed lamellar disc and hence less surface energy will be stored at the maximum deformation of the disc, which afterwards converts into reflexive flow. Moreover, the kinetic energy of the regions of the non-interaction acts as suppressing energy against the reflexive flow. To evaluate the interaction regions, Ashgriz and Poo (1990) used a prolate geometry to represent the interaction region, while Hu et al. (2017) used a spherical cap geometry. However, it was found that invalid formulas were used to capture both of these geometries.

In regard of considering the viscous loss, Hu et al. (2017) apply an incorrect approach to consider the effect of the viscous loss by using a single fitting parameter that represents the ratio of the total viscous loss to the kinetic energy. This is because this ratio does not scale with viscosity, as it is ∼100% at the instant of the reflexive separation, and the seen scaling trend is due to the use of the empirical criteria of Ashgriz and Poo (1990), which includes 100% loss of the kinetic energy of water droplet collisions at the onset of the reflexive separation regime.

The viscous loss is considered in more details in the model of Tang et al. (2012). However, the model only considers head-on collisions. Therefore, it has been extended to account for the effect of B. This was done by deriving the correct spherical cap interaction regions formulas and looking into the dynamics in 3D imaging to describe the right mechanism that derives the trend of the boundary with B.

Observing the front view of the dynamics shows that at off-centre collisions the stretching energy does not have a direct effect at the reflexive flow. This is because the droplets still make a thin-rimmed lamellar disc at the maximum deformation and the geometry of that disc stays still for few microseconds, which means the flow of the non-interaction regions vanishes before the reflexive flow. However, the effect of the non-interaction regions was seen as rotational energy as the rotation of the disc was observed and hence it can be ignored in the model.

On the other hand, the side view shows that the off-centre collisions produce a non-uniform rim thickness at the maximum deformation of the disc compared to the head-on collisions where a uniform rim was seen. This results in asymmetric disc retraction as the thinner parts of the rim retract faster than the thicker parts, which, consequently, leads to weaker reflexive flow, than that of the head-on collisions. This is believed to contribute heavily in shaping the boundary of the reflexive separation regime. Therefore, the effect of the asymmetrical shrinking of the rim was empirically introduced to the model as an extra viscous loss during the stage of the disc retraction through a power low as a function of B. This power law was adapted to fit the model to a wide range of experimental data generated in this work in addition to data reproduced from the literature.

Ultimately, this chapter highlights some errors in the existing models and shed light on a new understanding of the effects of the impact parameter on the dynamics of the reflexive separation. Consequently, a new universal model to fit the boundary of the reflexive separation regime was developed that has a better insight into the underlying physics.

Chapter 7: A new model for the bouncing regime boundary

In the previous chapter, we started the modelling part of this thesis where the boundary of the reflexive separation regime was discussed in great details and a new model was suggested. This chapter represents the last part of the work conducted in this thesis, in which, we continue our modelling work by considering the modelling of the bouncing regime boundary.

7.1 Introduction

In chapter 2, we highlighted that the modelling of the lower boundary of the bouncing regime has received less attention in comparison with the modelling of the other boundaries. Sommerfeld and Kuschel (2016); Kuschel and Sommerfeld (2013); Sommerfeld and Lain (2017) reported that the model of Estrade et al. (1999) can reasonably predict the lower boundary of the bouncing regime above the triple point by adapting the shape factor to let the curve fit the experimental data. However, the model fails to predict the boundaries below the triple point. The only attempt to modify this model was by Hu et al. (2017) who discussed the considered kinetic energy and added a viscous loss term. However, the performance of this model was only validated against simulation data of collisions of equal-size alumina droplets.

This chapter will start with a short background about the bouncing process to help in understanding the assumptions of the models. The existing models will be derived, afterward, to highlight the made assumptions. Then, the performance of these models will be assessed against experimental data and the neglected physics that undermine the performance of the models will be defined. Finally, we propose a modified model to fit the boundary of the bouncing regime.

7.2 Theory of bouncing

In this section, the theory of bouncing will be explored based on what has been reported in the previous studies of binary droplets collisions. The theory provides a simple background, about the bouncing phenomenon of binary droplets collisions, which helps

to understand the logic behind the assumptions of bouncing modelling that will be explained in sections 7.3 and 7.4.

The phenomenon of droplet bouncing has been widely studied experimentally and numerically. Bouncing occurs at a critical impact kinetic energy range, above and below which merging occurs (Qian and Law, 1997; Tang et al., 2012). This is widely attributed to the presence of an air layer between the two colliding droplets (Orme, 1997). At low impact velocity, the air has sufficient time to be discharged. However, if the velocity is increased the air will be trapped between the two droplets and hence the droplets deform. A flattened interface will be formed between the two droplets, which causes pressure to build up in the air layer that prevents droplets from merging. This leads to consumption of the impact kinetic energy by the deformation of the droplets, as it will be converted into surface energy and internal flow that relaxes later by the effect of the viscous dissipation. Once the impact kinetic energy vanished, bouncing occurs by the action of the surface tension which tends to recover the spherical shape to minimize the surface energy. Further increasing the impact velocity forces the air layer to be discharged and rupture the interface and therefore merging with large deformation would occur (fast coalescence).

Apart from the impact velocity, the bouncing regime was found to depend on the material of the droplets and the surrounding gas. For example, at atmospheric pressure hydrocarbon droplets show bouncing at the entire range of the impact parameter, whilst water shows bouncing only at high values of impact parameter. In addition, milk droplets show no bouncing at the entire range of impact parameter (Finotello et al., 2018). The merging of two droplets was attributed to van der Waals forces (Zhang and Law, 2011; Pan et al., 2008). However, the thickness of the air layer between the colliding droplets should be small enough for the van der Walls forces to be effective. Therefore, the difference in the bouncing observation could be more related to the difference in molecular dynamics at the surface of the droplets of different liquids. In addition, changing the conditions of the surrounding gas shows a noticeable effect on the collision outcome (Krishnan and Loth, 2015; Qian and Law, 1997). Increasing the gas pressure, density or molecular weight would promote the bouncing regime. However, the presence of the droplet's liquid vapour in the surrounding gas would promote the

coalescence regime (Qian and Law, 1997). All that makes it difficult to define a bouncing criterion that allows distinguishing between bouncing and coalescence based on the impact details such as We and B.

7.3 The existing models of bouncing

The model of Estrade et al. (1999) for the bouncing regime boundary is based on an energy criterion. It states that bouncing occurs if the component of kinetic energy that contributes to the deformation of the droplets is less than the increase in surface energy required to reach the limit of maximum deformation. However, if this kinetic energy exceeds the maximum deformation limit, merging is assumed to occur. A number of assumptions are made to derive this criterion and the subsequent equation for the boundary, these are detailed in Table 7.1.

Table 7.1. Assumptions that Estrade et al. (1999) made to develop the bouncing model.

Assumptions	Justifications
1- No viscous loss is considered; hence all the dissipated kinetic energy is converted into surface energy.	The model was derived for inviscid droplet collisions.
2- No work against air.	No noticeable delay time was noticed before the threshold of the deformation.
3- Shape factor is fixed for the entire impact parameter range.	The regime maps of inviscid droplets exhibit bouncing boundary that falls in a narrow range of high impact parameter values.
4- The deformation is caused by the kinetic energy of the interaction region only (see Figure 7.1).	The non-interacted regions have less deformation.
5- The rotational energy at the point of maximum deformation is equal to the initial energy of the non-interacting portion of the droplets, *i.e.* $E_{C_e} = E_{rot}$.	Rotational movement at the instant of the collision was noticed.

Applying the assumptions 1 and 2 in Table 6.1 an energy balance can be written between the system energy just prior to the collision and at the point of maximum deformation,

$$E_{C_e} + E_{K,ini,cont} + E_{\sigma,ini} = E_{\sigma,fin} + E_{rot}, \tag{7.1}$$

where E_{C_e} is the part of the droplet kinetic energy that does not contribute to the deformation, $E_{K,ini,cont}$ is the kinetic energy that contributes to the deformation, $E_{\sigma,ini}$ is the surface energy of the droplets before the collision, $E_{\sigma,fin}$ is the surface energy of the droplets at the maximum deformation, and E_{rot} is the rotational kinetic energy.

Applying assumption 4, the kinetic energy that contributes to the deformation is that of the interacting volumes, shown in Figure 7.1, given by

$$E_{K,ini,cont} = \frac{1}{2}\rho V_l (u_r \cos\theta)^2. \tag{7.2}$$

Where V_l is the volume of the interaction region, which is given by

$$V_l = X_l \frac{\pi d_l^3}{6} \tag{7.3}$$

Where X_l is the ratio of the interaction region volume, of the large droplet, to the total droplet volume, as given by Eq. (2.8) and re-given here by

$$X_l = \begin{cases} 1 - \frac{1}{4}(2-\tau)^2(1+\tau) & \text{for } h > \frac{d_l}{2} \\ \frac{1}{4}\tau^2(3-\tau) & \text{for } h \le \frac{d_l}{2} \end{cases} \tag{7.4}$$

Where τ is defined by

$$\tau = (1 - \mathrm{B})(1 + \Delta). \tag{7.5}$$

Where, $\Delta = d_s/d_l$ is the size ratio, and

$$h = \tfrac{1}{2}(d_l + d_s)(1 - \mathrm{B}). \tag{7.6}$$

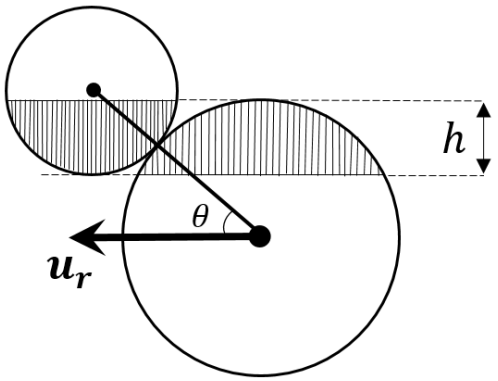

Figure 7.1 A schematic representation of the interaction regions (in grey).

The surface energy of a droplet is the product of the surface tension and the droplet surface area. Thus, the total surface energy of the droplets before the collision is given by

$$E_{\sigma,ini} = \pi\sigma(d_s^2 + d_l^2). \tag{7.7}$$

The droplets reach the maximum deformation limit just before bouncing separation, i.e. when the kinetic energy of the interaction regions, Eq. (7.2), is completely converted into surface energy (assumptions 1 and 2). Estrade et al. (1999) described the surface energy at the maximum deformation by

$$E_{\sigma,fin} = \pi\sigma d_l^2 \phi'(1 + \Delta^2). \tag{7.8}$$

Where, ϕ' is a shape factor that is given by

$$\phi' = \frac{2}{3}\left(\frac{3}{\phi^2} + 1\right)^{-\frac{2}{3}} + \frac{1}{3}\left(\frac{3}{\phi^2} + 1\right)^{\frac{1}{3}}. \tag{7.9}$$

Estrade et al. (1999) reported that in the case of collisions between unequal size droplets the shape factor can be either calculated based on the small droplets, $\phi = h_s/r_s$ or it can be based on the large droplet, $\phi = h_l/r_l$, see Figure 7.2.

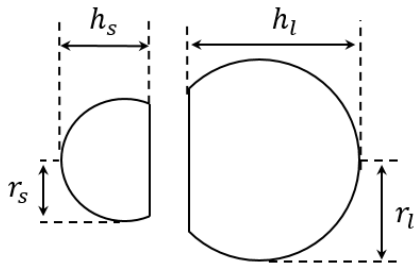

Figure 7.2 Droplet shape at the instance of maximum deformation according to Estrade et al. (1999).

Substituting Eq. (7.2), Eq. (7.7), and Eq. (7.8), in Eq. (7.1) and applying assumption 5 with rearrangement gives

$$\mathrm{We_c} = \frac{12\Delta(1+\Delta^2)(\phi'-1)}{X_l(1-\mathrm{B}^2)}, \tag{7.10}$$

which is the critical We that describe the boundary of the bouncing regime as a function of B.

Hu et al. (2017) extended the model of Estrade et al. (1999) to higher viscosity systems, by considering the viscous dissipation within the droplet E_μ. Thus, the energy balance becomes

$$E_{C_e} + E_{K,ini,cont} + E_{\sigma,ini} = E_{\sigma,fin} + E_{rot} + E_\mu. \tag{7.11}$$

The viscous dissipation was considered a fixed percentage (independent of B) of the kinetic energy that contributes to the deformation. Thus, Eq. (7.11) becomes

$$E_{C_e} + E_{K,ini,cont} + E_{\sigma,ini} = E_{\sigma,_{fin}} + E_{rot} + \alpha_2 E_{K,ini,cont} \tag{7.12}$$

Moreover, Hu et al. (2017) used a different approach in defining the kinetic energy that contributes to the deformation, as given by

$$E_{K,ini,cont} = \frac{1}{2}\rho\,(\frac{1}{6}\pi d_s^3(u_s\cos\theta)^2 + \frac{1}{6}\pi d_l^3(u_l\cos\theta)^2). \tag{7.13}$$

Where, $u_s = u_r/(1+\Delta^3)$ and $u_l = \Delta^3 u_r/(1+\Delta^3)$, at the mass-centre coordinate (Ashgriz and Poo, 1990). Importantly, Eq. (7.13) considers the entire droplet volume, instead of just the interaction regions.

Substituting Eq. (7.13), Eq. (7.7), and Eq. (7.8), in Eq. (7.12), as well as applying assumption 5, gives the model of Hu et al. (2017), which predicts the critical We of the lower boundary of the bouncing regime as a function of B:

$$\mathrm{We_c} = \frac{12(1+\Delta^3)(1+\Delta^2)(\phi'-1)}{\Delta^2(1-\alpha_2)(1-\mathrm{B}^2)}. \tag{7.14}$$

It should be noted that Estrade et al. (1999) and Hu et al. (2017) have a different definition to the kinetic energy that contributes to the deformation at head-on collisions (i.e. where both models use the entire mass of the droplets in $E_{K,ini,cont}$) Eq. (7.2) and Eq. (7.13), respectively. As Estrade et al. (1999) approach assumes one droplet is not moving while the other approaching at the relative velocity. Whereas, Hu et al. (2017) considers the movement of both droplets. This will be investigated in further details in section 7.4.2.1.1.

7.4 Results and discussion

7.4.1 HPMC regime maps

In the following sections, the modelling of the bouncing boundary will be discussed by assessing the existing models and a new model will be proposed. For simplicity, the models will be assessed against data of collisions of identical droplets of three HPMC systems, 2%, 4%, and 8%. The regime maps of these systems are shown in Figure 7.3. Once the limitation of the existing models are addressed and a new model is proposed, the model will be examined against the various data of identical and non-identical collisions provided in the previous chapters as well as against regime maps of 6% HPMC presented for the first time in this chapter.

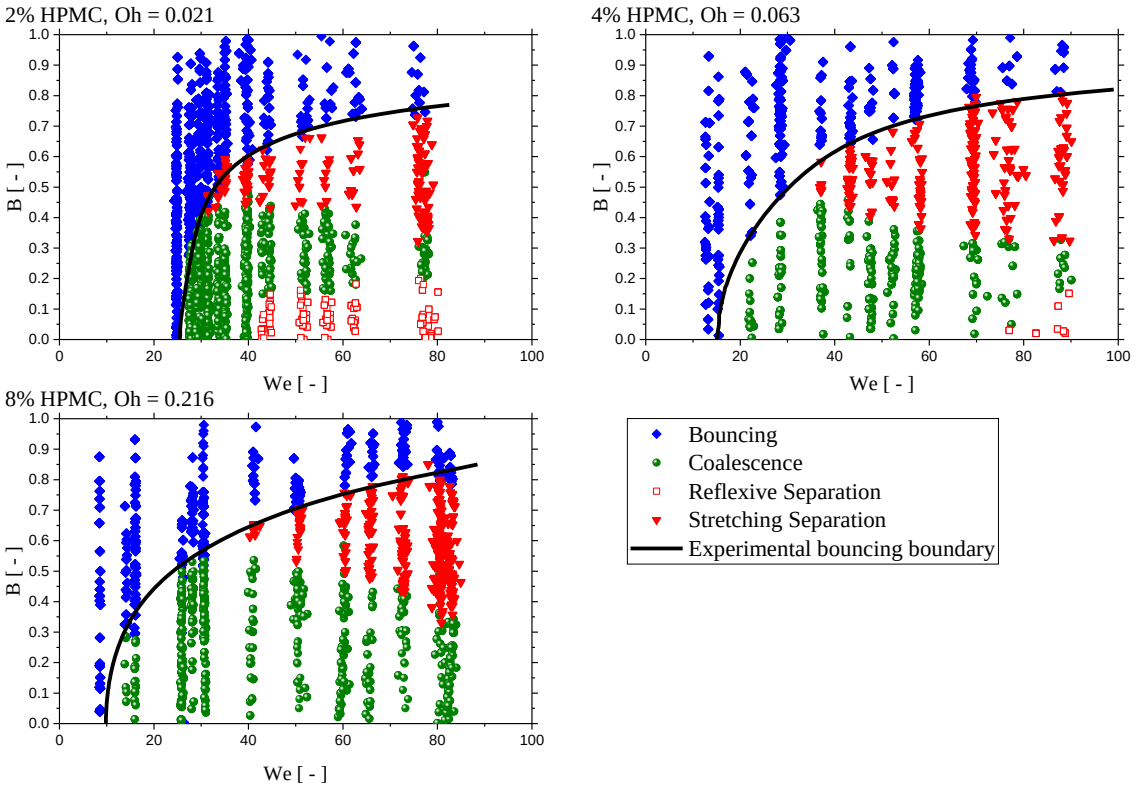

Figure 7.3 HPMC regime maps for the three concentrations 2%, 4%, and 8%.

7.4.2 Assessment of the existing bouncing models

To assess the performance of the models of Estrade et al. (1999) and Hu et al. (2017) a line defining the boundary of the bouncing regime was manually fitted to the experimental data, see Figure 7.3. This curve was digitized using Origin 2017 with a B increment of 0.01. These data points were used to optimize the shape factor ϕ' by minimizing the Mean Absolute Error (MAE):

$$\mathrm{MAE} = \frac{1}{n}\sum_{i=1}^{n} \mid \mathrm{We}_{\mathrm{model}} - \mathrm{We}_{\mathrm{exp.}} \mid_{i.} \tag{7.15}$$

The use of the MAE quantitatively characterizes the performance of the models. The viscous dissipation parameter in Hu et al. (2017) model was set as 0.5 for the three HPMC solutions. This value was used as an approximation based on the numerical simulation of Xia and Hu (2014) who reported that the viscous loss of alumina droplets that has viscosity 14 mPa.s is approximately 50% of the kinetic energy.

Figure 7.4 clearly reveals that the models of Estrade et al. (1999) and Hu et al. (2017) are not adequate to predict the boundary of bouncing regime for all range of B. However, plotting them with different viscosities would be helpful to theoretically analyse their limitations, as will be shown in the following discussion.

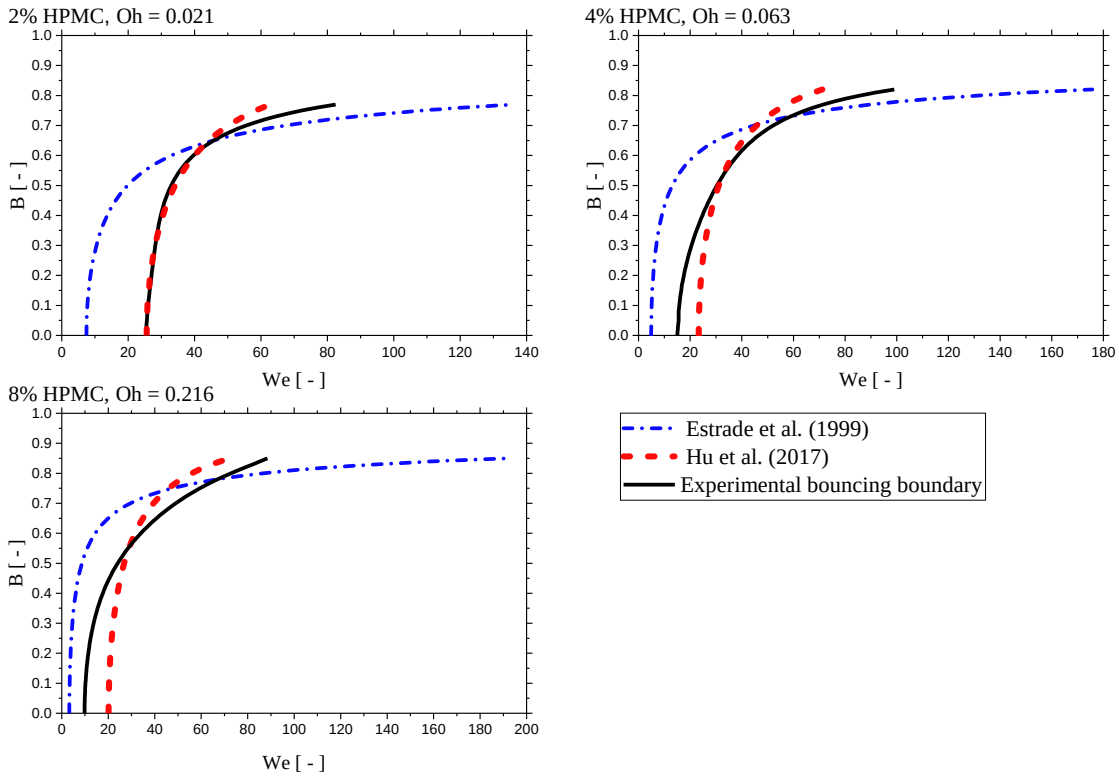

Figure 7.4 The performance of Estrade et al. (1999) model in Eq. (7.10) and Hu et al. (2017) model in Eq. (7.14) on the HPMC regime maps for the three concentrations that used in this work, 2%, 4%, and 8%.

Table 7.2 A quantitative summary of the performance of the models of Estrade et al. (1999) and Hu et al. (2017).

	Estrade *et al.* (1999) Eq. (7.10)		Hu *et al*. (2017) Eq. (7.14)		
	ϕ'	MAE	ϕ'	α_2	MAE
2% HPMC	1.31	16.05	1.27	0.50	1.77
4% HPMC	1.21	15.18	1.24	0.50	6.10
8% HPMC	1.14	14.63	1.21	0.50	8.35

Table 7.2 shows an overall improvement in the prediction when Hu et al. (2017) model is used where the MAE remains in the range of 1.74 to 8.35 for the three systems, whereas, Estrade et al. (1999) model shows MAEs in the range of 14.63 to 16.05. It can also be noticed from Table 7.2 and Figure 7.4 that Estrade et al. (1999) model shows an increasing accuracy as the viscosity increases, as the MAE was reduced from 16.05 in 2% HPMC to 14.63 in 8% HPMC. In contrast, Hu et al. (2017) model exhibits an opposite behaviour, where the MAE increased from 1.74 in 2% HPMC to 8.35 in 8% HPMC, respectively. Moreover, qualitatively, for the three systems, the model of Estrade et al. (1999) could not follow the trend of the experimental boundary starting from under-prediction of $\mathrm{We_c}$ at low B and crosses the experimental curve above the triple point to over-prediction of $\mathrm{We_c}$ at high B. However, the boundary predicted by the model of Hu et al. (2017) crosses the experimentally observed boundary near the triple point, especially in the cases of 4% and 8% HPMC, by over-predicting $\mathrm{We_c}$ at low B and under-predicting $\mathrm{We_c}$ at high B. The following paragraphs explain the reasons behind these observations.

In both models, it is assumed that the maximum deformation limit is independent of the impact parameter (i.e. constant shape factor, assumption 3 in Table 7.1). However, the maximum deformation limit decreases significantly as the impact parameter increases, as can be seen in case of 2% HPMC in Figure 7.5. Consequently, an over-prediction of $\mathrm{We_c}$ would be expected at high B values if the model is fitted to the experimental $\mathrm{We_c}$ at $\mathrm{B} = 0$, as shown in Figure 7.6. This explains the trend of the model of Estrade et al. (1999) in Figure 7.4, as the minimum MAE fits the model at a B value near the triple point (the cross point). This means the selected ϕ' value produces less surface area at the maximum deformation limit than that at near head-on collisions and thereby under-prediction of $\mathrm{We_c}$ below the cross point and higher than that at high B values above the cross point which cause the over-prediction of $\mathrm{We_c}$.

However, the model of Hu et al. (2017) shows an under-prediction of $\mathrm{We_c}$ at high values of B when the model fits the experimental boundary at $\mathrm{B} = 0$, as shown in Figure 7.6. This trend is contrary to expectations due to the constant shape factor assumption. This can be explained by the overestimation of kinetic energy, at high B values, that is considered by using the entire droplet mass regardless of the percentage of interaction

regions. The excessive kinetic energy that is considered to contribute to the deformation has an opposite effect to the constant shape factor assumption. This opposite effect reduces the impact of these assumptions on the model, which explains the overall improvement in the prediction of the model of Hu et al. (2017) compared to the model of Estrade et al. (1999). However, the excessive kinetic energy seems to have a larger impact on the curve than that of the constant shape factor assumption. This leads to an under prediction of $\mathrm{We_c}$ at high B values when the model is fitted to the experiments at head-on collisions, as shown in Figure 7.6. That explains the trend of the model of Hu et al. (2017) in Figure 7.4, as the Minimum MAE selects ϕ' value that fits the model at a cross point near the triple point and thereby an under-prediction of $\mathrm{We_c}$ above this point and an over-prediction of $\mathrm{We_c}$ below it.

The case of 8% HPMC in Figure 7.5 shows that at high viscosity, the assumption of constant shape factor has less significance in comparison to the case of 2% HPMC. This because the bouncing boundary occurs at low $\mathrm{We_c}$ and hence at low kinetic energy. Due to the high viscosity, a significant amount of this kinetic energy would be dissipated. Consequently, less kinetic energy will be transformed into surface energy and hence low deformation occurs at low B, which makes the shape factor more comparable with that at higher B values in comparison to the bouncing of lower viscosity droplets. Therefore, the prediction accuracy increases with the increase of the viscosity by using the model of Estrade et al. (1999). However, the accuracy of the model of Hu et al. (2017) decreases by increasing the viscosity as the opposite effect of the constant shape factor to the effect of the excess kinetic energy is lower than that at low viscosity.

Although Estrade et al. (1999) and Hu et al. (2017) have a different definition to the kinetic energy that contributes to the deformation at head-on collisions, this should not affect the above discussion as both models are optimized by fitting the shape factor for the minimum MAE. This means any difference due to the difference in the kinetic energy will be recovered by the fitted shape factor. Similarly, the existence of the viscous loss term in the model of Hu et al. (2017) should not affect the discussion. Ultimately, the difference in the shape of the two models is due that Estrade et al. (1999) consider the mass of the interaction regions in the kinetic energy that contributes to the deformation

while Hu et al. (2017) consider the entire mass; this cannot be recovered by the fitted shape factor because X is a function of B while the shape factor is not.

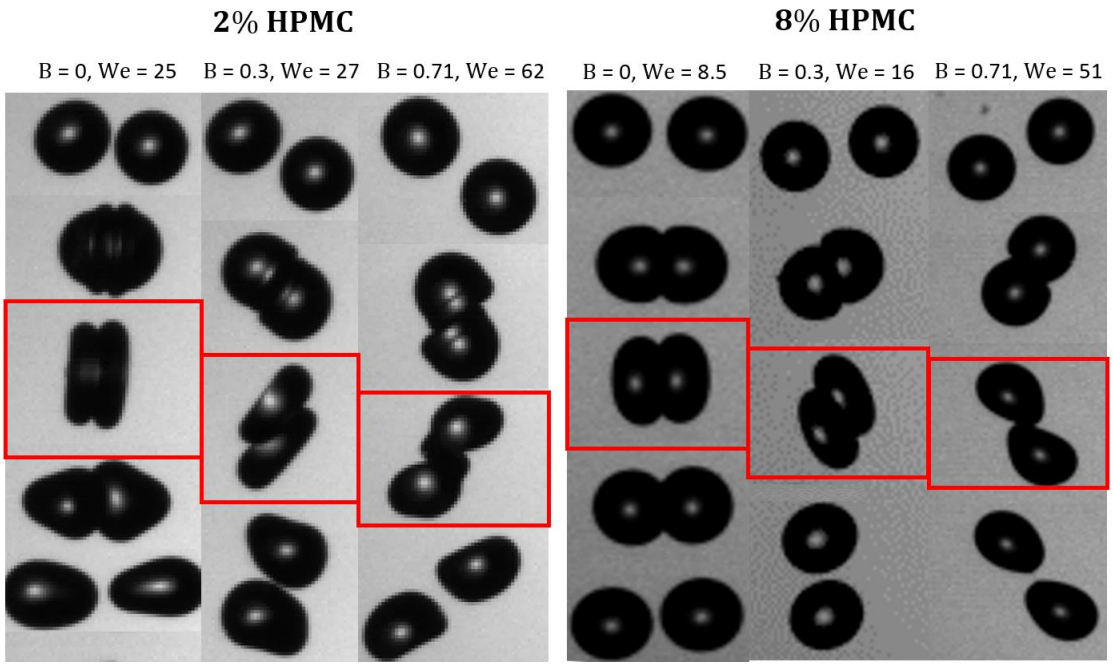

Figure 7.5 The maximum deformation of 2%and 8% HPMC at different values of impact parameter for Weber numbers that occur on the boundary of the bouncing regime.

From the discussion in this section, an accurate model that can evaluate the boundary of the bouncing regime requires a shape factor that accurately reflects the geometry of the droplet at maximum deformation, correct definition of the kinetic energy that contributes to the deformation, good estimation to the viscous losses, and implementing the effect of the impact parameter on the shape factor and the kinetic energy that contributes to the deformation. Therefore, in the next sections, these parameters will be assessed firstly at head-on collisions then the analysis will be extended to the entire range of B.

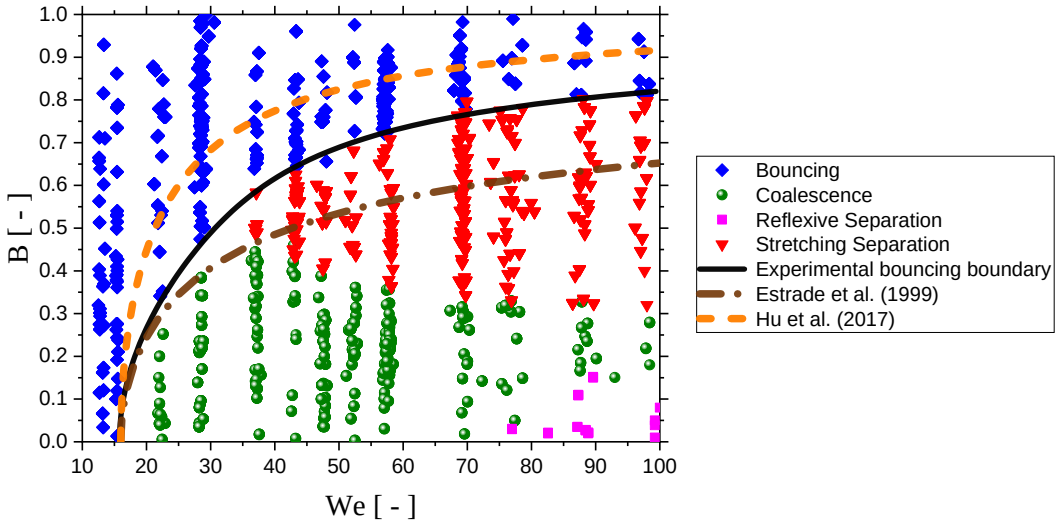

Figure 7.6 The performance of the existing models when they are fitted to the onset of coalescence at head-on collisions, which show the over-prediction of the model of Estrade et al. (1999), Eq. (7.10), and the under-prediction of the model of Hu et al. (2017), Eq. (7.14) on 4% HPMC regime map. ϕ' is 1.6 in the model of Estrade et al. (1999) while it is 1.16 in the model of Hu et al. (2017) and α_2 is 0.5.

7.4.2.1 Assessment of the models' parameters at head-on collisions

7.4.2.1.1 Kinetic energy assessment

As mentioned earlier, the two models have a different definition of the kinetic energy that contributes to the deformation. To assess the validity of these two different approaches, they are examined for head-on collisions, where both approaches consider the kinetic energy of the total drop mass.

The momentum of a moving droplet is given by $P = mu$, where m and u are mass and velocity of the droplet respectively. Therefore, the kinetic energy of the droplet is given by:

$$E_k = \frac{1}{2}uP. \tag{7.16}$$

This relation will show that whether the two approaches of the kinetic energy conserve the momentum in a zero-momentum frame.

In head-on bouncing collisions of equal diameter (d) droplets, if each droplet has a velocity equal to $u = u_r/2$, the total momentum of the droplets is

$$P = \frac{\pi}{6}\rho d^3 u_r \tag{7.17}$$

Substituting Eq. (7.17) in Eq. (7.16) gives the total kinetic energy of the droplets

$$E_k = \frac{\pi}{24}\rho d^3 u_r^2. \tag{7.18}$$

At head-on collisions, X_l and $\cos^2\theta$ are both equal one. Thus, the kinetic energy of the model of Estrade et al. (1999), from the combination of Eqs. (7.2-6), is $E_{K,ini,cont} = (1/12)\pi\rho d^3 u_r^2$. This reveals that Estrade et al. (1999) double the kinetic energy that contributes to the deformation compared to Eq. (7.18). However, the approach of Hu et al. (2017) is universal, as simplifying Eq. (7.13), for head-on collisions of equal size droplets, gives $E_{K,ini,cont} = (1/24)\rho d^3 u_r^2$, which recovers Eq. (7.18). Thus, the approach of Hu et al. (2017) will be the considered in the rest of this paper.

7.4.2.1.2 Shape factor assessment

By looking at the both aforementioned models, Eq. (7.10) and Eq. (7.14), it can be realized that the shape factor ϕ' should always have a value >1, otherwise the models would produce zero or negative values of $\mathrm{We_c}$. This implies that ϕ must have a value that is always less than 0.40, according to Eq. (7.9), as shown in Figure 7.7. However, $\phi \equiv 2$ for grazing collisions, when $\mathrm{B} = 1$, and the direct measurement at head-on collision from the images of 2% HPMC in Figure 7.5 at maximum deformation reveals that $\phi \sim 0.648$ for 2% HPMC. This range of ϕ (from 2 to 0.648) is above 0.4, which implies that the shape factor $\phi' < 1$, as shown in Figure 7.7. Thus, this shows that the commonly used shape factors of the existing models are not seen in reality, and hence the suggested equation for the maximum deformation seems to be invalid. To verify the validity of this equation, the shape factor of spherical cap was derived again in this work, see Appendix C. The new derivation of the shape factor proved that Eq. (7.9) should be in the following form

$$\phi_c' = \frac{2}{3}\left(\frac{6}{\phi} - 2\right)^{-\frac{1}{3}} + \frac{1}{3}\left(\frac{2}{\phi} - 2\right)^{\frac{2}{3}}. \tag{7.19}$$

and the form of Eq. (7.9) is might be due to a derivation mistake by Estrade et al. (1999). Eq. (7.19) shows that $\phi_c{}'$ >1 for the visible range of ϕ (from 0 to 2), as shown in Figure 7.7.

As the shape factor was corrected in Eq. (7.19), it would be interesting to use it, by measuring ϕ from the experimental images, to evaluate the critical $\mathrm{We_c}$ of the onset of coalescence at head-on collisions. This by using the model of Hu et al. (2017) as it implements the correct kinetic energy as justified in the previous section. The model firstly tested without considering the viscous losses (i.e. $\alpha_2 = 0$). The model slightly over-predicts the onset of coalescence in case of 2% HPMC and gives a reasonable agreement in 4% HPMC and 8% HPMC, as illustrated in Table 7.3. However, adding viscous losses would further over-estimates We_c. This implies that the spherical cap geometry over-estimates the surface energy at the maximum deformation. Thus, there is a requirement for a shape factor that has a better agreement with the geometry of the droplets at the maximum deformation. Thus, a new shape factor will be proposed, in the next sub-section.

Table 7.3. Comparison between the experimental and the predicted We_c of the onset of coalescence using Eq. (7.14) using different shape factors (spherical cap and oblate spheroid) at $\mathrm{B} = 0$, and $\alpha_2 = 0$.

		Spherical cap geometry		Oblate spheroid geometry	
	We_c	ϕ_c'	We_c	$\phi_{o.s.}'$	We_c
	Experimental	Eq. (7.19)	Eq. (7.14)	Eq. (7.24)	Eq. (7.14)
2% HPMC	26 ±1	1.59	28.51	1.46	22.01
4% HPMC	16 ±3	1.33	16.05	1.24	11.45
8% HPMC	12 ±2	1.21	10.32	1.14	6.67

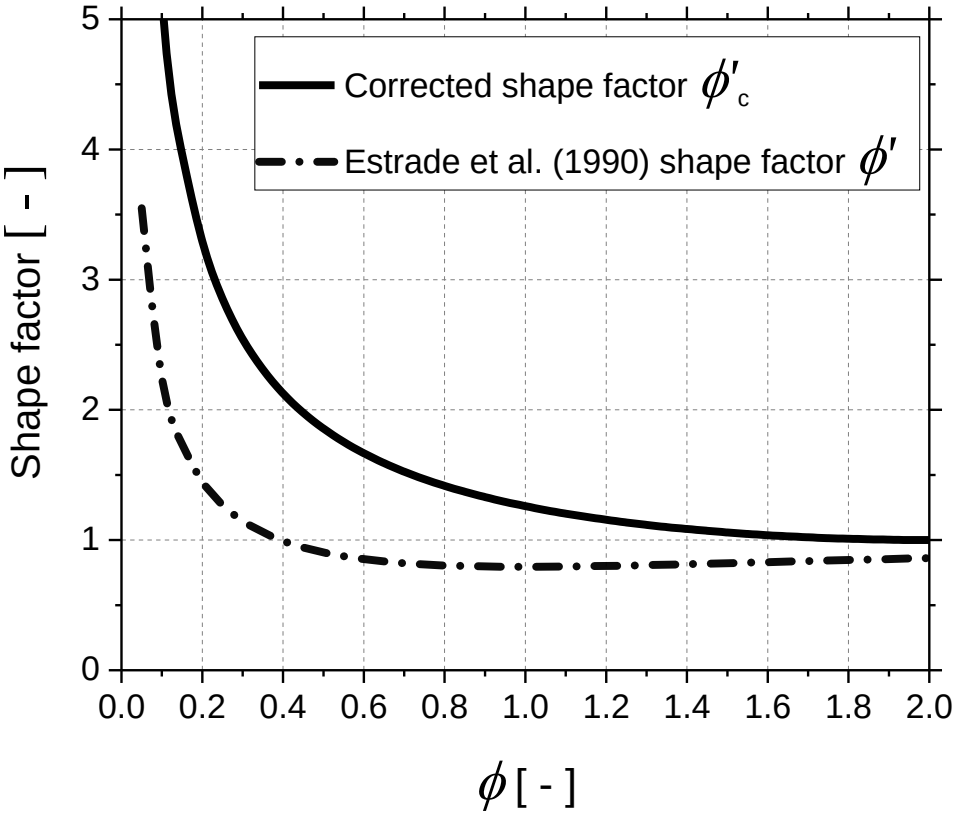

Figure 7.7 The shape factor ϕ' in Eq. (7.9) and Eq. (7.19) as a function of the shape parameter ϕ.

7.4.2.1.3 The proposed shape factors

The images in Figure 7.5 reveal that the maximum deformation of the droplets at head-on collisions have a shape that approximates an oblate spheroid more than spherical cap. The surface area of an oblate spheroid is given by

$$S_{oblate} = 2\pi a^2 + \pi \frac{c^2}{e} \ln\left(\frac{1+e}{1-e}\right) \tag{7.20}$$

Where, a and c are shown in Figure 7.8, and $e^2 = 1 - \frac{c^2}{a^2}$. Thus, the surface energy equation at the maximum deformation can be approximated by

$$E_{S_f} = 2\pi\sigma a_l^2 + \pi\sigma \frac{c_l^2}{e_l} \ln\left(\frac{1+e_l}{1-e_l}\right) + 2\pi\sigma a_s^2 + \pi\sigma \frac{c_s^2}{e_s} \ln\left(\frac{1+e_s}{1-e_s}\right), \tag{7.21}$$

which considers the effect of size ratio by implementing e_l and e_s. Where, $e_l^2 = 1 - (c_l^2/a_l^2)$ and $e_s^2 = 1 - (c_s^2/a_s^2)$. It should be noted that e_l^2 and e_s^2 are expected to be

unequal in case of collisions between droplets that have non-identical size. This is due to the difference in the capillary pressure ($4\sigma/d$) between the droplets, as the small droplet has higher capillary pressure and hence higher resistance to the deformation. This is in contrary to the assumption of Estrade et al. (1999) that $\phi = h_l/R_l = h_s/R_s$.

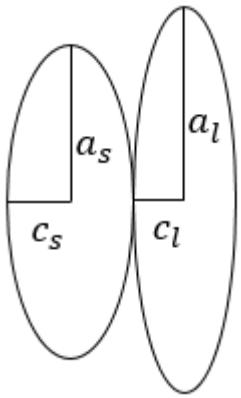

Figure 7.8 The oblate spheroid shape that is proposed for the maximum deformation at head-on collisions.

From mass/volume conservation before the collision and at the maximum deformation, the volume of the oblate spheroid, given by $V_{oblate} = (4/3)\pi a^2 c$, is equal to a volume of a sphere, given by $V_{sphere} = (1/6)\pi d^3$, that has a diameter d equal to the droplet diameter before the collision.

$$4a^2c = \frac{1}{2}d^3. \tag{7.22}$$

Solving Eq. (7.22) for a, c, and d and substituting it in Eq. (7.21) gives

$$E_{S_f} = \frac{1}{2}\pi\sigma d_l^2\left(\left(\left(\frac{1}{1-e_l}\right)^{\frac{1}{3}} + \frac{1}{2}\left(\frac{(1-e_l)^{\frac{2}{3}}}{e_l}\right)\ln\left(\frac{1+e_l}{1-e_l}\right)\right) + \Delta^2\left(\left(\frac{1}{1-e_s}\right)^{\frac{1}{3}} + \frac{1}{2}\left(\frac{(1-e_s)^{\frac{2}{3}}}{e_s}\right)\ln\left(\frac{1+e_s}{1-e_s}\right)\right)\right). \tag{7.23}$$

From the analogy between Eq. (7.23) and Eq. (7.8), the shape factor of an oblate spheroid geometry ($\phi'_{o.s.}$) is given by

$$\phi'_{o.s.} = \frac{1}{(2+2\Delta^2)}\left(\left(\left(\frac{1}{1-e_l}\right)^{\frac{1}{3}} + \frac{1}{2}\left(\frac{(1-e_l)^{\frac{2}{3}}}{e_l}\right)\ln\left(\frac{1+e_l}{1-e_l}\right)\right) + \Delta^2\left(\left(\frac{1}{1-e_s}\right)^{\frac{1}{3}} + \frac{1}{2}\left(\frac{(1-e_s)^{\frac{2}{3}}}{e_s}\right)\ln\left(\frac{1+e_s}{1-e_s}\right)\right)\right). \quad (7.24)$$

Using the new shape factor of the oblate spheroid, Eq. (7.24), rather than the shape factor of the spherical cap, Eq. (7.19), with keeping $\alpha_2 = 0$, results in an under-prediction of $\mathrm{We_c}$ for the three HPMC solutions, as shown in Table 7.3, which is the expected scenario due to the neglect of the viscous losses. This reveals that the oblate spheroid geometry is better in describing the geometry of the droplet at the maximum deformation, since its produce shape factor that have less value than the spherical cap, as illustrated in Table 7.3, and hence lower surface energy at the maximum deformation.

7.4.2.1.4 Viscous losses estimation

The process of bouncing can be divided into two stages: the initial deformation from the time of contact, t_o, to the point of maximum deformation, t_{m1}, and a period of oscillating relaxation where the droplets return to their original spherical shape at t_{rn}, as shown in Figure 7.9. The total viscous dissipation in the bouncing collision process takes place during both these periods due to the induced internal flow. Assuming viscous losses are the only sources of energy loss, then the viscous energy loss, $E_{\mu,tot}$, is equal to the difference in the system kinetic energy before and after the head-on collision, i.e. $E_{\mu,tot} = E_{K,ini} - E_{K,f}$. Where, $E_{K,f}$ is the kinetic energy of the droplets at post collision and given by mu_f^2, where u_f is the velocity of the rebounding droplets. This velocity can be measured by tracking the separating droplets.

The viscous loss in the bouncing model, E_μ is that due to the deformation in the period from t_o to t_{m1}. Therefore, to estimate E_μ it is necessary to estimate the ratio of the viscous losses during period of t_0 - t_{m1} to the total viscous losses, $E_{\mu,tot}$. If the droplets are viscous and recovered their spherical shape without oscillation, this fraction will be

$\sim$ 50% and hence $\alpha_2 \sim 0.5E_{\mu,tot}/E_{K,ini}$. This is based on the assumption that the losses during the compression period from t_o to t_{m1}, is equal to that of the relaxation period when the droplet returns to its spherical shape at t_{r1}. In the more general case when the droplets show oscillations during the relaxation period, see Figure 7.10, estimating α_2 requires an estimate of the viscous losses in this period.

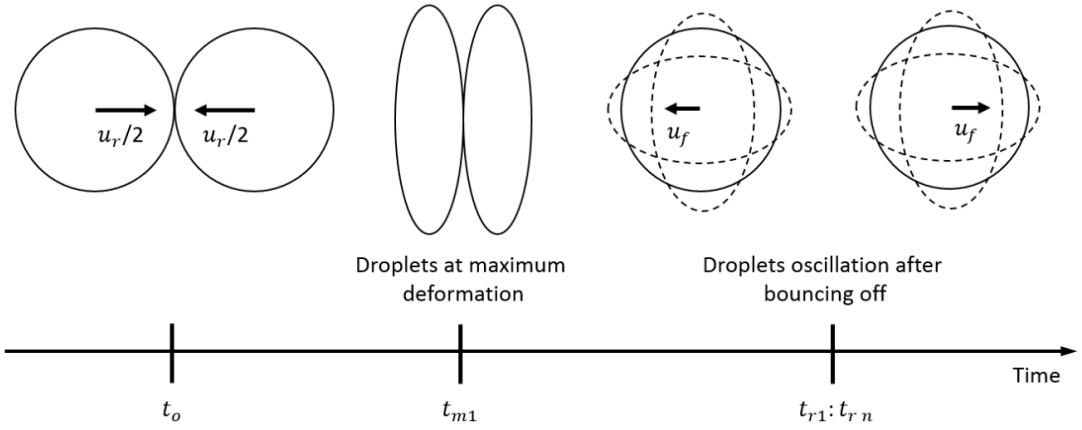

Figure 7.9 The stages of bouncing process.

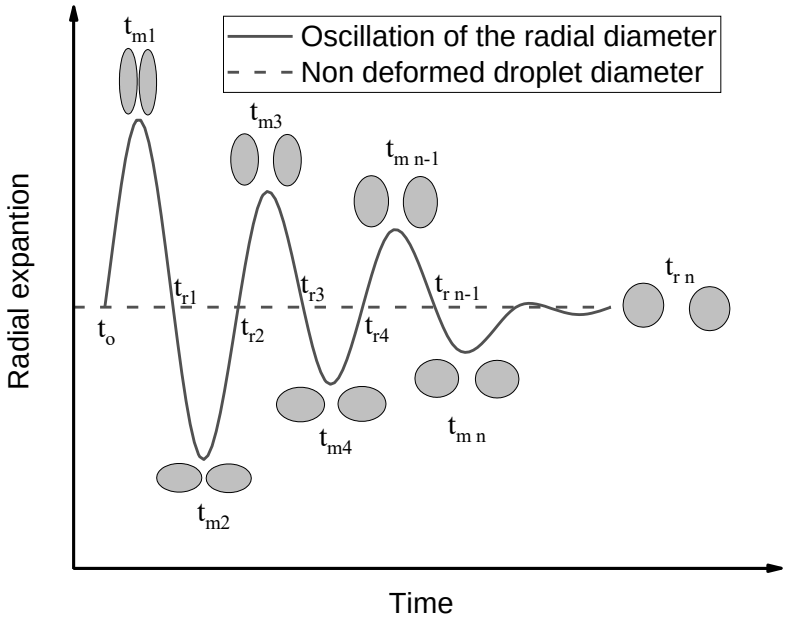

Figure 7.10 The radial oscillation of the droplets during the bouncing collision.

If the assumption is made that the viscous energy loss in each overshoot is proportional to the elongation of the droplet, $\left|d_r\,|_{t_{mi}} - d\,|_{t_o}\right|$, then the contribution of deformation of the period t_{r1}- t_o to the total viscous losses can be approximated by

$$\frac{E_\mu \big|_{t_{r1}-t_o}}{E_{\boldsymbol{\mu,tot}}} \sim \frac{d_r \big|_{t_{m1}} - d \big|_{t_o}}{\sum_{i=1}^{n} \; | \, d_r \big|_{t_{mi}} - d \big|_{t_o} \, |} \tag{7.25}$$

Where, d_r is the length of the droplet measure along it principal axis. However, the viscous loss that considered in the bouncing model is roughly half the viscous loss in the period $t_{r1} - t_o$. Thus, the viscous losses factor is in the order of

$$\alpha_2 \sim 0.5 \, \frac{E_\mu \big|_{t_{r1}-t_o}}{E_{K,ini}}. \tag{7.26}$$

8% HPMC shows that 88% of $E_{K,ini}$ is dissipated by the total viscous losses, and no oscillation after t_{r1}, which means $\alpha_2 \sim$ 44%, as detailed in Table 7.4. While, 4% HPMC shows 70% of $E_{K,ini}$ is dissipated by the total viscous losses, and of one cycle after t_{r1} (i.e. reaches its final relaxation state at t_{r2}). More oscillations were noticed in 2% HPMC, which shows six cycles after t_{r1}; and 75% of $E_{K,ini}$ is dissipated by the total viscous losses. Applying Eq. (7.26) to 2% HPMC and 4% HPMC gives that the viscous dissipation factor is approximately 0.11 and 0.33, respectively, as shown in Table 7.4. Using these approximated values of α_2 in the model of Hu et al. (2017) with the measured values of the proposed shape factor Eq. (26), shows good agreement of the predicted $\mathrm{We_c}$ with the experiments, as shown in Table 7.4.

Table 7.4 Comparison, at head-on collisions, between the experimental and the predicted $\mathrm{We_c}$ of the onset of coalescence using Eq. (7.14) with the oblate spheroid shape factor, Eq. (7.24), and Eq. (7.26) for the viscous dissipation factor.

	α_2 Eq. (7.26)	$\phi'_{o.s}$ Eq. (7.24)	$\mathrm{We_c}$ experimental	$\mathrm{We_c}$ Eq. (7.14)
2% HPMC	0.11	1.46	26 ±1	24.72
4% HPMC	0.23	1.24	16 ±3	15.8
8% HPMC	0.44	1.14	12 ±2	11.90

7.4.2.2 The effect of the impact parameter

7.4.2.2.1 Kinetic energy assessment

As mentioned early, considering the total mass of the droplet in $E_{K,ini,cont}$ leads to under-predict $\mathrm{We_c}$ at high values of B. Therefore, the mass of the interaction regions should be considered in the approach of Hu et al. (2017) in evaluating the kinetic energy that contributes to the deformation. This should be considered for both small and large droplet, in case of collisions of unequal size droplets. Therefore, the equation of the kinetic energy that contributes to the deformation will be

$$E_{K,ini,cont} = \frac{1}{2}\rho\left(\tilde{X}'_{\mathrm{l}}\frac{1}{6\Delta^3}\pi d_{\mathrm{s}}^3\left(\frac{\Delta^3 U_r}{1+\Delta^3}\cos\theta\right)^2 + X'_{\mathrm{s}}\frac{1}{6}\pi d_{\mathrm{s}}^3\left(\frac{U_r}{1+\Delta^3}\cos\theta\right)^2\right) \tag{7.27}$$

Where, X'_l and X'_s are given by the spherical cap interaction regions that were derived in chapter 6 and re-given by Eq. (7.28) and Eq. (7.29). Note that, to conserve the momentum at head-on collisions, in Eq. (7.27), X'_l is normalized by its value at B = 0. This because in collisions of unequal-size droplets $X'_l < 1$ and it is belived that all mass contribute to the deformation as no rotation is seen at head-on collisions.

$$X'_l = \begin{cases} \frac{1}{4}\tau^2(3-\tau) & \text{for B} > \frac{d_l - d_s}{d_l + d_s} \\ 1 - \left(\frac{2h_1^2\left(\frac{2}{3}d_l - h_1\right)}{d_l^3}\right) - \left(\frac{2h_2^2\left(\frac{2}{3}d_l - h_2\right)}{d_l^3}\right) & \text{for B} \le \frac{d_l - d_s}{d_l + d_s} \end{cases}, \tag{7.28}$$

and,

$$X'_s = \begin{cases} \frac{\tau^2(3\Delta - \tau)}{4\Delta^3} & \text{for B} > \frac{d_l - d_s}{d_l + d_s} \\ 1 & \text{for B} > \frac{d_l - d_s}{d_l + d_s} \end{cases}. \tag{7.29}$$

Where h_1 and h_2 are given by

$$h_1 = \frac{d_l - ds}{2} + \frac{\mathrm{B}(d_l + d_s)}{2} \tag{7.30}$$

$$h_2 = \frac{d_l - ds}{2} - \frac{\mathrm{B}(d_l + d_s)}{2} \tag{7.31}$$

Where, τ and h are defined in Eq. (7) and Eq. (8), respectively.

7.4.2.2.2 Shape factor assessment

As mentioned before the degree of deformation decreases with the impact parameter (i.e. decrease in the surface area at the maximum deformation), see Figure 7.5. Therefore, to predict the lower boundary of the bouncing regime, for the entire range of B, the decrease in the surface area of the droplet at the maximum deformation needs to be considered. In Figure 7.5, it can be noticed that the deformation has less dependency on the impact parameter at the range from 0 to 0.3 than at the range from 0.3 to 0.7, especially in case of 2% HPMC. Thus, we need to account for the non-linear decrease in shape factor seen with increasing B. As the factor e is an indicator of deformation, the surface area can be correlated with B via e^2 and the following power-law correlation is proposed

$$e' = \sqrt{\frac{e^2}{1+B^k}}. \tag{7.32}$$

Where k is a positive constant that can be optimized to fit the data. Therefore, $\phi''_{o.s.}$ is the new shape factor that considers the effect of B, which is similar to that in Eq. (7.24) but using e' instead of e. Eq. (7.32) allows for the fact that at $\mathrm{B} = 0$, $e' = e$ and hence $\phi''_{o.s.} = \phi'_{o.s.}$.

a. The performance of the new model

Using Eq. (7.27) and the proposed shape factor $\phi''_{o.s.}$, the bouncing boundary model will be

$$\mathrm{We_c} = \frac{12\Delta^2(1+\Delta^2)(1+\Delta^3)^2(\phi''_{o.s.} - 1)}{(Xs + \Delta^3 X_{l)}(1-\mathrm{B}^2)(1-\alpha_2)}. \tag{7.33}$$

Using this model, Eq. (7.33), with the approximated values of α_2 in section 7.4.2.1.4., and the measured values of $\phi''_{o.s.}$ at head-on collisions, in Table 7.4, and then Optimizing k for the minimum MAE, show significant improvement in the fitting of the bouncing

boundary, as shown qualitatively in Figure 7.11. The proposed model shows excellent agreement with experimental data whether above or below the triple point for the three HPMC solutions. Quantitatively, the first three rows in Table 7.5 show that the MAE of the proposed model is significantly reduced compared to that of the models of Estrade et al. (1999) and Hu et al. (2017) in Table 7.2. Compare to the model of Estrade et al. (1999), the MAE was reduced by 92%, 97%, and 86% for 2% HPMC, 4% HPMC, and 8% HPMC, respectively. And compare to the model of Hu et al. (2017), it was reduced by 35%, 91%, and 75% for 2% HPMC, 4% HPMC, and 8% HPMC, respectively.

Table 7.5 Bouncing model, Eq. (7.33), parameters. Note that the Oh of the non-identical viscosities is the average.

	Oh	α_2	$\phi''_{o.s.}$ (at $B = 0$)	k	e^2	MAE
2% HPMC	0.021	0.11	1.46	3.05	0.895	1.15
4% HPMC	0.063	0.23	1.25	3.78	0.81	0.53
8% HPMC	0.260	0.44	1.14	4.29	0.71	2.11
2% HPMC (L)	0.020	0.04	1.44	3.46	0.89	2.31
2% HPMC (S)	0.027	0.12	1.25	3.43	0.81	1.63
4% HPMC (S)	0.080	0.25	1.176	5.28	0.75	1.09
6% HPMC (L)	0.109	0.26	1.37	3.2	0.83	3.06
6% HPMC (S)	0.155	0.30	1.13	5.08	0.70	1.57
2% vs. 4% HPMC	0.042	0.14	1.36	3.43	0.88; 0.84	4.15
2% vs. 8% HPMC	0.141	0.26	1.34	3.37	0.87; 0.79	3.83
4% vs. 8% HPMC	0.162	0.3	1.25	3.33	0.83; 0.79	2.26

Likewise, the model was fitted to the other regime maps of identical droplets collisions of 2% and 4% HPMC presented in chapter 5 and to two more regime maps of identical droplets collisions of 6% HPMC (μ=17.7 mPa s, σ=0.046 N m^{-1}, and ρ=1000 kg m^{-3}) of two droplet-sizes 500 μm and 250 μm. The model shows reasonable fittings to the

experimental data, as shown quantitatively in Table 7.5, with MAE ≤ 3, and qualitatively in Figure 7.12.

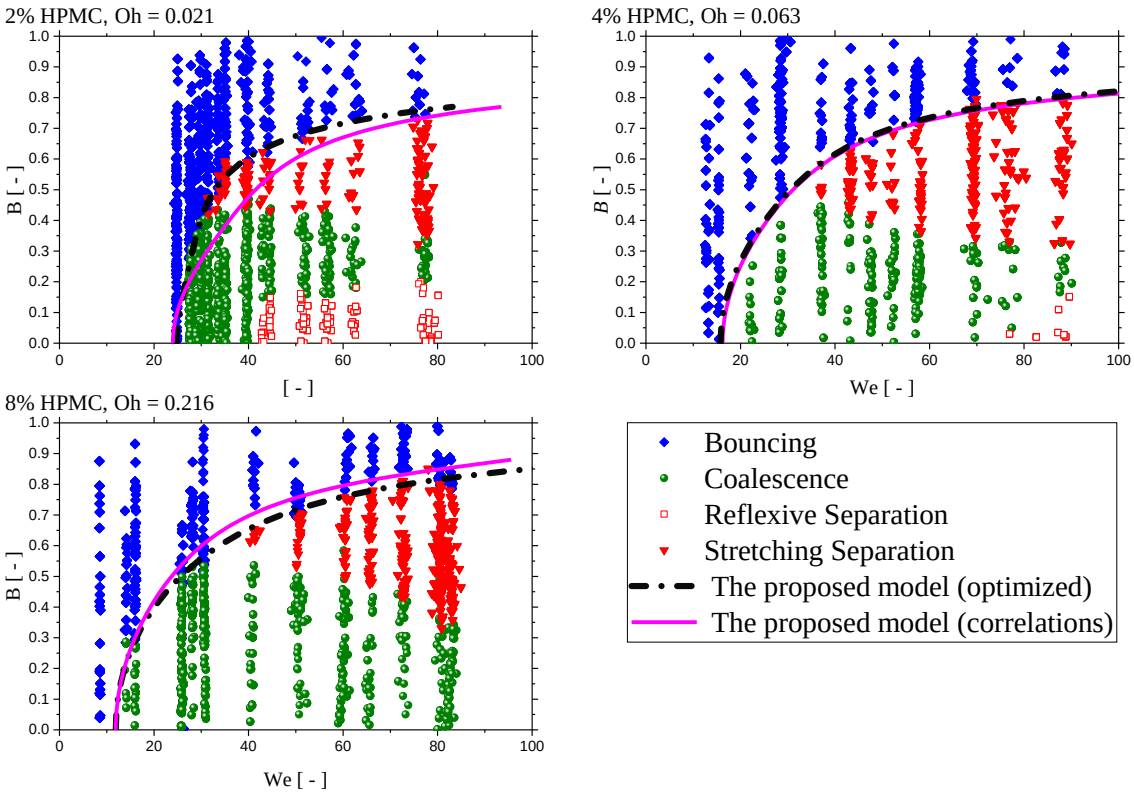

Figure 7.11 The performance of the proposed model Eq. (7.33) compare to bouncing boundaries on the HPMC regime maps for the three concentrations, 2%, 4%, and 8%.

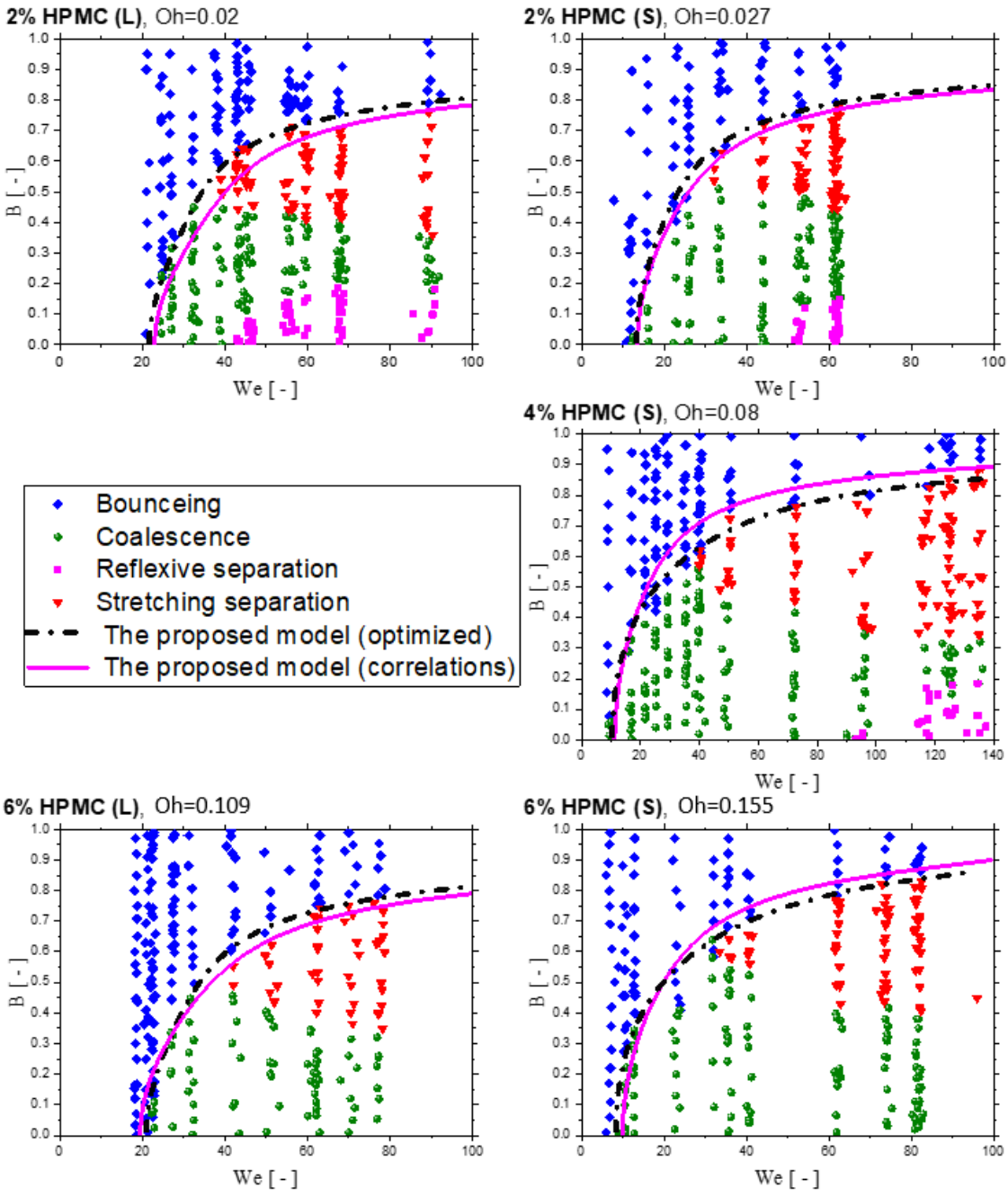

Figure 7.12 The performance of the proposed model Eq. (7.33) compare to bouncing boundaries on the HPMC regime maps for collisions of identical droplets.

7.4.3 Collisions of equal-size droplets with non-identical viscosities

In collisions of non-identical viscosities, the colliding droplets differ in their deformation degree, as shown in Figure 4.3, which means they differ in e value. The difference in e value between the colliding droplets can be taken into account in the shape factor $\phi''_{o.s.}$,

Eq. (7.24), via e_s and e_l. To evaluate $\phi''_{o.s.}$, e_s and e_l were measured directly from the images at the maximum deformation at $\mathrm{We}_{\mathrm{B/FC}}$ using ImageJ. Once $\phi''_{o.s.}$ is measured, the viscous loss factor α_2 was estimated by fitting the model to the experimental data at $B = 0$. Subsequently, the model was fitted to the experiments by optimizing k in the same way of the identical collisions. Table 7.5 summarises the values of the fitting parameters that are used in this model for different cases. The model shows excellent performance on the non-identical viscosities' collisions, quantitatively, MAE ≤ 4 and qualitatively as shown in Figure.7.13.

7.4.4 Correlating the viscous loss and the deformation change

Although the model shows good fits to a wide range of data, it anticipates two fitting parameters α_2 and k. Therefore, these parameters require scaling laws.

Planchette et al. (2017) showed that, during the compression phase in reflexive separation, the viscous loss factor α scales with Oh. They observed that the viscous loss increases by increasing Oh at Oh < 0.02, then there is a plateau at moderate Oh while the viscous loss increases again by increasing Oh at high Oh > 0.15, details in chapter 2. Plotting the viscous loss of bouncing α_2, in Table 7.5, versus Oh shows a similar trend. At Oh < 0.06, α_2 increases with Oh ($\alpha_2 = 3.09\ \mathrm{Oh} + 0.0175$), as shown in Figure 7.14. A plateau is observed at 0.06 < Oh < 0.15, where $\alpha_2 \sim 0.25$. At Oh > 0.15, α_2 increases again with Oh ($\alpha_2 = 1.44\ \mathrm{Oh} + 0.065$).

In Figure 7.15, the factor k is plotted against Oh. It shows the data scatter between 3.05 and 5.28 around an average value of 3.8. It was found that the model, in most systems, does not show great sensitivity to k value within this scattering range. Thus it is suggested that $k = 3.8$ to be used as a universal value.

Using the model with the correlated values of α_2 and the average value of k shows good agreement with the experimental data in most of the systems, see Figures 7.11, 7.12, and 7.13. Scattering from the optimum curve is seen in 2% HPMC in Figure 7.11, due to the relatively higher value of the average k compared to its optimum in this system. In all the systems, the model shows an excellent fit at head-on collision, which reveals the robustness of the correlations of α_2 in Figure 7.14.

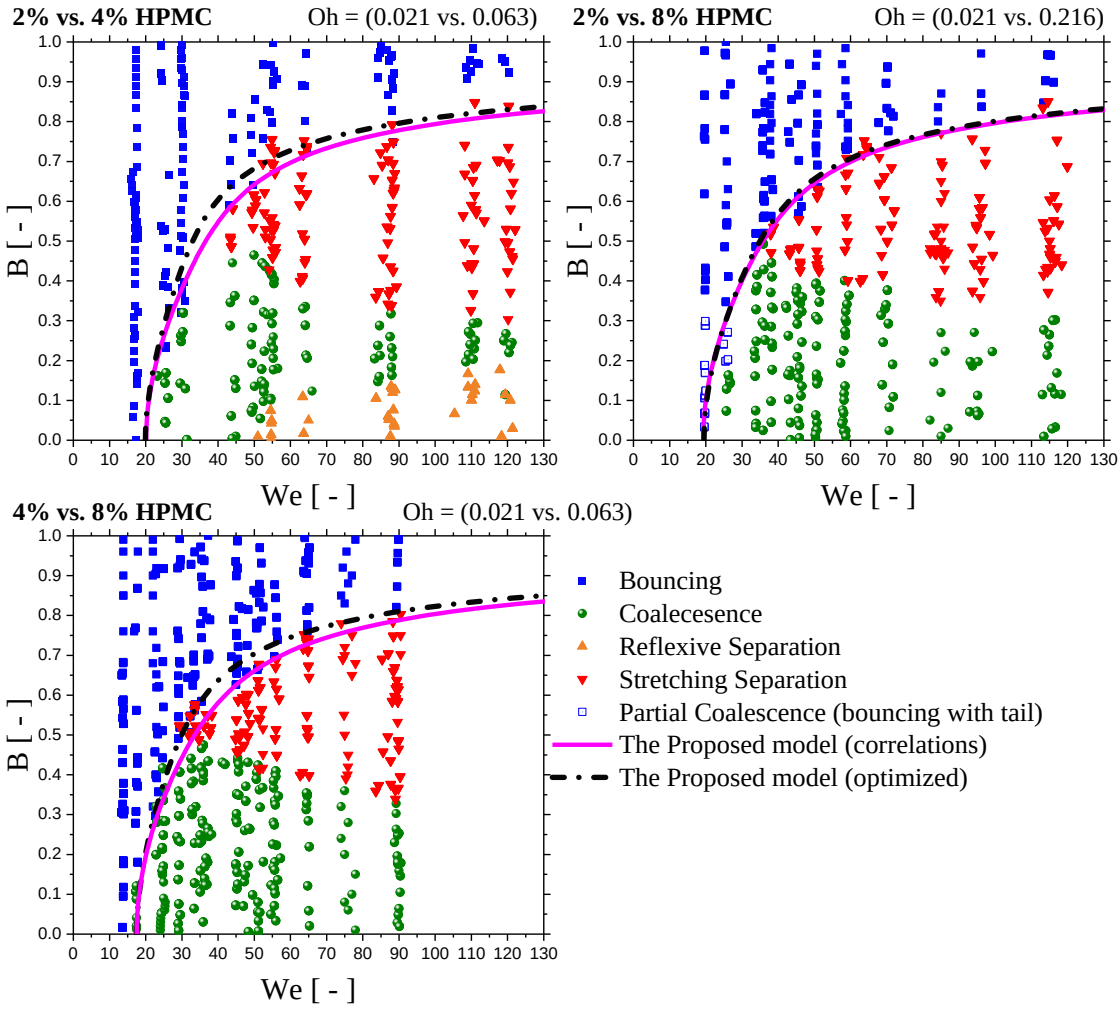

Figure 7.13 The performance of the proposed model Eq. (7.33) compare to bouncing boundaries on the HPMC regime maps for collisions of non-identical viscosities.

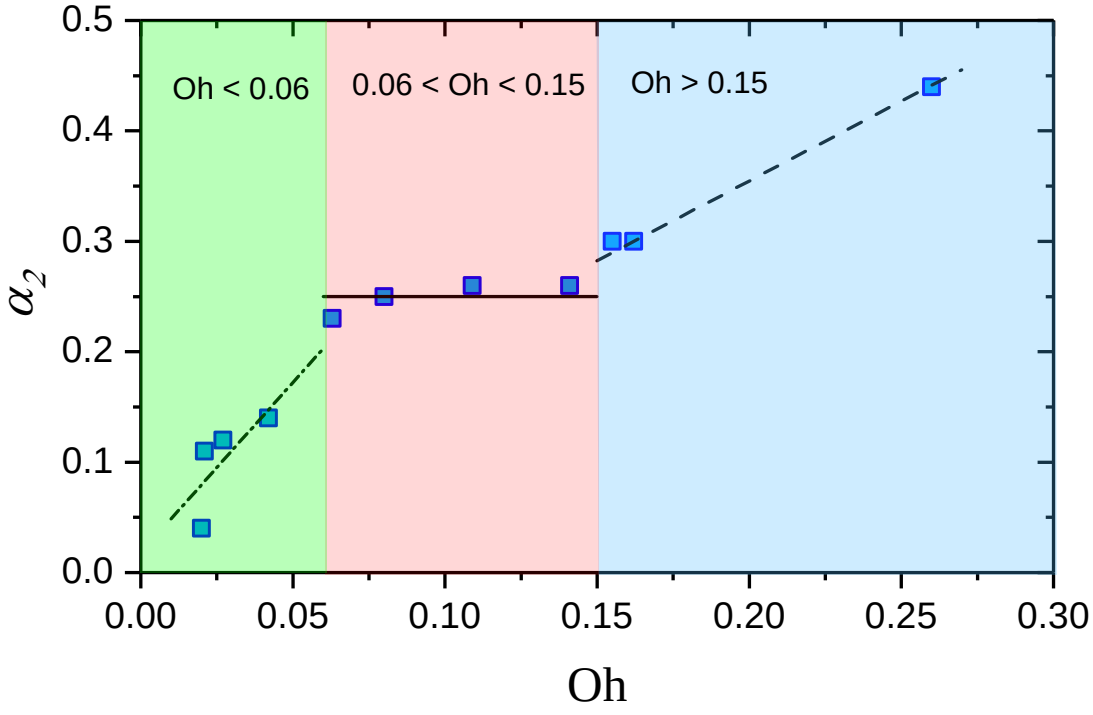

Figure 7.14 The viscous loss factor α_2 as a function of Oh. For Oh < 0.06, $\alpha_2 = 3.09\ \mathrm{Oh} + 0.0175$. for 0.06 < Oh < 0.15, $\alpha_2 = 0.25$. For Oh > 0.15 $\alpha_2 = 1.44\ \mathrm{Oh} + 0.065$.

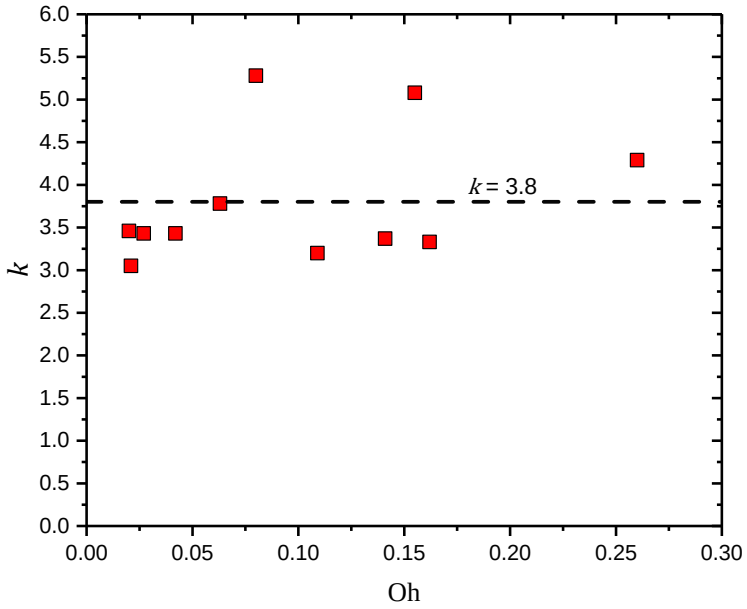

Figure 7.15 The factor k versus Oh. The dashed line is the average value of the scattered data.

7.4.5 Collisions of unequal-size droplets

The model was also applied to collisions of unequal-size droplets by measuring e_s and e_l, at the maximum deformation, and choosing α_2 that fits the model to the experimental boundary of the bouncing at head-on collisions, as detailed in Table 7.6. It should be noted that the maximum deformations of the colliding droplets occur at different times as the small droplet reaches its maximum deformation faster, as mentioned in chapter 5, thereby e_s and e_l were measured at different instants, at their corresponding times of the maximum deformation. k was optimized based on the minimum MAE by comparing with a manually fitted boundary using the same procedure explained in section 7.4.2.

Note that 4% HPMC does not show head-on bouncing, however, at We = 10 it shows late coalescence, see Figure 5.5, where the droplets do not coalesce at the maximum deformation. Therefore, $\mathrm{We} = 10$ was taken as the starting point of the model at head-on collisions, where e_s and e_l were measured. Likewise, the model was fitted in collisions of non-identical viscosities where the late coalescence was seen at We = 11, as shown in Figure 5.7.

The fitted model shows unexpected values of the viscous loss factor α_2, which are significantly higher than the range seen in the equal-size collisions, in Figure 7.14. One of the main reasons for the high viscous loss values is the small droplet reaches the maximum deformation faster than the large droplet. The difference in the deformation time between the colliding droplets leads to the bouncing of the small droplet before the large droplet, which consequently leads to the fact that the kinetic energy of the large droplet is not equal to zero at the maximum deformation, as explained in Chapter 5. However, the model assumes zero kinetic energy at the maximum deformation, thereby in case of unequal-size collisions, the remaining kinetic energy of the large droplet is considered as viscous loss. Therefore, the fitted values of α_2 are significantly higher than the range of Figure 7.14. Another reason that could contribute to the high values of α_2 is that the measured We can be higher than that at the mass-centre coordinates if the large droplet has higher momentum than that of the small droplet. This is because some of the extra momentum of the large droplet might do not contribute to the deformation of the droplets but it might rather move the whole centre

of mass in the original direction of the large droplet. Thus, this energy will not affect the outcome of the collision, however, it is still considered in the measured We and hence the model counts this energy as viscous loss energy.

The viscous loss factor α_2 of unequal-size droplets might be approximated, at the mass-centre coordinates, by $\alpha_2 \sim \left(\alpha_{2,s}\left(E_{k,ini}\right)_s + \alpha_{2,l}\left(E_{k,ini}\right)_l\right)/\left(E_{k,ini}\right)_{tot}$ where $\alpha_{2,s}$ and $\alpha_{2,l}$ are the vicious loss of the small droplet and the large droplet, respectively, estimated from the correlations produced in Figure 7.14 using the corresponding Oh, i.e. Oh_s and Oh_l. $\left(E_{k,ini}\right)_s$ and $\left(E_{k,ini}\right)_l$ are the kinetic energy of the small and the large droplet, respectively. However, defining clear mass-centre coordinates in such collisions is quite complicated. This is due to the complex inelastic nature of such collisions and the difference in the deformation time scale between the colliding droplets. For example, even if it is experimentally ensured that unequal-size droplets are collided with the same momentum, the small droplet loss more energy, due to the deformation, than the large because of the higher Oh_s and hence the centre of mass will move with the large droplet which means some of the large droplet energy does not contribute to the deformation. The significance of such a scenario is expected to increase with increasing the viscosity, decreasing the size and decreasing the size ratio. Thus, to quantify the mass-centre coordinates of unequal-size droplets collisions, there is a need for a systematic study for wider ranges of size ratios and Oh, ideally for systems show head-on bouncing, which is out of the scope of this thesis.

The factor k shows higher average value compared to the identical size collisions, $k = 6$. This difference is not surprising due to the change of the interaction regions with the size ratio for a given impact parameter, as shown in the example in Figure 5.9, which consequently change the trend of the deformation change with B.

Table 7.6 The parameters of the bouncing model, Eq. (7.33), for collisions of unequal-size droplets.

HPMC	Δ	α_2	$\phi''_{o.s.}$ (at $B = 0$)	k	e_s^2	e_l^2	MAE
2%	0.6	0.80	1.33	6.43	0.88	0.7	1.72
4%	0.6	0.80	1.30	6.01	0.86	0.7	2.47
2%(L) vs. 4%(s)	0.6	0.80	1.32	5.92	0.87	0.74	3.20
2%(S) vs. 4%(L)	0.6	0.80	1.32	5.58	0.87	0.73	3.52

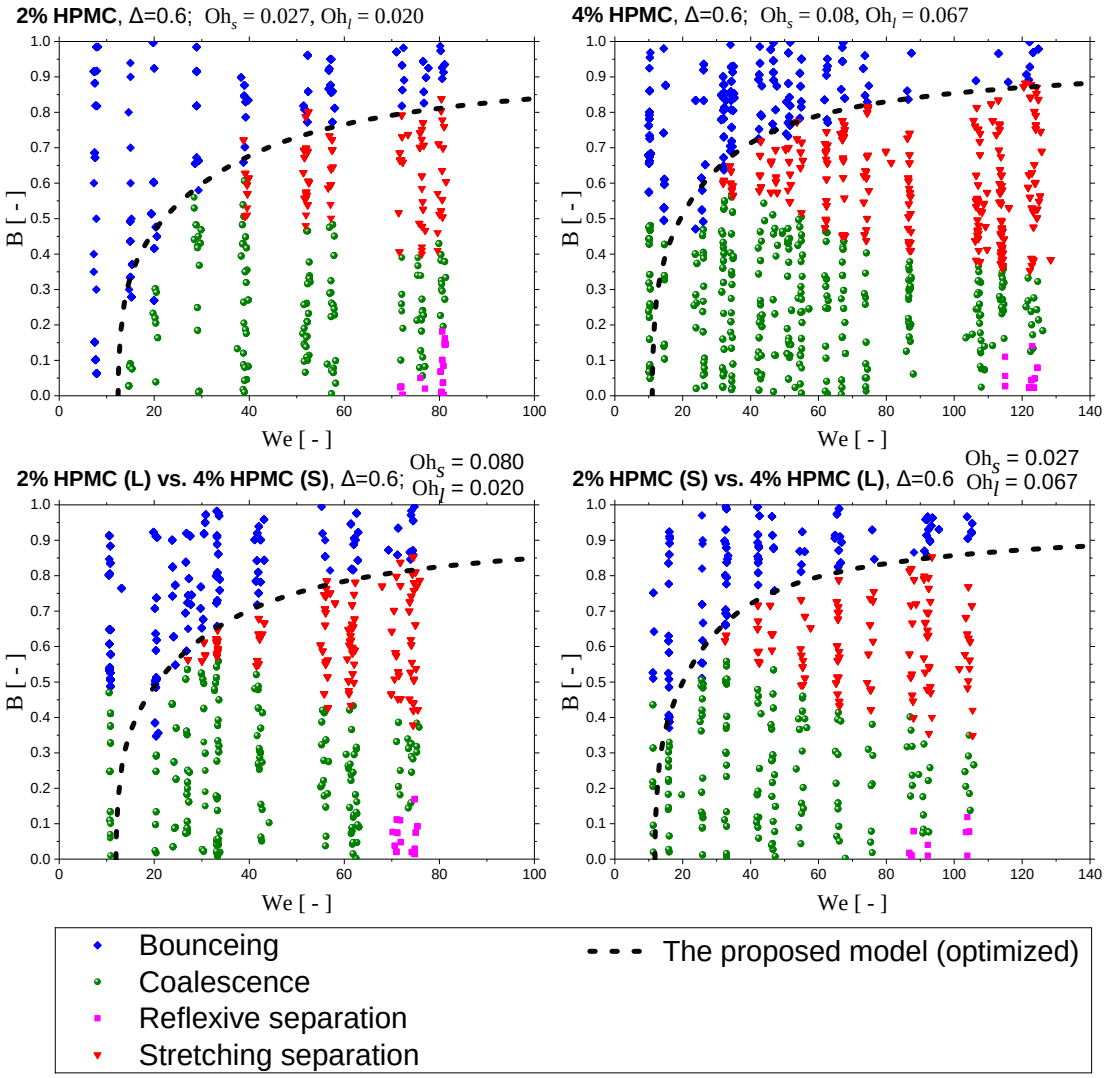

Figure 7.16 The performance of the proposed model Eq. (7.33) in collisions of unequal-size droplets.

7.5 Conclusion

Three regime maps of identical droplets collisions presented in chapter 4, 2%, 4% and 8% HPMC, were used to assess the performance of the existing models in predicting of the boundary of the bouncing regime using the mean absolute error as a quantitative measure. Generally, the model of Hu et al. (2017) shows better accuracy than the model of Estrade et al. (1999). The poor performance of the model of Estrade et al. (1999) is primarily attributed to the assumption that the surface energy at the maximum deformation is independent of the impact parameter, i.e. constant shape factor. However, the experimental images clearly show that the deformation reduces significantly with the impact parameter and consequently, a constant shape factor cannot be assumed. Hu's approach also assumes a constant shape factor however the inclusion of the entire droplet kinetic energy in the energy balance, in contrast to Estrade et al. (1999) who only include the interacting regions, counteracts this assumption and reduces the deviation of the model from the experimental data. (The addition of the loss factor in Hu's model does not help improve the fit as it does not change the shape of the curve.)

Several errors in the derivation of the models were also identified. The derivation of the spherical cap shape factor of Estrade et al. (1999), which was reapplied by Hu et al. (2017), was shown to contain an error. However, an oblate spheroid geometry was found to give a better fit to the droplet shape at maximum deformation for head-on collisions than the spherical cap. Therefore, the oblate spheroid surface area was applied to derive a new shape factor. Additionally, it was found that the definition of the collisional kinetic energy in the model of Estrade et al. (1999) was not general and led to errors, for example, it doubles the kinetic energy in the case of head-on collisions. The definition of Hu et al. (2017) is universally applicable and conserves momentum.

Using the proposed oblate spheroid shape factor and the kinetic energy definition of Hu et al. (2017) but accounting only for the mass of the interaction regions, a modified model for the bouncing regime boundary was proposed. The shape factor for head-on collisions was taken directly from measurements, and the reduction in shape factor with increasing B fitted empirically using a power-law model. Viscous dissipation was also taken into account in the proposed model and for each HPMC concentration, a viscous

dissipation factor was estimated directly from the experimental observations by analysing the decay in the oscillations of bubble shape which occurs after each collision.

The proposed model shows a great fit to the experimental results. For all three HPMC concentrations, the critical *We* number for head-on collisions is well predicted and the fit to the boundary of the bouncing regime is excellent for across the range of We numbers tested, whether above or below the triple point. Quantitatively, the MAE was reduced by an order of magnitude compared to the literature models.

The model was also applied to other systems of equal-size droplets collisions of identical and non-identical viscosities, presented through this thesis. It shows good fits in all the systems. That provided a good set of data to the viscous loss factor α_2 and the deformation change factor k. Plotting the vicious loss versus Oh shows similar trend seen by Planchette et al. (2017) during the compression phase in reflexive separation. At Oh < 0.06, α_2 increases with Oh then a plateau is observed at 0.06 < Oh < 0.15, where $\alpha_2 \sim 0.25$ then α_2 increases again with Oh at Oh > 0.15. on the other hand, k was found to scatter around an average value of 3.8. Using the empirical correlations of α_2 and the average value of k shows good fits with experiments.

Using the model in collisions of unequal-size collisions is not straight forward and requires a clear definition to the mass-centre coordinates. Otherwise fitting the model to the experiments produces significant overestimated viscous loss values. This is attributed to the complex inelastic nature of such collisions and the difference in the deformation time scale between the colliding droplets. Therefore, more research is required to quantify the mass-centre coordinates in collisions of unequal-size droplets collisions.

The factor k shows higher average value compared to the identical size collisions, $k = 6$. This difference is due to the change of the amounts of the interaction regions with the size ratio for a given impact parameter which consequently change the trend of the deformation change with B.

Overall, the proposed model is considered as an important advancement in predicting the collisions' outcomes, which is very important for many applications such as spray drying. To make better use from the model, more investigation is required to quantify

the maximum deformation limit and to avoid the need for the direct measurements of the shape factor. This might need a deep understanding of the role of the intervening gas layer. However, with the current model, the whole bouncing boundary can be predicted if the maximum deformation of one experimental point on the bouncing regime boundary is available.

Chapter 8: Concluding Remarks and Future Work

8.1 Summary

In the previous studies, droplet collisions have been studied by constructing regime maps for the collision's outcomes in the parameter space of the We and B. In these regime maps, five distinct collisions outcomes have been reported: slow coalescence, bouncing, fast coalescence, reflexive separation and stretching separation. These regimes have clear boundaries; however, they are not universal, and they change with viscosity and size ratio, which are not captured in We. Therefore, attempts have been reported to produce models, that account for these two factors, to predict the regimes' boundaries.

Although studies of the size ratio were reported, it has not been studied systematically, especially at high Oh. On the other hand, the reported models either lack accuracy or generality by not considering one or more of the following factors: size ratio, viscous loss and B. In addition, the reported studies are limited to collisions of identical liquid and immiscible liquids.

In this work, a rig was designed and developed to conduct experiments of binary droplets collisions. Regime maps of HPMC solutions were constructed to extend the understanding of the effects of size, size ratio and viscous loss in collisions of droplets of identical liquid. In addition, the role of the viscosity difference in collisions of miscible droplets was investigated for equal-size and unequal-size droplets. The performance and the applicability of the existing models of the boundaries of the regimes to such collisions were assessed, and new accurate and general models were proposed.

8.2 Experimental observations

8.2.1 Bouncing

- In collisions of identical droplets, increasing the viscosity and/or reducing the size of droplets promotes fast coalescence by shifting the boundary of the bouncing regime toward lower We. This is due to the higher viscosity decreasing the

droplet deformation and allowing more rapid drainage of the air layer between the colliding droplets. Whilst, reducing the size provides higher curvature and capillary pressure, which also enhance the air film drainage between the colliding droplets and that consequently promotes the coalescence.

- Unequal-size collisions of the low viscosity droplets, 2% HPMC, show similar bouncing regime to that of the equal-size collisions of the small droplet. However, collisions of higher viscosity droplets, 4% HPMC, show less bouncing (no bouncing at head-on collisions) compared to the equal-size collisions of the small droplet. This is attributed to that the small droplet reaches its maximum deformation and starts bouncing off before the large droplet, which still moves towards the small droplet. Therefore, the small droplets of the low viscosity collisions bounce in faster velocities than those of the higher viscosity, due to less viscous loss, and hence more chance to escape from the large droplet.
- In collisions of equal-size droplets of non-identical viscosities, the boundary of the bouncing regime occurs at an intermediate We between that of the two identical cases of the low and the high viscosity. In comparison to identical collisions at the lower viscosity, the deformation is only reduced in one of the droplets, therefore the drainage of the air layer only benefits from half the change versus the collisions at the higher viscosity. A new phenomenon, *partial bouncing*, is also observed at high viscosity ratio, whereby a thin ligament between the bounced droplets is observed.
- In collisions of unequal-size droplets of non-identical viscosities, both cases of non-identical viscosities, 2% (L) vs 4% (S) HPMC, and 2% (S) vs 4% (L) HPMC, show no bouncing at head-on collisions. This might be due to the less air entrapment in the presence of the high viscosity droplet that consequently, when the small droplet starts bouncing, the large droplet has a high chance to catch it as it chases it and hence late coalescence occurs.

8.2.2 Stretching separation

- In identical collisions, at the high $\mathrm{Oh} > 0.1$ studied, increasing the viscosity shifts the boundary of the stretching separation regime to higher B values this might be anticipated due to the increase in the viscous loss and the relative importance

of the viscosity term in the Oh number. However, at low $Oh < 0.1$ increasing the viscosity showed the opposite behaviour, this may be due to the increased role of surface tension. The reasons are not entirely clear and more investigation into this behaviour is required.

- In collisions of identical droplets, on reducing the droplet size, the boundary of the stretching separation regime moves to a higher B. This is because the smaller droplets have higher Oh. However, the sensitivity of these boundaries' shifts depends on the viscosity of the droplets as Oh of the low viscosity droplets is less sensitive to the droplet size.
- It should be noted that, although Oh increases by reducing the size or/and increasing the viscosity, the shift of the stretching separation boundary to high B at Oh < 0.1 that is seen by increasing the viscosity, is not seen by reducing the size. The reason behind this is also still not clear.
- Reducing the size ratio shifts the boundary of the stretching separation regime towards higher B, higher than the equal-size cases of the large and the small droplets. This is because, for a given B, the non-interaction region of the small droplet, which is the controller in the stretching energy, gets smaller by reducing the size ratio.
- In the case of collisions of equal-size and unequal-size droplets of non-identical viscosity, the stretching separation regime boundaries remain very similar to the identical viscosity cases for lower viscosity droplets. This was shown to be due to the filament being drawn mainly from the lower viscosity droplet and consequently, its breakup behaviour occurs at the low viscosity region and being like the low viscosity case. In addition, the satellite droplets produced from the breakup of the ligament during stretching separation, have a similar composition to the lower viscosity with a small amount of mixing.

8.2.3 Reflexive separation

- For identical droplets, the transition from fast coalescence to reflexive separation is shifted to higher We by increasing the viscosity, due to increased viscous loss. On the other hand, by reducing the size, the boundary of the reflexive separation regime moves to a higher We. This is because the smaller

droplets have higher Oh. Like the stretching separation, the sensitivity of these boundaries' shifts depends on the viscosity of the droplets as Oh of the low viscosity droplets is less sensitive to the droplet size.

- By reducing the size ratio, the boundary of the reflexive separation regime moves to a higher We than the equal size cases of the small and the large droplets. This is due to the loss of the symmetry, which leads to a one side reflexive flow.
- In collisions of equal-size droplets of non-identical viscosities, the boundary of the reflexive separation moves to intermediate values of We compared to the identical cases. Partial mixing is seen between the colliding droplets and hence a viscosity gradient in the necking ligament. The lower viscosity droplet detaches at the low viscosity end of the ligament. This leads to a smaller low viscosity droplet and a larger droplet composed of both the higher viscosity fluid mixed with a little lower viscosity fluid.
- In collisions of unequal-size droplets of non-identical viscosities, if the large droplet is the lower viscosity, 2% (L) vs 4% (S) HPMC, the reflexive jet is from the low viscosity and no significant mixing occurs. Consequently, the onset of the reflexive separation has similar We to that of the collisions of the unequal-size droplets with identical viscosities of 2% HPMC. In addition, the separated droplets are a small droplet of low viscosity, 2% HPMC, and a large mixed droplet. On the other hand, if the large droplet is the higher viscosity, 2% (S) vs 4% (L) HPMC, a significant mixing occurs. Consequently, the onset of the reflexive separation has an intermediate We between those of the collisions of unequal-size droplets with identical viscosities of 2% HPMC and 4% HPMC.

8.3 Modelling of the regime boundaries

8.3.1 Bouncing boundary

The existing models of the bouncing regime boundaries, of Estrade et al. (1999) and Hu et al. (2017), show poor performance in predicting the experimental bouncing boundaries. The poor performance is primarily attributed to the assumption that the surface energy at the maximum deformation is independent of the impact parameter, i.e. constant shape factor. However, the experimental images clearly show that the

deformation reduces significantly with the impact parameter and consequently, a constant shape factor cannot be assumed.

Several errors in the derivation of the models were also identified. The derivation of the spherical cap shape factor of Estrade et al. (1999), which was reapplied by Hu et al. (2017), was shown to contain an error. However, an oblate spheroid geometry was found to give a better fit to the droplet shape at maximum deformation for head-on collisions than the spherical cap. Therefore, the oblate spheroid surface area was applied to derive a new shape factor. Additionally, issues in the definition of the collisions' kinetic energy were identified, as in Estrade et al. (1999) the momentum is not conserved, while Hu et al. (2017) overpredict the energy contributes to the droplet deformation in collisions of B > 0.

Using the proposed oblate spheroid shape factor, and a corrected kinetic energy definition, a modified model for the bouncing regime boundary was proposed. The shape factor for head-on collisions was taken directly from measurements, and the reduction in shape factor with increasing B fitted empirically using a power-law model. Viscous dissipation was also considered in the proposed model through a single viscous dissipation factor. The viscous dissipation factor was estimated directly from the experimental observations by analysing the decay in the oscillations of droplet shape which occurs after each collision.

The proposed model shows a great fit to the experimental results. For all HPMC systems, the critical We number for head-on collisions is well predicted and the fit to the boundary of the bouncing regime is excellent for across the range of We numbers tested.

Applying the model to eleven regime maps, of identical and non-identical viscosity collisions, provided a good set of data to the viscous loss factor α_2 and the deformation change factor k to produce scaling laws that allow quantifying them for a wide range of Oh. Plotting the vicious loss versus Oh shows similar trend seen by Planchette et al. (2017) during the compression phase in reflexive separation. At Oh < 0.06, α_2 increases with Oh then a plateau is observed at 0.06 < Oh < 0.15, where $\alpha_2 \sim 0.25$ then α_2 increases again with Oh at Oh > 0.15. On the other hand, k was found to scatter around

an average value of 3.8. Using the empirical correlations of α_2 with Oh and the average value of k shows good fits with experiments.

Using the model in collisions of unequal-size droplets is not straight forward and requires a clear definition to the mass-centre coordinates. Otherwise fitting the model to the experiments produces significant overestimated viscous loss values. This is attributed to the complex inelastic nature of such collisions and the difference in the deformation time scale between the colliding droplets. Therefore, more research is required to quantify the mass-centre coordinates in collisions of unequal-size droplets collisions.

The factor k of unequal-size collisions shows a higher average value compared to the identical size collisions, $k = 6$. This difference might be due to the change of the amounts of the interaction regions by changing the size ratio, for a given impact parameter, which consequently changes the way that the deformation changes with B.

Overall, the proposed model is considered as an important advancement in predicting the collisions' outcomes, which is very important for many applications such as spray drying. To make better use from the model, more investigation is required to quantify the maximum deformation limit and to avoid the need for the direct measurements of the shape factor. This might need a deep understanding of the role of the intervening gas layer. However, with the current model, the whole bouncing boundary can be predicted if the maximum deformation of one experimental point on the bouncing regime boundary is available.

8.3.2 Stretching separation boundary

The model of Jiang et al. (1992) can predict the shape of the stretching separation boundary if its adjustable parameter C_a is known. However, it was found that C_a cannot be correlated with Oh because it scales differently with Oh changes by μ than Oh changes by d. Thus, more investigations are required to find a general scaling law for C_a or to produce a new model for the boundary of the stretching separation regime.

8.3.3 Reflexive separation boundary

Considering the effect of the impact parameter in the modelling of the reflexive separation regime has received poor attention in the literature. The existing models which consider the effect of the size ratio and B are the inviscid model of Ashgriz and Poo (1990) and the model of Hu et al. (2017), which is a modified version of the former by considering the viscous loss. However, it was found that these models have many issues related to considering the effect of B and the viscous loss.

Previously, in both models, it was believed that the suppression of the reflexive separation as B increases, is driven by the reduction in the interaction regions. This reduction reduces the kinetic energy that contributes to the formation of the rimmed lamellar disc and hence less surface energy will be stored at the maximum deformation of the disc, which afterwards converts into reflexive flow. Moreover, the kinetic energy of the regions of the non-interaction acts as suppressing energy against the reflexive flow. Ashgriz and Poo (1990) used a prolate geometry to represent the interaction region, while Hu et al. (2017) used spherical cap geometry. However, it was found that invalid formulas were used to represent both geometries.

In regard of considering the viscous loss, Hu et al. (2017) apply an incorrect approach to consider the effect of the viscous loss by using a single fitting parameter that represents the ratio of the total viscous loss to the kinetic energy. This is because this ratio does not scale with viscosity, as it is $\sim$100% at the instant of the reflexive separation, and the seen scaling trend is due to the use of the empirical criteria of Ashgriz and Poo (1990), which includes 100% loss of the kinetic energy of water droplet collisions at the onset of the reflexive separation regime.

The viscous loss is considered in more details in the model of Tang et al. (2012). However, the model only considers head-on collisions. Therefore, it has been extended to account for the effect of B. This was done by correcting the spherical cap interaction regions formulas and looking into the dynamics in 3D imaging to understand the mechanism that gives the shape of the boundary with B. Observing the front view of the dynamics shows that at off-centre collisions the stretching energy does not have a direct effect at the reflexive flow. This is because the droplets still make a thin-rimmed

lamellar disc at the maximum deformation and the geometry of that disc stays still for few microseconds, which means the flow of the non-interaction regions vanishes before the reflexive flow. However, the effect of the non-interaction regions was seen as rotational energy as the rotation of the disc was observed and hence it can be ignored in the model. On the other hand, the side view shows that the off-centre collisions produce a non-uniform rim thickness at the maximum deformation of the disc compared to the head-on collisions where a uniform rim was seen. This results in non-uniform disc retraction as the thinner parts of the rim retract faster than the thicker parts. Consequently, the disc asymmetric retraction leads to a weaker reflexive flow, than that of the head-on collisions. This what mainly contributes to suppressing of the reflexive separation regime by increasing B. Therefore, the effect of the asymmetrical shrinking of the rim was empirically introduced to the model as an extra viscous loss during the stage of the disc retraction using a power law as a function of B. This power law was adapted to fit the model to a wide range of experimentally generated data in this work in addition to data reproduced from the literature.

8.4 Future Work

Many questions have been left for future work. These are summarised in the following:

8.4.1 Bouncing

In the modelling of the bouncing boundary, it is assumed that the kinetic energy of the droplets at the maximum deformation equals to zero. However, in unequal-size collisions, the small droplets reach their maximum deformations faster than the large droplets and hence they bounce faster. Consequently, the kinetic energy of the large droplet will not be equal to zero at its maximum deformation. Because of this, fitting the model to experiments requires higher values of viscous loss, α_2, compared to those seen in the equal-size collisions. Therefore, the correlations, $\alpha_2 = f(\mathrm{Oh})$, developed in Chapter seven cannot be used in collisions of unequal-size droplets. Thus, there is a need for a systematic investigation to the bouncing of unequal-size droplets to study the remaining energy of the large droplet as a function of the size ratio. Then, the understanding arises from such study needs to be incorporated in the model of the bouncing regime boundary via adding the remaining kinetic energy of the large droplet to the energy balance, Eq. (7.12).

The model of the bouncing boundary can be significantly improved by developing a criterion that can evaluate the transitional We between bouncing and fast coalescence. This requires a deep understanding to the dynamics of the thin air film that is trapped between the droplets. This might be achieved by studying the critical thickness of the air film and linked to the effective distance of the intermolecular forces. Then, effects of parameters such as size, size ratio, viscosity, density and surface tension on We required to a chive the critical air film thickness need to be studied as well. These studies might be possible by using interferometry imaging techniques similar to that used by Langley (2019). Moreover, numerical modelling with same capabilities of Pan et al. (2017) and Chubynsky et al. (2019) can be helpful to be used alongside the experiments. In addition, molecular dynamics simulations as in Zhang et al. (2016) can be useful to be integrated with the numerical and the experimental studies to provide a criterion for the bouncing regime which is still a big gap of knowledge.

8.4.2 Stretching separation

Increasing the viscosity of the droplets is expected to shift the boundary of the stretching separation to higher B values. However, the experiments in this study show that, at Oh < 0.1, increasing the viscosity shifts the boundary to lower B values. Therefore, a numerical systematic investigation to the role of the viscosity in the stretching separation regime at Oh < 0.1 might be helpful to understand the underlying physics.

In terms of modelling the boundary of the stretching separation, although the model of Jiang et al. (1992) can predict the boundary shape, it is still lack for a general correlation to evaluate its fitting parameter C_a. Therefore, there is a need for more investigation in the modelling of the boundary of the stretching separation regime.

8.4.3 Reflexive separation

It is interesting to systematically study the dynamics of the asymmetric retraction of the lamellar disc in reflexive separation collisions at B > 0 to provide a theoretical function that accounts for the role of B instead of the empirical one that we have used in Chapter 6.

8.4.4 post-collisions trajectories

Most of the conducted work in binary droplet collisions is to study the collisions' outcomes and to develop models to the regimes' boundaries in order to be used in the numerical simulations of sprays applications, for example. However, in these simulations, there is a need for models to predict trajectories of droplets after collisions. Such models have poorly studied in the literature. Therefore, it is important to incorporate the developed knowledge of the underlying physics, from the studies of the collision's outcomes, in modelling the post-collisions trajectories of the droplets.

Chapter 9: References

Adam, J.R., Lindblad, N.R. and Hendricks, C.D., 1968. The collision, coalescence, and disruption of water droplets. Journal of Applied Physics, 39(11), pp.5173-5180.

Alanazi, F.K., El-Badry, M. and Alsarra, I.A., 2006. Spray-dried HPMC microparticles of indomethacin: impact of drug-polymer ratio and viscosity of the polymeric solution on dissolution. Saudi Pharmaceutical Journal, 14(2), pp.100-107.

Almohammed, N. and Breuer, M., 2019. Towards a deterministic composite collision outcome model for surface-tension dominated droplets. International Journal of Multiphase Flow, 110, pp.1-17.

Andrade, R.D., Skurtys, O. and Osorio, F.A., 2012. Atomizing spray systems for application of edible coatings. Comprehensive Reviews in Food Science and Food Safety, 11(3), pp.323-337.

Ashgriz, N. and Poo, J.Y., 1990. Coalescence and separation in binary collisions of liquid drops. Journal of Fluid Mechanics, 221, pp.183-204.

Basu, A.S., 2013. Droplet morphometry and velocimetry (DMV): a video processing software for time-resolved, label-free tracking of droplet parameters. Lab on a Chip, 13(10), pp.1892-1901.

Blanchette, F. and Bigioni, T.P., 2006. Partial coalescence of drops at liquid interfaces. Nature Physics, 2(4), p.254.

Brazier-Smith, P.R., Jennings, S.G. and Latham, J., 1972. The interaction of falling water drops: coalescence. Proceedings of the Royal Society of London. A. Mathematical and Physical Sciences, 326(1566), pp.393-408.

Castrejon-Pita, A.A., Castrejon-Pita, J.R. and Hutchings, I.M., 2012. Breakup of liquid filaments. Physical review letters, 108(7), p.074506.

Chen, R.H. and Chen, C.T., 2006. Collision between immiscible drops with large surface tension difference: diesel oil and water. Experiments in fluids, 41(3), pp.453-461.

Chen, R.H., 2007. Diesel–diesel and diesel–ethanol drop collisions. Applied Thermal Engineering, 27(2-3), pp.604-610.

Chubynsky, M.V., Belousov, K.I., Lockerby, D.A. and Sprittles, J.E., 2019 Bouncing off the walls: The influence of gas-kinetic and van der Waals effects in drop impact.

Finotello, G 2019, 'Droplet collision dynamics in a spray dryer: experiments and simulations', PhD thesis, Technische Universiteit Eindhoven, Eindhoven.

Finotello, G., De, S., Vrouwenvelder, J.C., Padding, J.T., Buist, K.A., Jongsma, A., Innings, F. and Kuipers, J.A.M., 2018a. Experimental investigation of non-Newtonian droplet collisions: the role of extensional viscosity. Experiments in Fluids, 59(7), p.113.

Finotello, G., Kooiman, R.F., Padding, J.T., Buist, K.A., Jongsma, A., Innings, F. and Kuipers, J.A.M., 2018b. The dynamics of milk droplet–droplet collisions. Experiments in Fluids, 59(1), p.17.

Finotello, G., Padding, J.T., Buist, K.A., Jongsma, A., Innings, F. and Kuipers, J.A.M., 2019a. Droplet collisions of water and milk in a spray with Langevin turbulence dispersion. International Journal of Multiphase Flow, 114, pp.154-167.

Finotello, G., Padding, J.T., Buist, K.A., Schijve, A., Jongsma, A., Innings, F. and Kuipers, J.A.M., 2019b. Numerical investigation of droplet-droplet collisions in a water and milk spray with coupled heat and mass transfer. Drying Technology, pp.1-23.

Finotello, G., Padding, J.T., Deen, N.G., Jongsma, A., Innings, F. and Kuipers, J.A.M., 2017. Effect of viscosity on droplet-droplet collisional interaction. Physics of Fluids, 29(6), p.067102.

Focke, C., Kuschel, M., Sommerfeld, M. and Bothe, D., 2013. Collision between high and low viscosity droplets: direct numerical simulations and experiments. International journal of multiphase flow, 56, pp.81-92.

Francia, V., Martín, L., Bayly, A.E. and Simmons, M.J., 2016. Agglomeration in counter-current spray drying towers. Part A: Particle growth and the effect of nozzle height. Powder Technology, 301, pp.1330-1343.

Gao, T.C., Chen, R.H., Pu, J.Y. and Lin, T.H., 2005. Collision between an ethanol drop and a water drop. Experiments in Fluids, 38(6), pp.731-738.

Gavaises, M., Theodorakakos, A., Bergeles, G. and Brenn, G., 1996. Evaluation of the effect of droplet collisions on spray mixing. Proceedings of the Institution of Mechanical Engineers, Part C: Journal of Mechanical Engineering Science, 210(5), pp.465-475.

Gotaas, C., Havelka, P., Jakobsen, H.A., Svendsen, H.F., Hase, M., Roth, N. and Weigand, B., 2007. Effect of viscosity on droplet-droplet collision outcome: Experimental study and numerical comparison. Physics of fluids, 19(10), p.102106.

Gotaas, C., Havelka, P., Jakobsen, H.A., Svendsen, H.F., Hase, M., Roth, N. and Weigand, B., 2007b. Effect of viscosity on droplet-droplet collision outcome: Experimental study and numerical comparison. Physics of fluids, 19(10), p.102106.

He, C., Xia, X. and Zhang, P., 2019. Non-monotonic viscous dissipation of bouncing droplets undergoing off-center collision. Physics of Fluids, 31(5), p.052004.

Hicks, P.D. and Purvis, R., 2010. Air cushioning and bubble entrapment in three-dimensional droplet impacts. Journal of Fluid Mechanics, 649, pp.135-163.

Hilton, J.E., Ying, D.Y. and Cleary, P.W., 2013. Modelling spray coating using a combined CFD–DEM and spherical harmonic formulation. Chemical Engineering

Hu, C., Xia, S., Li, C. and Wu, G., 2017. Three-dimensional numerical investigation and modeling of binary alumina droplet collisions. International Journal of Heat and Mass Transfer, 113, pp.569-588.

Huang, K.L., Pan, K.L. and Josserand, C., 2019. Pinching Dynamics and Satellite Droplet Formation in Symmetrical Droplet Collisions. Physical Review Letters, 123(23), p.234502.

Jia X, Yang JC, Zhang J, Ni MJ. An experimental investigation on the collision outcomes of binary liquid metal droplets. International Journal of Multiphase Flow. 2019 Jul 1;116:80-90.

Jiang, Y.J., Umemura, A. and Law, C.K., 1992. An experimental investigation on the collision behaviour of hydrocarbon droplets. Journal of Fluid Mechanics, 234, pp.171-190.

Karim, F.T., Sarker, Z.M., Ghafoor, K., Al-Juhaimi, F.Y., Jalil, R.U., Awang, M.B., Amid, M., Hossain, M.S. and Khalil, H.A., 2016. Microencapsulation of fish oil using hydroxypropyl methylcellulose as a carrier material by spray drying. Journal of Food Processing and Preservation, 40(2), pp.140-153.

Ko, G.H. and Ryou, H.S., 2005. Droplet collision processes in an inter-spray impingement system. Journal of aerosol science, 36(11), pp.1300-1321.

Kolinski, J.M., Rubinstein, S.M., Mandre, S., Brenner, M.P., Weitz, D.A. and Mahadevan, L., 2012. Skating on a film of air: drops impacting on a surface. Physical review letters, 108(7), p.074503.

Krishnan, K.G. and Loth, E., 2015. Effects of gas and droplet characteristics on drop-drop collision outcome regimes. International Journal of Multiphase Flow, 77, pp.171-186.

Kuschel, M. and Sommerfeld, M., 2013. Investigation of droplet collisions for solutions with different solids content. Experiments in fluids, 54(2), p.1440.

Langley, K., Li, E.Q. and Thoroddsen, S.T., 2017. Impact of ultra-viscous drops: air-film gliding and extreme wetting. Journal of Fluid Mechanics, 813, pp.647-666.

Lefebvre, Arthur H. McDonell, Vincent G.. (2017). Atomization and Sprays (2nd Edition) - 2.5.1 Flat Sheets. CRC Press.

Li, J., Wu, F., Lin, X., Shen, L., Wang, Y. and Feng, Y., 2015. Novel application of hydroxypropyl methylcellulose to improving direct compaction properties of tablet fillers by co-spray drying. Rsc Advances, 5(85), pp.69289-69298.

Low, T.B. and List, R., 1982. Collision, coalescence and breakup of raindrops. Part I: Experimentally established coalescence efficiencies and fragment size distributions in breakup. Journal of the Atmospheric Sciences, 39(7), pp.1591-1606.

Mazloomi Moqaddam, A., Chikatamarla, S.S. and Karlin, I.V., 2016. Simulation of binary droplet collisions with the entropic lattice Boltzmann method. Physics of Fluids, 28(2), p.022106.

McKinley, G.H., 2005. Dimensionless groups for understanding free surface flows of complex fluids.

Mezhericher, M., Levy, A. and Borde, I., 2008. Droplet–droplet interactions in spray drying by using 2D computational fluid dynamics. Drying Technology, 26(3), pp.265-282

Notz PK, Basaran OA. Dynamics and breakup of a contracting liquid filament. Journal of Fluid Mechanics. 2004 Aug; 512:223-56.

Ochs III, H.T., Beard, K.V., Laird, N.F., Holdridge, D.J. and Schaufelberger, D.E., 1995. Effects of relative humidity on the coalescence of small precipitation drops in free fall. Journal of the atmospheric sciences, 52(21), pp.3673-3680.

Ohnesorge, W.V., 1936. Die bildung von tropfen an düsen und die auflösung flüssiger strahlen. ZAMM-Journal of Applied Mathematics and Mechanics/Zeitschrift für Angewandte Mathematik und Mechanik, 16(6), pp.355-358

Orme, M., 1997. Experiments on droplet collisions, bounce, coalescence and disruption. Progress in Energy and Combustion Science, 23(1), pp.65-79.

O'Rourke, P.J. Collective drop effects on vaporizing liquid sprays. United States: N. p., 1981. Web.

Pan, K.L., Tseng, Y.H., Chen, J.C., Huang, K.L., Wang, C.H. and Lai, M.C., 2016. Controlling droplet bouncing and coalescence with surfactant. Journal of Fluid Mechanics, 799, pp.603-636.

Park, R.W., 1970. Behavior of Water Drops Colliding In Humid Nitrogen. Department of Chemical Engineering, p.577 Ph.D. thesis.

Pawar, S., Padding, J., Deen, N., Jongsma, A., Innings, F. and Kuipers, J.H., 2015. Numerical and experimental investigation of induced flow and droplet–droplet interactions in a liquid spray. Chemical Engineering Science, 138, pp.17-30.

Planchette, C., Hinterbichler, H., Liu, M., Bothe, D. and Brenn, G., 2017. Colliding drops as coalescing and fragmenting liquid springs. Journal of fluid mechanics, 814, pp.277-300.

Planchette, C., Lorenceau, E. and Brenn, G., 2010. Liquid encapsulation by binary collisions of immiscible liquid drops. Colloids and Surfaces A: Physicochemical and Engineering Aspects, 365(1-3), pp.89-94.

Planchette, C., Lorenceau, E. and Brenn, G., 2011. Binary collisions of immiscible liquid drops for liquid encapsulation. Fluid dynamics & materials processing, 7(3), pp.279-301.

Planchette, C., Lorenceau, E. and Brenn, G., 2012. The onset of fragmentation in binary liquid drop collisions. Journal of fluid mechanics, 702, pp.5-25.

Plateau, J., 1873. Statique expérimentale et théorique des liquides soumis aux seules forces moléculaires (Vol. 2). Gauthier-Villars.

Post, S.L. and Abraham, J., 2002. Modeling the outcome of drop–drop collisions in Diesel sprays. International Journal of Multiphase Flow, 28(6), pp.997-1019.

Qian, J. and Law, C.K., 1997. Regimes of coalescence and separation in droplet collision. Journal of Fluid Mechanics, 331, pp.59-80.

Rabe, C., Malet, J. and Feuillebois, F., 2010. Experimental investigation of water droplet binary collisions and description of outcomes with a symmetric Weber number. Physics of fluids, 22(4), p.047101.

Rayleigh, L., 1892. XVI. On the instability of a cylinder of viscous liquid under capillary force. The London, Edinburgh, and Dublin Philosophical Magazine and Journal of Science, 34(207), pp.145-154.

Rayleigh, L., 1945. The Theory of Sound, vol. 2, Dover.

Roisman, I.V., 2004. Dynamics of inertia dominated binary drop collisions. Physics of Fluids, 16(9), pp.3438-3449.

Saffman, P.G.F. and Turner, J.S., 1956. On the collision of drops in turbulent clouds. Journal of Fluid Mechanics, 1(1), pp.16-30.

Sangalli, M.E., Maroni, A., Foppoli, A., Zema, L., Giordano, F. and Gazzaniga, A., 2004. Different HPMC viscosity grades as coating agents for an oral time and/or site-controlled delivery system: a study on process parameters and in vitro performances. European Journal of Pharmaceutical Sciences, 22(5), pp.469-476.

Schwarzkopf, J.D., Sommerfeld, M., Crowe, C.T. and Tsuji, Y., 2011. Multiphase flows with droplets and particles. CRC press.Estrade, J.P., Carentz, H., Lavergne, G. and Biscos, Y., 1999. Experimental investigation of dynamic binary collision of ethanol droplets–a model for droplet coalescence and bouncing. International Journal of Heat and Fluid Flow, 20(5), pp.486-491.

Schwarzkopf, J.D., Sommerfeld, M., Crowe, C.T. and Tsuji, Y., 2011. Multiphase flows with droplets and particles. CRC press.

Sommerfeld, M. and Kuschel, M., 2016. Modelling droplet collision outcomes for different substances and viscosities. Experiments in Fluids, 57(12), p.187.

Sommerfeld, M. and Pasternak, L., 2019. Advances in Modelling of Binary Droplet Collision Outcomes in Sprays: A Review of Available Knowledge. International Journal of Multiphase Flow.

Southwell, D.B. and Langrish, T.A.G., 2000. Observations of flow patterns in a spray dryer. Drying Technology, 18(3), pp.661-685.

Tang, C., Zhang, P. and Law, C.K., 2012. Bouncing, coalescence, and separation in head-on collision of unequal-size droplets. Physics of Fluids, 24(2), p.022101.

Tsuru, D., Tajima, H., Ishibashi, R. and Kawauchi, S., 2010. Droplet collision modelling between merging immiscible sprays in direct water injection system. In ILASS Europe, 23rd annual conference on liquid atomization and spray systems, Brno, Czech Republic.

Verdurmen, R.E.M., Houwelingen, G.V., Gunsing, M., Verschueren, M. and Straatsma, J., 2006. Agglomeration in spray drying installations (the EDECAD project): Stickiness measurements and simulation results. Drying Technology, 24(6), pp.721-726.

Verdurmen, R.E.M., Menn, P., Ritzert, J., Blei, S., Nhumaio, G.C.S., Sonne Sørensen, T., Gunsing, M., Straatsma, J., Verschueren, M., Sibeijn, M. and Schulte, G., 2004. Simulation of agglomeration in spray drying installations: The EDECAD project. Drying technology, 22(6), pp.1403-1461.

Wang, C.H., Hung, W.G., Fu, S.Y., Huang, W.C. and Law, C.K., 2003. On the burning and microexplosion of collision-generated two-component droplets: miscible fuels. Combustion and flame, 134(3), pp.289-300.

Willis, K. and Orme, M., 2003. Binary droplet collisions in a vacuum environment: an experimental investigation of the role of viscosity. Experiments in fluids, 34(1), pp.28-41.

Zhang, Y.R., Jiang, X.Z. and Luo, K.H., 2016. Bounce regime of droplet collisions: A molecular dynamics study. Journal of Computational Science, 17, pp.457-462.

Appendix A Viscous loss

Figure A.1 shows that the viscous loss in the compressions phase ($E_{\mu,1}$) is linearly correlated with the initial kinetic energy of the collisions ($E_{k,ini}$). This agrees with the findings of Planchette et al (2017). The calculation procedure is described in detail in Planchette et al. (2017). The slop in 2% and 4% HPMC is 0.67 ± 0.02, which is equal to the value of a at the plateau region of α vs. Oh in Figure. 10 in Planchette et al. (2017). However, in 8% HPMC the slope is higher due to the high $\mathrm{Oh} > 0.1$ (the maximum Oh of the plateau region).

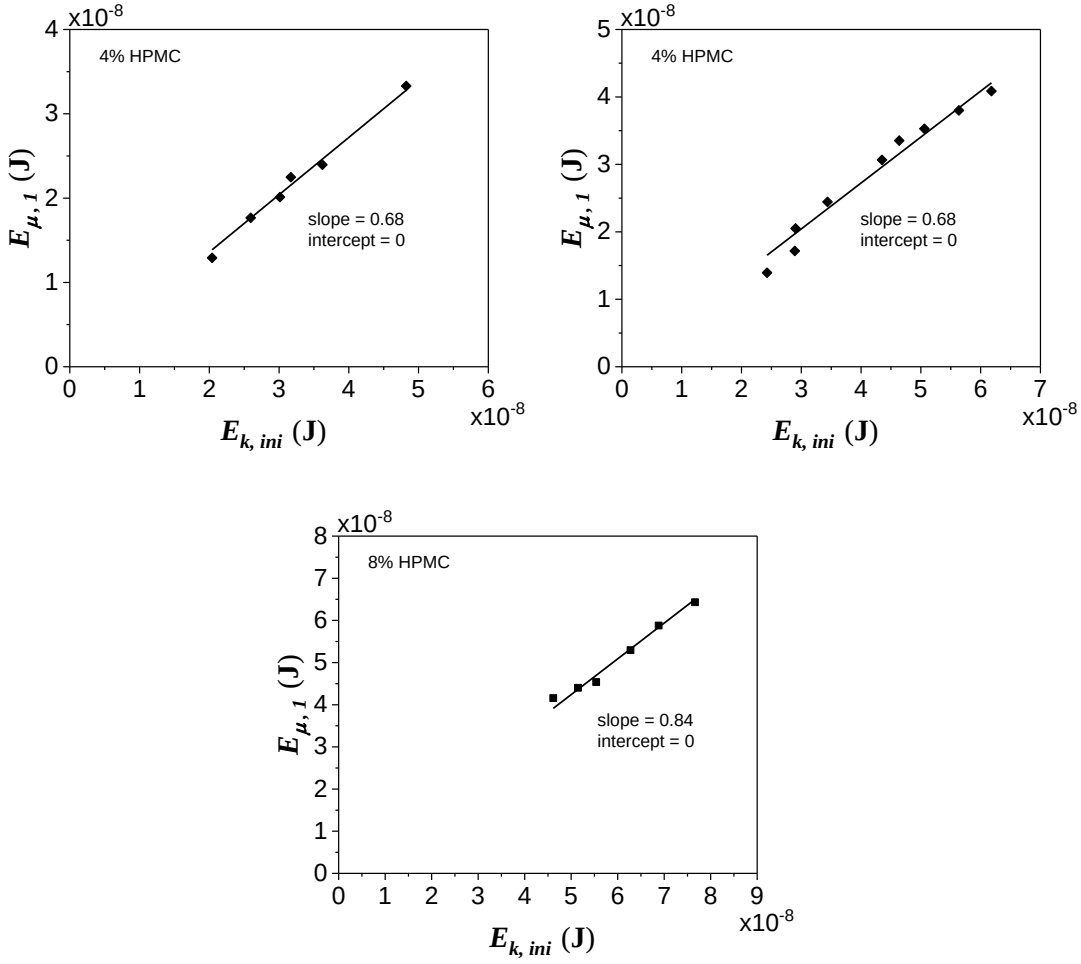

Figure A.1 The viscous loss as a function of the initial kinetic energy of head-on collisions for the 2%, 4% and 8% HPMC systems.

Appendix B Evaluation of the volume ratio of the non-interaction regions

The interaction regions can be divided into two cases: the first case is when the whole small droplet interacts with the large droplet and the second case is whine both droplets have non-interaction regions, as shown in Figure B.1 (a and b), respectively.

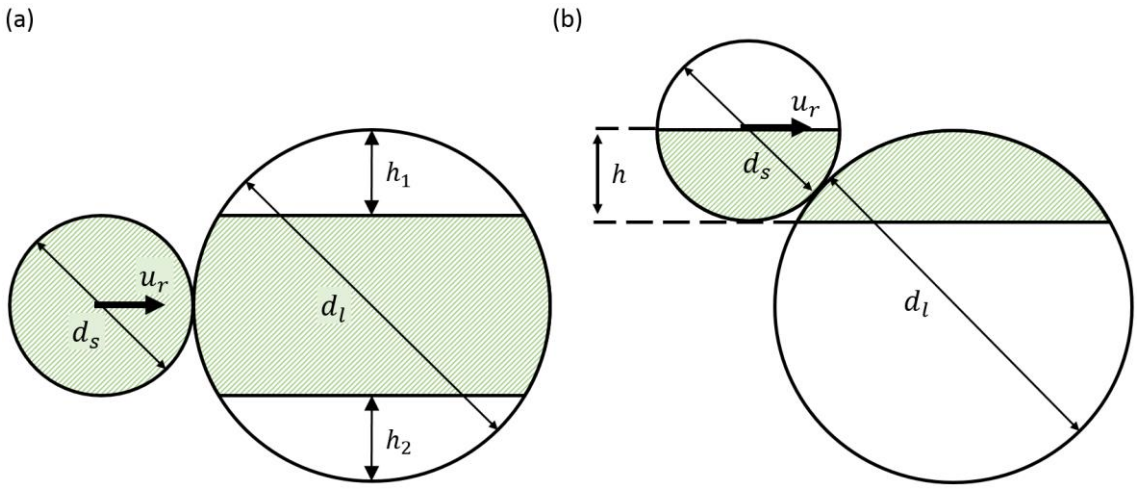

Figure B.1 Two cases of the non-interaction regions. a) the whole small droplet interacts with the large droplet; b) both droplets have non-interactions regions.

The first case, in Figure B.1a, can be represented by an impact parameter limit given by the condition

$$B \leq \frac{d_l - ds}{d_l + d_s}. \tag{B.1}$$

In this case the interaction region of the large droplet can be given by

$$X'_l = 1 - X_{h_1} - X_{h_2}, \tag{B.2}$$

where X_{h_1} and X_{h_2} are the volume ratios of the unshaded spherical caps, in Figure B.1a, and given by

$$X_{h_i} = \frac{V_{cap,i}}{V_{sphere,l}} = \frac{2h_i^2\left(\frac{3}{2}d_l - h_i\right)}{d_l^3}. \tag{B.3}$$

Substituting Eq. (B.3) in Eq. (B.2) gives

$$X'_l = 1 - \left(\frac{2h_1^2\left(\frac{2}{3}d_l - h_1\right)}{d_l^3}\right) - \left(\frac{2h_2^2\left(\frac{2}{3}d_l - h_2\right)}{d_l^3}\right), \tag{B.4}$$

where h_1 and h_2 can be evaluated from

$$h_1 = \frac{d_l - ds}{2} + \frac{\mathrm{B}(d_l + d_s)}{2} \tag{B.5}$$

and

$$h_2 = \frac{d_l - ds}{2} - \frac{\mathrm{B}(d_l + d_s)}{2}. \tag{B.6}$$

The second case when the two droplets have non-interaction regions as in Figure b is when

$$B > \frac{d_l - ds}{d_l + d_s}. \tag{B.7}$$

$$X'_i = \frac{V_{cap,i}}{V_{sphere,i}} = \frac{2h^2\left(\frac{3}{2}d_i - h\right)}{d_i^3}, \tag{B.8}$$

where the subscript i here means s or l (the small or the large droplet).

In this case the height h of both spherical caps of the regions of the interactions is represented in terms of the impact parameter by

$$h = \frac{1}{2}(d_l + d_s)(1 - B). \tag{B.9}$$

Substituting Eq. (B.9) in Eq. (B.8) gives

$$X'_l = \frac{1}{4}\tau^2(3 - \tau) \tag{B.10}$$

and

$$X'_s = \frac{\tau^2(3\Delta - \tau)}{4\Delta^3}, \tag{B.11}$$

where

$$\tau = (1 - B)(1 + \Delta). \tag{B.12}$$

Note that the non-interaction regions are only considered in the front view. The non-interaction regions of the large droplet from the side view that would result from cases of $\Delta < 1$ are not considered in the above derivations. This because it is believed that it has a negligible effect on the collisions outcomes compared to those result from the offset.

Appendix C Spherical cap shape factor derivation

The volume of a spherical cap is

$$V_{cap}\frac{\pi h^2}{3}(3r_d - h), \tag{C.1}$$

Where, r_d is the radius of the deformed droplet (spherical cap), and h is the height of the cap as defined in Figure 7.2. From the mass conservation, Eq. (C.1) will be equal to sphere volume, hence

$$r_d = \frac{d^3}{6h^2} + \frac{h}{3}, \tag{C.2}$$

where, d is the diameter of the non-deformed droplet. The surface area of the spherical cap is given by

$$S.A_{cap} = \pi(4r_d h + h^2). \tag{C.3}$$

Substituting Eq. (C.2) in Eq. (C.3) and evaluating for the surface energy of colliding droplets at maximum deformation give

$$E_{\sigma,fin} = \pi\sigma\left(\frac{2}{3}\frac{d_{lo}^3}{h_l} + \frac{1}{3}h_l^2\right) + \pi\sigma\left(\frac{2}{3}\frac{d_{so}^3}{h_s} + \frac{1}{3}h_s^2\right). \tag{C.4}$$

From mass conservation and substituting $\phi = \frac{h}{r_d}$,

$$h = d_o\left(\frac{6}{\phi} - 2\right)^{\frac{1}{3}}. \tag{C.5}$$

Sub (C.5) in (C.4) gives

$$E_{\sigma,fin} = \pi\sigma d_{lo}^2\left(\frac{2}{3}\left(\frac{6}{\phi} - 2\right)^{-\frac{1}{3}} + \frac{1}{3}\left(\frac{6}{\phi} - 2\right)^{\frac{2}{3}}\right)(1 + \Delta^2). \tag{C.6}$$

From the analogy between Eq. (C.6) and Eq. (7.8), the correct shape factor of spherical cap is

$$\phi_c' = \frac{2}{3}\left(\frac{6}{\phi} - 2\right)^{-\frac{1}{3}} + \frac{1}{3}\left(\frac{6}{\phi} - 2\right)^{\frac{2}{3}}. \tag{C.7}$$

Appendix D The viscosity effect on the boundary of the bouncing regime.

Figure D.1 shows the effect of the viscosity on the whole boundary of the bouncing regime.

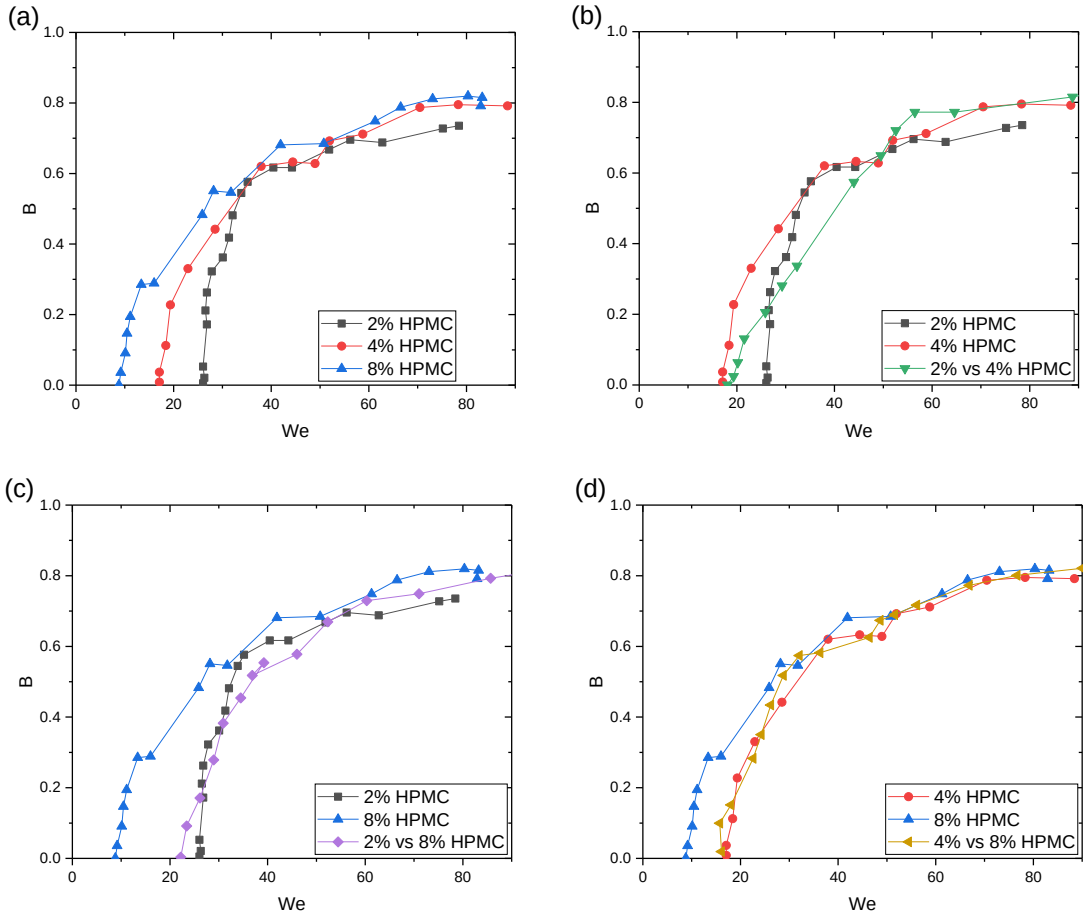

Figure D.1 The effect of the viscosity on the whole bouncing boundary for the HPMC data presented in Chapter 4.